Investigations of the Nematic Phase Structure and Biaxiality of Selected Oxadiazole Mesogens Employing an Optimized Force Field

BOYD, NICOLA,JANE

Investigations of the Nematic Phase Structure and Biaxiality of Selected Oxadiazole Mesogens Employing an Optimized Force Field

Nicola Jane Boyd

Department of Chemistry
Durham University

December 2016
Submitted in the partial fulfilment of the requirements for the degree of
Doctor of Philosophy

Abstract

A unique class of bent-core nematics, based on the *bis*-phenyl-oxadiazole motif, have attracted considerable attention due to their unusual properties, including the possibility of forming the elusive biaxial nematic phase, a phase with significant potential for technological applications. A summary of current research into biaxial nematics is given, including experimental evidence, controversies, and the different computational models used to study this phase. Fully atomistic molecular dynamic simulations were employed to study the differences and relationships in the mesophase molecular organization of four closely related oxadiazole bent-core molecules. As an accurate force field is essential to model liquid crystal systems, it was first found necessary to partially re-parametrize the General Amber Force Field, (GAFF), to accurately reproduce phase transitions of liquid crystal mesogens. Dramatic improvements of phase transition temperature predictions for a number of liquid crystals were achieved with the new force field, compared to the original GAFF predictions.

Using the improved force field, GAFF-LCFF, the uniaxial and biaxial orientational order parameters were deduced for the four oxadiazole derivatives. These were found to be in good agreement with experimental data, where available. Small differences in the magnitude of the biaxial order parameters were found between the four oxadiazole systems in their respective nematic phases, with the bent-core mesogen, C5-Ph-ODBP-Ph-OC12 displaying the largest values. The simulations confirm that the nematic phase biaxiality is predominantly local and not macroscopic, and do not support the presence of large cybotactic clusters with inherent biaxial order.

The atomistic simulations enabled the distinct differences in structure and molecular organization in the nematic phase of the four systems to be identified and analyzed, and the simulations were found to accurately represent a range of experimental observables, including the manifestation of enhanced local biaxial correlations for a trimethlylated oxadiazole based mesogen.

The study also provides the novel result of the first simulation insight into the local structure of the dark conglomerate (DC) phase, and shows evidence of pretransitional fluctuations relating to the onset of the DC phase in the bent-core mesogen

C5-Ph-ODBP-Ph-OC12. A number of explanations linking key molecular chemical and structural features to mesophase behaviour have also been proposed.

Declaration

The work in this thesis is based on research carried out at Durham University. The material contained in this thesis has not previously been submitted for any other degree at Durham University or any other institution. The research within this thesis has been conducted by the author unless indicated otherwise.

Nicola Jane Boyd

December 2016

Acknowledgments

Completing this thesis has been a journey for me, both scientifically and emotionally. Without the support I received, I would not have been able to even commence this journey, let alone complete it, and I would like to acknowledge my thanks for the help and support provided. Firstly, I would like to thank my supervisor, Professor Mark Wilson, for his guidance and advice throughout my studies. I would also like to thank Dr. Henk Slim, of the Computing and Information Service, a man whom I have never met, for assisting with technical computing issues. Without the Open University I would never have had the opportunity to undertake a Ph.D. in the first place, and I give great thanks to Dr. Elizabeth Grayson, who introduced me to the Chemistry Department at the University of Durham and who has given me moral support along the way. Finally, I would like to thank my husband for his help and support throughout, and my cats - Flush, Lui, Benny, three legged Smudge, and not forgetting Savvy - for keeping me company as I worked in my shed.

Abbreviations

AA	All atom
ACD	Advanced Chemical Development
A131	2-methyl-3-[4-(4-octyl-benzoyloxy)-benzylidene]-amino-benzoic acid 4-(4-dodecyl-phenylazo)-phenyl ester
BCM	Bent-core mesogen
BCN	Bent-core nematic
5CB	5-alkyl-cyanobiphenyl
8CB	4-n-octyl-4-cyanobiphenyl
CC	Coupled cluster
DC	Dark conglomerate
DFT	Density functional theory
DPD	Dissipative particle dynamics
DSC	Differential scanning calorimetry
FF	Force field
FRM	Fragmentation reconstruction method
GAFF	General AMBER force field
GB	Gay-Berne
GED	Gas electron diffraction
HF	Hartree-Fock
IR	Infrared

LC	Liquid crystal
LINCS	LINear constraint solver
LJ	Lennard-Jones
LL	Lebwohl-Lasher
MC	Monte Carlo
MD	Molecular dynamics
MFT	Mean field theory
MPn	Møller-Plesset perturbation theory
$\mathbf{N_U}$	Uniaxial nematic
$\mathbf{N_B}$	Biaxial nematic
NMR	Nuclear magnetic resonance
NPT	Constant temperature and constant pressure conditions
ODBP	2,5-diphenyl,1,3,4-oxadiazole
PB	Phenyl benzoate
Phenylester-LC	1,3-benzenedicarboxylic acid,1,3-bis(4-butylphenyl)ester
PME	Periodic boundary conditions
POM	Polarized optical microscopy
PRS	Polarized Raman scattering
QC	Quantum chemical
RB	Ryckaert-Bellemans
SAXS	Small angle X-ray scattering
SmA	Smectic-A
SmC	Smectic-C
$\mathbf{T_{NI}}$	Nematic to isotropic phase transition temperature
vdW	van der Waals
WAXS	Wide angle X-ray scattering
XRD	X-ray scattering
ZPVE	Zero-point vibrational energies

Contents

List of Figures

List of Tables

Chapter 1

Introduction

1.1 Introduction and background

The three states of matter familiar to us - gases, liquids and solids - can be described in terms of the translational and rotational motion of their constituent molecules. In the crystalline solid, intermolecular interactions are strong enough to hinder the motion and confine the molecules to specific sites in a lattice, whereas in a gas the intermolecular interactions are much weaker, resulting in unrestricted molecular motion and large average distances between the molecules.[132] In an ordinary liquid, the competition between short-ranged repulsive and long-ranged electrostatic intermolecular interactions results in a very short-ranged structural arrangement of the molecules, and coherence into a liquid state between the solid's melting point and the liquid's boiling point. The orientation of the molecules is random and the liquid phase is described as isotropic as it possesses full rotational and translational symmetry. As a consequence, measurable physical properties such as viscosity, magnetic susceptibility and refractive index do not change under any rotations or translations.[32,58]

However, between the isotropic liquid and solid crystalline state there exists a set of materials that possess varying amounts of orientational and sometimes translational order of their constituent molecules. These are called liquid crystal phases or mesophases. The defining attribute of molecules or mesogens that form such phases is their highly anisotropic shape, which results in anisotropic interactions between

molecules and the emergence of a degree of orientational and/or translational order across macroscopic distances. Unlike isotropic liquids, the physical properties of liquid crystal phases have measurably different values along different directions.[37,58]

Liquid crystal phases exist in natural and in man-made materials, such as in cell membranes, silk, insect wings, crude oil, liquid crystal displays, televisions and computers. Man-made materials exploit liquid crystals unique anisotropic and low viscosity properties which cause them to be particulary responsive to external stimuli, such as mechanical forces, electric or magnetic fields.[139] A few examples of different types of mesophases are shown in Figure 1.1.

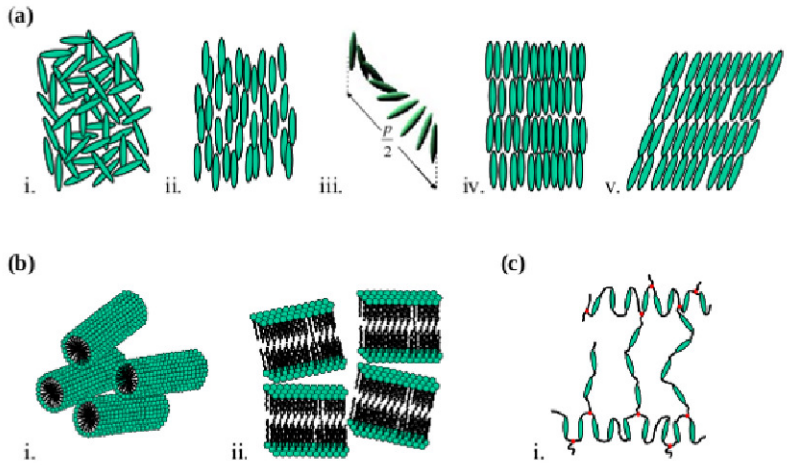

Figure 1.1: Examples of the different types of liquid crystal phases: **(a) Thermotropic**: i) isotropic, ii) nematic, iii) helical cholesteric, iv) smectic A, v) smectic C. **(b) Lyotropic**: i) cylindrical nematic, ii) lamellar nematic. **(c)** i) nematic liquid crystal elastomer. Reproduced from P. Palffy-Muhoray, *Physics Today*, 60:8-23, 2007 with the permission of the American Institute of Physics.

Many fluid systems exhibit one or more mesophases before transforming into an isotropic liquid. Those which show transitions as a function of temperature are called thermotropic and those which do so as function of solvent concentration and temperature are known as lyotropic. Nematic phases possess orientational but not translational order, whereas smectic phases possess both orientational and a degree of translational order. Some mesogens form chiral phases where the axes of adjacent molecules are twisted relative to one another.[139]

1.2 The thermotropic nematic phase

The thermotropic nematic phase is currently the most important phase for technological applications.[38] The uniaxial nematic phase (N_U) is the least ordered and the most fluid liquid crystal phase.[58] The preferred direction of the molecular orientations in the uniaxial phase is defined by the unit vector **n**, called the director. The director is parallel to the average direction of the long axis for nematic phases composed of rod-like molecules and parallel to the average direction of the short axis for those made up of disk-like molecules (see Figure 1.2).[171] The director may vary with time and also with different regions of a material and so is a variable which is dependent on both space and time coordinates, **n**(**x**,t). The overall symmetry of the uniaxial nematic phase is $D_{\infty h}$, which results in macroscopic properties with cylindrical symmetry.

The term 'uniaxial' refers to the optical properties of this phase where there is one axis along which a plane polarized light beam can travel without the state of the polarization being altered.[119] Although a wide range of molecular architectures can form the uniaxial nematic phase, the most common mesogens possess rod-like or disk-like shapes. Rod-like mesogens usually consist of a fairly rigid core composed of ring systems (often benzene) either directly joined together or through linking groups. Terminal flexible chains, such as akyl groups, are often linked to either end of the cores. Lateral groups such as CN, methyl and halogens are also often included in the structure. Liquid crystals composed of rod-like mesogens are usually described as calamitic. Disk-like mesogens generally consist of a symmetrical core with 3-12 substituents linked around their periphery.[39]

The various parts of a mesogen - the core, terminal and lateral groups - all have an effect on the mesogenic properties of a nematic phase, in particular the melting temperature and the nematic to isotropic transition temperature (T_{NI}). For example, the core, which is usually composed of conjugated aromatic sytems, promotes strong intramolecular attractions resulting in high melting temperatures and also helps enable liquid crystal phases to form. Lateral groups reduce the length to breadth ratio of a mesogen and hence usually lower the T_{NI}.[54] The upper temperature limit T_{NI} determines the nematic phase stability and the term 'nematic

range' refers to the range over which the nematic phase exits. Some materials can be supercooled to a metastable nematic state below their melting point and are described as monotropic, whereas other materials exhibit a stable nematic phase above their melting point and are called enantiotropic.[40] In summary, the current state of knowledge about the dependence of mesomorphic properties of the uniaxial nematic phase on molecular structure of rod and disk-like mesogens are reasonably well understood.[51]

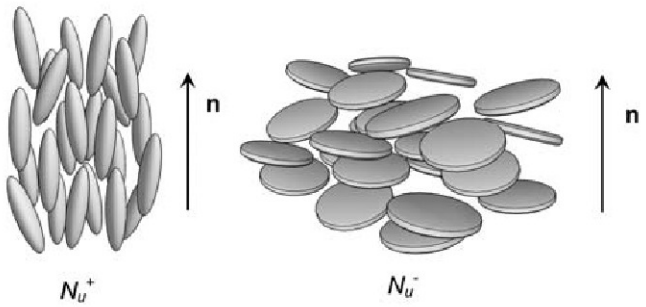

Figure 1.2: The uniaxial nematic phases of $N_U{}^+$ (rod-like molecules) and $N_U{}^-$ (disk-like molecules). Reproduced from ref.[171] with permission from The Royal Society of Chemistry.

In the uniaxial phase there is no preferred orientational order of the molecular axes perpendicular to the director **n**. However, it is possible for there to be orientational order of one of these perpendicular directions (**l** or **m**). The result is a phase with reduced symmetry D_{2h} (orthorhombic) and restricted rotation around the long axis: the biaxial phase.[171] Molecules forming the biaxial phase are usually represented by board-like shapes (see Figure 1.3).[171] In addition, there are two axes along which a plane polarized light beam can travel without the state of polarization being altered, hence the term biaxial is used to describe this nematic phase.[119]

There is great interest in the biaxial nematic phase, in particular those formed from low molecular mass materials as they could be used in a new class of liquid crystal devices. Faster switching could be possible due to rotation around the long

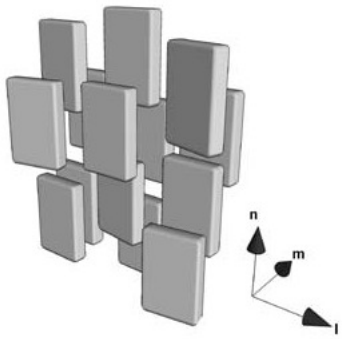

Figure 1.3: The biaxial nematic phase (N_B) of board-like molecules with D_{2h} symmetry. Reproduced from ref[171] with permission from The Royal Society of Chemistry.

axis (lower viscosity), instead of rotation around the short axis currently used in uniaxial devices.[171] The molecular features that may favour the formation of an N_B phase are not yet fully understood. For example, considering shape biaxiality alone in the design criteria has not been successful in generating biaxial nematics.[19] A key objective of current research in this field is to identify thermotropic biaxial nematic (N_B) phases that are stable at room temperature, along with understanding the molecular features that are responsible for the biaxial nematic phase.

1.3 Scope of the thesis

The characteristics of liquid crystalline materials are intrinsically strongly linked to both single molecule and collective properties, and therefore fully atomistic simulations appear as a natural choice for the investigation of such materials. They link a molecular description of the inter and intra molecular interactions, with the resulting macroscopic (mesophase) properties.[23] In particular, a more detailed description of molecular ordering in terms of molecular segments and their arrangement relative to one another can be gained, as well as a more detailed understanding of the effects of electrostatic charges and the flexibility of molecules and mesophase stability.[11,187]

The scope of this thesis was therefore to employ detailed molecular dynamics at

the fully atomistic level, in order to examine the mesophases of selected liquid crystal molecules. The primary focus was to investigate the structural organization at the molecular level, as well as orientational order, of the nematic phases of selected members of the *bis*-(phenyl)oxadiazole(ODBP) family of bent core mesogens, as a number of these have been proposed to form the biaxial nematic phase. However, early on in the course of the thesis it was found that the force field (a set of equations and associated parameters) used to describe the interactions of liquid crystal molecules, was inaccurate in replicating the experimental phase transition temperatures. As this is a stringent test of the quality of the force field employed, and analogous to a musical instrument requiring tuning before playing, it was necessary to partly re-parametrize the force field with the aim of producing more accurate phase transition temperatures. This in turn was expected to improve the predictive capability of the simulations and provide increased confidence in the results from a more in depth investigation of the mesophase behaviour displayed by these mesogens.

Chapter 2 commences with a brief overview of the biaxial nematic phase, acquired from experimental studies, theoretical aspects and computer simulations. Chapter 3 describes the computational methods and details used in this thesis. This is followed in Chapter 4 with the strategy for the selective re-parametrization of a standard force field, along with the results and discussion of testing the optimized force field on the estimates of the experimental nematic-isotropic transition temperatures of selected liquid crystal molecules. In Chapters 5 and 6, the optimized force field is used to investigate structure and order in the nematic phase of a number of *bis*-(phenyl)oxadiazole(ODBP) bent core mesogens. Although the nematic phase was the primary focus of these chapters, adjacent phases have also been briefly mentioned where these were considered relevant to the discussion of the nematic phase. Conclusions and suggestions for further developments of this work are contained in Chapter 7.

Chapter 2

The Biaxial Nematic Phase

2.1 Experimental evidence for the existence of the biaxial nematic phase

Although predicted theoretically by Freiser and Straley forty years ago, definitive experimental confirmation of the biaxial nematic (N_B) phase has proved to be more difficult.[11] The first convincing observation was reported in 1980 for a lyotropic system of board-like shaped micelles in a small temperature and concentration region.[171] Ten years later this was followed by the observation of phase biaxiality in thermotropic side-chain liquid crystal polymers in which the mesogens were attached laterally to the backbone of the polymer[19] (see Figure 2.2) . In 2004 further experimental evidence, apparently confirming the existence of thermotropic N_B phases, was presented for low molar mass bent-core mesogens, based on an oxadiazole core with an apex angle of approximately $140°$[120,124] (see Figure 2.1) and shortly afterwards, a Raman scattering study provided evidence of biaxial order for an additional oxadiazole derivative.[162] Biaxial order was also reported for a class of organo-siloxane and tetrapodes consisting of laterally tethered calamitic mesogens.[11] Biaxial nematic phases have also been found and investigated for a colloidal system of goethite mineral particles with fixed and well defined board-like shapes.[174–176]

For the side-chain liquid crystal polymers and the tetrapodes, the observed biaxiality has been attributed to restricted rotation of the mesogenic long axis, when

attached to the polymer backbone (side on attachment) or the central unit of the tetrapode. In both these systems the mesogenic units can be quite varied in shape,

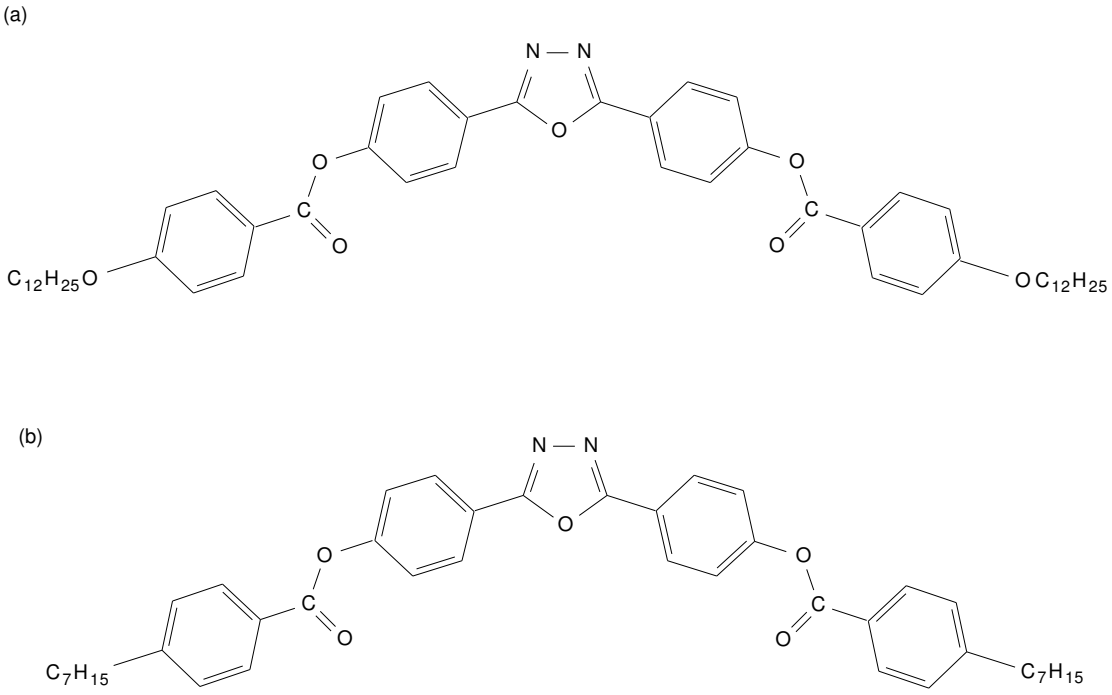

Figure 2.1: Examples of bent-core mesogens claimed to display a biaxial nematic phase

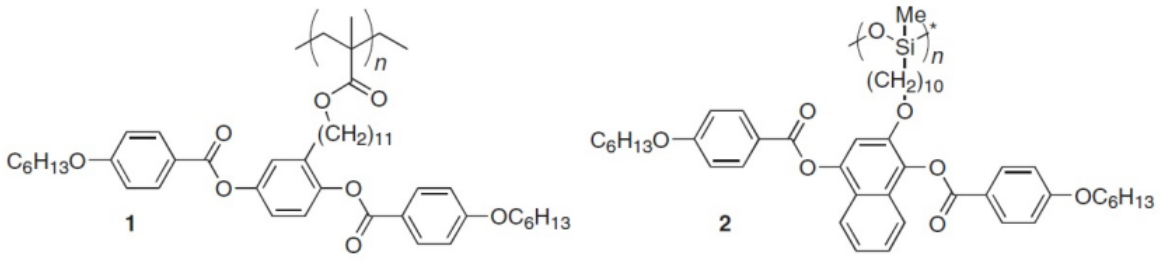

Figure 2.2: Polymers reported by Finkelman *et al.* to display biaxial nematic phases. Reproduced from reference[19] with permission from Willey Periodicals Inc.

ranging from rod-like to board-like, which indicates that molecular shape alone is less important for promoting phase biaxiality in these systems.[171] The relatively high molecular mass and high viscosity of both the polymers and the tetropodes means that they are not particularly suitable for practical applications,[171] and therefore recent attention has focused on low molecular mass bent-core mesogens which have the potential to form the ferroelectric phase as well as the N_B phase, properties that are potentially useful in device applications.[102]

The original research into the bent-core oxadiazole derivatives,[124] provided evidence for N_B organization from X-ray diffraction (XRD), polarized microscopy (POM), conoscopy, Raman spectroscopy and deuterium NMR methods.[11] Madsen *et al.* suggested that a subtle combination of excluded volume effects, due to the particulary strong biaxial shape of the oxadiazoles and strong intermolecular associations resulting from the large electric dipole across the oxadiazole ring, were responsible for stabilizing the N_B phase. However, for these oxadiazole derivatives, their high transition temperatures (biaxial nematic phase above 100°C) made this class of mesogens less suitable for biaxial nematic devices. Recent developments in attempting to lower the transition temperatures of these oxadiazole derivatives have included adding lateral methyl groups to the benzene rings, which led to a dramatic reduction in the nematic onset temperature.[45] Additionally, very recent XRD studies have indicated enhanced local molecular biaxial order for two trimethylated oxadiazole derivatives, with both showing reduced nematic onset temperatures.[182,183]

Additional bent-core mesogens that have been the focus of investigations for nematic phase biaxiality include those based on the 1,3,-phenylene central bent-core motif, of which one (abbreviated to A131) has been the subject of intense investigations. There is evidence from both XRD and optical methods that the A131 molecule displays an N_U - N_B transition.[146,194] It has been proposed that the transition is driven by a change in the average molecular shape from a more linear to a hockey stick shape mesogen, and accompanied by a change in the average bend angle.[60] This shape change was deduced from the measurements of local orientational order parameters of the aromatic rings of the mesogen core and it was suggested that conformational changes within the core region of V-shaped mesogens

may be an important feature when searching for other potential N_U - N_B transitions. Contrary to this evidence for an N_U - N_B transition, an electro-optic study of the A131 mesogen confirmed the nematic phase to be uniaxial, and that the previously reported biaxiality was due to surface effects.[178]

Other attempts to achieve room temperature N_B phases include studies of shape persistent (rigid) bent-core mesogens, consisting of a bent fluorenone core and two rigid wings with an apex angle of 90°.[114] Cyano groups were attached to one or both ends, introducing local dipoles essential for the formation of the nematic phase, and lateral substituents were attached to the wings to help reduce the tendency to form the crystalline phase. These have been investigated with XRD and POM methods and although the nematic phase was monotropic, a non-symmetric fluorenone did result in a low temperature biaxial phase, but at room temperature this transformed to a nematic glass. The authors suggest that both dipole-dipole interactions as well as $\pi - \pi$ interactions between mesogens may influence mesomorphic behaviour and possible stabilization of the N_B phase. More recently, further engineering of these molecules has resulted in a non-symmetric fluorenone mesogen with a wide enantiotropic nematic range with a low temperature stable biaxial phase, but which is still a nematic glass at room temperature.[115] The biaxial phase was confirmed by deuterium NMR as well as by XRD and POM methods.

Other rigid bent-core mesogens, including phenylene ethylene derivatives with a thiazole or thiadiazole central core, apex angles of approximately 160° and transverse dipoles along the bisector of the bent-core, have also revealed features from XRD and POM studies that may be indicative of a nematic phase with biaxial order.[116] Both these compounds and the fluorenone compounds have been proposed as promising starting structures for the design of room temperature biaxial nematics.[115,117]

2.1.1 Current controversies regarding the identification of the biaxial nematic phase

All the examples given previously for the existence of stable thermotropic biaxial nematics have come from studies using a number of independent experimental methods. However, their findings are still contested for two main reasons. Firstly, there

is the reliability of the different experimental methods, with concerns regarding the role that confinement, sample preparation, external fields and boundaries may play in reporting the observed biaxial phase.[11] Of the four main experimental methods used to identify biaxial phases - deuterium NMR , XRD, optical methods (polarized optical microscopy and conoscopy) and polarized infrared absortion or Raman scattering measurements - deuterium NMR is considered to be the most reliable.[59,171] This may place some doubt on Lehmann *et al.'s* claims for phase biaxiality in shape persistent mesogens where NMR was not used.[114]

Secondly, there is controversy over the interpretation of the experimental data. The vast majority of the experimental evidence for thermotropic biaxial nematics has been interpreted under the assumption of the phase possessing D_{2h} (orthorhombic) symmetry.[171] However, the possible symmetries for apolar biaxial nematics also include C_{2h} (monoclinic) and C_i (triclinic) symmetry[99] and for polar biaxial nematics (observed for some bent-core systems) includes C_{2v} symmetry.[171] Analysis of the experimental measurements of phase biaxiality therefore requires a consideration of all the possible symmetries for the biaxial phase, in order to avoid mis-identification or incorrect quantification of this phase.[144] For example, Madsen *et al.*[124] assume that all biaxial nematics possess D_{2h} symmetry, but the results in the paper do not provide any evidence of this symmetry for the observed biaxial phase.[144]

Interpretation of experimental data has also led to two opposing viewpoints on the nature of the nematic biaxial phase. There are those that claim the observed biaxiality is the result of orientationally ordered single molecules[102] and those who claim that the nematic phase consists of biaxial cybotactic clusters which respond to an external field or surface anchoring to produce macroscopic biaxiality.[11,179] In the latter case, the term 'cybotactic' represents local supramolecular positional correlations observed in some nematics, as opposed to cybotaxis that is present in all liquids - very short-range, non-specific nearest neighbour correlations.[151] The cybotactic cluster interpretation has led to the cybotactic model for the nematic phase biaxiality observed for the bent-core mesogens.[144,171] The essential feature of this model is that the nematic phase consists of biaxial microdomains, which in the absence of external stimuli, such as an electric or magnetic field, are uniaxially dis-

tributed. However, fields of relatively low strength can induce collective allignment of the microdomains perpendicular to the uniaxial director, resulting in macroscopic biaxiality (see Figure 2.3). The cybotactic cluster model can also be used to describe the biaxial polar phase composed of bent-core mesogens, where each cluster possesses local biaxial and transverse polar order. However, some authors contradict this interpretation of nematic biaxiality for bent-core mesogens, suggesting instead that the observed biaxiality from XRD data is due to SmC pretransitional fluctuations that grow in amplitude when the underlying low temperature is a SmC phase, and not due to biaxiality of the nematic phase.[180]

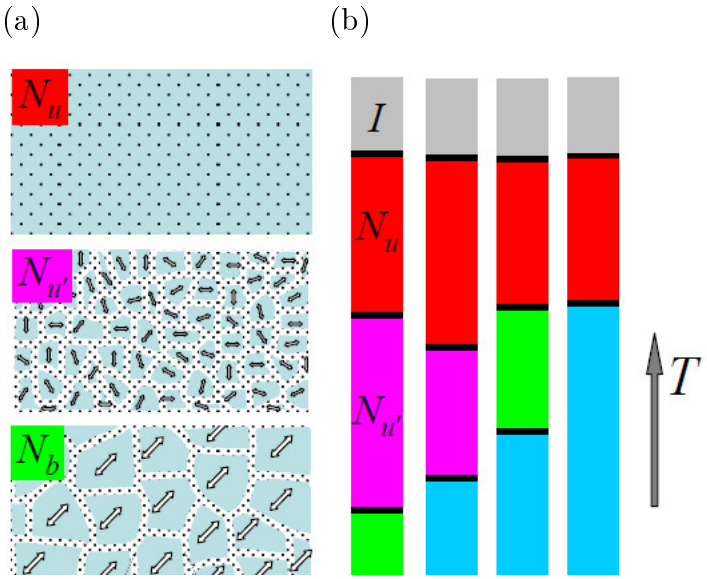

Figure 2.3: (a) Cross section of a nematic sample illustrating its biaxial cluster composition in the three possible phases of the model system. (b) Schematic represention of the possible thermotropic phase sequences of the system. $N_{U'}$ represents an intermediate phase between the uniaxial and biaxial nematic phases consisting of biaxial microdomains. In (b), light blue represents the crystal phase. Reproduced from reference[144] with permission from Taylor and Francis.

The deduced biaxiality from XRD data has also been reported for a number of different thermotropic nematics besides the bent-core mesogens, where it has again been attributed to the pretransitional manifestations of the SmC phase at the low temperature end of the nematic phase.[98] However, two recent studies of two different types of thermotropic mesogens (an oxadiazole and laterally substituted rod-like mesogens both as monomers and octamers) contradict this interpretation, as neither display an underlying SmC phase.[64,98] In both these studies, the nature of

the nematic phase was described as consisting of biaxial cybotactic clusters, where the clusters contained a layered, tilted arrangement of mesogens and the biaxial clusters were distributed to form a uniaxial nematic host medium.

Although there does not appear to be definitive experimental evidence for the spontaneous formation of the macroscopic thermotropic biaxial nematic phase, there is increasing evidence for the biaxial cybotactic cluster interpretation for the mesogens claimed to have formed a biaxial nematic phase.[171] However, there is still uncertainty concerning the origin of cybotactic clusters and the real nature of the short-range correlations leading to the formation of cybotatic clusters with biaxial ordering.[64]

According to Lehmann *et al.*, it appears that the generation of a true, spontaneous, enantiotropic biaxial nematic phase is hampered by the vicious circle of molecular design. From the viewpoint of possible applications in fast switching biaxial LC displays, Lehmann *et al.* state that the ideal mesogen should possess an enantiotropic biaxial nematic phase at ambient temperature with sufficiently low viscosity.[114] However, for the low molecular mass systems, such as the bent-core oxadiazole derivatives, the presence of strong intermolecular interactions due to relatively strong dipole moments, which help to promote biaxiality, also lead to a highly viscous phase composed of clusters. In addition, many of these low molecular mass systems exist in the nematic state only at relatively high temperatures, beyond the useful range for technological applications.

2.2 Theoretical approaches to understanding the relationship between molecular biaxiality and N_B phase stability

Theoretical models enable links to be made between the behaviour of single molecules and the characteristics of the liquid crystal macroscopic phase, although approximations and assumptions are usually incorporated into these models. With regards to N_B systems, theoretical models have provided the foundations from which exper-

imental and computational N_B studies have been developed.[11,41] The earliest and most common approach, but not the only way to finding a relationship between the biaxiality of the constituent molecules and the ability to form the N_B phase, has been within the context of molecular or mean field theory (MFT). In 1970, Freiser first predicted the existence of the N_B phase, followed shortly afterwards by Straley, by extending MFT for uniaxial mesogens to biaxial shaped molecules with D_{2h} (orthorhombic) symmetry.[69,167]

Molecular field theory is a theoretical model for the thermotropic uniaxial phase, in which molecular structural details are simplified. The theory assumes that every molecule is surrounded by a 'sea' of many other molecules, and calculates an average conformational independent potential for each molecule. Differences in the orientational biasing of each distinct conformation are not considered in the potential. Within the context of MFT, Frieser and Straley introduced a biaxial shape parameter, λ, and explored the relationship between λ and the stability of the N_B phase. Optimum shape biaxiality is found when the parameter λ is equal to $1/\sqrt{6}$ (≈ 0.41, the Landau point) which is derived from a definition of λ given by

$$\lambda = (3/2)^{1/2} L(B - W) / \{L(B + W) - 2BW\}, \tag{2.1}$$

where L, B and W represent the length, breadth and width of a cuboidal shaped mesogen respectively. The phase behaviour as a function of molecular biaxiality, λ, is shown in Figure 2.4. Limiting values of λ are found for $B = W$ ($\lambda = 0$), representing rod-like, uniaxial molecules and $L = B$ ($\lambda = \sqrt{3/2}$) representing disc-like uniaxial molecules. However, in between these extremes, and representing a deviation from molecular uniaxial symmetry, the N_B phase is injected into the phase diagram and at a particular point when $\lambda = 1/\sqrt{6}$ there is a direct second order transition from the isotropic to the N_B phase where the change in entropy is equal to zero. Most typical mesogens freeze at a reduced temperature, T/T_{NI} ($T*$), of approximately 0.8 (the dashed line in Figure 2.4) and the N_U - N_B transition occurs at temperatures where the formation of crystal or smectic phases are likely to intervene. Molecular biaxiality is therefore restricted to values very close to

$1/\sqrt{6}$ in order to form a N_B phase.[19,119]

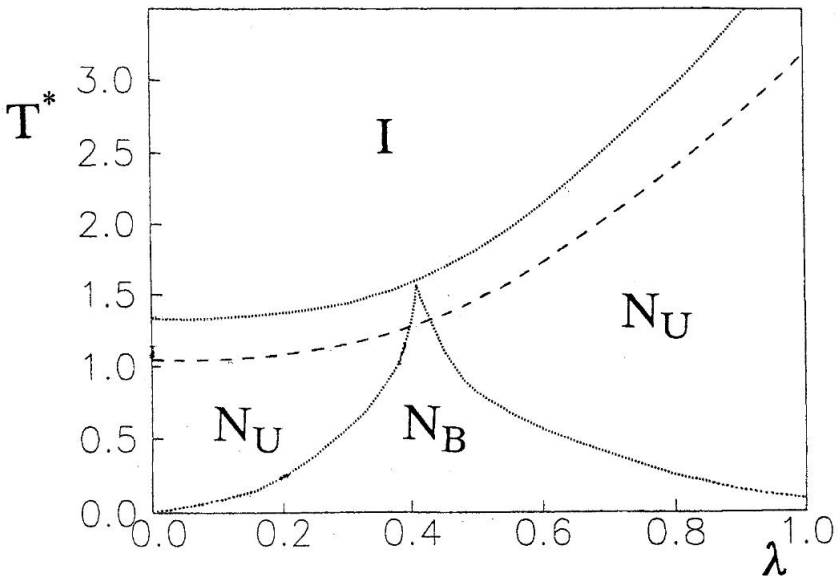

Figure 2.4: The phase diagram predicted by the molecular field theory for a system of biaxial molecules as a function of the molecular biaxiality, λ. The dashed line shows the anticipated freezing point of the mesogen at a reduced temperature of 0.8. Reproduced from reference[119] with permission from Elsevier.

Molecular field theory has been used to describe the phase behaviour of alternative biaxial shaped molecules, for example V-shaped molecules, where in this instance the apex angle is varied to provide a measure of molecular biaxiality analogous to the biaxial shape parameter, λ.[119] The phase behaviour predicted by MFT shows a uniaxial nematic phase for the two extremes of 180° and 90°. In between these values the N_B phase appears below the N_U phase in the phase diagram, except at a particular angle of 109.47° (tetrahedral angle) where there is a direct second order transition from the isotropic to the N_B phase (the Landau point). However, similar to the predictions made for the cuboidal shaped molecules, it is likely that the uniaxial nematic will freeze before the biaxial nematic phase is formed, except for a very narrow range of angles close to the tetrahedral angle of 109.47°.

In summary, MFT predicts that there is only a small opportunity for biaxiality to occur. Outside the optimal values, smectic or crystal phases are more likely to be generated. However, claims made for the discovery of the N_B phase have

included mesogens with unusual structures, for example tetropodes and V-shaped molecules with apex angles other than 109.47°. Additionally, attempts to construct mesogens with high molecular shape biaxiality with D_{2h} (orthorhombic) symmetry have not necessarily generated a N_B phase.[19,75] These factors indicate that the MFT used in the original prediction for the existence of this phase incorporates too many approximations, and that the interactions responsible for the generation of this phase are more complicated and involve more complex shapes. For example, MFT assumes that mesogenic molecules are rigid, with a well defined shape and D_{2h} symmetry, and ignores the variety of conformers possible, especially for those with a large number of internal degrees of freedom. This has created difficulties in comparing experimental findings with theory. For example, significant discrepancies between theory and experiment have arisen for the molecule p-quinquephenyl, an almost cylindrically symmetric mesogen without flexible tails, which is close to the idealised shape used in MFT for the uniaxial nematic phase.[58]

Recent developments in MFT which incorporate additional features that may be important in the stability of the N_B phase include the addition of molecular flexibility within the model.[121] This takes into account that molecular anisotropy and biaxiality can change due to flexibility, resulting in a coupling of the conformational distribution to the orientational order of the system. This coupling is expected to be particularly important for the formation of the N_B phase, since different conformers are likely to differ in their biaxiality. The authors development of MFT enables interactions between numerous conformers to be calculated and these are then employed in the determination of the phase diagram.

Another recent development in the molecular theory of biaxial nematics has focused on finding a relationship between the symmetry of the constituent biaxial molecules (other than the assumed D_{2h} symmetry) and the affect this has on the phase diagram predicted by MFT for biaxial nematics.[75,122] Gorkunov *et al.* constructed a model of a rigid biaxial molecule with C_{2h} (monoclinic) symmetry. The model consists of four parallel uniaxial mesogenic groups located at the corner of a rectangular frame. The biaxiality is controlled by the anisotropy of the geometrical frame and the angle between the mesogenic groups and the axes of the frame. Tilting

of the mesogenic groups alters the overall shape of the model from rectangular to a parallelogram shape. Molecular field theory of biaxial nematics was then employed to study the phase diagram for this model. The results of the study showed that the intermolecular potential could be controlled by the tilt angle of the mesogenic groups, and that increasing the tilt led to an increase in the uniaxial- biaxial transition temperature and hence an increase in the stability of the biaxial nematic phase. The authors conclude that this may explain why biaxial ordering has been observed in systems composed of molecules with C_{2h} symmetry, for example tetrapodes, and not for those with rectangular shape and D_{2h} symmetry.

2.3 Computer simulations of biaxial nematics

The first successful computer simulations of liquid crystal systems were performed at a much later stage than the development of theories. Their main roles in the study of liquid crystal behaviour include testing established theories, comparing results of modelling with experimental evidence and establishing relationships between molecular characteristics and bulk properties.[190] The essential feature of a simulation model is the description of how particles interact with one another, in other words the interparticle potential. There are three broad categories of simulation model with progressively increasing computational complexity.[187] These are:

- Single-site lattice models,
- Single-site off-lattice models,
- Multi-site and fully atomistic models.

There are two main techniques for simulating a liquid crystal system using the above model potentials. These are molecular dynamics (MD) and Monte Carlo (MC) techniques. The MD approach involves treating the dynamics of atoms and molecules by classical mechanics. This means specifying the initial location, orientation, translational velocity and rotational velocity for each molecule, and then solving Newton's equations of motion to specify these four quantities a small time step later. Once the system has reached equilibrium, ensemble average values for

macroscopic quantities can be calculated as time averages over a large number of time steps. Time-dependent quantities can be measured by observing how certain parameters of the system change with time.[42]

The MC approach also involves specifying an initial configuration for the system, although in this case no time steps are required. An algorithm is used to change the initial configuration of the system using random numbers and the energy of the new configuration is then recalculated. The energy difference $\triangle E = E_{\mathrm{New}} - E_{\mathrm{Old}}$ is used to accept or reject the new configuration. If $\exp(-\triangle E/k_B T)$ is greater than a random number between zero and one, the configuration is accepted. This guarantees that configurations are generated from a Boltzmann distribution. The process of generating random configurations is repeated many times and averages of the configurations can be used to produce macroscopic quantities. The main disadvantage of the MC technique is that time-dependent quantities cannot be calculated due to the random changes generated for the system.

Simulations of liquid crystals should also be able to generate the phases of interest as well as their phase transitions and the relevant anisotropic properties of particular systems. In terms of gaining a deeper understanding of the behaviour of biaxial nematics, computer simulations should not only be able to test theories against experimental evidence, but also aid in the design of molecules that have not yet been synthesized and which may have the potential for forming biaxial nematic phases with specific properties for applications.[197]

2.3.1 Single-site lattice models

The simplest model for investigating biaxial nematic (N_B) behaviour, and the first to show thermotropic N_B ordering, is an adaption of the lattice-based Lebwohl-Lasher (LL) model.[11,187] This model was originally developed for simulating uniaxial nematics and employs vectors which represent a molecule or clusters of molecules at sites on a regular lattice. The particles are assumed to have uniaxial symmetry and interact with their nearest neighbours through an

orientation-dependent potential of the form

$$U_{ij} = -\varepsilon P_2(\cos\theta_{ij}) = -\varepsilon\left(\frac{3}{2}\cos^2\theta_{ij} - \frac{1}{2}\right), \tag{2.2}$$

where the angle θ_{ij} is the angle between two vectors. The lattice model has been important in the determination of phase transitions and the calculation of orientational order in the nematic phase and has been shown to reproduce quite accurately the temperature dependence of the order parameter in real nematics.[187]

In order to study biaxial nematic behaviour, the LL model has been adapted to account for biaxial particles with D_{2h} symmetry instead of the assumed cylindrically symmetric particles used in the original model. The potential has the following form

$$U(\omega_{ij}) = -\varepsilon_{ij}\left\{P_2(\cos\beta_{ij}) + 2\lambda\left[R^2_{02}(\omega_{ij}) + R^2_{20}(\omega_{ij})\right] + 4\lambda^2 R^2_{22}(\omega_{ij})\right\}, \tag{2.3}$$

where λ is the biaxiality parameter that accounts for the deviation from cylindrical molecular symmetry and $\omega \equiv (\alpha, \beta, \gamma)$ is the set of Euler angles specifying the orientation of a molecule. R^l_{mn} are combinations of Wigner functions, which have been adapted for the D_{2h} group of the two particles.[195]

This model has been used to investigate the temperature dependence of the phase transitions as a function of molecular biaxiality.[15] The phase diagram produced from the simulations shows some subtle differences from predictions made by MFT (see Figure 2.5). For example MFT predicts a sharp increase in T_{NI} with λ, whilst the lattice model shows an almost constant T_{NI} with λ, at least up to the Landau point. Additionally the entire range of λ at which T_{NI} occurs for the lattice model is lower than that predicted by MFT and it has been suggested that the biaxial region for higher values of λ occur at temperatures too low to be readily accessible by most experimental methods.[196]

Extensions of the LL model have been developed by Bates and Luckhurst for the investigation of $\mathrm{N_B}$ behaviour displayed by V-shaped molecules and rod-disc dimers.[6,7,9,10] Bates claims that the advantage of using a lattice model includes the use of a small number of parameters and also, due to the absence of translational

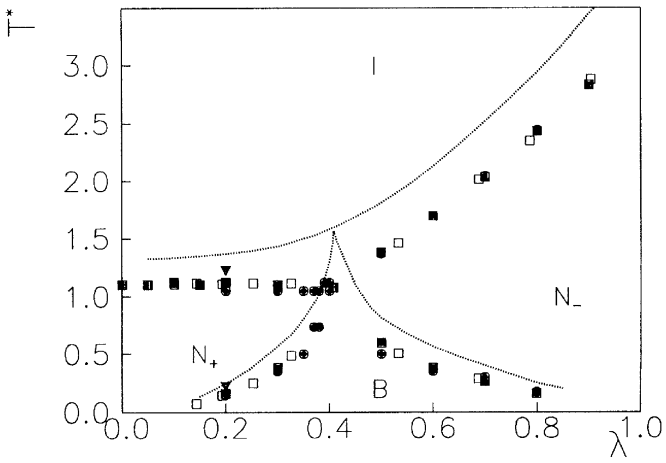

Figure 2.5: The phase diagram for a lattice model of a biaxial mesogen showing the reduced transition temperature versus molecular biaxiality λ. The points are simulation results while the continuous curves are the mean field predictions. Reproduced from reference[15] with permission from the American Physical Society.

freedom, regions of interest in the phase diagram can be explored which would otherwise be highly likely to display smectic or crystal phases. He also claims that the LL model can be used to identify a N_B phase that exists over a wide temperature range from which the associated parameters can be used as starting points for investigating real systems or further off-lattice models. For example, using a lattice model and Monte Carlo simulations, Bates and Luckhurst studied the phase behaviour of non-symmetric V-shaped molecules where the anisotropies of the two arms were different.[9] In this study, each lattice site contained two rods of type A and B joined at a fixed angle, θ, and these interacted with their six nearest neighbours. As the anisotropy in the interactions between rods of type A and B is different, a parameter ϵ^* was introduced into the model which reflected the relative difference in the anisotropies of the two rods representing the molecule. Phase behaviour was investigated as a function of both θ and ϵ^*. Their results showed that for $\epsilon^*= 1$, reflecting symmetric V-shaped molecules, the N_B- I transition temperature (Landau point) occurred when the apex angle was 109.47°, in agreement with the prediction of MFT for symmetric molecules. However, increasing ϵ^* led to a shift in the Landau point to lower angles and higher temperatures, and also led to a wider biaxial nematic temperature range. Increasing ϵ^* further to a value of two showed optimal

biaxiality for $\theta = 90°$, after which, for values of $\epsilon^* > 2$, led to the disapperance of the Landau point for all angles studied and the emergence of a biaxial phase only after a uniaxial phase (see Figure 2.6). This study suggests that non-symmetric V-shaped molecules could be possible candidates for forming the N_B phase.

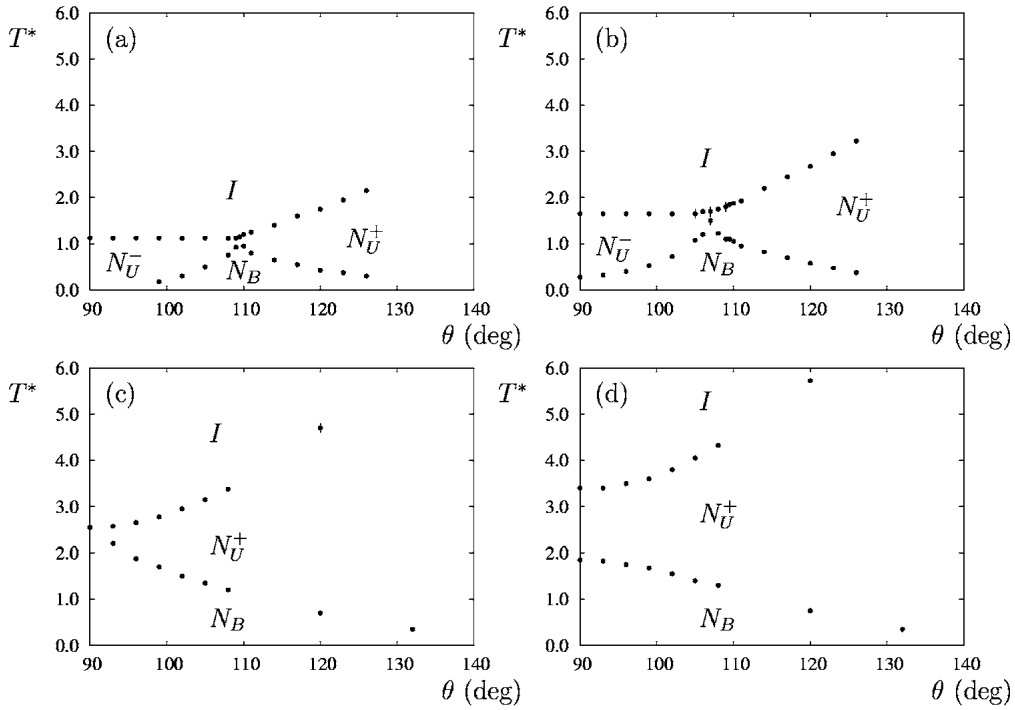

Figure 2.6: The phase diagrams for V-shaped molecules as a function of the interarm angle θ for a selection of values for the relative anisotropy of the mesogenic arms (a) $\epsilon^* = 1$, (b) $\epsilon^* = \sqrt{2}$, (c) $\epsilon^* = 2$, (d) $\epsilon^* = \sqrt{5}$. Reproduced from reference[9] with permission from the American Physical Society.

Experimental studies by Lehmann *et al.* offer some tentative support for these findings.[114,115] They found evidence of biaxial order in the low temperature nematic range for V-shaped molecules with non-symmetrical arms and a 90° apex angle, although the value of ϵ^* in these cases is not known.

Bates and Luckhurst also used a lattice model and Monte Carlo simulations to study the effects of a transverse dipole on the phase behaviour of bent-core molecules.[7] The behaviour of the system was investigated as a function of bend angle, dipole moment and temperature. Results showed that increasing the transverse dipole strength led to a range of angles from 107° to 122°, for which the N_B - I transition temperature occurred, resulting in a Landau line. This is in contrast

to MFT, which predicts the transition temperature should occur at a single point and at an angle of 109.47°. Bates and Luckhurst concluded that a strong transverse dipole may increase the range of bend angles for which a molecule can exhibit a direct N_B - I transition, and could help support the experimental evidence put forward by Madsen *et al.*[124] and Lehmann *et al.*[117] concerning the stability of the biaxial nematic phase composed of bent-core mesogens with wide bend angles and large transverse dipoles.

The key advantages of employing lattice models for investigating the phase behaviour of liquid crystal systems are that they are computationally efficient to perform and large sample sizes can be studied.[190] However, their main drawbacks are that they cannot be used to study transitions to phases with translational order, nor be used to predict or explain the behaviour of a specific molecule.[7]

2.3.2 Single-site off-lattice models

In contrast to the simple lattice models discussed in the previous section, single-site off-lattice models incorporate particles with full translational and rotational freedom.[11] The earliest models employed rigid, hard, anisotropic particles, usually ellipsoids or spherocylinders, where shape alone is the only important factor in determining phase behaviour. These models are based on Onsager's theoretical description of liquid crystals, where phase behaviour is governed exclusively by changes in density and not temperature, and demonstrates that hard-core repulsion between rigid, rod-like molecules, is sufficient to stabilize the nematic phase without the addition of attractive (electrostatic and dispersive) interactions.[28,52]

Studies by Allen and Camp[11,26] of a model of hard ellipsoids with three different axes (aspect ratios), where transition pressures and densities were measured as a function of molecular biaxiality, exhibited isotropic, calamatic N_+, biaxial and discotic N_- phases. However, the range of geometries for which a biaxial phase was found was very small, in particular for moderate molecular biaxiality the nematic $N_\pm$ to biaxial transition occurred at high densities, indicating a direct transition to the crystal phase.

Although repulsive single-site off-lattice models have proved useful for studying

the entropic effects that are important in stabilizing the N_B phase, they do not form nematic phases upon compression for particles with aspect ratios closer to those of conventional mesogens. For example, uniaxial hard ellipsoids and hard spherocylinders with aspect ratios equal or less than 1:1:3 and 1:1:5 respectively do not form nematic phases.[11] Additionally, hard particle models may resemble the lyotropic system from which the original N_B phase was discovered and therefore not be particularly appropriate for gaining insight into the nature of the thermotropic N_B phase, where attractive interactions are also known to be important in stabilizing this phase.[12]

The most popular model to have been developed which includes the effect of attractive particle-particle interactions as well as entropic effects is the Gay-Berne (GB) model and variants of it. The model uses a soft potential whose behaviour resembles that of a Lennard Jones potential, a simple model for describing spherical shaped particles in liquids, where attractive and repulsive contributions decrease as 6 and 12 inverse powers of intermolecular distance.[197] Using a soft potential means that phase behaviour will also depend on temperature, making it particularly useful for investigating thermotropic liquid crystal phases.[187] The GB potential for uniaxial ellipsoids has the following form[8,190,197]

$$U_{ij}(\hat{\mathbf{u}}_i, \hat{\mathbf{u}}_j, \mathbf{r}_{ij}) = 4\varepsilon_{ij}(\hat{\mathbf{u}}_i, \hat{\mathbf{u}}_j, \hat{\mathbf{r}}_{ij}) \times \left[\left(\frac{\sigma_s}{r - \sigma(\hat{\mathbf{u}}_i, \hat{\mathbf{u}}_j, \hat{\mathbf{r}}_{ij}) + \sigma_s} \right)^{12} - \left(\frac{\sigma_s}{r - \sigma(\hat{\mathbf{u}}_i, \hat{\mathbf{u}}_j, \hat{\mathbf{r}}_{ij}) + \sigma_s} \right)^{6} \right], \tag{2.4}$$

where for particles i and$j$, the well depth parameter ε and the range parameter σ are all dependent on the orientation vectors, $\hat{\mathbf{u}}_i$, $\hat{\mathbf{u}}_j$ and their separation vector $\hat{\mathbf{r}}_{ij}$ (the cap indicates a unit vector so that $\hat{\mathbf{r}}_{ij} = \frac{\hat{\mathbf{r}}_{ij}}{r_{ij}}$)

The potential contains four parameters (κ, κ', μ, ν) which together determine the anisotropy in the repulsive and the attractive forces. These are:

- κ, the shape anisotropy parameter and is the ratio of the end-to-end and side-to-side contact distance $\frac{\sigma_e}{\sigma_s}$, and enters into the expression for $\sigma(\hat{\mathbf{u}}_i, \hat{\mathbf{u}}_j, \hat{\mathbf{r}}_{ij})$ and $\varepsilon_{ij}(\hat{\mathbf{u}}_i, \hat{\mathbf{u}}_j, \hat{\mathbf{r}}_{ij})$,

- κ', the ratio of the well depths for the side-to-side and end-to-end configurations and is the parameter that determines the tendency of the system to form a smectic phase,

- μ and ν, these are tuning parameters that adjust the shape of the potential and enter into the expression for $\varepsilon_{ij}(\hat{\mathbf{u}}_i, \hat{\mathbf{u}}_j, \hat{\mathbf{r}}_{ij})$. In particular they influence the nematic and smectic forming ability of the anisotropic forces in a subtle way.

By varying the parameters (κ, κ', μ, ν), a wide range of liquid crystal phases have been generated representing many different thermotropic mesogens. Early simulations using the GB model employed the parametrization (3, 5, 2, 1) which generated isotropic, nematic and smectic B phases. However, the nematic range was found to be fairly narrow, and alternative parametrizations were explored such as (3, 5, 1, 3) which led to stronger side-to-side interactions and a nematic with a wider temperature range.[197] Developments in the GB model have resulted in parametrizations that are expected to reflect more realistically real mesogenic molecules. For example, the parameters (4.4, 20, 1, 1) have generated isotropic, nematic, smectic A and smectic B phases, along with reasonably accurate transitional properties with the exception of the density change at the nematic-to-isotropic phase transition, which was reported to be ten times larger than that observed experimentally for real liquid crystals.[8]

Although the the single-site GB model was originally designed for modelling uniaxial particles, a biaxial version has been developed by Berardi *et al.*[14] that incorporates biaxial contributions in the model from biaxial shaped particles with different semi-axes σ_x, σ_y and σ_z. This enables the side-to-side, face-to-face and end-to-end configurations to be made in the attractive and repulsive interactions between particles. To reflect the change from uniaxiality in both the repulsive and attractive interactions, two parameters are introduced into the GB model. These are:

Shape biaxiality

$$\lambda_\sigma = \sqrt{3/2}\frac{\sigma_x - \sigma_y}{2\sigma_z - \sigma_x - \sigma_y}, \tag{2.5}$$

and attractive interaction biaxiality

$$\lambda_\epsilon = \sqrt{3/2}\frac{\epsilon_x^{-1/\mu} - \epsilon_y^{-1/\mu}}{2\epsilon_z^{-1/\mu} - \epsilon_x^{-1/\mu} - \epsilon_y^{-1/\mu}}. \tag{2.6}$$

These parameters are significant in that they can help identify the adjustments required to widen the temperature range and increase the stability of the N_B phase, especially as for real thermotropic systems it is estimated that there is only a very small opportunity for the potential N_B phase to exist due to competition with smectic or crystal phases.[197]

Using this modified GB potential, Berardi and Zannoni[12] performed a MC study of a system of N identical biaxial particles and were able to generate biaxial nematic and smectic phases. They investigated the effect of changing the attractive interaction biaxiality, λ_ϵ, whilst choosing a fixed value for the shape biaxiality, λ_σ. Their results show that for $\lambda_\epsilon = 0$ (no biaxiality in the attractive interactions), the biaxial nematic occurred at a much lower temperature than the isotropic to nematic transition temperature, indicating that the transition is directly from the nematic to a biaxial smectic phase, which they suggest may explain the difficulty of obtaining a biaxial phase purely on the basis of shape anisotropy. Biaxial smectic phases were also generated for positive λ_ϵ values, where it was found that face-to-face configurations were energetically favoured over that of side-to-side or end-to-end configurations. A negative λ_ϵ value however, had the effect of energetically favouring side-to-side configurations and resulted in a biaxial nematic with a fairly wide temperature range, suggesting that enhancing lateral attractive interactions may be useful in obtaining a stable biaxial nematic (see Figure 2.7).[12]

An area that has received very little attention so far is the behaviour of biaxial shaped disk-like mesogens. An example of Monte Carlo simulation using the GB model employing alternative parametrization to represent disk-like mesogens is given in reference.[13] In this study it was also found that an N_B phase was generated when the attractive interaction biaxiality λ_ϵ was negative, thus favouring side-to-side configurations of the disk-like mesogens.

However, an attempt to promote the N_B phase by introducing appropriate lateral

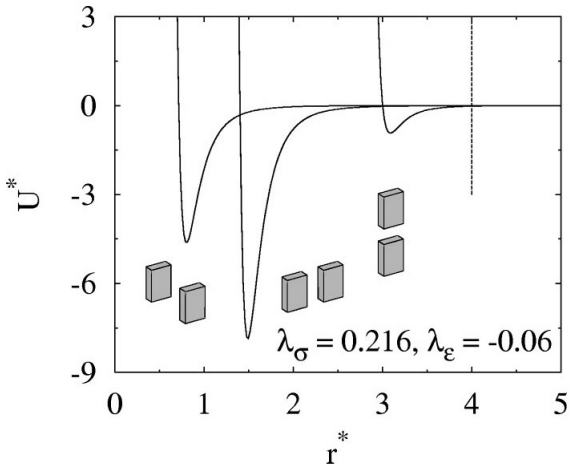

Figure 2.7: Distance dependence of the biaxial GB U^* energy for the face-to-face, side-to-side and end-to-end configurations with shape biaxiality $\lambda_\sigma = 0.216$ and interaction biaxiality $\lambda_\epsilon = -0.06$. Reproduced from reference[12] with permission from AIP Publishing LLP.

groups perpendicular to the principle molecular axis of disc-like palladium(ll)imine based mesogens, did not result in the formation of any N_B phases.[36] In this study the authors concluded that the palladium bound core structure is already predisposed to lateral correlations, and that the addition of lateral groups only served to increase the stability of the SmA phase and not the formation of N_B phases.

It is clear that the GB model contains a number of useful features.[14,190] These include:

- Manipulation of parameters to reflect changes in the shape of molecules,
- The avoidance of discontinuities inherent in purely hard models,
- The exhibition of the most important liquid crystal phases,
- Low computational cost and the possibility of modelling large systems.

The main disadvantage of GB models, and single site models in general, is the fact that it is not possible to study the relationship between fine molecular detail and mesogenic behaviour. Attempts to overcome this problem has led to the development of multi-site and fully atomistic models.[11] These are discussed in the next section.

2.3.3 Multi-site and fully atomistic models

The main features of multi-site models are the ability to explore in more detail the relationship between the mesogen shape and interaction energy, and also the influence that minor changes in molecular structure can have on phase behaviour.[11] Multi-site models range from fairly simple models composed of rigidly connected particles which could be in a linear or V-shaped arrangement,[27] to complex fully atomistic models where every atom is represented within a simulation. However, the only models in this category to have generated an N_B phase have been a board-like model composed of 8 to 11 repulsive GB discs arranged along a line[156] and a fully atomistic simulation of a bent-core mesogen.[143]

Although there have been a large number of fairly simple multi-site models used to investigate the phase behaviour of bent-core mesogens, including those that incorporate dipoles and flexible chains, the vast majority of the simulations show smectic organizations, with nematic phases being rather rare.[11] There are significant anomalies concerning the features necessary for the stabilization of the N_U phase with respect to the smectic phase. For example, Dewar and Camp[56] show that a transverse dipole moment along the C_2 symmetry axis of V-shaped arrangement of rigidly connected LJ soft spheres slightly favours the N_U over the smectic phase, whilst other studies show that the presence of a transverse dipole suppresses the N_U phase.[96,136] Additionally, there does not appear to be a general consensus regarding the size of the apex angle required for the stablization of the nematic phase, although a number of studies have shown that a fairly large apex angle favours the nematic phase with respect to smectic phases.[11] This indicates that simplistic multi-site models of bent-core mesogens have not yet generated the defining key elements that are necessary for stabilizing the nematic phase, and therefore knowledge regarding the minimal molecular features necessary for obtaining an N_B phase for these molecules is still uncertain.[11]

Fully atomistic simulations provide a more detailed description of molecular ordering in terms of molecular segments and their arrangement relative to one another, as well as a more detailed understanding of the effects of electrostatic charges and the flexibility of molecules and mesophase stability.[11,187] Due to their sensitivity to fine

chemical detail, atomistic simulations can also play a crucial role in the intepretation of experimental data. In terms of biaxial nematics, the only atomistic simulations to have been performed of a mesogen claimed to display this phase, has been of a bent-core mesogen based on the *bis*-(phenyl)oxadiazole motif (ODBP-Ph-C_7)[143] - see Figure 2.1 b. The system size for this study consisted of 256 ODBP-Ph-C_7 molecules and the results showed a small degree of biaxiality. The results also showed some interesting features in terms of structural organization of the molecules and interactions that may be responsible for the observed biaxiality. For example, visual analysis showed the formation of small, ferroelectrically ordered domains, with a parallel alignment of the molecular cores. This was also confirmed quantitively by calculating the pairwise dipole correlation function for the molecular short axis. The mechanism responsible for the formation of the ferroelectric domains was attributed to the electrostatics of the system and not to preferential packing of the molecular cores, as removal of the partial charges resulted in destabilization of these domains and a reduction in biaxiality. The interactions considered responsible for the observed biaxiality were thought to be the transverse dipole across the centre of the oxadiazole ring associated with the parallel alignment of the cores within small ordered domains. This also indicates that the anisotropic shape of the molecules alone is not sufficient to promote the N_B phase.[11,143]

The use of fully atomistic simulations clearly has advantages for gaining a better understanding of liquid crystal phases such as the biaxial nematic phase, and therefore atomistic studies form the key component of this thesis. However, the benefits of using atomistic simulations are entirely contingent on the accuracy of the force field employed.

Chapter 3

Computational Methods and Details

3.1 Introduction

The computer simulations performed in this thesis employed fully atomistic molecular dynamics (MD). Sections 3.2 and 3.3 provide an overview of the components of a force field and the methods involved in preparing and running MD simulations. Part of the process of amending the GAFF force field involved deriving a number of new torsional parameters in order to gain a more accurate description of molecular conformations. This entailed obtaining the torsional energy from quantum chemical (QC) calculations. Due to the large number of QC methods available, each with their own strengths and weaknesses, it was necessary to briefly survey this area so that a more informed choice could be made in determining the most accurate calculations, whilst also considering the computational cost. Section 3.4 therefore provides a brief precis of the theoretical background to QC calculations, as well as the fitting procedure for deriving new torsional parameters.

Finally, section 3.5 describes the methods employed in data analysis, including the measurement of orientational order and the analysis of mesophase structure. Additional computational details specific to individual chapters are described in the chapters themselves.

3.2 Molecular force fields

Molecular force fields enable the total potential energy of a system to be calculated and contain two distinct components.[177] These are:

1. The set of equations (the potential functions) used to generate the potential energies and their derivatives (the forces). The general expression for the total potential energy is given by the following equation

$$\begin{aligned} E_{\text{total}} &= \sum E_{\text{bonds}} + \sum E_{\text{angles}} + \sum E_{\text{dihedrals}} \\ &+ \sum E_{\text{improper}} + \sum E_{\text{coulomb}} + \sum E_{\text{vdw}} \end{aligned}, \tag{3.1}$$

   where E_{bonds} is the energy function for stretching a bond between two atoms, E_{angles} represents the energy required for bending an angle, $E_{\text{dihedrals}}$ is the torsional energy for rotation around a bond, E_{improper} represents the energy required to maintain planarity of planar groups and $E_{\text{coulomb}}$and E_{vdw} describe the non-bonded atom to atom interactions.

2. The parameters used in this set of equations, for example, charges, force constants and equilibrium bond lengths and angles.

There are many different force fields used for simulation studies, with the main difference between them being the functional form of each equation and the types of information used to derive the parameters. Each force field is designed to reproduce a small set of macroscopic features for a particular set of molecules within a determined thermodynamic range, and therefore have significant strengths in the area for which they have been parametrized.[23] The general form of the potential functions are described below.

The non-bonded interactions are computed on the basis of a neighbour list (a list of non-bonded atoms within a certain radius) in which exclusions are already removed, for example, atoms connected by a common bond. They contain a repulsion and a dispersion term for the van der Waals interactions and a Coulomb term for the electrostatic interactions. The repulsion and dispersion terms are usually

represented within the Lennard-Jones (LJ) potential

$$V_{LJ} = 4\epsilon_{ij}\left[\left(\frac{\sigma_{ij}}{r_{ij}}\right)^{12} - \left(\frac{\sigma_{ij}}{r_{ij}}\right)^{6}\right], \tag{3.2}$$

where r_{ij} is the interatomic distance, ϵ is the minimum energy (well depth) and σ_{ij} is the interatomic distance, so that $V_{LJ} = 0$. Both parameters depend on pairs of atom types. The standard Lorentz-Berthelot mixing rules of $\varepsilon_{ij} = (\varepsilon_i \varepsilon_j)^{1/2}$ and $\sigma_i = (\sigma_i + \sigma_j)/2$ are applied for calculating the LJ parameters between different types of atoms. The Coulomb (electrostatic) interaction between point charges is represented by the following equation

$$V(r_{ij}) = \frac{1}{4\pi\varepsilon_0}\frac{q_i q_j}{r_{ij}}, \tag{3.3}$$

where ε_0 is the dielectric constant and q_i, q_j are the atomic charges.

The following functions are used to describe the bonded interactions. The potential function for bond stretching between two covalently bonded atoms is represented by a harmonic approximation (a Taylor expansion around the equilibrium bond length which is terminated at second order) and is given by

$$E_{\text{bond}}(r_{ij}) = \frac{1}{2}k_{ij}(r_{ij} - r_0)^2, \tag{3.4}$$

where r_0 represents the equilibrium bond length between atoms i and j, and k_{ij} represents the force constant for the i-j bond.

The energy for bending an angle formed by three atoms i, j, and k can also be expressed by the harmonic approximation and is given by

$$E_{\text{angle}}(\theta_{ijk}) = \frac{1}{2}k^{\theta}_{ijk}(\theta_{ijk} - \theta_0)^2, \tag{3.5}$$

where k^{θ}_{ijk} represents the angle bending force constant and θ_0 represents the equilibrium bond angle.

The torsional energy, E_{dihedral} describes the energy associated with rotation around a bond $i-j$ in a four atom sequence $h-i-j-k$ and differs from E_{bond} and

E_{angle} in three main ways:[91]

- The torsional energy has contributions from the non-bonded (van der Waals and Coulombic) terms and is therefore coupled to the non-bonded parameters
- The torsional energy is periodic in the angle ϕ ,which means if the bond is rotated 360° the energy should return to the same value
- The cost in energy for distorting a molecule around a bond is usually low, therefore a Taylor expansion is not appropriate.

To accommodate the periodicity, E_{dihedral} is written as a Fourier series and is given by

$$E_{\text{dihedral}}(\phi_{hijk}) = \sum_n V_n \cos(1 + (n\phi - \delta_n), \tag{3.6}$$

where V_n represents constants that determine the size of the barrier for rotation around the $i - j$ bond, n is the number of times the rotation is periodic and δ_n are the phase angles.

Changes in the potential energy arising from deviations in improper dihedral angles, ω (for example in aromatic groups), are represented by cosine functions using the force constants, K_{d}, the harmonic coefficients, n_{d} and the phase angles, ω_{d}

$$E_{\text{improper}}(\phi_{hijk}) = \sum_n K_{\text{d}}(1 + \cos(n_{\text{d}}\omega - \omega_{\text{d}}). \tag{3.7}$$

The basic force field employed to run the MD simulations carried out in this research was the Generalised AMBER Force Field (GAFF) where AMBER represents a family of force fields where each member has its own parameter set and name. The GAFF force field has been specifically designed and parametrized for simulating small organic molecules. The main difference between GAFF and other standard force fields is in the derivation of the atomic charges. In most standard force fields the charges are optimized to fit experimental properties of organic liquids, for example heats of vaporization and densities, whereas the charges for the

GAFF force field are obtained from fitting to electrostatic potential surfaces from *ab initio* calculations.[97]

To run the MD simulations, a topology file is required that describes the parameters that must be applied to the various potential functions and which also describes the atoms or combination of atoms these potential functions must act on.

3.3 Molecular preparation and atomistic simulations

All the calculations in this thesis were performed using the GROMACS 4.5.5 package, an engine used to perform molecular dynamics simulations and energy minimization.[177] To reduce the CPU time the simulations were run in parallel over more than one processor. This enables the system to be decomposed into spatial domains with each one assigned to a processor, which then integrates the equations of motion for the particles that reside there.

All molecules including the mesogens selected for this study were built and optimized using the AVOGADRO 1.0.0 program.[89] The OpenBabel code was used to extract coordinate files including the connectivity information. The Antechamber software from AmberTools 1.4 was used to generate GAFF topologies, with the point charges derived through the AMI-BCC method. The GAFF topologies and coordinate files were converted into the GROMACS format using the **acpype_py** script.

The general procedure for constructing a simulation box is to firstly build and place one molecule in a box using the GROMACS program **editconf**. This is then stacked, using the GROMACS program **genconf**, to generate a larger cubic box containing the required number of molecules. To avoid surface effects due to the small system size, periodic boundary conditions (PBCs) were applied. This involves representing the system as a unit cell which is then surrounded by copies of itself. If the trajectory of an individual molecule takes it through the right wall of the simulation box, its image simultaneously appears through the left wall of the cell, thus avoiding any molecules interacting within a vacuum.[47]

The simulations of the mesogens were conducted under constant temperature

and constant pressure conditions (NPT ensemble) since this ensemble is directly related to most experimental conditions. To reach the required temperature and the equilibration of the system, the Berendsen thermostat was used as this is very efficient at relaxing a system to the target temperature.[177] As the temperature is related to the kinetic energy of a system, the role of thermostats in MD simulations is to maintain the correct average temperature and ensure that the kinetic fluctuations are of the correct size. This is implemented by coupling the system to an external heat bath with a fixed temperature, T_0. The Nosé-Hoover thermostat is then normally employed for the production runs as this is a more appropriate thermostat to use once a system has reached equilibrium.[177] Final coordinates from the production runs became the starting configuration for the subsequent heating (or cooling) runs.

The simulations were conducted at a pressure of 1 atm using the Berendsen barostat for equilibration runs and the Parrinello-Rahman barostat for the production runs. The barostats allow a system to maintain a constant pressure during the simulations by modifying the volume. This is achieved by scaling the location of the particles and changing the size of the unit cell in a system with PBCs.[48]

A timestep of 2 fs was used for all the MD runs and the LINear Constraint Solver (LINCS) method was employed to constrain all bonds. As the fastest processes are the stretching vibrations, in particular those involving hydrogen, and these have little effect on many properties, the constraint method for keeping bond lengths fixed enables a larger timestep to be used and a consequent reduction in the simulation time.[92] Additionally, the LINCS algorithm is the most applicable constraint algorithm to use with domain decomposition, since parts of molecules can reside on different processors.[177]

All the MD simulations performed for this thesis employed a cut-off distance of 1.2 nm for both the van der Waals and electrostatic short-ranged interactions. As the LJ potential describing the van der Waals interactions decays very rapidly, truncating these interactions at a cut-off distance is not considered problematical. The general consensus is that cut-off distances from 0.8 to 1.2 nm for the van der Waals interactions only leads to minor disparities in the energy of a system. How-

ever, electrostatic interactions decay much more slowly and therefore truncation of these at a specified distance is not appropriate, and long-range contributions need to be included.[49] The simulations performed here employed the Particle Mesh Ewald (PME) method for evaluating the electrostatic interactions outside the cut-off distance (reciprocal space). Here, the charges are assigned to a grid which is then Fourier transformed, resulting in a single sum for the reciprocal energy.

In addition to the above MD simulations, the GAFF force field[88] was employed to investigate the conformational behaviour of single molecules in the gas phase. This involved performing long simulations using a stochastic dynamics integrator, which adds a friction and a noise term to Newton's equation of motion. These were conducted under constant volume, constant temperature and with no periodic boundary conditions.

3.4 Quantum chemical calculations (theoretical background)

The foundations of QC calculations are based on the laws of quantum mechanics, as opposed to classical physics, and are based on the concept that the electron has wave-like properties. There are two major categories:

- *Ab initio* methods,
- Density functional methods.

3.4.1 *Ab Initio* methods (molecular orbital theory)

Ab initio methods, often called wave function approaches to quantum calculations, involve approximate solutions to the time-independent Schrödinger equation

$$\hat{H}\Psi = E\Psi, \tag{3.8}$$

where $\hat{H}$ is the Hamiltonian operator defined as $\hat{H} = \hat{T}_e + \hat{T}_N + \hat{V}_{Ne} + \hat{V}_{ee} + \hat{V}_{NN}$ and $\hat{T}_e$ and $\hat{T}_N$ represent the kinetic energy of the electrons and nuclei respectively,

$\hat{V}_{Ne}$ represents the attractive electrostatic interations between the nuclei and the electrons (often referred to as the external potential V_{ext}) and $\hat{V}_{ee}$ and $\hat{V}_{NN}$ represent the repulsive electron-electron and nuclei-nuclei interactions. Solutions to the Schrödinger equation are called wave functions, and from these all the properties of a molecular system can be derived, including the energy of the system. There are no fitting parameters or empirical approximations employed in these methods. Instead, a small number of physical constants are used in the calculations. These are:

- The speed of light,
- The masses and charges of electrons and nuclei,
- Planck's constant.

Solutions to the Schrödinger equations for an electron, known as orbitals, involve a set of mathematical functions representing the orbitals called a basis set and are described in more detail in Section 3.4.3. The complexity of the wave function increases exponentially with the number of electrons due to the fact there are $4N$ variables for each electron (three spatial and one spin coordinate), which means there is no strategy for solving the Schrödinger equation exactly, except for the very smallest of systems. However, a procedure for approaching the wave function of the ground state (the state which delivers the lowest energy) has been developed using the variational principle. This states that the calculated wave function energy can only be above or equal to the exact wave function energy but never below this energy.[63,131,150]

Ab initio theory generally falls into two types, the Hartree-Fock (HF) method, and electron correlated methods. The HF approach makes use of the variational principle and allows the wave function to be a product of one-electron wave functions (referred to as molecular spin orbitals).[63,147] It utilizes three approximations in its attempt to solve the many electron Schrödinger equation. These are:

- Born-Oppenheimer approximation, which states that electrons act independently of nuclei,

- Electrons experience an average 'field' of all other electrons in the system,
- Molecular orbitals can be constructed as linear combinations of atom-centred orbitals.

While the HF method accounts for the vast majority of the total energy of a molecule and has been reasonably successful at addressing a wide range of chemical problems, it also has limitations, in particular, an inadequate treatment of the instantaneous interactions (correlations) between electrons within a molecular system.[63,147] Although the major correlation arising from electrons with the same spin, defined as exchange correlation, is accounted for within HF theory, the motion of electrons of opposite spin (coulomb type) remains uncorrelated. This can have a specific effect on the accuracy of calculations, in particular where dispersion interactions are important.[63] Attempts to include more explicit interactions of electrons, known as correlated methods, usually start with the HF wavefunction and improve this by adding varying amounts of electron-electron interactions. This is performed through the inclusion of excited states into the ground state wave function, usually classified as single, double, triple or quadruple....(S,D,T,Q....) excitations, and allowing the wave function to be a linear combination of many electron configurations. This has the effect of improving the description of the electron distribution, as well as avoiding unphysical representations such as electrons approaching one another too closely.[131,150]

The main requirements of electron correlation theories have been proposed by Raghavachari and Anderson and these are:[147]

- The theory should provide a unique total energy for each electronic state at a given geometry and provide a continuous potential energy surfaces as the geometry changes.
- The resulting energy should be variational, ie. an upper bound to the exact energy.
- The theory should possess the property of size consistency which refers to the linear scaling of the energy with the number of electrons.

One of the first correlation methods to be applied to chemical systems was the Møller-Plesset Perturbation theory, frequently abreviated to MP2, MP3....MP/n, where n indicates the extent to which excited states are considered.[106,150] Møller-Plesset Perturbation theory has the advantage of being size consistent, with MP2 level calculations being the most computationally economical in terms of accounting for electron correlation, although the scaling factor for the MP2 level calculations is still N^5 where N = number of basis functions. The MP2 calculations perform reasonably well at predicting equilibrium structures and the conformational energy differences between minima for many systems. However, the main disadvantage of the MPn theory is that it is not variational and that calculated energies maybe lower than the exact energy. In addition, the calculated electron correlation energy is often too large, although this is usually compensated for by basis set limitations which introduce error in the opposite direction.[46]

Other approaches to including electron correlation within *ab initio* theories include the Coupled Cluster (CC) methods. These methods provide a more accurate description of electron correlation beyond the MP4 level, and retain the advantage of being size consistent. The CC method is carried out with single and double excitations, denoted CCSD, whereas CCSD(T) also includes triple excitations, with the brackets representing the fact that these are included in an approximate manner. A major drawback of CC methods is that they depend significantly on the basis set employed in their calculations, with large basis sets producing more accurate results. As the scaling factor for these methods is N^7, larger basis sets combined with this level of theory can be computationally prohibitive.

In summary, the accuracy of *ab initio* calculations strongly depends on the degree of electron correlation accounted for in the theoretical method and the size of the basis set employed. Therefore the choice of basis set and theory involves a trade-off between accuracy and computational cost.

3.4.2 Density Functional Theory

Density Functional Theory (DFT) was developed as an alternative and simpler approach to finding a solution to the Schrödinger equation. In principle, it enables

properties to be determined by the electron density, a function of just three variables, $r = (x, y, z)$ therefore making it computationally more efficient than the wave function method, with it's dependence on $3N$ spatial and N spin variables. Early attempts at formulating density functional theory considered a system to behave in a classical manner, with the molecular energy expressed as a functional of the electron density, $[\rho(r)]$ given by the following equation[46,106]

$$E[\rho(r)] = V_{Ne}[\rho(r)] + V_{ee}[\rho(r)] + T[\rho(r)], \tag{3.9}$$

where $V_{Ne}[\rho(r)]$ represents the attraction between the nuclei and the electron density, $V_{ee}[\rho(r)]$ represents the electron-electron Coulomb interactions of a classical charge distribution and $T[\rho(r)]$ is the kinetic energy which was formulated as a simple expression describing a uniform electron gas.[46] However, this theory was not rigorously defined, as for example, the variational principle was not established. The $V_{ee}[\rho(r)]$ term also contained large approximations, in particular, the quantum mechanically expressed exchange-correlation energy was omitted from this term. In addition, the expression for the classical Coulomb electron-electron interactions leads to the unphysical situation of the charge distribution of one electron interacting with itself, referred to as self-interaction.[46] This particular problem is eliminated in wave function methods but remains a problem in current DFT approaches.[63] The approximation for $V_{ee}[\rho(r)]$ combined with the approximation for the kinetic energy based on a uniform electron gas, led to large errors in molecular calculations.[46]

Further developments of DFT occurred with two theorems proved by Hohenberg and Kohn.[107] These were crucial in establishing DFT as a viable approach to quantum chemical calculations. The first theorem stated that the electron density $\rho(r)$, determines the external potential - a unique arrangement of the nuclei (number, charge and position) and therefore proved that the many particle ground-state energy is a unique functional of the ground-state electron density. This in turn showed that the ground-state density determines the Hamiltonian operator from which all properties of a system can be obtained.[46,106] The second theorem introduced the

variational principle, which stated that the functional that delivers the ground state energy of the system will deliver the lowest energy if, and only if, the input density is the true ground state density, $\rho_0(r)$. Any other input density leads to higher energy values.[106] Both these theorems established that the electron density determines the external potential and therefore the Hamiltonian, which ultimately determines the wave function from which the energy and other properties can be computed. However, this approach did not have the potential of being any simpler than the wave function approach based on molecular orbital theory. In addition, it was not clear how to construct an appropriate functional that would correctly reproduce the ground state energy.[46] A major breakthrough came with Kohn and Sham who recognized that problems with previous DFT methods were related to how the kinetic energy was determined. In their approach, the kinetic energy was calculated assuming non-interacting electrons and therefore an orbital based approach analogous to the Hartree-Fock (HF) method was reintroduced in order to calculate the majority of the kinetic energy with reasonable accuracy. The remaining small part of the kinetic energy, relating to the interaction of electrons in a real system, was absorbed into a term for the exchange-correlation energy, E_{xc} which also contained a correction to the classical self-interaction problem described earlier.[46,106]

A general DFT energy expression can then be written in the following way[92]

$$E[\rho(r)] = V_{Ne}[\rho(r)] + V_{ee}[\rho(r)] + T_{ni}[\rho(r)] + E_{xc}[\rho(r)]. \tag{3.10}$$

The Kohn-Sham model is similar to the HF method, in that it includes the same structure for the kinetic energy (non-interacting electrons, T_{ni}) the electron-nuclei and the electron-electron interaction energies. However, the specific form for the remaining energy, the exchange-correlation $E_{xc}[\rho(r)]$ term, has remained elusive. The main objective of DFT has therefore been to develop approximate functionals for $E_{xc}[\rho(r)]$ that can deliver as accurate as possible values for this component of the energy.

One particular group of approximate exchange-correlation functionals are the hybrid functionals. These approaches express the exchange-correlation energy as a mixture of HF exchange (which can be calculated exactly) and DFT exchange, as

well as DFT correlation as shown by the following equation[63]

$$E^x_{hybrid} = c_{HF}E^x_{HF} + c_{DFT}E^{XC}_{DFT}, \tag{3.11}$$

where the c's are constants. The inclusion of a certain amount of HF exchange in these functionals has led to a general improvement in the calculated results and has been attributed to the reduction of the self-interaction error.[93] An example of a hybrid functional is the B3LYP method which is considered to be one of the most successful in terms of overall performance.[93]

The re-introduction of orbitals (often referred to as KS orbitals to distinguish them from HF orbitals) increases the number of variables to $3N$ and therefore increases the computational cost. However, this method is still considerably less complicated and more efficient than the HF method and significantly less computationally expensive than *ab initio* correlated methods, where the scaling factor with the system size ranges from N^5 to N^7. However, there are certain circumstances for which DFT performs poorly. In particular, DFT methods do not adequately account for the weak interactions due to dispersion forces which arise from electron correlation at the long range. This is a result of the energy being a function of the density, or the gradient of the density at a given location, and therefore long range dispersion forces cannot be properly described. This can result in inaccurate calculations for specific properties of a system where electron correlation is particulary important.

An additional problem with DFT is in the prediction of rotational barriers in π-conjugated systems. Many functionals overstabilize π-conjugation in planar conformers, which results in overestimated energy barriers. This appears to be partly due to the problems in correcting for the classical self-interaction energy, which results in functionals favouring systems having more highly delocalized densities over more localized ones.[46,128,129,154] In spite of the problems, DFT methods, in particular hybrid functionals, have been shown to perform particularly well when compared to sets of reference data: i.e. empirically derived thermochemical databases.[94,106]

However, the success of one particular functional for a specific property of a particular system cannot be assumed to be the same when applied to another system, and therefore it is important that DFT calculations are compared with experimental data (when available) or high quality wave function results.

3.4.3 Basis Sets

A basis set is a mathematical description of the orbitals within a molecular system. Basis sets are employed in both DFT and wave function based methods, although the large collection of current basis sets used in QC calculations have been largely constructed in the context of *ab initio* theory. It is generally recognized that larger basis sets are crucial for *ab initio* correlated methods, where the accuracy of the calculations is heavily dependent on the basis set size. However, in Kohn-Sham DFT methods, orbitals play an indirect role and therefore basis set requirements in the calculations are less stringent than for wave function based methods.[106]

Typical basis sets generally employed in QC calculations consist of linear combinations of atom-centered gaussian functions, due to the ease at which they can be mathematically manipulated. A more accurate description of orbitals can be gained by using large basis sets, as these impose less restrictions on the locations of electrons in space. Different types of basis set are characterized by the number of basis functions they contain and by the people who have developed them. For example, split valence basis sets have two or more different sizes of basis functions for each valence orbital. The most commonly used are the split valence basis sets developed by Pople *et al.*,[95] including 6-31G (double valence) and 6-311G (triple valence) basis sets, and those of Dunning and co-workers, for example cc-pVDZ (double valence) and cc-pVTZ(triple valence) basis sets.[46,106] The 'cc' stands for correlation-consistent and refers to the fact that these basis sets were designed specifically for wave function based methods. Split valence basis sets enable the orbitals to change size but not to change shape. A better description is provided by the addition of angular momentum functions to the basis set, commonly referred to as polarized basis sets. For example, the polarized basis set 6-31G(d,p) adds polarization functions (d functions) to heavy atoms (post 1st row atoms) and p functions to the hydrogen atoms. Higher angular

momentum functions are essential for describing interactions between electrons in electron correlated methods. For example, the basis set 6-311G(3df,2pd) places 3d functions and 1f function on heavy atoms as well as 2p functions and 1d function on hydrogens. The Dunning's correlation-consistent basis sets include polarization functions by definition.[63,93]

There are certain circumstances where the addition of diffuse functions to basis sets are required. These are extended versions of specific functions which enable orbitals to occupy a larger region of space. Diffuse functions are particularly important for describing systems where electrons are relatively far from the nucleus as for example, molecules with lone pairs of electrons,[155,191] anions and systems in excited electronic states.[50,63] In addition, diffuse functions appear to be necessary for improving the description of delocalized electrons in π-conjugated systems[155,191] and also for a more accurate description of the dihedrals in molecules containing highly electronegative atoms.[108,192] Diffuse functions are represented by a '+' in the Pople family of basis sets, such that a 6-31+G(d) basis set adds diffuse functions to all heavy atoms, whereas 6-31++G(d) adds diffuse functions to hydrogens as well. In the Dunning family of basis sets, diffuse functions on all atoms are prefixed with 'aug', as in the aug-cc-pVTZ basis set. Diffuse functions on hydrogen atoms seldom make a significant difference to the accuracy of QC calculations.[46,63] According to Boese *et al.*, diffuse functions are more important in improving accuracy when combined with the Pople basis sets in contrast to the Dunning's basis sets.[16]

The choice of basis set employed in QC calculations plays a significant role in determining the accuracy of the results and is particularly important for wave function methods. However, it appears that for many systems, a subtle combination of theoretical method and basis set is required for accurate calculations, and combinations that perform well for one molecular system are not necessarily appropriate for another. The choice of QC calculations employed in this work was therefore guided by the above considerations and are described below.

3.4.4 Quantum chemical calculations and fitting procedure used in this thesis

The calculations were performed using either density functional theory (DFT) employing the B3LYP functional, or the Møller-Plesset perturbative method at the MP2 level. All calculations were carried out with the Gaussian09 suite of programs. Various basis sets were used, including the Pople type polarized, split-valence (double and triple) basis sets and the Dunning's correlation-consistent basis sets. Initial structures were optimized using the z-matrix coordinate system and the B3LYP/6-31g(d,p) level of theory. These were further improved by using them as starting structures for more accurate optimizations at a higher level of theory and/or larger basis sets. The dihedral angles were scanned from 0° to 360°, with a step size of 6°, so that at each scan point, the dihedral remained fixed whilst all the other structural parameters were allowed to relax and become fully optimized. In order to save CPU time, the dihedral of interest was scanned from 0° to 180° if this was the mirror image of 180° to 360°. Zero-point vibrational energies (ZPVE) have been neglected in all the calculations as these have been shown to contribute less than 1.0 kJ mol^{-1} to the torsional potential profiles of conjugated systems.[152,153]

The procedure used for the parametrization of the dihedral angles consisted of minimizing the squared difference, χ^2, between the molecular mechanics (MM) and the QC calculations

$$\sum_{i=1}^{N_{\text{pts}}} \left[E^{\text{QM}}(\varphi_i^j) - E^{\text{MM}}(\varphi_i^j)\right]^2 = \chi^2, \tag{3.12}$$

where $E^{\text{QM}}(\varphi_i^j)$ and $E^{\text{MM}}(\varphi_i^j)$ are the QC and MM energies and N_{pts} represents the number of QC points for calculating the rotational profile of dihedral angle (φ_i^j). The $E^{\text{MM}}(\varphi_i^j)$ can be expressed as:

$$E^{\text{MM}}(\varphi_i^j) = E_{\text{torsion}}(\varphi^j) + E^{\text{ff}}, \tag{3.13}$$

where E^{ff} represents the other force field terms that contribute to the dihedral of interest in addition to the torsional terms which are being fitted.

3.5 Data analysis

3.5.1 Measuring uniaxial and biaxial orientational order in liquid crystal phases

The analysis of molecular organization in liquid crystals firstly involves defining molecular orientation vectors (or reference axes). Correlation between these vectors can then be evaluated. In the current work, the molecular axes were defined as follows: (a) a set of orthogonal vectors representing the three principle axes of the molecule were obtained by diagonalizing the inertia tensor; (b) three orthogonal vectors were obtained for the aromatic core only, by calculating vectors running along the molecular arms up to the end of the outer phenyl ring and subtracting one arm vector from the other to obtain the long axis vector, and then summing them to obtain a vector along the short axis (generating a third vector for the second short axis from the cross product of the other axes). Calculation of uniaxial order parameters predominantly used a vector parallel with the long axis (z axis) of the mesogen core. Alternatively, a molecular vector associated with the smallest eigenvalue of the inertia tensor matrix (and hence long axis of the molecule) was used as a reference axis for a small number of calculations. Figure 3.1 shows a generic molecular frame of reference for a standardized bent-core mesogen.

The instantaneous average of a specified molecular vector for each molecule in a simulation cell, defined a system director, denoted $\mathbf{n}$. The degree of order with respect to this director, usually called S (a scalar quantity) represents the uniaxial order of the system and is commonly calculated as the average of the second Legendre polynomial

$$S = \langle P_2 \cos\theta \rangle = \left\langle 3\cos^2\theta - 1 \right\rangle /2, \tag{3.14}$$

where θ is the angle between the molecular vector and the director, $\mathbf{n}$. The uniaxial order parameter, S can vary from 1 (perfectly aligned sample) to -1/2 if the molecules are aligned in the plane orthogonal to $\mathbf{n}$. Molecules are randomly orientated if $S = 0$. In the liquid crystal state it is normal for S to be positive

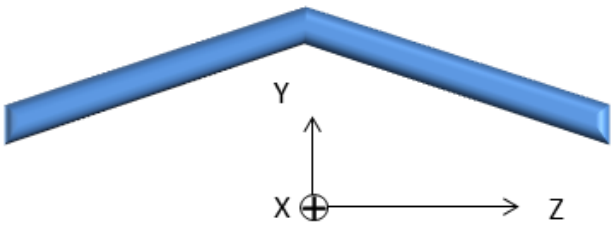

Figure 3.1: Generalised molecular structure and molecular frame of reference for a bent-core mesogen

$0 < S < 1$ and in the temperature range of most nematics, S ranges from 0.35 to 0.7 and decreases with increasing temperature.[132,171]

In order to be able to calculate the uniaxial order parameter from the simulations the director, $\mathbf{n}$, associated with the average direction of the molecular long axes needed to be defined. A common approach, which was adopted in this thesis, is to extract this information from the diagonalization of a Q tensor (second rank 3×3 ordering matrix) which is based on Cartesian coordinates and is expressed as

$$Q_{\alpha\beta} = \frac{1}{2N} \sum_{i=1}^{N} \left[3u_{i\alpha}u_{i\beta} - \delta_{\alpha\beta} \right], \tag{3.15}$$

$$\delta_{\alpha\beta} = \begin{cases} 0 \,\text{if} \alpha \neq \beta \\ 1 \,\text{if} \alpha = \beta \end{cases}, \tag{3.16}$$

where the sum runs over all N molecules in the system, $\alpha, \beta = x, y, z$ coordinates of the long axis and $u_{i\alpha}$ is the α component of the molecular long axis vector, $\mathbf{u}$. The largest eigenvalue of the Q tensor represents P_2 and the associated eigenvector is the director, $\mathbf{n}$. The definition of the uniaxial order parameter, P_2 extracted from Q tensors is given by

$$P_2 = Q_{00}^2 = \langle Z \cdot Q^{zz} \cdot Z \rangle \,, \tag{3.17}$$

where the superscript 2 denotes that this is a second rank orientational order parameter, and the subscript 00 represents the ordering of the molecular z axis (long axis) with respect to Z (the director vector, $\mathbf{n}$). In this thesis, the notation P_2, is used to represent the uniaxial order parameter for the long molecular axis.

In order to calculate biaxial orientational order for a liquid crystal phase, the scalar uniaxial order parameters associated with the directors ($\mathbf{l}$ and $\mathbf{m}$) perpendicular to $\mathbf{n}$ also need to be defined. This involves constructing the ordering tensors, Q^{yy} and Q^{xx}, and extracting from these the dominant eigenvalues and associated eigenvectors. These additional uniaxial order parameters are denoted as $Q_{00}^2 = \langle X \cdot Q^{xx} \cdot X \rangle$ and $Q_{00}^2 = \langle Y \cdot Q^{yy} \cdot Y \rangle$ where X and Y are the director vectors, $\mathbf{l}$ and $\mathbf{m}$, and x and y represent the molecular axes. The biaxial nematic state is expected to exist when the three scalar order parameters in the three perpendicular directions are different.[118]

One way of measuring biaxiality is to calculate the difference between how well the molecular x and y axes are aligned with the X and Y system directors respectively, and how well they are aligned with the Y and X directors respectively. This measure of biaxial order can be expressed as an ensemble average and is given by

$$Q_{22}^2 = \frac{1}{3}\big\langle XQ^{xx}X + YQ^{yy}Y - XQ^{yy}X - YQ^{xx}Y \big\rangle, \tag{3.18}$$

where the superscript 2 of Q_{22}^2 denotes that this is a second rank orientational order parameter and the subscript 22 represents the differences in ordering of the molecular x and y axes with respect to the director vectors, X and Y. If the molecular x and y axes are perfectly aligned with X and Y (or with Y and X directions respectively), this quantity is 1 (or -1) while if they are equally likely to point in any direction perpendicular to Z, this value is 0. A non-zero value therefore indicates a degree of biaxiality in the system.[118] Although there are a number of other order parameters used to fully characterize the biaxial phase, Q_{22}^2

is usually calculated in simulations to determine whether the phase is biaxial or not. In this thesis, the biaxial order parameter, Q_{22}^2, was calculated for the investigated oxadiazole bent-core mesogens and the results are presented in Chapters 5 and 6. It should also be noted that there are alternative formulations used elsewhere in the literature to represent all the above order parameters with their own specific notation.[11]

3.5.2 Characterizing structure in liquid crystal phases

In order to describe and characterize liquid crystal systems investigated in this thesis, various pair distribution functions were calculated and are described below. The role of pair distribution functions includes:[142,186]

- elucidation of the local structure (the nearest environment around a molecule),
- information about the structure at more remote distances from a reference particle,
- differentiating between phases (eg. the nematic and smectic phases),
- distinguishing between different types of interlayer organization in the smectic phase,
- identifying pretransitional molecular organization in the isotropic phase.

The simplest pair distribution function is $g(r)$, a radial distribution function (RDF) which calculates the most probable intermolecular distances between two particles irrespective of orientation, and has the form

$$g(r) = \frac{V}{N^2}\left\langle \sum_{i}^{N}\sum_{i\neq j}^{N} \delta(\mathbf{r} - \mathbf{r}_{ij}) \right\rangle, \tag{3.19}$$

where $\mathbf{r}_{ij}$ is the vector between the centres of mass of two molecules, δ is the Dirac delta and V and N are the volume and number of molecules respectively. The characteristic peaks of a radial distribution function showing values greater than one, represent a higher probability of two particles being found at a particular

distance. Sharp high peaks are associated with a more structured organization, such as found in a crystal or smectic phase, and values close to one indicate an unstructured, isotropic fluid.

The anisotropic nature of liquid crystal phases requires additional distribution functions to differentiate between phases. These are $g_{\parallel}(r)$, which evaluates the intermolecular components of $g(r)$ that are parallel to the director, and $g_{\perp}(r)$, the components that are perendicular to the director. These two functions can be used to distinguish between the nematic and smectic phases and also determine interlayer organization in smectic phases.

In addition to the above distribution functions, information on the intermolecular orientations can be obtained from the orientational distribution functions, $g_1(r)$ and $g_2(r)$. For example, $g_1(r)$ can provide information on the most favourable geometric arrangement between nearest neighbour molecules. In particular the local polar ordering of molecules possessing large dipole moments, can be characterized by

$$g_1(r) = \langle \delta(r - r_{ij})(\mathbf{u}_i \cdot \mathbf{u}_j) \rangle \,, \tag{3.20}$$

where $\mathbf{u}_i$ is a chosen molecular vector and r is the distance between the reference centres of two different molecules.

The orientational distribution function, $g_2(r)$, calculates the average relative orientation of molecules separated by a distance r and has the form

$$g_2(r) = \left\langle \delta(r - r_{ij}) \left(\frac{3}{2}(\mathbf{u}_i \cdot \mathbf{u}_j)^2 - \frac{1}{2} \right) \right\rangle. \tag{3.21}$$

In the isotropic phase this function decays to zero at large r, but in an orientational ordered phase approaches a value of $\langle P_2 \rangle^2$ at large r, and is therefore a useful function for identifying an isotropic to nematic phase transition.

Chapter 4

Optimization of the GAFF Force Field to Describe Liquid Crystal Molecules

4.1 Introduction

Computer simulations using different models, from coarse-grained to fully atomistic, provide a unique tool for the investigation of liquid crystal materials. Although coarse-grained models have the advantage of being able to study larger systems with reduced computational costs, fully atomistic simulations have the potential to link the fine details of chemical structure with the properties of a system.[23] For example, the phase transition and stability of particular mesophases are particularly sensitive to small changes in chemical structure. However, the phase diagram and mesophase properties derived from atomistic simulations strongly depend on the force field employed and its description of the molecular geometry and inter-molecular interactions involved in a specific system.[145]

In standard force fields, such as OPLS, GROMOS and AMBER, the parameters are derived from experimental data and quantum chemical (QC) calculations for a selected set of molecules. For the description of larger molecules, including liquid crystals, the parameters for atoms of small molecules are transferred to the larger entities, with the assumption that the chemical environment is similar.[21] How-

ever, the use of standard force fields for the study of liquid crystal systems often produces only approximate results, indicating that the transferability hypothesis cannot always account for specific molecular details that may affect the stability of the mesophases and the macroscopic properties. For example, Tiberio *et al.*[169] obtained a simulated nematic-isotropic transition temperature (T_{NI}) $\approx$ 120 K above the experimental value for the mesogen 5-alkyl-cyanobiphenyl (5CB) using a standard AMBER force field.[169] Recently, Chami *et al.* simulated 8CB employing an AMBER force field, and predicted a T_{NI} $\approx$ 61 K higher than the experimental value, as well as a nematic-smectic transition temperature, (T_{SN}), $\approx$ 33-53 K higher than experimental.[31] Similarly, Kuprusevicius *et al.* obtained a $T_{\mathrm{NI}} \approx$ 75 K higher than experimental for the same molecule with a force field based on OPLS-AA.[112] These results indicate that the T_{NI} is dependent on the force field employed, and that the higher transition temperatures compared with experimental values suggests that the force fields overestimate the attraction between molecules.

4.2 Development and evaluation of a liquid crystal force field: initial choice of GAFF

One approach to improving the description of liquid crystal materials is to develop an original force field from QC calculations only using the Fragmentation Reconstruction Method (FRM), as described by Cacelli *et al.*[20,22–24] Unlike standard force fields, which are based on two-body effective potentials, with three-body effects included in an average way, this approach is limited to two-body interactions due to the prohibitive computational cost. FRM results for a number of liquid crystal systems have led to good agreement between experimental data and a number of calculated structural and thermodynamic properties. However, inaccuracies have included the generation of an incorrect smectic phase and missing nematic phase for an azobenzene based mesogen [20], although good agreement with experimental data was obtained for the isotropic phase properties. Additionally, a significant overestimation of the density ($\approx$ 6%) was obtained for 5CB as well as an underestimation of the translational diffusion coefficients, although these have largely been rectified

in a recent paper by significant changes to the intramolecular potential as well as some adjustments to the intermolecular potential.[22]

Although defining a force field from QC calculations only has demonstrated some success, the process remains time consuming and computationally expensive. An alternative approach to obtaining a force field suitable for liquid crystal molecules is to focus on the refinement of standard force fields, *via* the amendment of some of the key parameters. Tiberio *et al.* tuned the vdW parameters of the AMBER united atom force field for the family of *n*-alkyl-cyanobiphenols (*n*-CBs) so that the densities, phase transition temperatures, orientational order parameters and NMR residual dipolar couplings could be reproduced with good accuracy.[169] In particular, the T_{NI} for 5-CB was reproduced within ±4 K of the experimental value. Another study by Zhang *et al.* employing the TraPPE-UA force field, involved re-optimizing a number of aromatic carbon vdW parameters of the biphenyl unit, with the aim of reproducing the experimental density of 5CB within 2%.[198] Due to the lack of suitable torsional potentials in TraPPE for some of the key dihedrals important in defining the conformations of the 5CB molecule, the chain dihedral torsional parameters were taken from the GROMOS force field and those for the dihedral between the phenyl ring and the aliphatic chain were taken from Stevensson *et al.*[166] This refined force field was then tested by comparing a number of thermodynamic, structural and dynamic properties extracted from molecular dynamic (MD) simulations with experimental data. Their results showed good agreement with the experimental measurements, in particular for density and T_{NI} transition temperatures.

Among the standard force fields available for atomistic simulations is the General AMBER Force Field (GAFF). This force field was developed with the objective of describing a wider range of molecules than those covered by the AMBER force fields, which were primarily developed for protein and nucleic acid systems.[185] Recently, Wang & Hou and Caleman *et al.* have carried out systematic studies to test the ability of GAFF in reproducing some key properties of liquids.[18425] The results for the predictions of both density and $\Delta_{\mathrm{vap}}H$ for 71 organic molecules containing the most common chemical functional groups, showed an average uncertainty estimate (AUE) of 0.0436 g cm^{-3} for density and an AUE of 3.9 kJ mol^{-1} for $\Delta_{\mathrm{vap}}H$.[184] The

authors also concluded that the prediction errors for both these properties could be reduced further by a systematic tuning of the vdW parameters of a number of GAFF atom types. For example, they found an improvement in the predicted densities and $\Delta_{\text{vap}}H$ values for a set of aromatic compounds by tuning the vdW parameters of the carbon atoms of benzene and transferring these to a selected number of aromatic compounds. In another study, GAFF was systematically tested on the reproduction of some key properties of liquids, including the densities and $\Delta_{\text{vap}}H$ of 146 molecules using the GROMACS molecular simulation package.[25] (A dedicated website with experimental and simulated physical properties in the form of a database can be found at http://virtualchemistry.org.) The overall performance of GAFF was considered to be reasonably good, considering the fact that parameter development was not aimed at liquids. However, their results showed an overall slight underestimation of densities for the compounds studied, along with an over estimation of $\Delta_{\text{vap}}H$ for the majority of the compounds.

Although GAFF was designed as a general purpose force field with wide applicability,[185] a number of recent attempts to reproduce accurate T_{NI} transition temperatures for mesogens have been unsuccessful. In the current study, simulations of a typical calamitic mesogen and a *bis*-phenyl oxadiazole (ODBP) bent-core mesogen using GAFF resulted in T_{NI} temperatures of $\approx$ 60 K and $\approx$ 110 K higher than the experimental values respectively. Another study of a T-shaped benzothiazole mesogen produced a T_{NI} temperature $\approx$ 200 K higher than the experimental value.[189]

A systematic approach to improving force fields, using small, incremental changes to multiple parameters, is prohibitively expensive in terms of time and computational resources when applied to large liquid crystal mesogens. To keep the number of parameter changes required to a minimum, this investigation attempted to improve GAFF for mesogenic molecules, *via* optimization and fitting some key torsional dihedrals (including a re-examination of existing conformational data for *n*-alkanes) and refinement of Lennard-Jones(LJ) parameters for mesogenic fragment molecules, in order to improve the reproduction of experimental densities and heats of vaporization ($\Delta_{\text{vap}}H$) for cases where GAFF parameters are not transferable. It is also

acknowledged that the intermolecular interactions in GAFF are modelled by electrostatic energies as well as LJ interactions. Preliminary findings indicate that the atomic charges do not play a significant role in determining T_{NI}. For example, simulations of 5CB with the atomic charges set to zero reduced the T_{NI} temperature by only 5 K, although significant changes to the short-ranged structure were observed.[169] It was therefore decided to retain the original GAFF atomic charges in the current work.

The remainder of this chapter is organised as follows: following computational details, the results of the amended force field parametrization, GAFF-LCFF, are presented in Section 4.4, along with a discussion of these results. Section 4.5 discusses the results from testing GAFF-LCFF parameters on a typical calamitic nematogen (1,3-benzenedicarboxylic acid,1,3-*bis*(4-butylphenyl)ester). Section 4.6 includes the results of testing the GAFF-LCFF on two ODBP bent-core mesogens along with justification for a further small refinement to the parameters relevant to these mesogens.

4.3 Computational details

All the calculations were performed using the GROMACS 4.5.5 package with GAFF as the basic force field. The energy function employed in the MD simulations was described in Chapter 3 (see equations 3.2 to 3.7). The following provides a summary of the simulation methods relevant to this chapter (see Chapter 3, Sections 3.1 and 3.2 for a fuller description). The procedure for obtaining new torsional parameters from QC calculations was described in Chapter 3, Section 3.4.4.

4.3.1 Atomistic simulations

Fragment molecules

The generation of a simulation box for each fragment involved firstly, placing one molecule in a $2 \times 2 \times 2$ nm^3 box, followed by the construction of a $5 \times 5 \times 5$ nm^3 box containing 125 molecules. Using the GROMACS **genconf** program, this was then stacked $2 \times 2 \times 2$ to generate a box containing 1000 molecules. This was then

simulated under high pressure (100) bar and 300 K to force the molecules into the liquid phase, followed by equilibration under normal pressure (1 bar). All of the liquid MD simulations employed periodic boundary conditions and the non-bonded cut-offs for calculating the van der Waals (vdW) and electrostatic interactions was set to 1.2 nm. The Particle Mesh Ewald (PME) method was used to calculate the full electrostatic energy and corrections to pressure and potential energies was employed to compensate for the truncation of the vdW interactions. All simulations were conducted at a pressure of 1 atm using the Berendsen barostat for the equilibration runs and the Parrinello barostat for the production runs. The temperatures of the simulations were selected to fit the experimental data available and were either 298 K or 293 K. Bond lengths were kept fixed at their equilibrium values using the LINCS algorithm and a timestep of 2 fs was employed in the simulations.

The heat of vaporization was calculated using the following equation

$$\Delta_{\mathrm{vap}}H = (E_{\mathrm{pot}}(\mathrm{g}) + k_{\mathrm{B}}T) - E_{\mathrm{pot}}(\mathrm{l}), \tag{4.1}$$

where $E_{\mathrm{pot}}(\mathrm{g})$ represents the intramolecular energy in the gas phase and $E_{\mathrm{pot}}(\mathrm{l})$ is the intermolecular energy in the liquid phase. The density, ρ was obtained from the liquid simulations using the GROMACS program, **g_energy**. The gas phase simulations were performed using a stochastic dynamics integrator.

Mesogens

Simulations of the 1,3-benzenedicarboxylic acid,1,3-*bis*(4-butylphenyl)ester mesogen (henceforth abbreviated to 'phenylester-LC') and the two ODBP bent-core mesogens were initially started from a low density gas phase and then compressed to a liquid at high temperature using the procedure described above. All simulations were started from well equilibrated, orientationally disordered configurations. Each system was then progressively cooled at 10 K intervals, with equilibration runs of at least 40 ns and long production runs of between 80 and 180 ns, depending on the size of the mesogen. The lengthy simulation times, coupled with cooling the system from disordered configurations, provides greater confidence in the results when observing the spontaneous onset of ordering in LC phases.[137,169,198] According to Palermo *et*

al. in their atomistic description of the nematic and smectic phases of 4-n-ocytyl-4 cyanobiphenyl (8CB), an average total simulation time of 150 ns for each temperature was considered to be more than appropriate, as this length of time was expected to be much greater than the rotational and correlation decay times.[137] In order to investigate system size effects on estimating the T_{NI} temperatures (presented in Section 4.6.1 for the ODBP bent-core mesogens) the small samples were replicated twice in each direction at selected temperatures and re-equilibrated for 10 ns followed by a production run of a further 20 ns. Table 4.1 summarises the simulation characteristics for both the mesogens and the smaller fragment molecules.

Table 4.1: Simulation characteristics for the different simulation types

Name	Time / ns	No.of molecules	Ensemble	Constraints	Electrostatics
Liquid (fragments)	20	1000	NPT	all bonds	PME
Liquid (mesogens)	110 to 240	248 to 2056	NPT	all bonds	PME
Gas	200	1	NVT	all bonds	all interactions

Calculation of molecular order and structure

The uniaxial order parameter, $\langle P_2 \rangle$, was calculated as the largest eigenvalue obtained from diagonalization of the ordering matrix, Q, with the chosen molecular reference axis (long or z axis) representing a vector parallel with the long axis of the aromatic core of the phenylester-LC or the Ph-ODBP-Ph unit of the bent-core mesogens. Alternatively a molecular vector associated with the smallest eigenvalue of the inertia tensor matrix (and hence long axis of the molecules) was used as a reference axis for a small number of calculations.

Structural organization and differentiation between phases was deduced by evaluating various pair distribution functions including; $g(r)$, $g_1(r)$, $g_2(r)$, $g_{\parallel}(r)$ and $g_{\perp}(r)$. (see Chapter 3 and Section 3.5.1 and 3.5.2 for full details and equations for measuring orientational order and structural organization).

4.4 Results and Discussion

4.4.1 Optimization of torsional potentials

Phenyl benzoate

Many liquid crystal forming molecules contain a phenyl benzoate (PB) fragment as part of their structure. The position and conformation of the ester (-C=O-O-) group is implicated in the development of spontaneous polarization in the ferroelectric phase and spontaneous chiral segregation of bent-core liquid crystals, as well as affecting the magnitude of the bend angle.[60,90,108,113] The two dihedrals, φ_1 and φ_2 (see Figure 4.1), are associated with the internal rotation around the C(=O)-C_{ar} and C_{ar}-O(ester) bonds respectively and are significant in defining the overall conformation of PB.[191] The torsion around the central C(=O)-O bond is generally considered to be rigid, with the associated dihedral assuming a fixed angle of 180°, thus simplifying the conformational space of PB.[191] There is some experimental data on the minimum energy structure and rotational energy barriers of PB but a limited number of theoretical studies.[35,172,191]

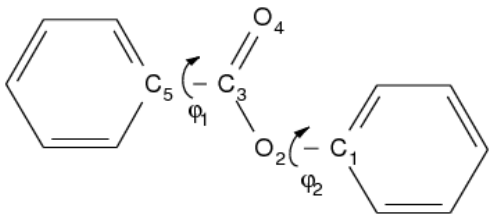

Figure 4.1: Structure of phenyl benzoate

The molecular structure of PB has been determined by gas electron diffraction (GED), and the relationship between structure and the T_{NI} was studied by comparing PB with closely related mesogens containing two phenyl rings but with different linking units.[172] The authors concluded that there was a relationship between the mesogen core structure and the T_{NI}. The features that lowered the T_{NI} of PB relative to other closely related mesogens were: non-planarity of the core, a relatively large dihedral φ_2 angle of 64° for the minimum energy structure, low torsional energy barrier for dihedral φ_2 and high flexibility of the phenyl ring attached to the ester oxygen atom. On the assumption that these structural features may be transferred

into larger mesogens that contain the PB unit and may play a part in determining the T_{NI}, it is therefore important that GAFF accurately represents these structural features of PB.

The results of the theoretical calculations for the equilibrium geometry and torsional barriers of the two key dihedrals φ_1 and φ_2 are presented in Table 4.2, along with the experimental values, GAFF predicted values and a number of results from references[35,191] for comparison.

Table 4.2: Rotational energy barriers for dihedrals φ_1 and φ_2.

Method	φ_1°	ΔE_{90} kJ mol^{-1}	φ_2°	ΔE_0 kJ mol^{-1}	ΔE_{90} kJ mol^{-1}
X-ray[a]	-8.7	-	67.6	-	-
Exp. GED[a]	0.0	14.64	64.0	5.02	0.13
GAFF	0.0	119.44[c]	45.0	5.80[c]	3.50
Amended GAFF (this work)	2.7	27.27[c]	73.3[d]	5.50[c]	≈0
B3LYP/6-31G(d)[a]	1.7	31.38	51.1	1.59	1.59
B3LYP/6-31G(d,p)	-	-	47.7	1.36	1.51
B3LYP/6-31+G(d,p)	-	-	63.7	2.83	0.26
B3LYP/6-311+G(d,p)	1.5	27.55	65.9	3.50	0.20
B3LYP/6-311+G(3df,3pd)	1.7	26.32	64.8	3.85	0.18
MP2/631+G (d)[b]	-	-	71	12.52	0.57
MP2/631+G (d,p)[b]	-	-	71	9.53	0.29
MP2/aug-cc-pVDZ	-		80.6	8.54	0.00
MP2/cc-pVTZ	1.3	26.41	66.4	5.99	0.18

[a] Results from ref.[191] [b] Results from ref.[35] [c] With bond length constraints. [d] Broad minimum energy well.

The torsional barrier for rotation around the C_3- C_5 bond deduced from the theoretical calculations and GED data show a strong rotational barrier at 90°and a minimum energy dihedral angle, φ_1, close to 0°. This indicates that π-conjugation due to π-delocalization is important in stabilizing a planar arrangement of the benzene ring and the C=O group. However, the GED barrier of 14.64 kJ mol^{-1} suggests that the strength of the experimental π-conjugation is less than that revealed by the DFT (B3LYP functionals) and MP2 calculations. It is generally recognized that molecules comprising a double bond in conjunction with a benzene ring represent a special problem with respect to DFT calculations of the rotational barriers, resulting in over stabilization of the planar conformation and overestimated energy

barriers.[128,129,191] The MP2/cc-pVTZ calculated barrier is similar to the most accurate DFT result. It has been suggested that the inclusion of diffuse functions with wave-function based methods, such as MP2, provide a better description of delocalized electrons,[155] and therefore it is likely that the larger aug-cc-pVTZ basis set may improve the results. The GAFF predicted minimum energy stucture is in agreement with the experimental and theoretical results, although the torsional barrier at 90° is significantly higher than either of these, indicating that rotation around this bond is more hindered than the experimental result suggests. As a compromise on CPU demands, the MP2/cc-pVTZ calculation was considered a sufficient improvement on the GAFF predicted torsional barrier and new torsional constants, C_n were obtained by fitting the profile into the Ryckaert-Bellemans (RB) function used to describe dihedral torsions in GROMACS, as described in Chapter 3. The new RB coefficients for this dihedral as well as those for the subsequent torsions in the following sections are presented in Table 4.7 at the end of Section 4.4.1

The experimental values as well as theoretical results indicate that φ_2 is particularly flexible with a wide minimum energy region and a small torsional barrier at 0° in addition to an insignicant barrier at 90° (see Figure 4.2).

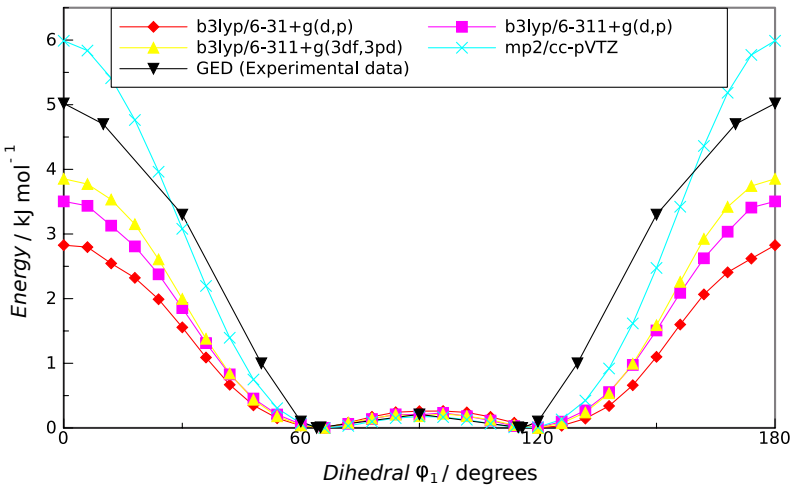

Figure 4.2: Quantum chemical torsional energy profiles for dihedral φ_2 of PB

The theoretical results are somewhat dependent on the level of theory and the basis sets employed in the calculations. Comparison with the GED data shows that the most accurate calculations for both the dihedral φ_2 angle and ΔE_0 barrier

height are given by the B3LYP/6-311+G(3df,3pd) and MP2/cc-pVTZ calculations. The addition of diffuse functions in the DFT calculations increases the accuracy of the results. This has been attributed to the fact that electron lone pairs (eg. the oxygen atom of dihedral φ_2) require the orbitals to occupy larger regions of space, which are better described with the addition of diffuse functions and is also been found to be particulary important when using DFT methods with the Pople basis sets.[16,191] The most accurate MP2 result in terms of the minimum energy structure and dihedral φ_2 torsional energy barriers is generated with the triple zeta, cc-pVTZ basis set. These are significantly more accurate than those generated in reference[35] where the use of a relatively small Pople basis set show deviations from experimental values, in particular for the ΔE_0 torsional barrier. In contrast to the experimental values and the most accurate theoretical calculations, the GAFF minimum energy dihedral φ_2 angle is $\approx 45°$ as opposed to $\approx 65°$, and there is a more significant torsional barrier at 90°. However, the main barrier at 0° is in reasonable agreement with the GED value.

The lack of any experimental data in the literature on the bulk properties of PB meant that it was not possible to compare the effects of amended torsional parameters on these calculated properties of PB. It was therefore decided to derive the torsional potential for the analogous dihedral φ_2 of phenyl acetate (C(phenyl ring)-O(ester)- see Figure 4.6) for which there is available experimental data on the bulk properties. This enabled the combined effects of the new parameters (torsional and vdW) on the calculated properties with experimental values. It was found that the torsional potential for dihedral φ_2 of phenyl acetate (PA) employing an MP2/cc-pVTZ calculation resulted in a similar minimum energy dihedral angle of $\approx 65°$ and torsional barriers as those calculated for PB, although the barrier at 0° was slightly less (≈ 1 kJ mol^{-1}) than that for PB.

2,5-diphenyl,1,3,4-oxadiazole (ODBP) torsional potential

The 2,5-diphenyl,1,3,4-oxadiazole (ODBP) fragment represents the central core unit of the oxadiazole based bent-core mesogens (see Figure 4.3). A literature search failed to reveal any reported experimental data or QC calculations for the inter-

ring (phenyl - heterocyclic ring) rotational energy barrier. However, there are numerous experimental structural studies of larger molecules containing the ODBP unit, and these indicate a planar geometrical arrangement of the oxadiazole and phenyl rings.[29,125] The degree of flexibility around the inter-ring bond in the ODBP fragment of bent-core mesogens may be implicated in the extent of local biaxial ordering[143] as well as influencing the nematic-isotropic phase transition.

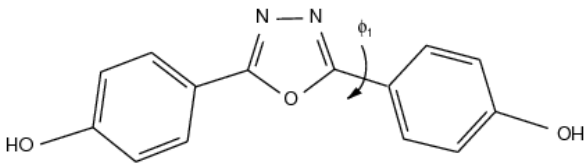

Figure 4.3: Structure of 2,5-diphenyl,1,3,4-oxadiazole

The results of the theoretical calculations for the inter-ring rotational energy barrier (dihedral ϕ_1) relative to the minimum energy structure are presented in Table 4.3.

Table 4.3: Rotational energy barriers for dihedral ϕ_1 in the ODBP molecule. [a] With bond length constraints.

Method	ΔE_{90} / kJ mol^{-1}
GAFF	97.49[a]
Amended GAFF	24.10[a]
B3LYP/6-31G(d,p)	27.79
B3LYP/6-31+G(d,p)	24.17
B3LYP/6-311+G(d,p)	23.83
B3LYP/6-311+G(3df,3pd)	23.47
MP2/cc-pVTZ	22.39

All calculated results show a single large barrier at 90°, ranging from 22.39 kJ mol^{-1} to 27.79 kJ mol^{-1}, indicating the enhanced stabilization of the planar conformation due to the π-conjugation between the electrons of the phenyl ring and those of the C=N electrons in the oxadiazole ring. The results employing the B3LYP functional show a gradual decrease in the barrier height when the basis set is augmented with diffuse and multiple polarization functions. However, as mentioned previously, DFT calculations consistently over stabilize the planar

conformation for π-conjugated systems, which results in overestimated rotational barriers. It would therefore be reasonable to deduce that the torsional barrier for dihedral ϕ_1 is less than 23.47 kJ mol^{-1}, the minimum value obtained with the DFT functionals. The MP2/cc-pVTZ calculation was considered to be the best compromise and significantly better than that given by the original GAFF force field, therefore new RB coefficients were fitted to this torsional profile.

Torsional potentials of *n*-Alkanes and optimization of the C−C−C−C torsion of *n*-heptane and *n*-butylbenzene

For flexible molecules such as *n*-alkanes, it is crucially important to correctly model the intramolecular interactions, as changes in conformational weights influence phase transition temperatures. Accurate modelling requires the correct reproduction of the entire distribution of instantaneous configurations.[62] This is also true for mesogens containing alkane chains. Depending on their length and the type of core unit they are attached to, these components play a key role in the generation of specific mesophases as well as a significant role in reducing melting points and T_{NI} temperatures.[43] It has been observed that the alkane chain conformations for the *n*CB series assume on average more elongated conformations on going from the isotropic liquid to the orientationally ordered nematic phase.[24]

Many standard force fields, including GAFF, perform poorly in the reproduction of liquid properties and phase transitions of *n*-alkanes.[57,123,168] There is some evidence that GAFF and OPLS-AA perform reasonably well for short-chain *n*-alkanes,[97,104,168,184] but significant deviations from experimental values are found for larger *n*-alkanes.[57,168] For example, the OPLS-AA force field results in liquid to gel phase transitions significantly higher than experimental values for longer *n*-alkanes.[168] Recently, a number of computer simulations employing the CHARMM27 and GROMOS force fields in the study of the structure and dynamics of lipid membranes containing long *n*-alkane chains, have shown some disagreement with experimentally observed properties (eg. area per lipid and NMR deuterium bond order parameters).[123] These problems have largely been attributed to an under prediction of the population of *gauche* states, leading to reduced flexibility, and in the

case of lipid tails, an overestimation of the deuterium order parameters at the end of the chains.[57,123,159] Attempts to change the *gauche* and *trans* conformer ratio and rectify some of these problems, have included refitting the torsional parameters of *n*-butane (as well as longer *n*-alkanes) to high quality *ab initio* data, or reducing the intramolecular vdW and electrostatic 1-4 scaling factors.[85,193] This has led to continuous refinements of standard force fields for more accurate simulations of *n*-alkanes and biomolecules containing alkane chains (eg CHARMM27r, L-OPLS-AA GROMOS 43A2 and 45A3).[104,158,159,168] These findings led within this current work to the re-examination of the source data, both experimental and theoretical, used in the original parametrization of *n*-alkanes in standard force fields, to look for some explanation for the discrepencies between the force field calculations and the experimental values.

The experimental and theoretical investigations of the conformational behaviour of *n*-alkanes has predominantly focused on butane, which exhibits two successive barriers (*trans-gauche* and *cis*) in its torsional profile, along with three conformers, *trans* (180° and the lowest energy minimum conformer) and *gauche* (+60° and -60° with the same absolute energy). The main factor governing the relative populations of butane, as well as larger *n*-alkanes, is the energy difference between the *trans* and *gauche* conformers. Most of the experimental studies have measured the enthalpy difference (ΔH_{g}) between the *trans* and *gauche* conformers of butane, and have been predominately performed in the gas phase using spectroscopic techniques. These have recently been summarized by Barna *et al.*[5] The results range from 2.08 to 4.58 kJ mol^{-1}, with a number of studies not specifying the temperature or providing uncertainty estimates.

The lack of consistency in the results has largely been attributed to the complexity of the vibrational spectra of gaseous butane, and as early as 1991 doubts were raised by Murphy *et al.,* and then later by Herrebout (1995), about previously calculated ΔH_{g} values, in particular those reporting larger values.[84,133] Most recently, Balabin (2008) stated that the ratio of *trans/gauche* (t/g) conformer concentrations could only be predicted with an error margin of 40%. Despite these concerns, the two most accepted evaluations for ΔH_{g} are Herrebout's value of 2.80 ± 0.40 kJ mol^{-1}

and Balabin's (2009) evaluation of 2.76 ± 0.09 kJ mol^{-1}, with the latter showing the least associated uncertainty.[4,84] These values have recently been revised by Barna *et al.* employing more sophisticated statistical analysis of the original data and are presented in Table 4.4.

Table 4.4: Summary of the most reliable experimental and theoretical values for the *trans/gauche* energy and enthalpy difference for *n*-butane

ΔH_g / kJ mol^{-1}	T / K	Method	Date (ref.)
2.80 ± 0.09	133-196	Raman spectroscopy	2009[4]
2.73 ± 0.52	223-297	Infrared spectroscopy	1995[84]
2.71± 0.03	298	FPA/CCSD (T)	2012[5]
2.83± 0.01	0	FPA/CCSD (T)	2012[5]
ΔE_g / kJ mol^{-1}			
2.49± 0.01	0	FPA/CCSD (T)	2012[5]

There are indications from experimental studies that the (t/g) liquid phase energy or enthalpy difference for *n*-butane is slightly less that in the gas phase, with the stability of the *gauche* conformer increasing by up to 0.42 kJ mol^{-1}.[4] In terms of the rotational barriers of *n*-butane, it is not possible to measure these directly from spectroscopic data and methods are therefore based on estimates. These suggest that the *t-g* and *cis* barriers are comparable in energy, with one estimate giving values of 15.15 and 16.56 kJ mol^{-1} for the *t-g* and *cis* barriers respectively.[81,161]

The torsional energy about the dihedral C-C-C-C in *n*-butane involves 1-4 interactions between the methyl groups and it is therefore expected that the torsional energy about single bonds in longer *n*-alkanes may result in different values for the *gauche* energy and the rotational barriers.[161] There are indications from experiment that the *gauche* energy is slightly lower in longer *n*-alkanes compared to that for *n*-butane. For example, a low-temperature gas-phase Raman spectroscopy study by Balabin[4] of the conformational equilibration of *n*-pentane resulted in a value of 2.59 kJ mol^{-1} for the enthalpy difference between the *trans-gauche* and all *trans* states. This is slightly lower than his previous value of 2.76 kJ mol^{-1} for *n*-butane. However, the author states that it is not clear whether the differences between the two alkanes are due to size differences or experimental uncertainty, and that further experimental values for various longer *n*-alkanes would be required to make general

conclusions about the dependence of *n*-alkane size and conformer energies.

There is also some evidence that the liquid phase energy or enthalpy difference between the *gauche* and *trans* conformers of longer *n*-alkanes is less than in the gas phase. For example, the results obtained from an infrared study gave an enthalpy difference of 2.08 ± 0.31 kJ mol^{-1} for *n*-pentane, and an average value of 2.13 ± 0.21 kJ mol^{-1} (ΔE_g) for liquid *n*-alkanes with n = 11-14 was obtained from a low frequency spectroscopy study.[157]

The results of theoretical calculations of the *t/g* energy and enthalpy difference for butane are also somewhat inconsistent and appear to be dependent on the level of theory and specific *ab initio* technique used in the calculations.[5] The relative stability of the conformers of *n*-alkanes is thought to be strongly influenced by intramolecular dispersion interactions, with electrostatic effects playing a less important role.[127,130] However, the quantative description of dispersion interactions still remains a great challenge for QC wave-function based methods, and in particular for density functional theories. The most accurate QC calculations are based on the coupled cluster (CC) single, doubles and pertabative triples {CCSD(T)} method. A number of sophisticated *ab initio* techniques have been developed to minimize the uncertainties in the calculations performed by improving the convergence of the electron correlation energy and addressing the problems arising from basis set incompleteness. These include focal point analysis (FPA) and Weizmann-n (Wn) methods, compound methods such as the Gaussian-2 (G2) method and complete basis set (CBS) methods.[5] Barna *et al.* claim that their study employing an improved *ab initio* method, with most of the energy contributions extrapolated to the CBS limit, currently provides the most reliable data for ΔE_g (see Table 4.4). It can be seen that their theoretical calculations for ΔH_g compare well with the experimental results. In terms of longer *n*-alkanes, there is some evidence from recent high level QC calculations that the *t/g* energy difference decreases with increasing chain length, at least up to *n*-octane.[104,105,161]

Unlike experimental estimates, *ab initio* calculated energy differences for the rotational barriers of *n*-butane indicate that the *cis* barrier is significantly higher compared with the *t-g* barrier.[81,161] For example, Smith and Jaffe employed CCSD(T)/cc-

pVTZ//MP2/6-311g(2df,p) level of theory, resulting in values of 13.85 ± 0.42 kJ mol^{-1} for the *t-g* barrier and 22.93 0.42 kJ mol^{-1} for the *cis* barrier.[161] There is also some evidence that there is a small reduction in the *t-g* barrier compared to *n*-butane with increasing chain length.

The parameters for alkanes in standard force fields are generally obtained by fitting to different sets of QC and experimental data for *n*-butane. Table 4.5 shows a number of ΔE_{g} values for various force fields. With the exception of the CHARMM and GROMOS 43A2 force fields, all ΔE_{g} values are higher than the most recent QC and experimental enthalpy and energy values, considered to be the most reliable. For example, the MM3 parametrization of the conformational energetics of *n*-butane[3] was derived to be in accordance with the experimental results of Compton *et al.* (1980)[44] and Bartel *et al.* (1982)[83] which have since been superceded. The rather large values for AMBER99 and GAFF suggest that the *ab initio* conformational energies used for fitting alkane torsional parameters were not of sufficiently high quality.

Table 4.5: ΔE_{g} values for *n*-butane for a number of standard and modified force fields[3,104]

Force Field	ΔE_{g} / kJ mol^{-1}
AMBER99	3.60
OPLS-AA	3.35
MM3	3.40
GAFF	4.50
CHARMM27	2.76
CHARMM27r	2.63
GROMOS 43A2	2.30

The original GAFF force field yields a *trans/gauche* (*t/g*) energy difference of ≈ 4.5 kJ mol^{-1} which is almost twice the value reported for the most recent experimental and high quality QC results. This suggests that the force field overestimates the energy difference between the *gauche* and *trans* states, leading to an overestimation of the average *trans* population. Associated with this would be reduced flexibility and possible deviations in calculated properties (for example, T_{NI} temperatures) compared with experiment. Consideration was given to altering the 1-4 intramolecular scaling factors to reduce the *t/g* energy difference. Reducing the

electrostatic 1-4 interactions in particular, proved successful for a *n*-alkanes, but raised considerable complexities when applied to the alkane fragments of larger LC molecules, as applying differential scaling factors was found to be a cumbersome approach. Instead, it was decided to re-parametrize the torsional dihedrals of *n*-alkanes and transfer these to the larger mesogens. However, the high level of theory and *ab initio* techniques required to calculate the relatively small energy difference with high accuracy, was deemed unfeasible for this study due to the computational time required. As a compromise it was decided to adopt the amended OPLS-AA torsional parameters from Sui *et al.*[168] which were specifically optimized for both short and long alkanes, and test these in the GAFF force field using *n*-heptane and butylbenzene. While butylbenzene is not an *n*-alkane, it does contain *n*-butane as a component and is a common terminal structural component of many liquid crystal molecules.

The new RB coefficients taken from the optimized OPLS-AA force field for short and long chain *n*-alkanes were transferred into the GAFF force field and a comparison of the torsional profiles obtained for the C-C-C-C torsion of both *n*-heptane and *n*-butylbenzene calculated with the original GAFF and the new RB coefficients are shown in Figure 4.4.

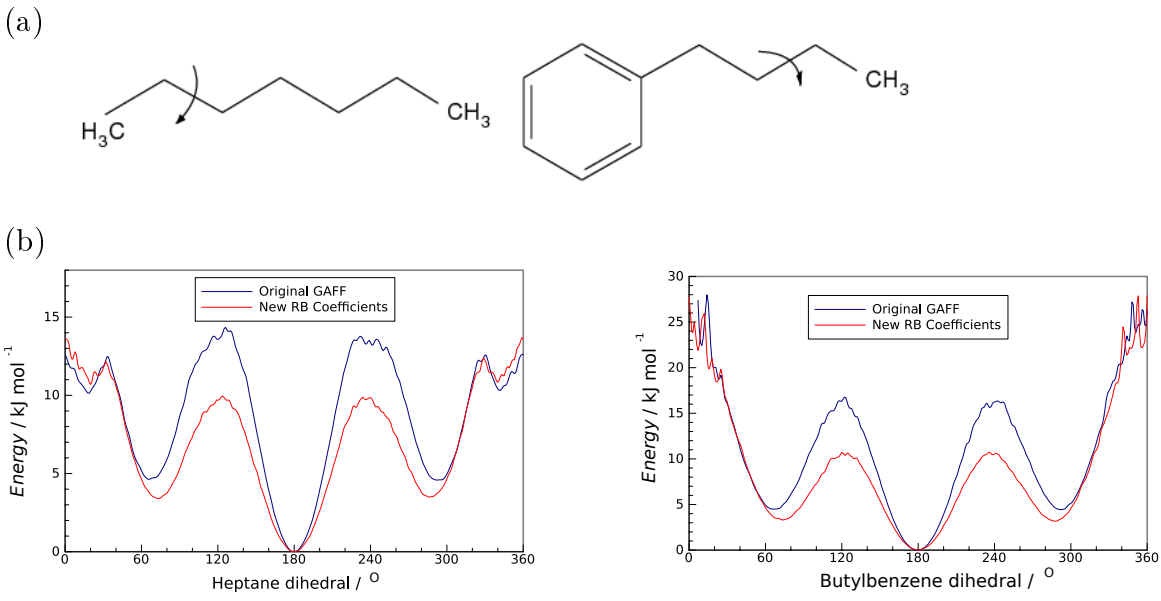

Figure 4.4: (a) Structure of *n*-heptane and *n*-butylbezene with dihedral angles shown. (b) Torsional energy profiles for the C-C-C-C torsion (GAFF atom types c3-c3-c3-c3).

The results show a decrease in the t/g energy from $\approx$ 4.5 kJ mol^{-1} to $\approx$ 3.0 kJ mol^{-1}, as well as a reduction in the *trans-gauche* energy barrier.

The new RB coefficients were also tested on the bulk properties (density and $\Delta_{vap}H$) for *n*-heptane and *n*-butylbenzene and the results show a small but not marked improvement on these calculated properties (see Table 4.6). This suggests that amending the torsional parameters has a limited affect on these calculated properties. However, as discussed in Section 4.2, there is a strong justification for improved force field parametrization of *n*-alkanes. It was considered that a more accurate reproduction of the t/g energy difference could affect the flexibility and possibly the length to breadth ratio of larger mesogens containing *n*-alkane fragments. Amending the torsional parameters could lead to an improved description of the phase transitions of liquid crystal systems.

Table 4.6: Density and heat of vaporization calculations using the original and amended GAFF parameters

Molecule	Property	T / K	Exp.	GAFF	New RB coefficients
n-heptane	Density / g cm^{-3}	298	0.6788	0.6782 ± 0.0001	0.6783 ± 0.0001
	Heat of Vap. / kJ mol^{-1}	298	36.60	40.37 ± 0.03	40.12 ± 0.02
n-butylbenzene	Density / g cm^{-3}	298	0.8559	0.8503 ± 0.0001	0.8505 ± 0.0001
	Heat of Vap. / kJ mol^{-1}	298	51.36	52.25 ± 0.02	51.95 ± 0.03

Experimental values taken from CRC Handbook of Chemistry Physics[82]

Aromatic ring - chain torsional potential

The mesogens investigated in this thesis contained either alkyl or alkoxy terminal chains attached to rigid aromatic core structures. The GAFF force field description of both these torsions was checked using the butylbenzene and ethoxybenzene fragments. An accurate description of the ring-chain torsion is considered to be an important feature in reproducing correct mesophase behaviour, as specific orientations at this junction are important in establishing the overall shape of a mesogen.[34] NMR experimental studies and DFT calculations of the smaller ethylbenzene frag-

ment, predict a minimum when the $C_{ca}-CH_2$ bond is in the plane perpendicular to the ring plane ($\pm 90°$).[24,61] Likewise, a minimum at $\pm 90°$ is also predicted for the analogous bond in the 4CB mesogen from NMR studies.[61] There is some uncertainty in the literature concerning the barrier to rotation about the $C_{ca}-CH_2$ bond. A DFT calculation with the B3LYP/6-311+G(2dp) basis set yielded a barrier height of 4.5 kJ mol^{-1} at 0° for ethylbenzene, whereas that obtained from NMR data is ≈ 3 kJ mol^{-1}. A significantly larger barrier height of > 22 kJ mol^{-1} obtained from NMR data is found for the $C_{ca}-CH_2$ bond of the 4CB mesogen, indicating a possible problem of parameter transferability from small fragments to larger molecules for this particular torsion.

In the current work, an MP2/ccpVTZ calculation of the $C_{ca}-CH_2$ torsion of butylbenzene resulted in a minimum at $\pm 90°$ and a barrier height of ≈ 7 kJ mol^{-1}. The original GAFF force field also predicts minima at $\pm 90°$, but a slightly higher barrier height of ≈ 12 kJ mol^{-1}. Due to the range of values found for the barrier to rotation for the $C_{ca}-CH_2$ bond depending on the molecular context, it was decided to retain the original GAFF RB coefficients for this torsion, particularly as the correct minimum geometry was predicted.

According to theoretical results, and in contrast to the $C_{ca}-CH_2$ torsion, the torsional potential for the $C_{ca}-OCH_2$ torsion has two equivalent minima corresponding to the O-CH_2 bond lying in the same plane as that of the aromatic ring.[111,173] An extensive *ab initio* approach employing MP2, MP3, MP4(SDQ), CCSD and CCSD(T) yielded a barrier height of ≈ 12.5 kJ mol^{-1} for the $C_{ca}-OCH_2$ torsion of the methoxybene fragment,[173] whilst for the analogous torsion of ethoxybezene (see Figure 4.5) a barrier height of ≈ 11 kJ mol^{-1} was obtained employing DFT at the B3LYP/6-311+G(2dp) level of theory.[34]

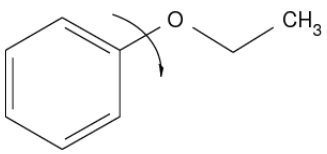

Figure 4.5: Ethoxybenzene

A slightly greater barrier height of ≈ 18 kJ mol^{-1} employing B3LYP/6-31G(d)

was calculated for the $C_{ca}-OCH_2$ torsion of a series of bent-core mesogens containing alkoxy chains of various lengths, although this value was dependent on the type of group connected to the *para* position of the ring with respect to the chain.[111] Additionally, the small basis set and absence of diffuse functions may have reduced the accuracy of the calculation. Testing GAFF on the description of the $C_{ca}-OCH_2$ torsion of ethoxybezene resulted in the correct minimum geometry but a barrier height of $\approx$ 2.5 kJ mol^{-1}, significantly lower than literature values for this particular torsion. New RB coefficients, C_n were obtained to replicate the torsional barrier of $\approx$ 11 kJ mol^{-1} derived from the DFT calculation above at the B3LYP/6-311+G(2dp) level of theory.

These new RB coefficients, along with a summary of all the amended Ryckaert-Belleman parameters for the selected dihedrals of the different fragments described previously, are presented in Table 4.7.

Table 4.7: Optimized Ryckaert-Bellemans parameters for the selected dihedrals

Dihedral	Molecule	C_0	C_1	C_2	C_3	C_4	C_5
dihedral φ_1	phenyl benzoate	7.335350	0.000000	-7.335350	0.000000	0.000000	0.000000
dihedralφ_2	phenyl benzoate	6.000000	0.000000	0.000000	0.000000	-6.000000	0.000000
dihedral ϕ_1	ODBP	4.000000	0.000000	-4.000000	0.000000	0.000000	0.000000
x-CH_2-CH_2- x[a]	heptane / butylbenzene	0.518587	-0.230192	0.896807	-1.491340	0.000000	0.000000
C_{ar}-OCH_2	ethoxybenzene	11.5312	0.000000	-11.5312	0.000000	0.000000	0.000000

[a] Taken from reference[168]

4.4.2 Optimization of van der Waals parameters

The vdW parameters in GAFF have been adapted from the AMBER force fields without further optimizations and were developed with short electrostatic cut-offs, with long range effects incorporated into the local interactions in an average way. It is possible that these factors could lead to deviations in molecular property calculations and this could be especially important when using modern simulation techniques, such as PME.[25] Additionally, density and $\Delta_{\text{vap}}H$ are almost exclusively associated with vdW parametrization, with density being particularly important in affecting mesophase formation and transition temperatures.[97,184] Focus was therefore placed primarily on vdW parameter optimizations so that density and $\Delta_{\text{vap}}H$ could be reproduced as accurately as possible.

The choice of atom types for vdW parameter amendments was largely based on the results reported by Wang & Huo and Caleman *et al.* As previously stated in Section 4.2, the prediction errors for the simulated densities and $\Delta_{\text{vap}}H$ for a number of aromatic compounds could be improved by tuning the aromatic carbon vdW parameters.[184] Therefore, this atom type was considered as a candidate for optimization in the context of a number of compounds containing phenyl rings. Examination of the database produced by Caleman *et al.* and the results of Wang & Huo, show significant deviations from experimental values for calculated densities and $\Delta_{\text{vap}}H$ for a number of compounds containing phenyl rings. Carboxylic acids containing highly polarizable groups with strong dipoles, such as C=O and OH groups, produced very poor results for the bulk properties (see Table 4.8). To a lesser extent, the calculated properties for ester compounds also displayed some significant deviations from experimental values. However, for aldehydes, ketones, alcohols and unbranched ethers, GAFF results showed better agreement with experimental values. Given these considerations, the esters, methylbenzoate, phenylacetate and methylformate were chosen for vdW parameter optimization as they are not only common fragments of liquid crystal molecules, but also displayed fairly high prediction errors when compared with experimental values.

Table 4.8: List of the experimental densities and heats of vaporization for a selection of compounds taken from Caleman *et al.*[25] [a]Values taken from Wang & Hou.[184]

Molecule	Property	T / K	Exp.	GAFF	% Diff.
Methanoic acid	Density (g/cm^3)	293.15	1.2200	1.3971± 0.0005	+14.5
	Heat of Vaporization (kJ/mol)	293.15	19.82	68.74 ± 0.06	+246.8
Acetic acid[a]	Density (g/cm^3)	298	1.0446	1.1200	+7.2
	Heat of Vaporization (kJ/mol)	298	51.59	56.00	+8.6
Propanoic acid[a]	Density (g/cm^3)	298	0.9882	1.026	+3.8
	Heat of Vaporization (kJ/mol)	298	55.02	60.34	+9.7
Methyl formate	Density (g/cm^3)	293.15	0.9713	1.0512 ± 0.0002	+8.0
	Heat of Vaporization (kJ/mol)	293.15	28.85	38.68 ± 0.03	+34.1
Methylacetate	Density (g/cm^3)	293.15	0.9342	0.9714 ± 0.0002	+4.0
	Heat of Vaporization (kJ/mol)	293.15	32.67	41.57± 0.07	+27.2
Ethenyl acetate	Density (g/cm^3)	298.15	0.9256	0.9790 ± 0.0001	+5.3
	Heat of Vaporization (kJ/mol)	298.15	34.58	43.40 ± 0.02	+25.5
Diethyl carbonate	Density (g/cm^3)	298.15	0.9691	1.0209 ± 0.0002	+5.3
	Heat of Vaporization (kJ/mol)	298.15	41.1	60.79 ± 0.09	+47.9
Methyl benzoate	Density (g/cm^3)	298.15	1.0840	1.1113 ± 0.0002	+2.5
	Heat of Vaporization (kJ/mol)	298.15	55.57	64.21 ± 0.03	+15.6
Heterocyclic compounds					
1-H -pyrrole	Density (g/cm^3)	293.15	0.9698	1.0201± 0.0003	+ 5.2
	Heat of Vaporization (kJ/mol)	293.15	45.7	52.93 ± 0.05	+15.8
1,3-dioxolane	Density (g/cm^3)	293.15	1.0600	1.1223 ± 0.0002	+5.9
	Heat of Vaporization (kJ/mol)	293.15	35.80	43.45 ± 0.02	+21.4
Morpholine	Density (g/cm^3)	293.15	1.0005	1.0880 ± 0.0003	+ 8.8
	Heat of Vaporization (kJ/mol)	293.15	45.32	59.56 ± 0.40	+31.4
Pyrimidine	Density (g/cm^3)	298.15	1.0164	1.1160 ± 0.0003	+ 9.8
	Heat of Vaporization (kJ/mol)	298.15	49.81	50.47± 0.03	+1.3
Furan	Density (g/cm^3)	298.15	0.9313	0.9660 ± 0.0002	+3.7
	Heat of Vaporization (kJ/mol)	298.15	27.46	30.33 ± 0.03	+10.5

Caleman *et al.* also tested the GAFF force field on reproducing densities and $\Delta_{\text{vap}}H$ values for the heterocyclic compounds, pyrrole, 1,3-dioxolane, pyrimidine, morpholine and furan. Their calculated densities ranged from 3.7 to 9.8% greater than experimental values, and with the exception of pyrimidine, all calculated $\Delta_{\text{vap}}H$ were higher than experimental (+10.5 to +31.4% - see bottom of Table 4.8). This suggests that heterocyclic compounds containing oxygen and nitrogen are not always adequately represented by GAFF, and that attraction between the molecules is over estimated.

The fragments 1,3,4-oxadiazole and 2,5-diphenyl-1,3,4-oxadiazole are components of the *bis*-phenyl ODBP family of mesogens and also possess heterocyclic rings (see Figure 4.7). A literature search has revealed very little experimental data on the bulk properties of these compounds. However, the predicted densities for the two oxadiazole fragments can be obtained from the Advanced Chemistry Development (ACD/Labs) software,[1] and these show considerably smaller densities compared to those predicted by GAFF. The heterocyclic rings furan and pyrimidine share similar features with the 1,3,4-oxadiazole ring, for example π- electron density and heteroatoms with lone pairs of electrons. As there is experimental data on the bulk properties of furan and pyrimidine, the vdW parameters of these compounds were optimized, and then transferred to 1,3,4-oxadiazole and 2,5-diphenyl-1,3,4-oxadiazole fragments .

Finally, the results produced by Caleman *et al.* also indicated that GAFF predicts the bulk properties for many small aliphatic and aromatic hydrocarbons reasonably accurately. In particular, the prediction errors for toulene, styrene and ethylbenzene are $< 1.3\%$ for density and $< 3.5\%$ for $\Delta_{\text{vap}}H$. Therefore aliphatic carbons and hydrogens were not considered for vdW parameter optimization.

The following sections present the results for the selected fragments chosen for the optimization of vdW parameters.

Ester compounds

The structure of phenyl acetate, methylbenzoate and methylformate are shown in Figure 4.6. Experimental values for density and heat of vaporization ($\Delta_{\text{vap}}H$) are

displayed in Table 4.9 along with those predicted by the original GAFF force field, with the latter showing deviations from the experimental values. Initial attempts to improve these predicted bulk properties through vdW parametrization, focused on the aromatic compounds phenyl acetate and methylbenzoate and adopting the vdW parameter change for aromatic carbon reported by Wang and Hou.[184] These authors selected benzene for optimizing the carbon vdW parameters and found that the two properties were not sensitive to the radius parameter, R_j, but a new depth of potential well, ε, that was slightly larger than the original was required to reduce the prediction errors for both density and $\Delta_{\text{vap}}H$. This new value for ε was then transferred to the carbons of the aromatic compounds, phenol, m-cresol, aniline and fluorobenzene and densities and $\Delta_{\text{vap}}H$ were calculated. Although the predicted properties for fluorobenzene were slightly better than those using the original GAFF parameters, for aniline and phenol only the $\Delta_{\text{vap}}H$ was improved, and for m-cresol both the predicted properties showed further deviations from the experimental data.

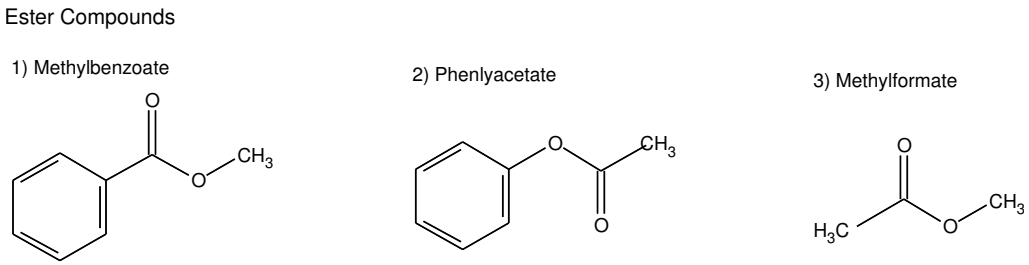

Figure 4.6: Ester structures

Testing this new ε parameter for the aromatic carbons of phenyl acetate in the current study also resulted in an increase in the predictions errors for both properties. However, it was found that reducing the well depth of aromatic carbon by small increments resulted in an improvement in the predicted density and to a lesser extent $\Delta_{\text{vap}}H$ for phenyl acetate, suggesting that deriving ideal vdW parameters for the aromatic carbons of benzene are not necessarily transferable to all aromatic compounds regardless of chemical environment.

Although a small reduction in the prediction errors was obtained by reducing the potential well depth of aromatic carbon for both phenyl actetate and methylbenzoate, the most accurate results were achieved by synchronously reducing the

potential well depth of both the carbonyl oxygen atom as well as the aromatic carbons. New values of ε =0.289824 kJ mol^{-1} for the aromatic carbons and ε =0.478608 kJ mol^{-1} for the carbonyl oxygen atom produced the most accurate results for these bulk properties (see Table 4.9). In addition, the new RB coefficients derived for the ester linkage of phenyl acetate were also tested with the altered vdW parameters and resulted in an insignificant change in the predicted properties, reinforcing the fact that the bulk density and $\Delta_{\text{vap}}H$ are almost exclusively associated with the non-bonded interactions.

The third ester fragment chosen for vdW parameter optimization, methylformate, showed significant deviations from experimental values for the bulk properties. An initial attempt to improve these predicted properties involved transferring the new ε value derived for the carbonyl oxygen atom of phenyl acetate and methylbenzoate to this fragment. This resulted in a small reduction in the predicted errors with values of 1.0227 $\pm$0.002 g cm^{-3} for density and 35.38 kJ mol^{-1} for $\Delta_{\text{vap}}H$. However, reducing the well depth of the ester oxygen in addition to the carbonyl oxygen resulted in a significantly better agreement with the experimental data (see Table 4.9).

Table 4.9: Density and heat of vaporization calculations using the original and amended GAFF parameters

Molecule	Property	T / K	Exp.	GAFF	% diff.	New Parameters	% diff.
Phenyl acetate	Density / g cm^{-3}	293	1.0739	1.1031	+2.7	1.0654 $\pm$ 0.0001	-0.8
	Heat of Vap. / kJ mol^{-1}	298	53.33	67.23 $\pm$ 0.02	+26.1	56.51 $\pm$ 0.02	+6.0
Methylbenzoate	Density / g cm^{-3}	298	1.0840	1.1105 $\pm$ 0.0001	+2.5	1.0796 $\pm$ 0.0002	-0.4
	Heat of Vap. / kJ mol^{-1}	298	54.28	65.41 $\pm$ 0.02	+20.5	54.98 $\pm$ 0.01	+1.3
Methylformate	Density / g cm^{-3}	298	0.9670	1.0467$\pm$ 0.0001	+8.2	0.9880$\pm$ 0.0001	+2.2
	Heat of Vap./ kJ mol^{-1}	298	30.59	38.89 $\pm$ 0.01	+27.1	32.14 $\pm$ 0.006	+5.1

The increased accuracy in the calculated bulk properties for these fragments does not necessarily imply any physical justification for the vdW parameter changes, but is most likely the result of a cancellation of errors due to the limitations of non-polarizable, atom-centred fixed charge force fields. Improving the description of intermolecular interactions involves the use of atomic multipoles and atomic polarizabilties (multibody effects). Together they describe a first-order and second-order

correction to the electrostatic energy.[33,86,110] Although there is implicit inclusion of multibody effects in standard force fields, there may be systems for which these are not accurate enough. A limitation of the use of atom-centred point charges in molecular force fields, which are isotropic by definition, is that they cannot realistically reproduce the electrostatic potential around conjugated systems, aromatic sytems and lone pairs.[110] Introducing higher order atomic multipole moments provides a more accurate representation of the electrostatic potential around small molecules, thus leading to a better description of the molecular interactions.[109,148,149] The fragments studied in this work contain π-conjugated systems which are known to possess large quadrupole moments, lone pairs as well as highly polarizable groups, such as the C=O group. The combination of these features may partly explain the larger prediction errors for the bulk properties calculated.

Heterocyclic compounds

The results for densities and $\Delta_{\text{vap}}H$ after tuning the vdW parameters of the heterocyclic compounds are presented in Table 4.10, along with those for the original GAFF parameters. The structures of the heterocyclic compounds are shown in Figure 4.7.

Figure 4.7: Heterocyclic structures

With the original GAFF parameters, pyrimidine displayed a significantly higher density compared with the experimental value, although $\Delta_{\text{vap}}H$ showed good agreement with experiment. A literature search revealed that the nitrogens of pyrimidine were assigned AMBER force field vdW parameters derived for the basic nitrogens in adenine without further optimization. Additionally, the nitrogen well depth value (ϵ) of 0.71128 kJ mol^{-1} in original GAFF was found to be significantly higher than

those for analogous nitrogens (basic nitrogens with a lone pair) in other force fields, where values ranged from ϵ = 0.4184 kJ mol^{-1} (N in pyrimidine, AMOEBA) to ε = 0.47369 kJ mol^{-1} (basic N in ring structure, TraPPE) and ε = 0.5857 kJ mol^{-1} (amine nitrogen[184]). In the current work, reduction of ε by 0.1 kJ mol^{-1} increments improved the density prediction error with ε = 0.41128 kJ mol^{-1} resulting in a density of 1.0598 ±0.0002 g cm^{-3}. However, this was still 4.7% higher than the experimental value and resulted in a significant deterioration in the calculated $\Delta_{\text{vap}}H$ (41.12 ± 0.02 kJ mol^{-1} compared with experiment = 49.81 kJ mol^{-1}). Increasing the nitrogen sigma parameter by 0.01 nm along with this new ϵ value improved the density prediction (1.0424±0.0001 g cm^{-3}) but had no effect on $\Delta_{\text{vap}}H$ which remained ≈ -18% too low. This suggested that tuning the nitrogen vdW parameters alone was not sufficient to provide accurate predictions for both density and $\Delta_{\text{vap}}H$.

GAFF assigns the same σ and ε parameters derived for aromatic carbons (ca) to all the carbon atoms of pyrimidine. However, the electronic nature of the C2, C4 and C6 atoms (see Figure 4.7) is different from the aromatic (ca) atoms of benzene, with a reduction in π- electron density and a tendency of the electrons to move towards the nitrogens. In GAFF the carbon atoms adjacent to the nitrogens could be distinguished from the aromatic (ca) carbons by assigning to them the cc atom type definition. Retaining the original vdW parameters for nitrogen and increasing both the values of σ and ε for these carbons resulted in a very accurate density (1.0104 ±0.0001 g cm^{-3}) but a deterioration in the calculated $\Delta_{\text{vap}}H$, which was 14.5% higher than experiment. It was therefore decided to use the optimized ε parameter for nitrogen described above and simultaneously tune the vdW parameters of the carbons, C2, C4 and C6 adjacent to the nitrogens. It was found that a small increase in the values of σ and ε for these carbon atoms, along with the reduction in the nitrogen ε parameter, gave a significantly improved density and a reasonably good $\Delta_{\text{vap}}H$. Although the latter was slightly worse than that with the original GAFF parameters, this was found to be the best compromise. The optimized vdW parameters for pyrimidine were, ε = 0.41128 kJ mol^{-1} for nitrogen and ε = 0.42982 kJ mol^{-1} for the carbons adjacent to the nitrogens.

In contrast to pyrimidine, the results for furan with the original GAFF parame-

ters show a considerably smaller prediction error for density, but a larger prediction error for $\Delta_{vap}H$. Furan, like benzene, is a π- electron rich aromatic compound and therefore it was decided to retain the original aromatic (ca) vdW parameters for the carbon atoms of the ring and focus on vdW parameter optimization of the oxygen atom. It was found that reducing the oxygen well depth only ($\varepsilon = 0.61128$ kJ mol^{-1}) brought both properties into good agreement with the experimental data.

In the absence of experimental densities for the compounds 1,3,4-oxadiazole and 2,5-diphenyl,1,3,4-oxadiazole, the predicted densities obtained with the ACD/labs software were used as reference values. These values suggest that the GAFF predicted densities are too high. Although there are large uncertainties associated with the ACD calculations, examination of a number of calculations for compounds for which there is available experimental data show good agreement (see Table 4.10).

Table 4.10: Comparison of ACD Labs calculated densities and experimental values

Molecule	ACD(Labs-software) / g cm^{-3} (293K)	Exp. / g cm^{-3} (293K)
Phenyl acetate	1.071 ± 0.06	1.0739
Butylbenzene	0.864 ± 0.06	0.8670
Furan	0.942 ± 0.06	0.9403
Benzene	0.873 ± 0.06	0.8790
m-cresol	1.038 ± 0.06	1.0338

The 1,3,4-oxadiazole ring shares some features with furan (5-membered heterocyclic ring containing an oxygen atom). However, the electronic nature of the oxadiazole ring is more closely related to that of pyrimidine, with relatively low π-electron density at carbon positions C2 and C5 (see Figure 4.7) and the presence of two basic nitrogen atoms that exert a withdrawal effect on the adjacent carbons. It was therefore decided to test the new vdW parameters derived for the nitrogens and carbons (cc) of pyrimidine and transfer these to the analogous atoms of the oxadiazole ring. This produced a density of 1.2028 g cm^{-3}, which is close to the ACD calculation. In addition to these changes it was found that reducing the well depth of the oxygen atom of the oxadiazole ring, to that of furan described above, gave the best overall result for density when compared with the ACD result.

The original GAFF predicted density for the 2,5-diphenyl,1,3,4-oxadiazole fragment was slightly higher than the ACD result. Testing the new RB coefficients

derived for the inter-ring dihedrals (see Section 4.4.1) resulted in a very small increase to the GAFF predicted density, taking it further away from the ACD value. Adopting the new vdW parameters for the oxadiazole ring described above and retaining the new RB coefficients reduced this density to 1.1897 ± 0.0003 g cm^{-3}. However, the best agreement with the ACD result was obtained through combining these changes with a reduction of the well depth of the carbon atoms of the phenyl rings to that derived for phenyl acetate and methylbenzoate described above (see Table 4.11). In addition, the new vdW parameters derived for the 2,5-diphenyl,1,3,4-oxadiazole fragment greatly improve the $\Delta_{\mathrm{vap}}H$ calculation bringing it closer to the experimental value.

Table 4.11: Density and heat of vaporization calculations using the original and amended GAFF

Molecule	Property	T / K	Exp.	GAFF	% diff.	New Parameters	% diff.
Pyrimidine	Density / g cm^{-3}	298	1.0164	1.1022 ± 0.0003	+8.4	1.0246± 0.0002	+0.8
	Heat of Vap.	298	49.81	48.63 ± 0.02	-2.4	46.87 ± 0.02	-5.9
Furan	Density / g cm^{-3}	298	0.9313	0.9495 ± 0.0003	+2.0	0.9379 ± 0.0005	+0.7
	Heat of Vap.	298	27.46	29.27 ± 0.02	+6.6	27.67 ± 0.01	+0.8
1,3,4-oxadiazole	Density / g cm^{-3}	293	1.1930[a]	1.3093 ± 0.0002	+9.8	1.1959 ± 0.0002	+0.2
	Heat of Vap.	298	37.10[a]	56.94 ± 0.04	+53.5	50.18 ± 0.01	+35.3
2,5-diphenyl,1,3,4-oxadiazole	Density / g cm^{-3}	293	1.1740[a]	1.1950 ± 0.0003	+1.8	1.1695 ± 0.0002	-0.4
	Heat of Vap.	563	49.96[b]	80.26 ± 0.07	+60.6	57.97 ± 0.03	+16.0

[a] Values taken from ACD/Labs software.[1] [b] Value taken from *Thermophysical Properties of Chemicals and Hydrocarbons,* Carl L. Yaws, 2008, ch. 3 (pub. William Andrew).
All Heat of Vap. in kJ mol^{-1}

In summary, a combination of factors may be responsible for the GAFF prediction errors for density and $\Delta_{\mathrm{vap}}H$ for the liquid crystal fragments. These include the adoption of vdW parameters from the AMBER protein force fields, which have not been subsesquently optimized to predict the bulk properties of liquids. In addition, particular features present in all of the fragments, for example lone electron pairs and conjugated systems, may require a better force field description. This would entail the use of polarizable force fields with distributed atomic multipoles instead of

fixed point charges. However, it appears that these factors can be largely compensated for by tuning a small number of specific vdW parameters, which has resulted in significantly improved prediction errors for both density and $\Delta_{\mathrm{vap}}H$.

Table 4.12 provides a summary of the amended vdW parameters for the ester and heterocyclic fragments descibed above.

Table 4.12: Amended vdW parameters for selected atom types. Marked values [a] are the original GAFF parameters.

Atom / description	GAFF atom types	σ / nm	ε / kJ mol^{-1}
O (sp^2O in carbonyl)	o	0.295992[a]	0.478608
C (sp^2 C in aromatic ring)	ca	0.339967[a]	0.289824
O (sp^3O in ester)	os	0.300001[a]	0.611280
N (inner sp^2 N in conjugated ring)	nd	0.325000[a]	0.411280
C (inner sp^2 C in conjugated ring)	cc	0.369967[a]	0.429824

4.5 Testing the amended force field, the GAFF Liquid Crystal Force Field (GAFF-LCFF): simulation of a typical calamitic nematogen

The ability to reproduce a stable nematic phase over a large temperature range, and more importantly provide a reliable estimate of the T_{NI} temperature for the mesogen shown in Figure 4.8, was considered a stringent test for the amended GAFF force field (GAFF-LCFF). The experimental phase transition temperatures for the 1,3-benzenedicarboxylic acid,1,3-*bis*(4-butylphenyl)ester mesogen (abbreviated to phenylester-LC in the following sections) are Cr 348 K N 452 K I . GAFF was found to overestimate the T_{NI} temperature by $\approx$ 60 K. The new parameters developed for the fragments which were described in Sections 4.4.1 and 4.4.2, were transferred to this mesogen, on the assumption that these parameters are valid for the larger mesogen. These new parameters are summarized in Tables 4.7 and 4.12.

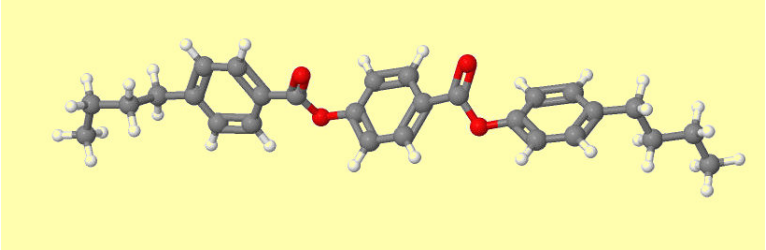

Figure 4.8: 1,3-benzenedicarboxylic acid,1,3-*bis*(4-butylphenyl)ester

4.5.1 Molecular order and structural organisation

Figure 4.9b shows the time evolution of P_2 at four different temperatures and for an $N = 256$ system. P_2 is calculated as the largest eigenvalue of the cartesian ordering matrix, $\mathbf{Q}(t)$. A value greater than 0.4 is considered to be typical of a nematic, whereas a value below 0.4 is considered to be isotropic.[198] The lengthy MD runs indicate that at the temperatures of 480 K, 470 K and 460 K the system is isotropic, with values for $\langle P_2 \rangle$ averaged over the last 80 ns equal to 0.19, 0.21 and 0.23 respectively. At 460 K, P_2 shows larger fluctuations which are indicative of the

system being close to a phase transition.[169] When the temperature decreases to 450 K, P_2 increases sharply over the initial 20 ns and over the last 80 ns $\langle P_2 \rangle$ is equal to 0.51, suggesting spontaneous ordering at this temperature. These results suggest that a phase transition occurs beween 450 K and 460 K.

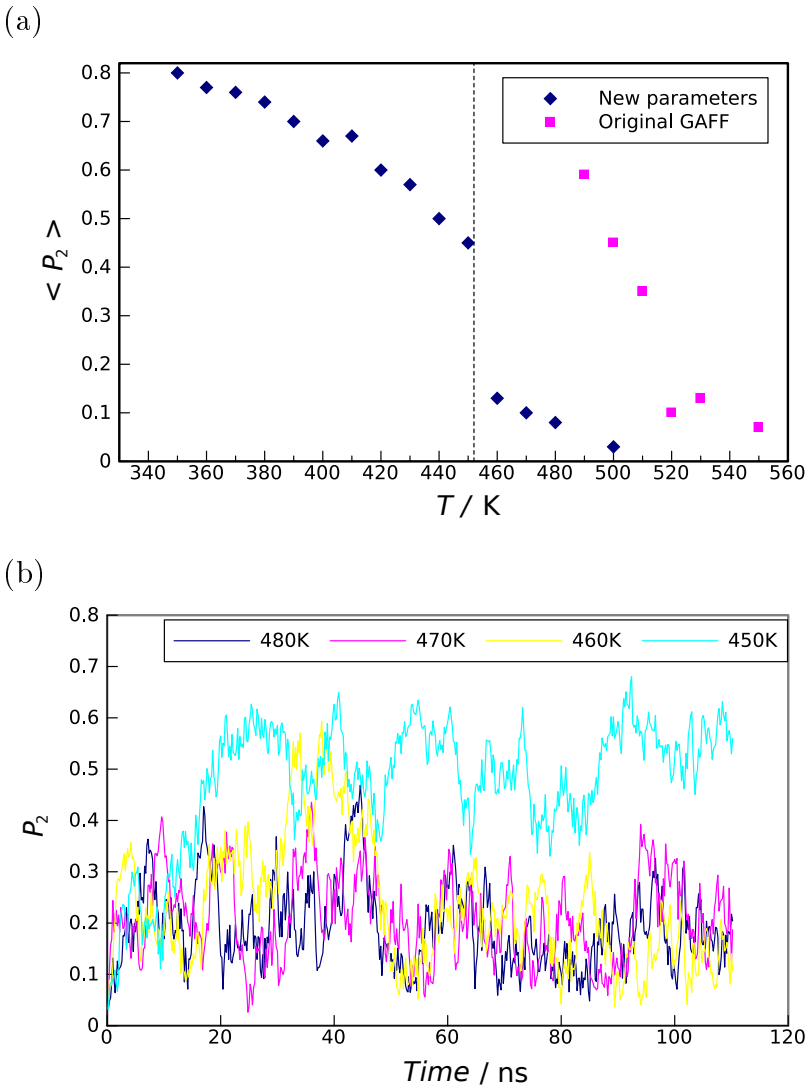

Figure 4.9: (a) Average simulated order parameter, $\langle P_2 \rangle$ as a function of temperature for phenylester-LC. The vertical black line indicates the experimental transition temperature. (b) Time evolution of the order parameter, P_2 at four different temperatures, starting from a well equilibrated isotropic configuration at 550 K ($N = 256$)

Further evidence for the existence of a phase transition occuring between these two temperatures is provided by Figure 4.9a, which shows the system progressively cooled from a disordered configuration and $\langle P_2 \rangle$ plotted as a function of temperature.

The mean order parameter has been calculated as $\langle P_2(t)\rangle = \langle -2\lambda_0(t)\rangle$ averaged over the last 80 ns of the trajectories. A $\langle P_2\rangle$ value of less than 0.15 is defined as typical of an isotropic phase, whereas $\langle P_2\rangle$ greater than 0.3 is characteristic of a nematic phase.[169] At a temperature just above 450 K there is a jump in the value of $\langle P_2\rangle$, which is in agreement with the weak first-order nature of a nematic to isotropic phase transition. This indicates that the re-optimized force field is sufficiently accurate at predicting the experimental nematic to isotropic phase transition of 452 K. Figure 4.9a also shows the temperature-dependent averaged order parameter obtained with original GAFF for comparison. A jump in the value of $\langle P_2\rangle$ occurs between 510 K and 520 K, indicating that the phase transition occurs approximately 60 K above the experimental value.

Additional information concerning the nature of the phases obtained, and location of the T_{NI} temperature, was provided through the calculation of various pair distribution functions for the phenylester-LC molecule. These are presented in Figure 4.10 for a number of selected temperatures. The standard radial distributional function $g(r)$ showed liquid-like behaviour over the temperatures selected (Figure 4.10a), with a characteristic peak at short range, $\approx$ 5 to 7 Å, followed by a convergence to a value of one at long range. At the lower temperatures of 400 K and 360 K, the main peak is split into two subsidary peaks. Additionally, the magnitude of the first peak increased with decreasing temperature, suggesting stronger correlations between neighbouring molecules. Examination of the orientational correlation function $g_2(r)$ (see Figure 4.10b) indicated that the phase is isotropic at 460 K and above as the function decays to zero in the long range. However, at 450 K, $g_2(r)$ converges to a value of ≈ 0.26 at large r distances. This value is consistent with the $\langle P_2\rangle^2$ value of (0.51^2) at 450 K and suggests the occurrence of spontaneous ordering into the nematic phase at a temperature somewhere between 460 K and 450 K. Analysis of $g_2(r)$ at 400 K also showed convergence to $\langle P_2\rangle^2$ indicating the nematic nature of the phase at this temperature.

To rule out the possibility of any translational ordering of the systems at the temperatures expected to be nematic, the contribution to the radial distribution function parallel, $g_{\parallel}(r)$ and perpendicular $g_{\perp}(r)$ to the director were also examined.

The $g_{\parallel}(r)$ function showed a stable value of approximately one for all distances at all temperatures examined, and the absence of peaks at regular intervals, which are characteristic of smectic ordering. With the exceptions of a small peak at short range, $g_{\perp}(r)$ also displayed minimal structure at 450 K, 400 K and 360 K (see Figure 4.10c) confirming the nematic nature of the phase at these temperatures.

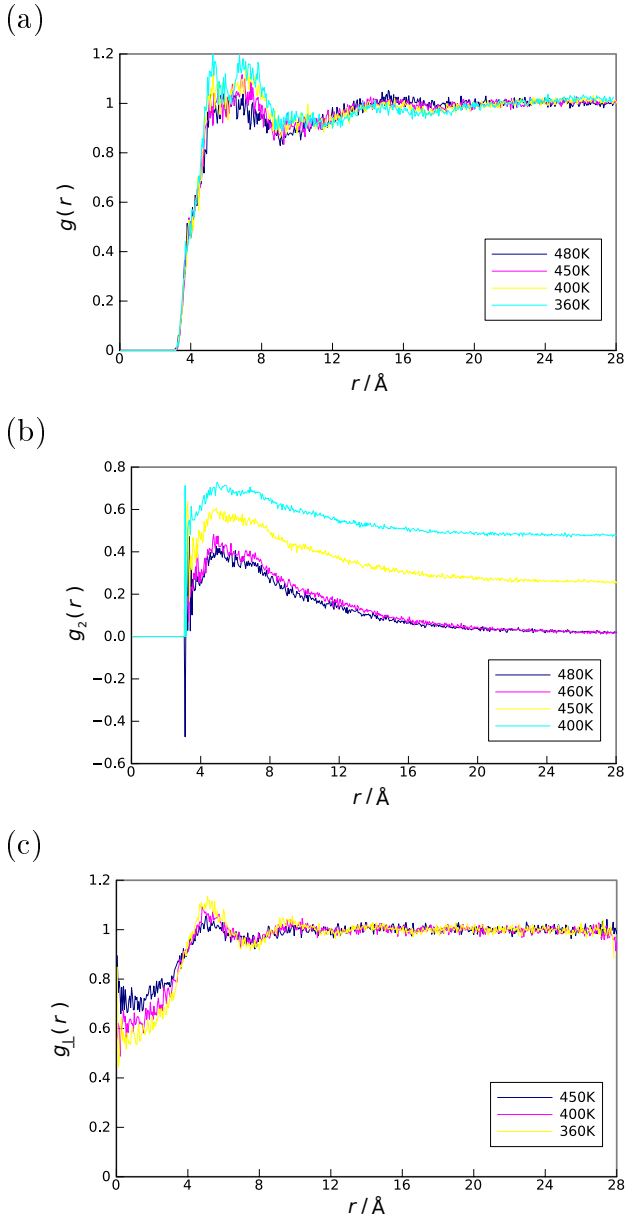

Figure 4.10: Radial distribution functions, (a) $g(r)$, (b) $g_2(r)$ and (c) $g_{\perp}(r)$ calculated as a function of distance between the centres of mass of the phenylester-LC molecules for several different temperatures.

4.5.2 Molecular theories of the nematic phase

Of particular interest is to relate the parameter changes to GAFF and the subsequent effect on the T_{NI} temperature of the phenylester-LC, to the molecular theories of nematic liquids and the isotropic-nematic phase transition, which explicitly describe the statistical mechanical details of the interparticle forces and correlations. These theories can be divided into three categories.[53,71]

The first category, *hard particle models,* attributes the onset of order to excluded volume effects, with short-range repulsions dominant and attractive forces excluded. Therefore density, rather than temperature, determines the onset of nematic ordering, and the T_{NI} temperature would be directly proportional to the external pressure. Amongst the hard particle models is the theoretical work of Onsager, which states that a fluid of (infinitely) thin spherocylinders with length L and diameter D, must undergo an I to N transition at a number density of order $1/(L^2D)$.[70] In all hard particle models, there is no energy contribution to the Helmholtz free energy as all allowed configurations have zero potential energy and all others have infinite energy and are therefore excluded. The entropy consists of two parts, translational (S_{trans}) as well as rotational (S_{rot}). The alignment of rods results in a decrease in S_{rot} but an increase in S_{trans} as there are more ways to pack aligned rods without them colliding with one another. At the I to N transition $\Delta S_{\mathrm{rot}} + \Delta S_{\mathrm{trans}} = 0$. Increasing the length to breadth ratio favours nematic formation as $\Delta S_{\mathrm{trans}} \approx k_B \rho\, L^2 D$. Computer simulations of an athermal system of elongated hard-core particles[70] show nematic ordering only if L/D is greater than three. Most typical mesogens have axial ratios greater than three and so would be expected to be in the nematic phase at all temperatures, which in reality is not true, suggesting that a contribution from attractive forces is required to stabilize the nematic phase.

The second category of molecular theories of nematic liquids, *attractive models*, is based on attractive interations between molecules. The most important of these was proposed by Maier and Saupe, in which the long-range ordering is related to angle-dependent intermolecular attractions in which the vdW dispersional interactions are assumed to dominate the energy.[71] The potential is mean-field averaged to give an effective one-body attraction. The Maier and Saupe theory predicts a first-order

I to N phase transition at a temperature, T_c for which the order parameter $S = 0.43$. As this theory assumes that the interaction is proportional to the anisotropy of the molecular polarizability, it is expected that molecules for which this property is very low, such as cyclohexylcyclohexanes, would not form a stable nematic phase, but nevertheless do.[53] This suggests that anisotropic dispersion forces are not the major contribution to the stabilization of the nematic phase, and that there exists a very subtle balance between repulsion and attractions in real thermotropic liquid crystals.[53]

The third category, *combined models*, includes theories that account for both hard-core anistropic repulsions as well as angle dependent attractions.[53,71] The relative roles of attractions and repulsions in determining the isotropic to nematic phase transition have been assessed by considering the quantity

$$\gamma \equiv -\rho \frac{(\partial \eta / \partial \rho)_T}{T(\partial \eta / \partial T)_\rho}, \tag{4.2}$$

which measures the relative dependence of the orientational order parameter on density and temperature.[71] Considering hard-core interactions only, in an athermal system, $\gamma = \infty$, whereas with angle-dependent attractions only, $\gamma = 1$. Measurements on a real mesogen for example, *para*-Azoxyanisole (PAA) show γ to be ≈ 4 which is in accordance with estimates provided by combined models. Additionally, theoretical calculations show that γ is very sensitive to the packing fraction, validating the dominant role of hard-core interactions at high density.[71]

The results of the current study suggest that reducing the density of the LC fragments, which were originally too high, and hence reducing the density of the phenylester-LC molecule, has had a significant effect on the phase behaviour of this mesogen. This sensitivity of the T_{NI} temperature to the density suggests that the dominant contribution to the onset of order are excluded volume effects as predicted by Onsager theory.

4.5.3 Molecular shape and flexibility

Discrepancies between molecular theories and experimental findings have largely been attributed to the exclusion of molecular flexibility, and therefore a consistent molecular theory of nematic liquid crystals needs to also account for molecular flexibility in some way.[53] Molecular shape, defined by the relative ratios between the molecule dimensions, their anisotropy and biaxiality, as well as mesogen flexibility, are important features in understanding LC phase stability.[17,145,169] These effects have been investigated through the use of hard and repulsive-attractive (combined) models, as well as semi rigid models that incorporate flexibility in their description of molecular interactions.[199] A number of studies have shown that a decrease in the molecular length to breadth ratio ($L : B$) is found to decrease the stability of the nematic phase and therefore shift the T_{NI} to lower temperatures.[197,198] A recent dissipative particle dynamics study (DPD)[199] of the phase behaviour of semi-rigid mesogens, where the flexibility was controlled by a bending constant, k_{ϕ}, has shown that the $L : B$ ratio is a decreasing function of both temperature and flexibility. Decreasing k_{ϕ} had the effect of reducing the ordering between mesogens and hence decreasing the T_{NI} temperature. The authors concluded that enhanced flexibility reduces the S_{trans} entropy contribution and had the same effect as shortening the rod length of rigid mesogens.

The effect of molecular shape and flexibility on LC phase stability and the change in transition temperatures has been investigated with atomistic simulations. For example, Tiberio *et al.*[169] have shown that the T_{NI} temperature of the *n*-cyanobiphenyl (with $n = 4$ to 8) series of mesogens is related to the average molecular $L : B$ ratio, with an increase in this ratio leading to an enhancement of the ordered phase stability. However CH_2 groups progressively added to the alkyl chain show an odd-even effect, with alternating T_{NI} (higher and lower) temperatures, but with an overall increase in T_{NI} with length of the chain. This affect has been attributed to changes in molecular breadth, where an increase in molecular breadth occured for even numbers of CH_2 groups only. The addition of even numbers of CH_2 groups appears to reduce the $L : B$ ratio in conjuction with enhancing the molecular biaxiality. This leads to a suppression of the effect of increasing chain

length and results in the characteristic profile of the T_{NI} temperatures displayed by this series.

An atomistic simulation of a linear oligothiophene based mesogen T6[145] has shown that the changes of mesophase, including the nematic to isotropic, are related to variations in the T6 conformations and average molecular shape. Torsional disorder was found to increase with temperature resulting in a change in the possible configurations for T6. This has been connected to the average value of the cosine of the central inter-ring dihedral where an increase in the number of molecules possessing dihedral angles different from 180° (linear planar shape) results in a broader distribution of molecules with a lower $L : B$ ratio as the temperature is increased. These investigations suggest that molecular shape, molecular biaxiality and the degree of internal disorder are important features in determining the T_{NI} temperature of a particular mesogen.

The influence of molecular shape on the location of the T_{NI} temperature of the phenylester-LC system was also examined in the current study. As shown in Figure 4.9a, at 480 K and 500 K, the simulated order parmameters indicate nematic ordering with original GAFF parameters ($\langle P_2 \rangle$ greater than 0.4) but isotropic phases with GAFF-LCFF ($\langle P_2 \rangle$ less than 0.1) with the latter in agreement with experimental evidence. This suggests that the average molecular $L : B$ ratio employing the original GAFF force field may be too large and hence lead to an ordered phase (nematic) at these temperatures.

An indication of the molecular dimensions, and hence overall shape, can be obtained from the average moment of inertia tensor, $\langle I \rangle$ where $\langle I_1 \rangle$, $\langle I_2 \rangle$ and $\langle I_3 \rangle$ are the averaged principle moments of inertia. These values enable the average length, $2a$, width, $2b$, and breadth, $2c$, of a mesogen to be calculated using $a = \sqrt{2.5(I_2 + I_3 - I_1)m}$ and cyclic permutations for b and c.[188] These molecular dimensions for the phenylester-LC are displayed in Table 4.13 for the phenylester-LC molecule at selected temperatures for both the original and the new GAFF-LCFF force fields. Both force fields show a very small increase in molecular length with decreasing temperatures. However, the main differences occur between different force fields, with GAFF-LCFF resulting in a decrease in length of ≈ 0.13 Å (in the

isotropic phase at 550 K) as well as a small increase in molecular width and breadth as compared to original GAFF.

This small change in molecular length with GAFF-LCFF is significant. It is probable that the amended torsional potentials introduced into the phenylester-LC have increased its flexibility, enabling the molecular structure to sample a broader range of configurations. This is likely to reduce the $L : B$ ratio and contribute to lowering the T_{NI} temperature, and is also in agreement with the results of the DPD simulations of semi-rigid mesogens described above.[199] The results are also in accordance with the findings of Tiberio *et al.*[145] and their investigations of the linear T6 mesogen, where a decrease in the average molecular length of less than 0.2 Å was found when going from the isotropic to the nematic phase.

Table 4.13: The average length, $2a$, width, $2b$ and breadth, $2c$, of the phenylester-LC molecule at the simulated temperatures of 550 K, 500 K and 480 K for the original and new GAFF-LCFF force fields.

	$\langle 2a \rangle$ / Å	$\langle 2b \rangle$ / Å	$\langle 2c \rangle$ / Å	$a/(b+c)$
Original GAFF				
550 K (isotropic)	29.63	5.86	3.63	6.24
500 K (nematic)	29.85	5.70	3.54	6.46
480 K (nematic)	29.93	5.62	3.51	6.55
GAFF-LCFF				
550 K (isotropic)	29.50	5.85	3.68	6.19
500 K (isotropic)	29.62	5.75	3.65	6.30
480 K (isotropic)	29.68	5.70	3.63	6.36

To test the relative effects of the changes in LJ parameters and torsions on the prediction of the T_{NI} temperature, an estimate of T_{NI} was obtained using GAFF-LCFF torsions only, while retaining the original GAFF LJ parameters (see Figure 4.11). These results suggest a T_{NI} of ≈ 45 K higher than the experimental value of 452 K and ≈ 15 K lower than that obtained with original GAFF. This indicates that the torsional parameters do have a significant effect, although the main improvement in the T_{NI} prediction arises from the optimized LJ parameters.

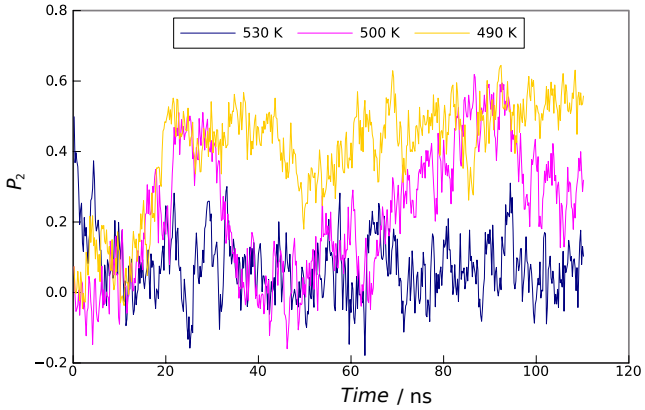

Figure 4.11: Estimate of T_{NI} for phenylester-LC with GAFF-LCFF torsions only.

4.6 Testing GAFF-LCFF: simulations of the C4-Ph-ODBP-Ph-C7 and C5-Ph-ODBP-Ph-OC12 mesogens

Following on from the success of providing a very good estimate of the experimental T_{NI} for the phenylester-LC molecule, the GAFF-LCFF force field was then tested on predicting the T_{NI} temperatures for C4-Ph-ODBP-Ph-C7 and C5-Ph-ODBP-Ph-OC12, members of the *bis*-(phenyl)oxadiazole family of bent core mesogens (see Chapter 5 and Figure 5.1 for structures and experimental phase transitions). The original GAFF force field significantly overestimates the experimental T_{NI} temperatures of 507 K (C4-Ph-ODBP-Ph-C7) and 512 K (C5-Ph-ODBP-Ph-OC12) by $\approx$ 100 to 110 K (see Figure 4.12). Initial estimates of the T_{NI} temperatures using the GAFF-LCFF force field, resulted in phase transitions of $\approx$ 20 to 30 K higher than experimental values, and although a significant improvement on the unmodified GAFF predictions, this suggested there was still room for further improvement.

A more recent paper that was not available during the initial refinement of the GAFF parameters in this work, highlighted the need for refining the Lennard-Jones(LJ) parameters for the carbon and hydrogen atoms of long carbon chains, so that the modelling of phospholipids could be achieved more accurately (GAFFlipid force field).[57] For example, it was found that original GAFF considerably overestimated the experimental density and $\Delta_{\mathrm{vap}}H$ for the 15 carbon chain, pentadodecane.

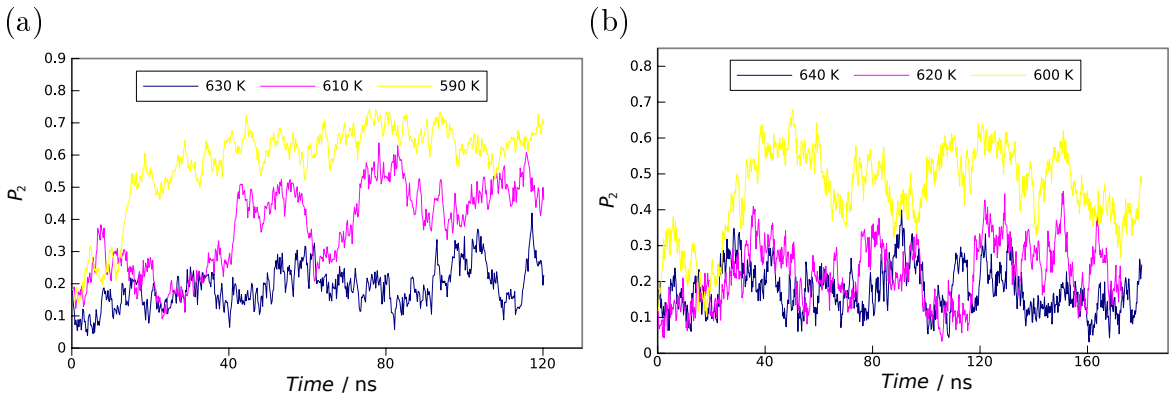

Figure 4.12: (a) Estimate of the T_{NI} with original GAFF; (a) C4-Ph-ODBP-Ph-C7 and (b) C5-Ph-ODBP-Ph-OC12

The GAFFlipid force field includes modified LJ parameters for carbon and hydrogen atoms in order to replicate more accurately the experimental properties of simple hydrocarbons. In addition to the refinement of LJ parameters for hydrocarbons, the C−C−C−C torsion in GAFFlipid was fitted to the high level QC calculation, MP4/6-311G(d,p)//MP2/6-31G*. This had the effect of reducing the *trans/gauche* (*t/g*) energy difference as well as the *trans-gauche* (*t-g*) barrier.

The importance of force fields accurately modelling the flexibility of *n*-alkanes and reduction of the *t/g* energy difference and *t-g* barrier to reproduce more recent experimental and QC data was discussed in Section 4.4.1, along with the results for the refinement of the C−C−C−C torsion. However, the LJ parameters for the carbon and hydrogen atoms of *n*-alkanes remained in their original GAFF form. The original GAFF predictions for both density and $\Delta_{\mathrm{vap}}H$ for butane (C4 carbon chain) were found to be in good agreement with experimental values (< 3 %).[184] This suggests that the unmodified LJ parameters for carbon and hydrogen atoms of the C4 chains of the phenylester-LC would have been acceptable in the process of obtaining a more accurate T_{NI} for this mesogen. This assumption does not appear to be valid for mesogens containing medium to long *n*-alkanes (see Table 4.14) where the discrepancy between calculated and experimental values increases with increasing chain length. In particular, the calculated $\Delta_{\mathrm{vap}}H$ values for pentadodecane and dodecane are particulary poor and the densities are ≈ 10 % greater than experimental values. Although the calculated densities for the smaller alkanes, pentane and heptane, are

in good agreement with experiment, the $\Delta_{\text{vap}}H$ values are still $\approx$ 8 to 10 % greater than experimental values. It was therefore considered that the varying length carbon chains of the C4-Ph-ODBP-Ph-C7 and C5-Ph-ODBP-Ph-OC12 mesogens, in particular the C5, C7 and C12 chains, may require further refinement of the LJ parameters. This was also thought to be the most likely explanation for the slightly overestimated T_{NI} temperatures for ODBP mesogens with the GAFF-LCFF force field.

Table 4.14: Density and heat of vaporization calculations for various n-alkanes using GAFF and GAFFlipid. [a]All values at 298 K. [b]Data taken from the CRC Handbook of Chemistry and Physics.[82] [c] Data taken from ref.[57] [d] GAFFlipid with LJ parameters modified.

n-alkane	Property[a]	Exp.[b]	GAFF	GAFFlipid	GAFFlipid (LJ modified)[d]
Pentadecane	Density / g cm^{-3})	0.7690	0.8420[c]	0.7510[c]	-
	Heat of Vap. / kJ mol^{-1}	76.77	105.88[c]	77.01[c]	-
Dodecane	Density / g cm^{-3})	0.7495	0.8240 $\pm$ 0.0003	0.7450 $\pm$ 0.0002	-
	Heat of Vap. / kJ mol^{-1}	61.52	96.21 $\pm$ 0.10	56.02 $\pm$ 0.05	-
Heptane	Density / g cm^{-3})	0.6795	0.6782 $\pm$ 0.0001	0.6637 $\pm$ 0.0002	0.6819 $\pm$ 0.0001
	Heat of Vap. / kJ mol^{-1}	36.57	40.37 $\pm$ 0.03	31.80 $\pm$ 0.05	35.70 $\pm$ 0.01
Pentane	Density / g cm^{-3})	0.6260	0.6132 $\pm$ 0.0001	0.5865 $\pm$ 0.0002	0.6119 $\pm$ 0.0002
	Heat of Vap. / kJ mol^{-1}	26.43	28.45 $\pm$ 0.02	21.98 $\pm$ 0.01	25.13 $\pm$ 0.02

The GAFFlipid LJ carbon and hydrogen parameters along with the GAFFlipid C$-$C$-$C$-$C torsional parameters were tested on dodecane (C12), heptane (C7) and pentane (C5). The results for the reproduction of experimental data are shown in column 5 of Table 4.14, along with the results for pentadecane (C15), taken from the original development of GAFFlipid.[57] These results indicate that the GAFFlipid parameters produce better agreement with experimental values, in particular for the calculated $\Delta_{\text{vap}}H$ values for the longer n-alkanes. However, for the shorter chains, heptane and pentane, the originally overestimated $\Delta_{\text{vap}}H$ values are significantly underestimated compared with experimental values, along with a small under prediction of densities. The best agreement with experimental values for heptane and pentane was obtained by a small modification to the GAFFlipid LJ parameters. It was found that multiplying the difference between original GAFF and GAFFlipid LJ parameters by 0.75 produced the best overall results for both these properties.

On the basis of the results shown in Table 4.14, the decision was taken that for *n*-alkanes of lengths greater than C10, the unaltered GAFFlipid LJ parameters would be most appropriate, whilst for medium length chains of C5 to C10, the modified GAFFlipid LJ parameters (0.75 times the difference between GAFF and GAFFlipid) appear to produce acceptable results. This means a wide range of *n*-alkanes can be described with minimal alterations to the original GAFF force field parameters.

To verify that the inclusion of GAFFlipid torsional parameters in conjunction with the adopted/amended GAFFlipid LJ parameters reduced the *t*/*g* energy difference and *t*-*g* energy barrier of *n*-alkanes of various length, the torsional profiles for the C−C−C−C dihedral of both dodecane and heptane were calculated. A small reduction in both these values is apparent compared with original GAFF (see Figure 4.13). In section 4.4.1, a similar result incorporating Sui *et al.* torsional parameters from the OPLS force field was obtained for the C−C−C−C torsion of heptane and butylbenzene. However it was considered that the GAFFlipid approach had the added advantage of addressing the need to amend the LJ parameters, in particular for medium to long *n*-alkanes, as well as refinement of the C−C−C−C torsional parameters. Finally, the experimental T_{NI} values for both ODBP mesogens differ by only 5 K, with C5-Ph-ODBP-Ph-OC12 possessing the higher value. The results in this study indicate that the difference in the simulated T_{NI} for both mesogens is slightly greater at $\approx$ 10 K. However, C5-Ph-ODBP-Ph-OC12 still displays the higher T_{NI} value.

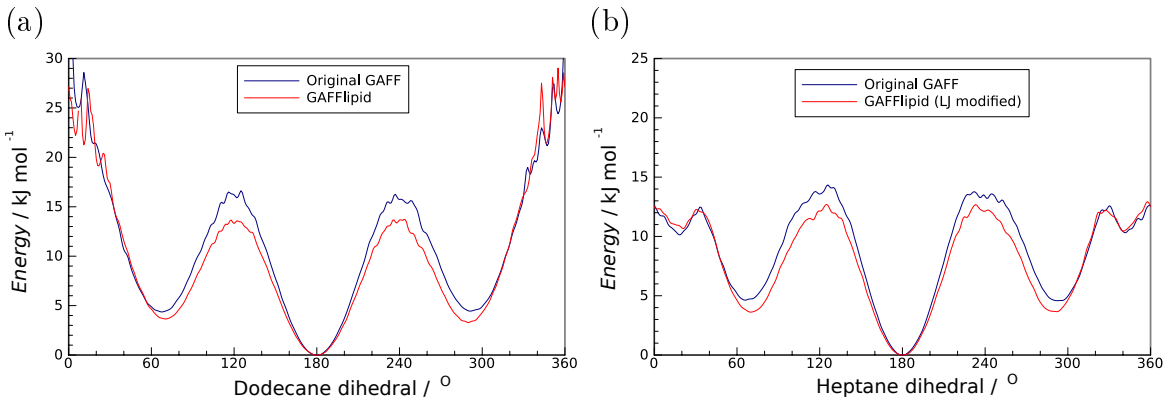

Figure 4.13: Torsion profiles for the $CH_2-CH_2-CH_2-CH_2$ dihedral of (a) dodecane and (b) heptane

In terms of the simulations of the two ODBP bent core mesogens, it was decided to retain all the amended parameters for GAFF-LCFF discussed in Section 4.4 except for the carbon chains, for which the GAFFlipid parameters were transferred to the C12 and C5 chains of the C5-Ph-ODBP-Ph-OC12 mesogen, whilst the modified GAFFlipid LJ parameters were transferred to the C7 and C4 chains of C4-Ph-ODBP-Ph-C7. Due to the fact that GAFF only assigns single atom types to the carbon and hydrogen atoms of carbon chains, it was not possible to differentiate the parameters on differing length chains of the unsymmetrical ODBP mesogens. Therefore, the most appropriate parameters were selected to represent the longer chain in each mesogen and applied to both chains on each side. The new LJ parameters are shown in Table 4.15 along with the original GAFF LJ parameters for the c3 and hc atom types. Table 4.16 summarizes the new Ryckaert-Belleman parameters for the C−C−C−C torsion adopted from the GAFFlipid force field which were incorporated into GAFF-LCFF.

Table 4.15: Original, GAFFLipid and modified GAFFLipid Lennard-Jones parameters

Atom parameter description	GAFF	GAFFlipid	GAFFlipid LJ parameters modified
c3 sigma / nm	0.33997	0.35814	0.35360
c3 epsilon / kJ mol^{-1}	0.45773	0.23012	0.28702
hc sigma / nm	0.26495	0.23876	0.24531
hc epsilon / kJ mol^{-1}	0.06569	0.10042	0.09173

Table 4.16: New Ryckaert-Bellerman derived from GAFFlipid C−C−C−C torsion (GAFF atom types c3-c3-c3-c3)

Dihedral	C_0	C_1	C_2	C_3	C_4	C_5
C−C−C−C	0.56568	1.69703	0.00000	-2.26271	0.00000	0.00000

4.6.1 Molecular order

Figure 4.14a shows the temperature dependent uniaxial order parameter, P_2 averaged over the last 60 ns of long production runs for $N = 256$ molecules for C5-Ph-ODBP-Ph-OC12. P_2 corresponds to the largest eigenvalue of the cartesian ordering matrix, $\mathbf{Q}(t)$, for two different choices of the molecular reference axis: i) a vector parallel with the long axis of the aromatic core only, ii) the eigenvector of the molecular inertia tensor corresponding to the lowest eigenvalue (see Chapter 3, Section 3.5 for a fuller description of measuring order in liquid crystals). To assess the system size effects, the $\langle P_2 \rangle$ values for a larger $N = 2048$ system for selected temperatures are also shown for comparison, with results given as average values calculated over 20 ns production runs.

Examining $\langle P_2 \rangle$ values for the small system indicates that the choice of molecular reference axis has an insignificant effect on the results. At the higher temperatures of 530 and 520 K, $\langle P_2 \rangle$ values assume effectively isotropic values of ≈ 0.2. At 510 K there is a small jump to $\langle P_2 \rangle > 0.3$, indicating a weak first order transition between 520 and 510 K. This is also supported by observing the evolution of the instantaneous P_2 as a function of time for temperatures close to the phase transition (see Figure 4.14b). At 520 K and over the last 180 ns, P_2 shows relatively small fluctuations of between ≈ 0.1 and 0.4, suggesting that at this temperature the system is approaching a phase transition, although the overall average over this period is only 0.22, a value considered to be isotropic. At 510 K the time evolution of P_2 shows larger fluctuations, ranging from 0.1 to 0.6, and an average value of 0.36 over the last 120 ns, which suggests that this is very close to a phase transition. Decreasing the temperature to 500 K, results in smaller oscillations of P_2 with time and after ≈ 60 ns, P_2 assumes an average value of 0.54, typical of a nematic phase. Both Figure 4.14a and 4.14b suggest a simulated T_{NI} in the vicinity of 510 K for

the small system, which is in very good agreement with the experimental T_{NI} of 512 K.

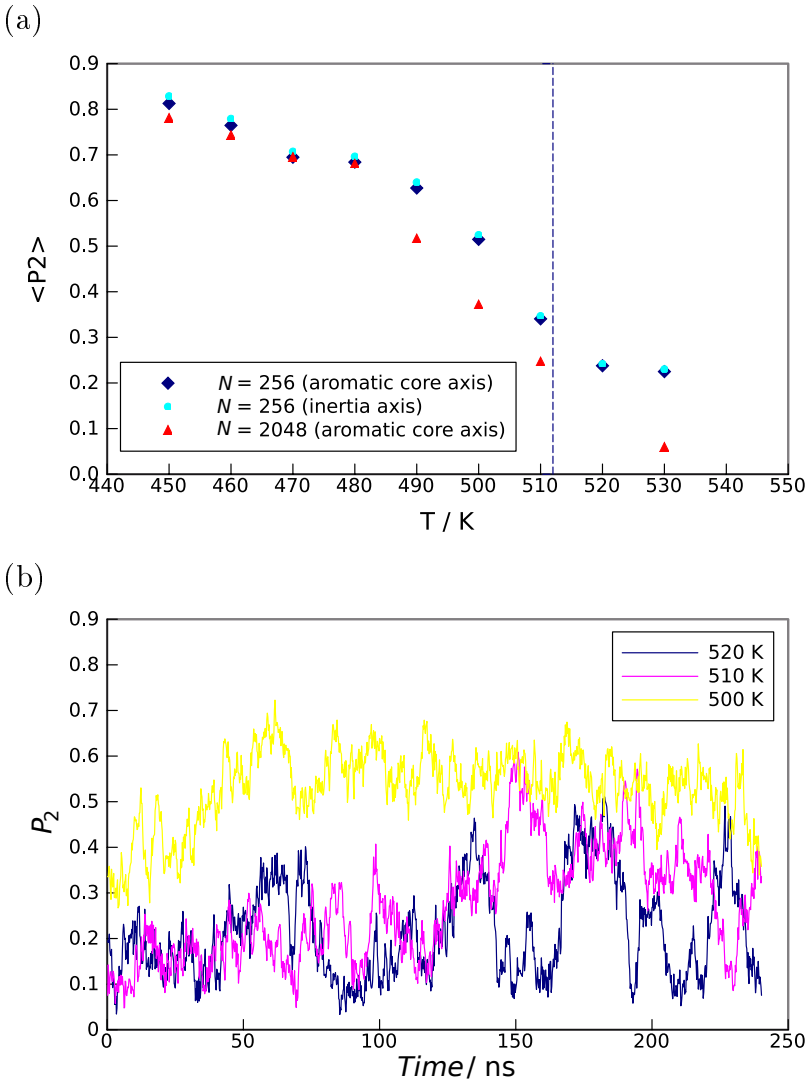

Figure 4.14: (a) Average order parameters for the $N = 256$ and $N = 2048$ systems as a function of temperature for C5-Ph-ODBP-Ph-OC12. The dotted line represents the experimental T_{NI} . (b) Order parameter as a function of time for temperatures close to the phase transition for $N = 256$ systems.

The larger $N = 2048$ system shows a small reduction in $\langle P_2 \rangle$ values compared with the smaller system, with these differences more pronounced in the isotropic phase and at higher temperatures in the nematic phase. The T_{NI} temperature is located approximately 5 K below that for the $N = 256$ system, indicating that the simulated T_{NI} temperature for the larger system is marginally lower than the experimental value. Limited system size effects have been noted for other atomistic simulations of different liquid crystal molecules. For example, a reduction of ≈ 15 K was found in the simulated T_{NI} temperature for a linear oligothiophene based mesogen when increasing the sample size from 140 to 1120 molecules,[145] and Palermo *et al.*[137] found a smaller reduction of ≈ 5 K in the simulated T_{NI} temperature of 8CB for 750 molecules compared with an earlier study employing 250 molecules.[169] These system size effects are expected, as the order parameter stability is very sensitive to the number of molecules. For small samples, oscillations in P_2 can lead to non-zero values in the isotropic phase of a simulation, whereas $P_2 = 0$ is measured in experiments.[22]

Figure 4.15 shows $\langle P_2 \rangle$ values plotted for the C4-Ph-ODBP-Ph-C7 system. The average order parameter over the last 60 ns of production runs assumes very low values of $\langle P_2 \rangle < 0.2$ between 530 and 510 K, which are indicative of an isotropic phase at these temperatures. At 500 K there is a slight increase in $\langle P_2 \rangle$ to ≈ 2.5, followed by a much larger increase at 490 K to ≈ 0.5, indicative of the ordered state. Examination of the behaviour of the order parameter plotted as a function of time at temperatures close to the phase transition (see Figure 4.15b) show that at 510 K, P_2 displays some relatively small oscillations, but the overall trajectory indicates that the system is still isotropic. However, at 500 K, P_2 displays larger fluctuations from ≈ 0.1 to ≈ 0.6, which when averaged over the full trajectory gives a $\langle P_2 \rangle$ of ≈ 0.3, higher than the average value for the last 60 ns. This suggests that 500 K is very close to the T_{NI} transition and although slightly lower than the experimental T_{NI} of 507 K, is still within 10 K of this value.

The larger $N = 1984$ system also displays marginally lower $\langle P_2 \rangle$ values compared with those for the smaller $N = 248$ system, although the greater divergence in these values occurs in the isotropic phase.

(a)

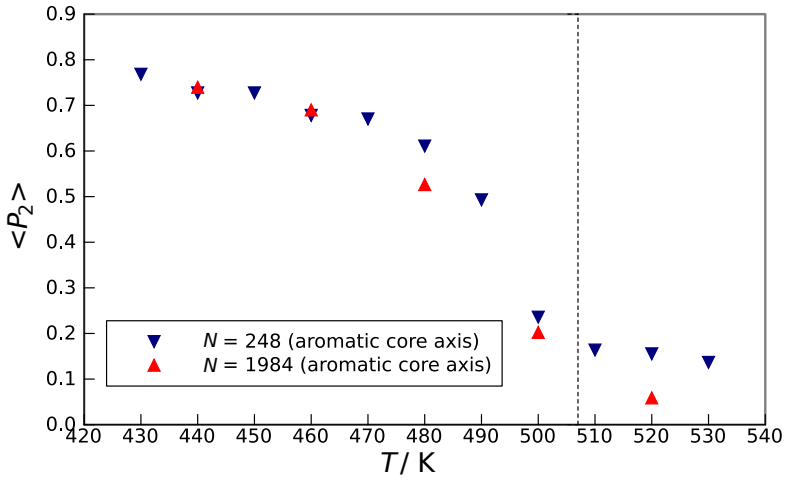

(b)

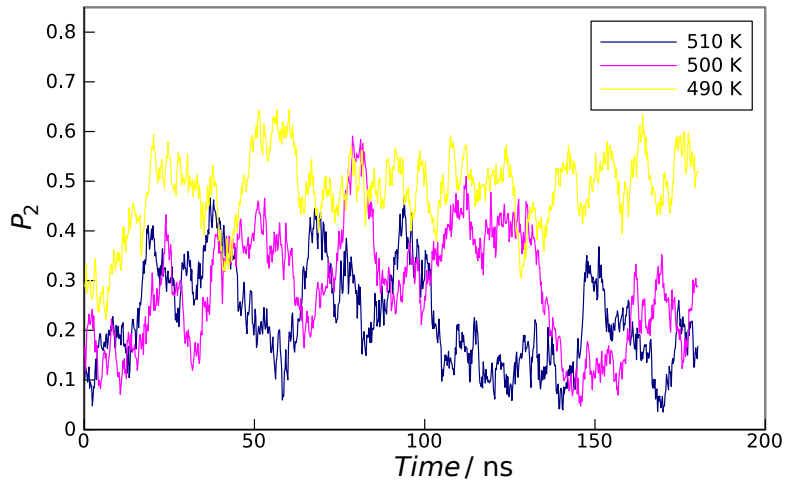

Figure 4.15: (a) Average order parameters for $N = 256$ and $N = 2048$ systems as a function of temperature for C4-Ph-ODBP-Ph-C7. Dotted line represents the experimental T_{NI} (b) Order parameter as a function of time at temperatures close to the phase transition for $N = 256$.

Finally, the experimental T_{NI} values for both ODBP mesogens differ by only 5 K, with C5-Ph-ODBP-Ph-OC12 possessing the higher value. The results in this study indicate that the difference in the simulated T_{NI} for both mesogens is slightly greater at $\approx$ 10 K. However, C5-Ph-ODBP-Ph-OC12 still displays the higher T_{NI} value.

4.7 Conclusions

The current study presents a strategy for optimizing the standard GAFF force field for the modelling of liquid crystal systems. In summary, the GAFF force field has been amended by:

- A careful tuning of a selected number of LJ parameters of component fragments of standard calamitic mesogens, with the aim of reproducing the experimental properties of density and $\Delta_{\text{vap}}H$ and in particular, to obtain a density deviation of less than 1% from experimental values.

- Re-parametrization of a number of torsional potentials of fragment molecules using high-level quantum chemical calculations, with the aim of improving the description of the overall 'shape' and flexibility of the mesogen.

MD simulations of a typical calamitic mesogen, 1,3-benzenedicarboxylic acid,1,3-*bis*(4-butylphenyl)ester (phenylester-LC), employing the amended GAFF-LCFF force field successfully predicts a T_{NI} temperature within 5 K of experiment and reduces the original GAFF prediction of the temperature by $\approx$ 60 K.

For the bent-core mesogens, C4-Ph-ODBP-Ph-C7 and C5-Ph-ODBP-Ph-OC12, the MD simulations produced T_{NI} estimates within 10 K of experiment, but only after a further refinement of parameters for simple hydocarbon chains of varying lengths, to account for the longer carbon chains present in these mesogens. This involved adopting or amending parameters from the GAFFlipid force field, depending on chain length. System size effects on the predicted T_{NI} temperatures were found to be very limited. The results represent huge improvements over the original GAFF force field, which over predicted T_{NI} values by $\approx$ 100 K for both these mesogens, and also provides increased confidence in the results of a more in depth study of these liquid crystals presented in Chapter 5.

Chapter 5

Investigations of the Nematic Phase Structure and Biaxiality of the C5-Ph-ODBP-Ph-OC12 and C4-Ph-ODBP-Ph-C7 Mesogens

5.1 Introduction

The nematic phases of bent-core mesogens were first discovered in 2000 and due to their unique properties, have since been the focus of extensive experimental, as well as theoretical investigations. A particularly interesting class of bent-core nematics are based on the 1,3,4-oxadiazole biphenyl (ODBP) core. As well as displaying many unique properties, a number of these mesogens have been considered promising candidates for the formation of the elusive biaxial nematic phase.[68] For these reasons, the two ODBP based bent-core mesogens shown in Figure 5.1 were selected for a detailed computational study.

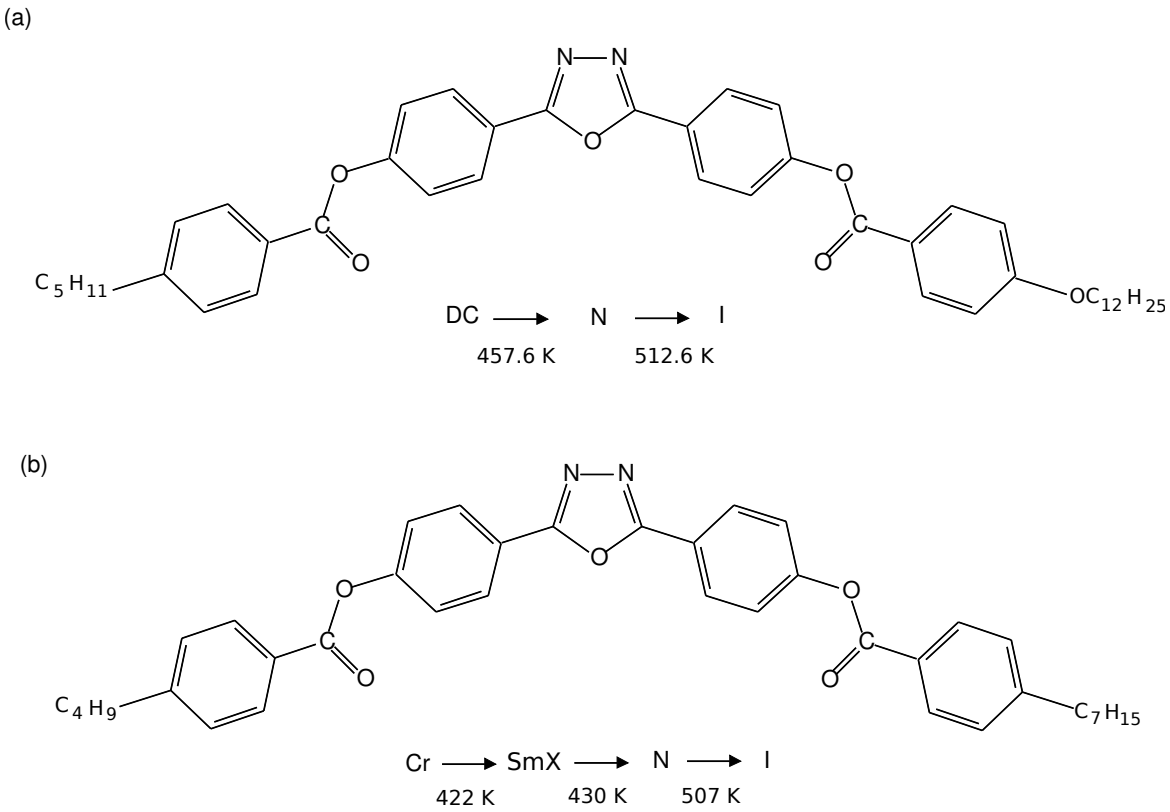

Figure 5.1: The chemical structures and experimental phase transition temperatures of (a) C5-Ph-ODBP-Ph-OC12 and (b) C4-Ph-ODBP-Ph-C7.

Both systems exhibit a wide nematic phase range, indicating significant stability of this phase (many mesogens based on the ODBP core do not exhibit nematic phases).[74] The computational study employed the recently developed GAFF-LCFF force field,[18] with further minor amendments to the alkyl chain parameters derived from the GAFFLipid force field[57] described in Chapter 4.

The following is a brief summary of the similarities and the experimentally observed properties common to both systems, followed by a more in depth description of the order and structural organization of the nematic phase of the C5-Ph-ODBP-Ph-OC12 system, for which there is more experimentally derived data. This is then followed by the objectives for this computational study.

Both achiral mesogens possess a bend angle of $\approx 140°$, a strong transverse dipole of ≈ 5 Debye and consequently show negative dielectric anisotropy.[78] Polarizing optical microscopy investigations of both materials show evidence for the segregation into domains of opposite handedness in the nematic phase. Additionally, there are

indications from differential scanning calorimetry (DSC) that the the transition to the nematic phase of both ODBP materials is preceded by a thermal event in the isotropic phase, suggesting that these liquids are structured at temperatures just above the formation of the nematic phase. The molecules then undergo a process of self-assembly before self organization into the nematic phase occurs. Once in the nematic phase this process results in the formation of chiral domains characterized by the presence of helical macrostructures. Helical structures of one sense may then assemble into spiralling ribbons. It has been proposed that the strong transverse dipole in the ODBP molecules leads to unusually strong intermolecular associations that enable chiral recognition amongst molecules, and hence the formation of self-assembled helical structures.

In addition, and under certain conditions, thermal, polarized light optical microscopy (POM) has shown the presence of unique filament textures at the onset of new order from the nematic phase. This may be due to the frustration caused by the competition to form layered structures and the desire to maintain bend at the transition from a nematic phase which has inherent polar properties. It is stressed however, that the formation of helical macrostructures and unique filament structures in the nematic phase of both materials are strongly kinetically driven and depend on the thermal and mechanical history of the samples. Helix formation can be suppressed by external forces such as surface interactions and instead a uniformly homogeneous nematic phase is observed which may be biaxial in the case of some ODBP materials.[76–78]

5.2 Experimental Studies of C5-Ph-ODBP-Ph-OC12

The bent-core mesogen, C5-Ph-ODBP-Ph-OC12, has attracted much attention as it displays unusual properties in the nematic phase at ≈ 35 K below T_{NI}, which are not yet clearly understood. In particular, the measurement of non-zero biaxial order parameters by Raman scattering, in the absence of any external electric or magnetic fields, indicate the existence of a thermotropic biaxial nematic phase.[100] To date there is sparse evidence of biaxiality in any ODBP materials. Other anomalies in

the low temperature regime include: non-standard electroconvection, unusual dielectric properties, reverse twist dislocations under the influence of an electric field and unusual behaviour of the bend elastic constant, K_{33}.[74] It is possible that some of these anomalies could be explained by the presence of cybotactic clusters or the emergence of biaxial order, although there is no clear evidence to support either of these explanations.[74] In particular, there is no clear x-ray evidence for pretransitional SmA or SmC clusters in the nematic phase,[162] and as stated by Kaur *et al.*[100], this would not be expected, given the first-order transition to a dark conglomerate (DC) phase directly below the nematic phase. The elastic constants, K_{11} (splay), K_{22} (twist) and K_{33} (bend) measured in the nematic phase show differences compared with most other bent-core systems, and it has been suggested that clustering cannot satisfactorily explain these differences. While the relationship $K_{22} < K_{33} < K_{11}$ is common to many other bent-core systems, the behaviour of K_{33} is quite distinct for this system, showing almost no temperature dependence and particularly low values at lower temperatures. In contrast to bent-core systems with underlying SmC phases, no pretransitional behaviour is observed for either K_{11} or K_{33}.[100,101] The ratio, $K_{33}/\ K_{11}$, which is equivalent to the square of the ratio of the correlation length parallel, ($\xi_{\parallel}$) and perpendicular ($\xi_{\perp}$), to the director, decreases with decreasing temperature.[100] Kaur *et al.* state that this behaviour is the opposite to that found for another oxadiazole bent-core nematic showing SmC-type clusters in the nematic phase, for which $(\xi_{\parallel}/\xi_{\perp})^2$ increases with decreasing temperature. They suggest that if clusters were present in the C5-Ph-ODBP-Ph-OC12 system, these would be characterized by an unusual shape, consisting of tens of molecules wide and only one molecule long. A detailed understanding of the nature of the nematic phase of this mesogen therefore remains unclear.

Although the nematic phase is the focus of this study, a brief description of the DC phase is given here, as unlike most other bent-core nematic systems, which possess the more usual underlying tilted smectic phase, this system shows a DC phase directly below the nematic phase. This means that many physical properties can be measured in the nematic phase and the behaviour extrapolated down into the DC phase.[134] Likewise the reverse maybe true in that a detailed understanding

of the DC phase maybe important in gaining a better picture of the structural organization of the overlying low temperature nematic regime, as well as gaining a better understanding of the unusual behaviour displayed in the nematic phase of this system.

DC phases are defined as soft isotropic phases, usually composed of chiral domains of opposite handedness in the ground state. In addition to the anomalies displayed in the low temperature nematic phase of C5-Ph-ODBP-Ph-OC12, this system also shows some unusual features in the DC phase.[134] These include two distinct temperature dependent regimes, and in contrast to other bent-core systems possessing an underlying DC phase, there is an absence of optically active chiral domains in the ground state throughout the temperature range of the DC phase. In the presence of an electric field, the DC phase exhibits a unique set of field-induced states, which appear to be related to the presence of both alkyl and alkoxy terminal chains. The experimental investigations indicate that the internal structure of the DC phase consists of tilted polar smectic layers with relatively short interlayer correlation length, with these layers curving continuously, forming a saddle type structure. In the ground state the orientation of the tilt and polarity is antiparallel (SmC_AP_A). Figure 5.2 a shows a schematic of a typical DC phase with saddle splay layer curvature and Figure 5.2 b is a schematic of the proposed saddle type structure of the C5-Ph-ODBP-Ph-OC12 system.

(a) (b)

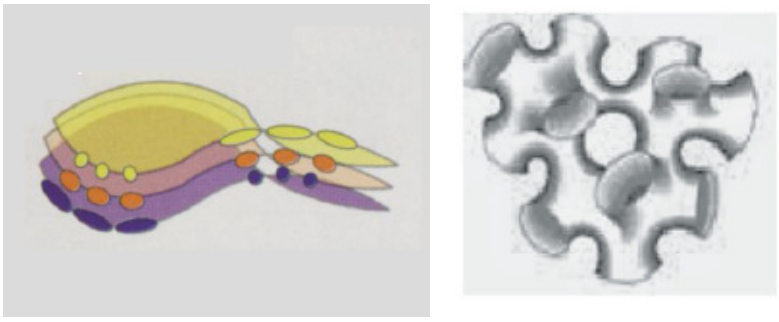

Figure 5.2: (a) Generic schematic of the saddle splay layer curvature in the DC phase. Reproduced from[87] with permission of The American Association for the Advancement of Science (b) Schematic of the saddle type structure of the C5-Ph-ODBP-Ph-OC12 system (scale not given). Reproduced from reference[134] with permission of the American Physical Society.

5.2.1 Orientational order and evidence for the emergence of biaxial order in the low temperature regime

In addition to IR absorption, NMR spectroscopy, X-ray diffraction and Conoscopy for the measurement of orientational order in liquid crystal phases, Polarized Raman Scattering (PRS) has become a promising technique for determining both uniaxial and biaxial order parameters in the nematic phase. PRS exploits the property that light incident on a material induces an oscillating dipole moment, μ, described by the molecular polarizability and the amplitude and frequency of the incident electric field. Raman scattered light is the product of periodic distortions in the molecular polarizability, resulting in a small proportion of light re-radiated at wavelengths other than the incident wavelength.[163] PRS probes the molecular ordering in a system by monitoring the scattering from "Raman active" modes within mesogenic molecules. A molecule with an anisotropic differential polarizability and Euler angles (α, β, γ) reflecting the orientational degrees of freedom of a molecule with respect to a frame of reference, enables the observed intensity of the Raman scattered light to be expressed as a function of the electric field and the orientational distribution function integrated over all possible orientations. Order parameters are then obtained from equations relating the intensities to the various order parameters.[163]

Uniaxial and biaxial orientational order parameters have been obtained for C5-Ph-ODBP-Ph-OC12 using this technique.[162] The phenyl stretching mode was used as the Raman probe as this is the strongest peak for bent-core molecules. To reflect the molecular symmetry specific to bent-core systems, and therefore model a biaxial unit, two Raman probes were used, with each positioned along a molecular arm. The Raman scattering intensity was then described by summing the electric field contributions from each arm.[73] This model also included a fixed molecular bend angle of 140°, which the authors state is how molecular biaxiality is included in the Raman analysis for the bent-core system. Both the measured uniaxial order parameters, $\langle P_{200} \rangle$ and $\langle P_{400} \rangle$ which are equivalent to $\langle P_2 \rangle$ and $\langle P_4 \rangle$, exhibited the expected magnitude and temperature dependence for a wide nematic phase.[162] The measured biaxial order parameters showed a clear uniaxial to biaxial transition at

≈ 30 K below T_{NI} , after which there was a gradual increase in the magnitude of the biaxial order parameters with decreasing temperature. However, this approach to obtaining biaxial order parameters involves fitting a large number of variables to a single set of experimental data which may lead to some uncertainty in the measured values.[73]

A similar approach undertaken by Park *et al.*,[141] using Raman scattering to measure the biaxial order parameters of a different bent-core system, A131, shown in Figure 5.3, produced significantly different results. While the authors reported a second order uniaxial to biaxial transition for the A131 system in the nematic phase, they also found exceptionally low uniaxial parameters in the uniaxial phase as well as unrealistic non-zero biaxial order parameters in this phase. Park *et al.* did not consider the molecular bend angle in their analysis of the Raman scattering data and it has been suggested that this omission may provide an explanation for their anomalous results.[72]

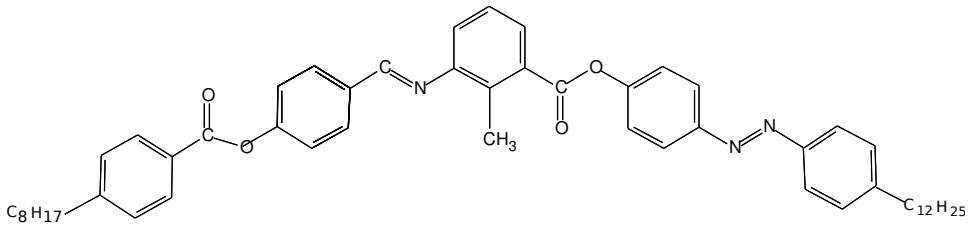

Figure 5.3: The chemical structure of the A131 bent-core mesogen

In response to comments in reference,[72] Park *et al.* suggest that the unusually low uniaxial orders parameters are attributed to fluctuations relating to the biaxial phase and that consideration of the bend angle is not critical, and may even lead to misleading results. They also draw attention to the small angle X-ray diffraction results for C5-Ph-ODBP-Ph-OC12, which were obtained by Southern *et al.*[162] as supplementary information to their results from the Raman scattering study. The small angle X-ray diffraction results show that the angular separation of the four observed diffraction peaks changes by $\approx 35^{\circ}$ as a function of temperature throughout the nematic range (see Figure 5.4). This, Park *et al.* state, can only arise from the form factor (Fourier transform of the electron density) which explicitly depends on the bend angle.[140] They suggest that if the bend angle is crucial, then a realistic

analysis of the Raman scattering data must account for a temperature dependent bend angle throughout the nematic range. However, observations of Figure 5.4 show a temperature dependence of the angular peak separation only close to the T_{NI} , after which it assumes a fairly stable value of between 70° and 76° for the rest of the nematic range.

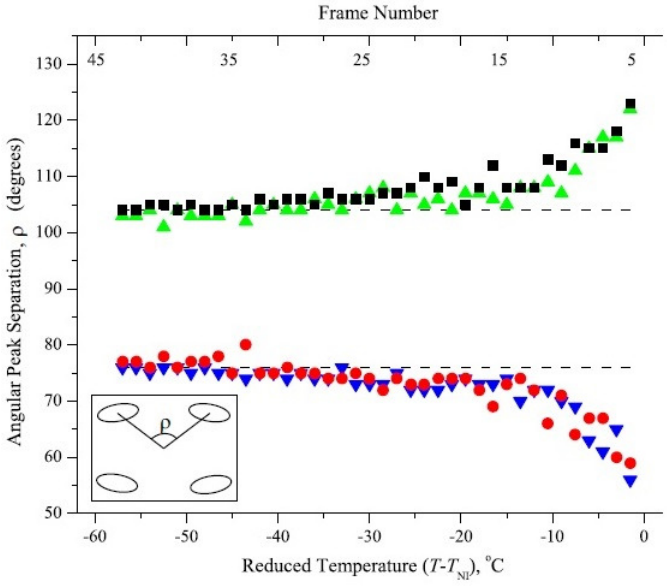

Figure 5.4: The angular separation of the four observed diffraction peaks as a function of temperature. Reproduced from reference[162] with permission of Europhysics Letters.

It appears that the measurement of both uniaxial and biaxial order parameters through the analysis of Raman scattering data may depend on whether or not the bend angle is taken into account, and if it is considered, whether it is assumed to be temperature dependent or not. Specifically, the measurement of biaxial order parameters, and the difficulties of fitting such a large number of variables, implies that confirmation of phase biaxiality for this bent-core mesogen through analysis of the available experimental data is still not definitively possible.

5.2.2 Cybotactic cluster model

Many of the unique features of bent-core nematic systems can be explained by the presence of nanometer sized cybotactic clusters embedded within the nematic phase

(N_{cyb}).[65,66,68,102,165,181] These cybotactic clusters typically consist of a few hundred molecules and are characterized by a higher degree of positional and orientational order, with the BCMs adopting a layered (usually tilted) arrangement denoted as N_{cybC}.[66] Within these clusters local biaxiality can occur. The specific patterns obtained from X-ray diffraction (XRD) investigations are often used to identify cybotactic nematic phases in bent-core systems, and therefore it is useful to compare the XRD results for the nematic phase of the C5-Ph-ODBP-Ph-OC12 system with the results for other bent-core nematics.

X-ray scattering produces two sets of diffuse peaks; the first set result from the wide angle X-ray scattering (WAXS) corresponding to the side-to-side correlations of molecules, and the second set results from the small angle X-ray scattering (SAXS), which corresponds to the end-to-end correlation of the molecules. According to Devries, if the SAXS is much greater in intensity than the WAXS then this indicates a cybotactic nematic phase composed of small smectic clusters.[55] In ordinary nematics, the small angle scattering is lower or equivalent to the WAXS. Although small smectic clusters can occur as pretransitional phenomena at the N-Sm transition, the cybotactic structure remains an intrinsic phase structure for many bent-core nematics, regardless of the presence or absence of an underlying smectic phase.[64,102] A two-spot SAXS pattern which is greater in intensity than the WAXS, is indicative of cybotactic nematics with a normal layered SmA-like structure within the clusters (N_{cybA}).[67]

Bent-core nematics, including C5-Ph-ODBP-Ph-OC12, usually show an angular peak separation (or splitting) of the small angle diffraction pattern into a four peak diffraction structure (or four-spot pattern) in the nematic phase. There are two explanations for the origin of the small angle splitting:

- The origin of this splitting has been attributed to the tilted organization of bent-core mesogens (BCMs) in SmC type clusters (the structure factor).[68,179,180]
- The splitting is due to the distinct bent shape of the mesogen and the concentration of electron density along each of the molecular arms (the form factor) as well as the structure factor of an anisotropic short-range, positional correlation function.[2]

The first explanation has been deduced from examining the relevant XRD structural parameters (interlayer spacing, d and the splitting angle, $\Delta\chi$) related to the four spot pattern. If these parameters change with temperature and $\Delta\chi$ /2 is equal or close to the mesogens tilt angle β, calculated as $\cos\beta_{\text{cal}} = d/L_{\text{mol}}$, where L_{mol} = molecular length, then this supports the hypothesis that the small angle splitting is due to the BCMs variable tilt in the clusters.[66,67] The cybotactic (N_{cybC}) model is generally accepted as the most credible description of the nematic phase of BCMs, in particular for the nematic phase of ODBP mesogens.[67,179,181]

Analysis of the SAXS data for the C5-Ph-ODBP-Ph-OC12 system in the nematic phase showed a slowly evolving four-peak scattering pattern with decreasing temperature (see Figure 5.5).[162] However, the resolution into four distinct peaks did not occur until T-$T_{\text{NI}} = -30$ K, after which further cooling resulted in an increased intensity of the peaks. The maximum of the small angle scattering corresponded to a interlayer spacing of $d = 43$ Å, which showed no temperature dependence and which the authors state approximates to the molecular length. The splitting of the small angle scattering, $\Delta\chi$ was $\approx 76°$, remaining almost constant throughout the nematic range except close to the T_{NI} temperature (T-$T_{\text{NI}} = 0$ to $-15°$) where there was an increase in $\Delta\chi$ values with decreasing temperature. It can be deduced that $\Delta\chi$ would need to be significantly less than 76° if SmC-type clusters were present, and there was a direct relationship between the tilt angle (calculated according to the equation $\cos\beta_{\text{cal}} = d/L_{\text{mol}}$) of molecules in the clusters and the measured value, $\Delta\chi/2$.

In contrast to C5-Ph-ODBP-Ph-OC12, the SAXS results for closely related but symmetrical ODBP-OC4, ODBP-OC12 and ODBP-C7 mesogens all displayed the four-spot pattern, but showed a strong temperature dependence of the structural parameters, d and $\Delta\chi$ in the nematic phase.[64,67] The molecular length remained almost constant, and $\Delta\chi/2$ was equal to the tilt angle, β in the cybotactic clusters. The SAXS data for ODBP-C7 suggested a structural transition from the tilted N_{cybC} at low temperature to the untilted N_{cybA} at high temperature, as this was associated with a gradual evolution of the 4-spot pattern into the 2-spot pattern with increasing temperature. Analysis of the SAXS data also provided values for

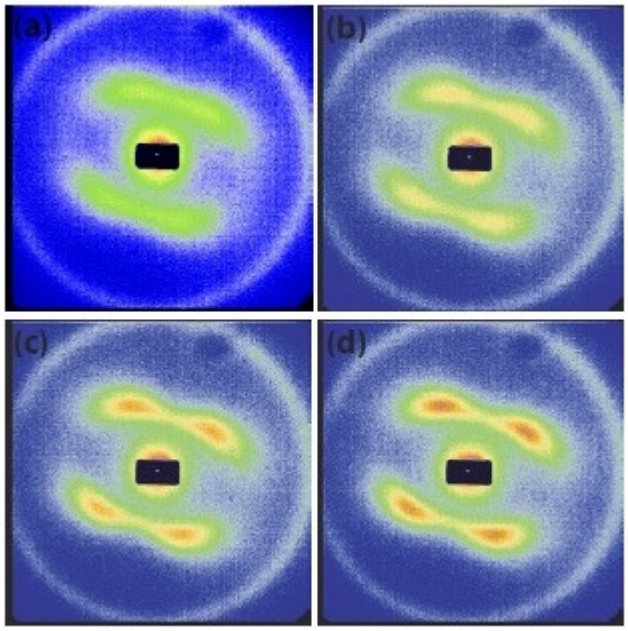

Figure 5.5: The SAXs patterns for C5-Ph-ODBP-Ph-OC12 for reduced temperatures ($T - T_{\mathrm{NI}}$): (a) -15 K; (b) -30 K; (c) -45 K and (d) -53 K. Reproduced from reference[162] with permission of Europhysics Letters.

the longitudinal and transversal correlation lengths, which showed weak temperature dependence and corresponded to a cluster size of ≈ 300 molecules for each mesogen. The SAXS intensity was also considerably stronger than the WAXS for each compound, indicating the presence of a $\mathrm{N_{cyb}}$ phase and supporting Devries' conclusions.[64,67] Both ODBP-OC12 and ODBP-C7 displayed an underlying SmC phase, whereas ODBP-OC4 did not, suggesting that the origin of the cybotactic clusters is not necessarily related to pretransitional fluctuations due to a N-to-SmC phase transition.

The lack of a strong temperature dependence of the SAXS structural parameters has been proposed as an argument for dismissing the cybotactic model for the nematic phase of the C5-Ph-ODBP-Ph-OC12 system.[100] However, recently the SAXS measurements for a different bent-core nematic, also lacking an underlying smectic phase, showed the structural parameters to be temperature independent, but with the presence of small, distinct SmC-like clusters of ≈ 60 molecules with an average of two layers in each cluster. These persisted within the nematic phase range and their average dimensions were only weakly temperature dependent.[30]

Comparisons can also be made with an in depth XRD study of the nematic phase of a series of 4-cyanorescisorcinol bent-core mesogens with varying length terminal alkyl chains (n = 2 to 14) conducted by Keith *et al.*[102] In common with the C5-Ph-ODBP-Ph-OC12 mesogen, all possess a bend angle of $\approx 140°$. Analysis of the SAXS patterns for the long chain compounds (n = 10 to 14) showed a strong 4-spot pattern with the splitting of the small angle scattering in the range of $\Delta\chi$ = 30-36° as well as a distinct temperature dependence of both d and $\Delta\chi$ in the nematic phase. It was proposed that the molecules were organized in relatively large SmC like clusters consisting of $\approx$ 500 molecules with a shallow tilt angle of $\beta_{cal} \approx$ 15-18°, and hence it was deduced that the structure factor was the main feature in determining the resulting SAXS patterns.

For compounds with a medium chain length (n = 6 to 9) there was a continuous decrease in $\Delta\chi$ with increasing chain length, and for each compound there was a large splitting and low intensity at the nematic high temperature region, but a smaller splitting with higher intensity in the lower nematic temperature region. A strong temperature dependence of cluster size was also found, indicating a temperature dependent structural transformation in the nematic phase. According to Keith *et al.*, the 4-spot pattern and associated splitting angle for the medium chain compounds were neither directly related to the bend angle (form factor) or the tilt of the molecules in the clusters (structure factor) but instead to a complex relationship between both of these features.

The small angle splitting for the short chain compounds (n = 2 to 4) showed the largest values, with $\Delta\chi$ occurring in the range of 70-80°. Unlike the medium and longer chain compounds, these displayed an increase in $\Delta\chi$ with decreasing temperature, but similar to the medium/long chain compounds there was a increase in the d value with decreasing temperature. According to Archarya *et al.* and their XRD investigations of ODBP based mesogens, a $\Delta\chi$ value of $\approx 80°$ is directly related to a bend angle of 140° and the distinct orientations of the molecular arms (form factor).[2] Keith *et al.* therefore suggest that the splitting of the small angle for the short chain compounds may indeed be attributed to the bent molecular shape, as proposed by Acharya *et al.*, and not the tilted arrangement of molecules

in SmC-type clusters. In addition, the cluster size was small, corresponding to less than the molecular length in the longitudinal direction and 2-3 molecules in the transversal direction. The scattering intensity was also weak and hence these nematic phases were deemed to be ordinary nematic phases with only short range correlation between nearest neighbour molecules.

Analysis of the SAXS data for the C5-Ph-ODBP-Ph-OC12 system infers that there is a closer relationship between this system and the short chain compounds investigated by Keith *et al.*, in which case the form factor, and hence the bent molecular shape, would be the dominant feature in explaining the resulting 4-spot pattern. This is also suggested by Southern *et al.*, although they do not entirely rule out the possibility of cybotactic groups contributing to the observed diffraction patterns, and propose that further experiment and clarification are required. Unlike the short chain compounds investigated by Keith *et al.,* where the relatively rigid core of $\approx 140^{\circ}$ may impose itself on the overall molecular structure, the longer terminal chains of the C5-Ph-ODBP-Ph-OC12 mesogen would greatly increase the number of conformations adopted by this mesogen and consequently a bend angle of 140° would be relatively arbitrary.[162] In addition, cluster formation is considered to be mainly caused by the specific bent shape of the mesogens and the segregation of the alkyl chains.[102,170] A bent-core mesogen such as C5-Ph-ODBP-Ph-OC12 with one long aliphatic terminal chain, would therefore be expected to show cybotactic organization in the nematic phase.

Very recently, an interesting observation was made of the SAXS patterns of the cybotactic nematic phases of a number of 1,2,4-oxadiazole bent-core mesogens with medium length alkyl/alkoxy terminal chains.[160] In contrast to the symmetric 1,3,4-oxadiazoles and due to the different positions of the O and N atoms of the heterocyclic ring, these possess an asymmetric central dipole and a slightly wider bend angle. For these compounds, additional weak and diffuse scattering maxima were observed on the meridian in addition to the typical small-angle 4-spot pattern. This has been attributed to the space and time-averaging of cybotactic clusters formed by SmC ribbon segments on an oblique lattice, in which the molecules are aligned parallel to the field direction but with different tilt orientations in distinct

clusters. It was suggested that this type of organization can lead to the tilt angle of the molecules in the layers of the cybotactic clusters deviating from the measured splitting angle, and in most cases it was found that $\Delta\chi/2$ was slightly larger than the tilt β_{cal} calculated using the relation $\cos\beta_{\mathrm{cal}} = d/L_{\mathrm{mol}}$. The authors propose that this interpretation needs to be considered when analyzing the SAXS patterns of cybotactic nematics. This may also have implications for the interpretation of the SAXS patterns for the C5-Ph-ODBP-Ph-OC12 system.

5.3 Main objectives

The purpose of this study was to gain a better understanding of the nature and structure of the nematic phase of the C5-Ph-ODBP-Ph-OC12 system by comparing and contrasting the structure and molecular organization of C5-Ph-ODBP-Ph-OC12 with a more typical ODBP mesogen, C4-Ph-ODBP-Ph-C7. It was considered that this approach may help to explain the anomalous and interesting behaviour displayed by C5-Ph-ODBP-Ph-OC12, and included the following objectives:

- The calculation of uniaxial and biaxial orientational order parameters to make comparisons between the two systems, as well as comparing the simulated values with experimental values where possible.
- To understand the structural organization of C5-Ph-ODBP-Ph-OC12 by comparing and contrasting this with the more standard C4-Ph-ODBP-Ph-C7 system, through evaluation of radial distribution functions, analysis of molecular topologies and visual observations of the nematic phase.

5.4 Computational details

Full details of simulation methods are given in Chapter 3, 3.3 and Chapter 4, Section 4.3. The following relates specifically to the two ODBP mesogens. Two sets of simulations were performed with $N = 248$ molecules (C4-Ph-ODBP-Ph-C7 system) and $N = 256$ molecules (C5-Ph-ODBP-Ph-OC12 system). Each system was started from a disordered configuration at 550 K and then progressively cooled at 10 K

intervals with equilibration runs of at least 60 ns and production runs of between 120 and 180 ns. The results of the simulations relate to averaged values over the final 60 ns of production runs. Larger systems were also investigated at specific temperatures, by replicating the smaller systems twice in each direction to give system sizes of $N = 1984$ and $N = 2048$ molecules for the two mesogens. These were then re-equilibrated for 10 ns followed by production runs of a further 20 ns.

5.5 Results and Discussion

5.5.1 Visual Analysis

Figure 5.6 shows snapshots of the C4-Ph-ODBP-Ph-C7 system at 460 and 430 K. For clarity, only the simplified ODBP cores are shown. Different perspectives of the systems at each temperature indicate a broadly homogeneous nematic state, with long-range order of the molecular long axes, and no indication of smectic-like layers. This type of molecular organization was also apparent at 480 K and at 490 K with the latter representing the temperature immediately below the nematic to isotropic transition.

(a)

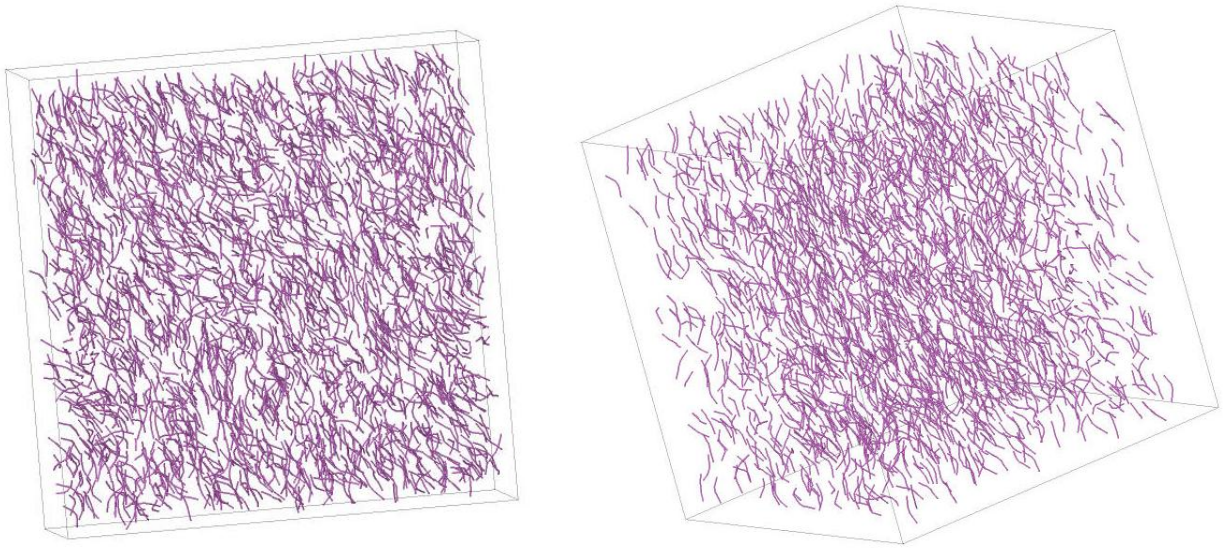

(b)

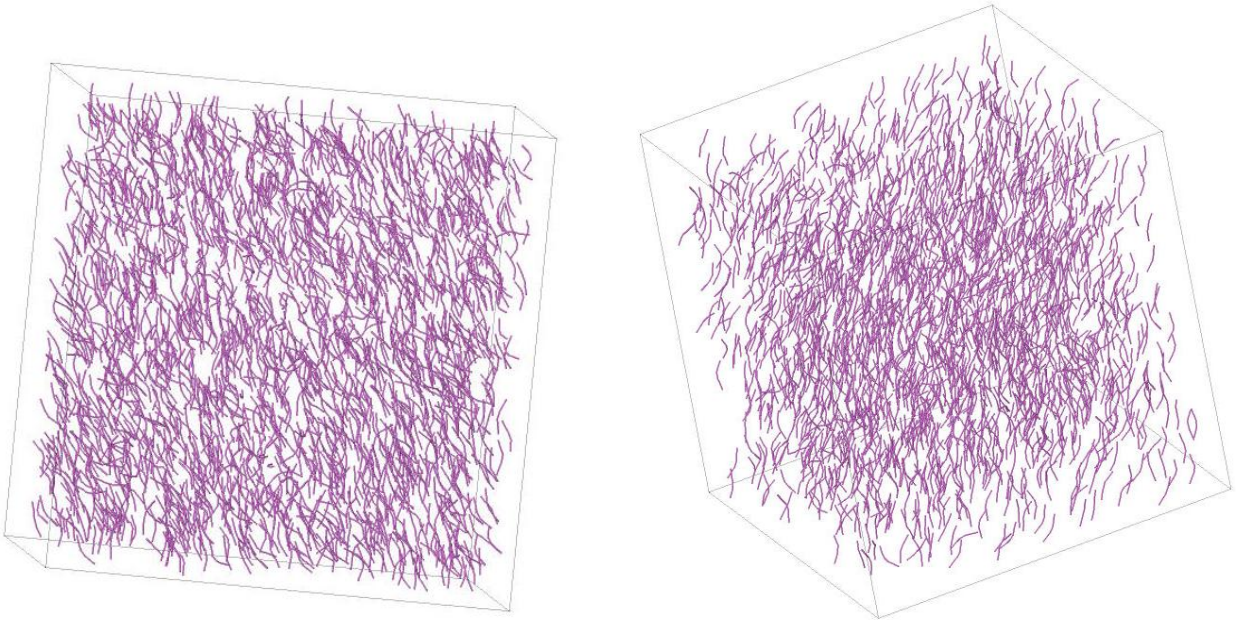

Figure 5.6: Snapshots of the C4-Ph-ODBP-Ph-C7 system showing a coarse-grained representation of the ODBP core structures only for $N = 1984$ molecules, (a) 460 K and (b) 430 K.

In contrast to C4-Ph-ODBP-Ph-C7, the C5-Ph-ODBP-Ph-OC12 system shows some differences in molecular organization. For example, at 480 K, representing the high nematic temperature range (see Figure 5.7a), the ODBP cores are slightly less evenly distributed than those of the C4-Ph-ODBP-Ph-C7 system, suggesting a small degree of segregation of the cores with respect to the alkyl tails. This segregation of the ODBP cores became more pronounced with decreasing temperature, and at 450 K culminated in the development of ribbon or wave like structures (see Figure 5.7b). At 430 K the molecular organization appears considerably more ordered, with distinct layers which appear distorted and splayed from certain perspectives (see Figure 5.8). It is possible that at this temperature, the system is exhibiting the expected DC phase which has been observed and characterized experimentally.[134] This may also suggest that above this temperature, at 450 K, some degree of pretransitional molecular organization is occurring with the initial development of distorted layer-like structures.

Although the two closely related ODBP mesogens display similar nematic-isotropic temperatures and broad nematic phases, visual inspection of the two systems suggests quite different and distinct molecular organizations. Visual analysis alone does not suggest any significant biaxial order (long-range order of the short axes as well as the long molecular axis) for either of the ODBP systems in their corresponding nematic phases.

(a)

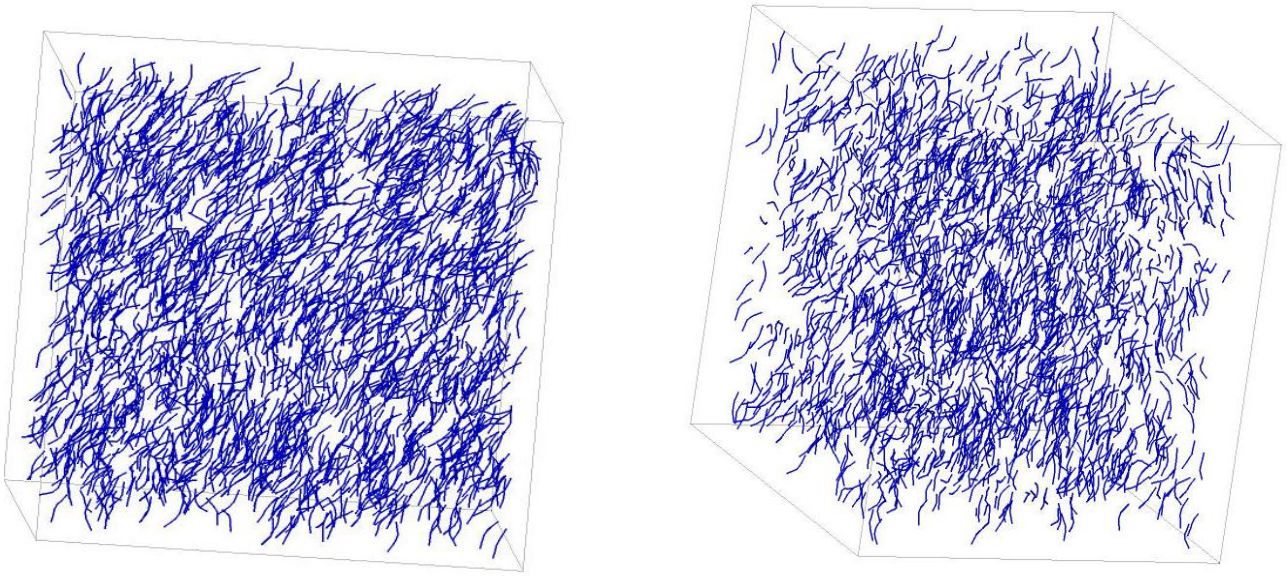

(b)

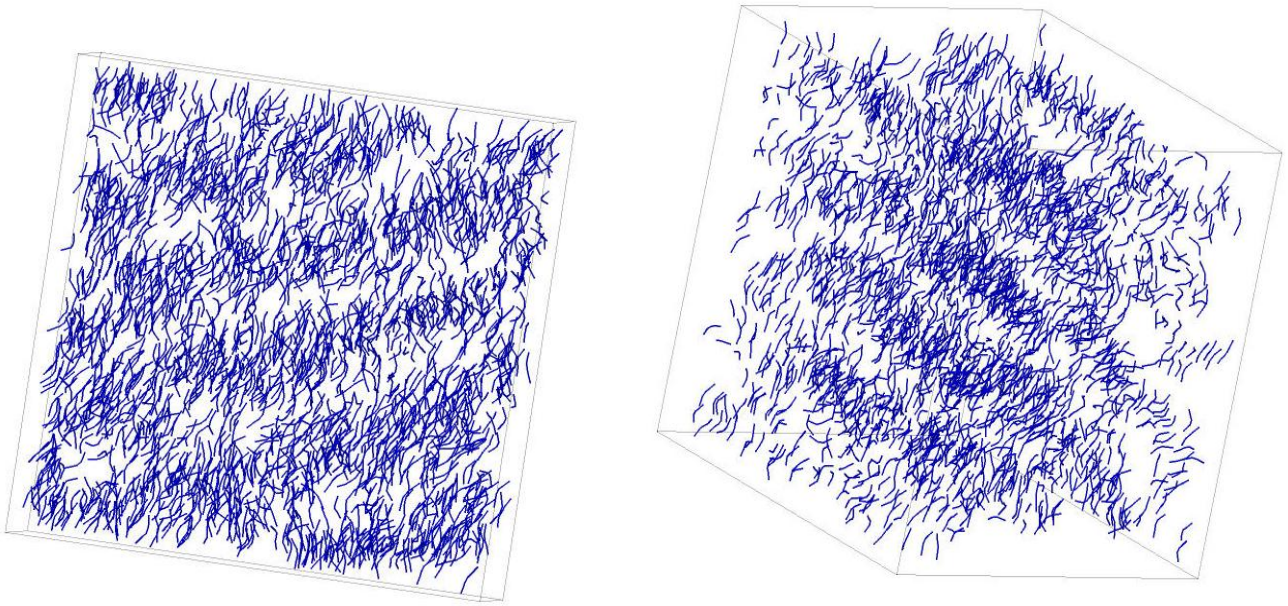

Figure 5.7: Snapshots of the C5-Ph-ODBP-Ph-OC12 system showing a coarse-grained representation of the ODBP core structures only for $N = 2048$ molecules, (a) 480 K and (b) 450 K.

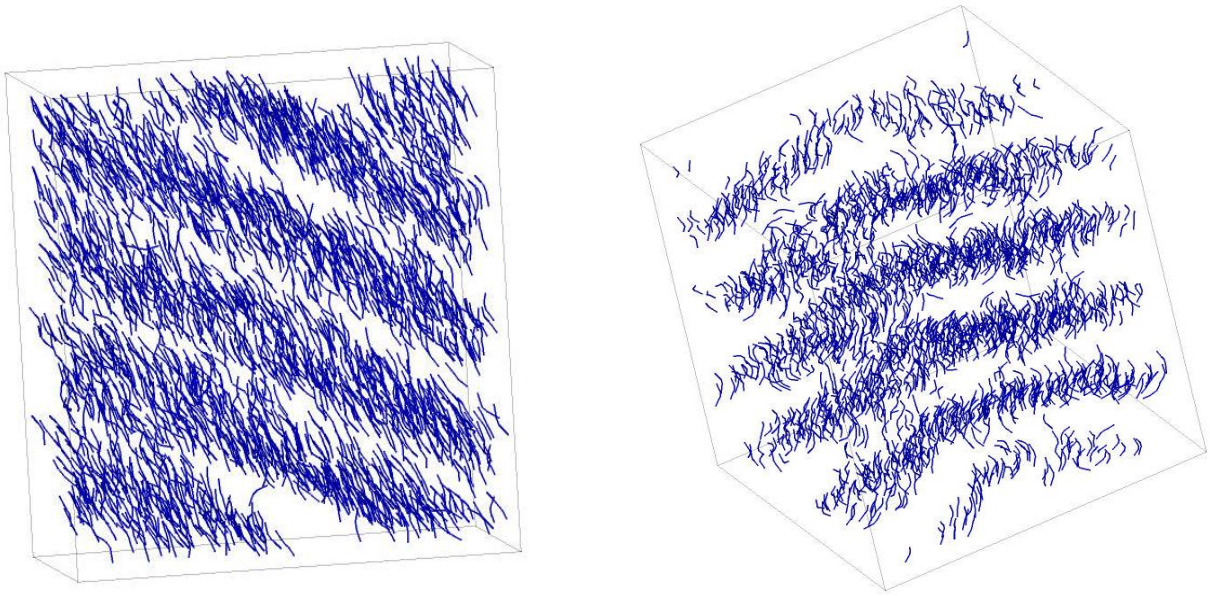

Figure 5.8: Snapshots of the C5-Ph-ODBP-Ph-OC12 system showing a coarse-grained representation of the ODBP core structures only at 430 K and for $N = 2048$ molecules.

5.5.2 Uniaxial orientational order in the nematic phase

C5-Ph-ODBP-Ph-OC12

In order to calculate the uniaxial and biaxial orientational order parameters, a set of orthogonal vectors representing the three molecular axes needed to be defined. Following the procedure developed in reference,[143] the molecular axes were defined as follows: (a) a set of orthogonal vectors representing the three principle axes of the molecule were obtained by diagonalizing the inertia tensor; (b) three orthogonal vectors were obtained for the aromatic core only, by calculating vectors running along the molecular arms up to the end of the outer phenyl ring and subtracting one arm vector from the other to obtain the long axis vector, and then summing them to obtain a vector along the short axis (generating a third vector for the second short axis from the cross product of the other axes). The latter definition of molecular axes was used in the majority of the calculations of the uniaxial and biaxial order parameters. However, in order to make comparisons with experimentally measured uniaxial order parameters, molecular reference axes parallel with the arms of the Ph-ODBP-Ph core (see Figure 5.9) were also used in a small number of calculations.

With a specific molecular axis chosen, the system director, **n**, is then obtained by evaluating the Q tensor which sums over all N molecules in the system. The largest eigenvalue of the Q tensor represents the uniaxial order parameter, P_2 and the corresponding eigenvector is the director, **n**. The uniaxial order parameter, P_4 was calculated as the fourth-rank Legendre polynomial (see Chapter 3 for full description of order parameters and equations).

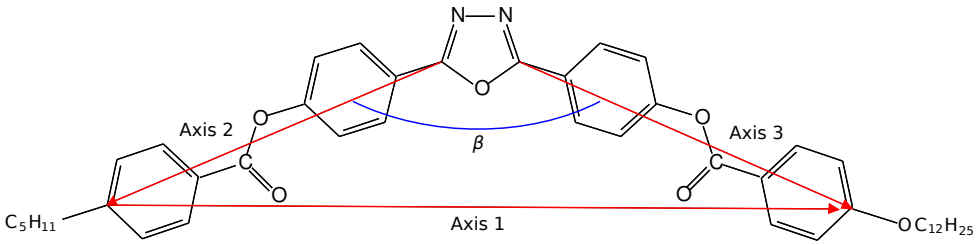

Figure 5.9: The chemical structure of C5-Ph-ODBP-Ph-OC12 showing the bend angle, β and molecular reference axes.

A number of issues concerning the interpretation of Raman scattering data and the measurement of orientational order in bent-core nematics were raised in Section 5.2.1. In particular, whether the inclusion of the molecular bend angle in the deduction of the order parameters is necessary, and if so whether the bend angle is temperature dependent or not.

Table 5.1 shows the average uniaxial order parameter, $\langle P_2 \rangle$, calculated for the different choices of molecular reference axis (see Figure 5.9). Reference axis 1 represents a vector parallel with the long axis of the Ph-ODBP-Ph core structure only, while reference axes 2 and 3 represent vectors parallel with the arms of the Ph-ODBP-Ph core. Figure 5.10a shows the values plotted as a function of temperature for ref. axis 1 and ref. axis 2 (the core arm vector adjacent to the C5 tail). Results for the uniaxial order parameters are shown for the $N = 256$ system only, as system size effects in reproducing T_{NI} through the monitoring of P_2 values for ref. axis 1, were found to be very small (see Chapter 4, Section 4.6.1).

Table 5.1: The average uniaxial order parameter, $\langle P_2 \rangle$, for C5-Ph-ODBP-Ph-OC12 and for the three different choices of molecular reference axis ($N = 256$).

T / K	$\langle P_2 \rangle$ Axis 1	$\langle P_2 \rangle$ Axis 2	$\langle P_2 \rangle$ Axis 3
520	0.2377	0.1947	0.2036
510	0.3405	0.2743	0.2922
500	0.5148	0.4150	0.4367
490	0.6274	0.5032	0.5350
480	0.6841	0.5430	0.5778
470	0.6948	0.5595	0.5930
460	0.7646	0.6158	0.6535
450	0.8128	0.6496	0.7037

Upon cooling into the nematic phase, $\langle P_2 \rangle$ for ref. axis 1 increases from ≈ 0.2 to 0.8 with decreasing temperature, whereas $\langle P_2 \rangle$values for ref. axes 2 and 3 are systematically lower compared with ref. axis 1. Interestingly, the $\langle P_2 \rangle$ values for ref. axis 3, (the core arm adjacent to the OC12 terminal chain) are marginally higher (≈ 0.03 to 0.05) than those for ref. axis 2, (the core arm adjacent to the shorter alkyl tail), indicating that the longer arm of the bent-core mesogen is slightly more ordered than the shorter arm.

The results for $\langle P_4 \rangle$ for the different choices of molecular reference axis are given in Table 5.2 and a plot of the temperature dependence of $\langle P_4 \rangle$ for ref. axis 1 and 2 is shown in Figure 5.10b. Systematically higher $\langle P_4 \rangle$ values are found for ref. axis 1 compared with those found for ref. axis 2 and ref. axis 3. The latter two representing the Ph-ODBP-Ph core arm vectors, again show that the longer arm is slightly more ordered compared with the shorter arm, with ref. axis 3 displaying marginally greater $\langle P_4 \rangle$ values than those for ref. axis 2.

Table 5.2: The average uniaxial order parameter, $\langle P_4 \rangle$ for C5-Ph-ODBP-Ph-OC12 and for the three different choices of molecular reference axis ($N = 256$).

T / K	$\langle P_4 \rangle$ Axis 1	$\langle P_4 \rangle$ Axis 2	$\langle P_4 \rangle$ Axis 3
520	0.0408	0.0224	0.0276
510	0.0897	0.0458	0.0563
500	0.1681	0.0848	0.1001
490	0.2382	0.1312	0.1620
480	0.3188	0.1559	0.1910
470	0.3487	0.1697	0.2069
460	0.4323	0.2061	0.2566
450	0.5254	0.2422	0.3223

The results from the simulations are compared with the experimental measurements of $\langle P_{200} \rangle$ and $\langle P_{400} \rangle$ from the Raman scattering study described in Section 5.2.1, where two different models were used to analyze the data (see Figure 5.10c). It can be observed that systematically lower order parameters are obtained for the model employing a Raman probe originating from one arm only, and hence neglecting the effect of the bend angle, compared with those obtained from two probes (one from each arm and summing the contributions from each arm). The authors suggest that accounting for the molecular bend angle in the analysis of the data is necessary in the analysis of the Raman scattering data, and have also reported $\langle P_{200} \rangle$ and $\langle P_{400} \rangle$ for five more oxadiazole compounds using this model, which they claim are in excellent agreement with theory.[73] Some caution needs to be applied in making direct comparisons with the experimental results for C5-Ph-ODBP-Ph-OC12 and the results from the simulations, due to the fitting procedure employed and the explicit use of a fixed bend angle parameter in one of the models in the Raman scattering study. However, the results from the simulations in Figure 5.10a and Figure 5.10b follow a similar trend, in that systematically lower values are found when calculating order parameters when choosing a molecular reference axis along one arm only, compared with those calculated for a molecular reference axis parallel with the mesogen core derived from vectors parallel with the arms of the core. In addition, the magnitude of the order parameters from the simulations are broadly similar to those obtained from the Raman scattering study.

In contrast to these results (both from experiment and simulations) Park *et*

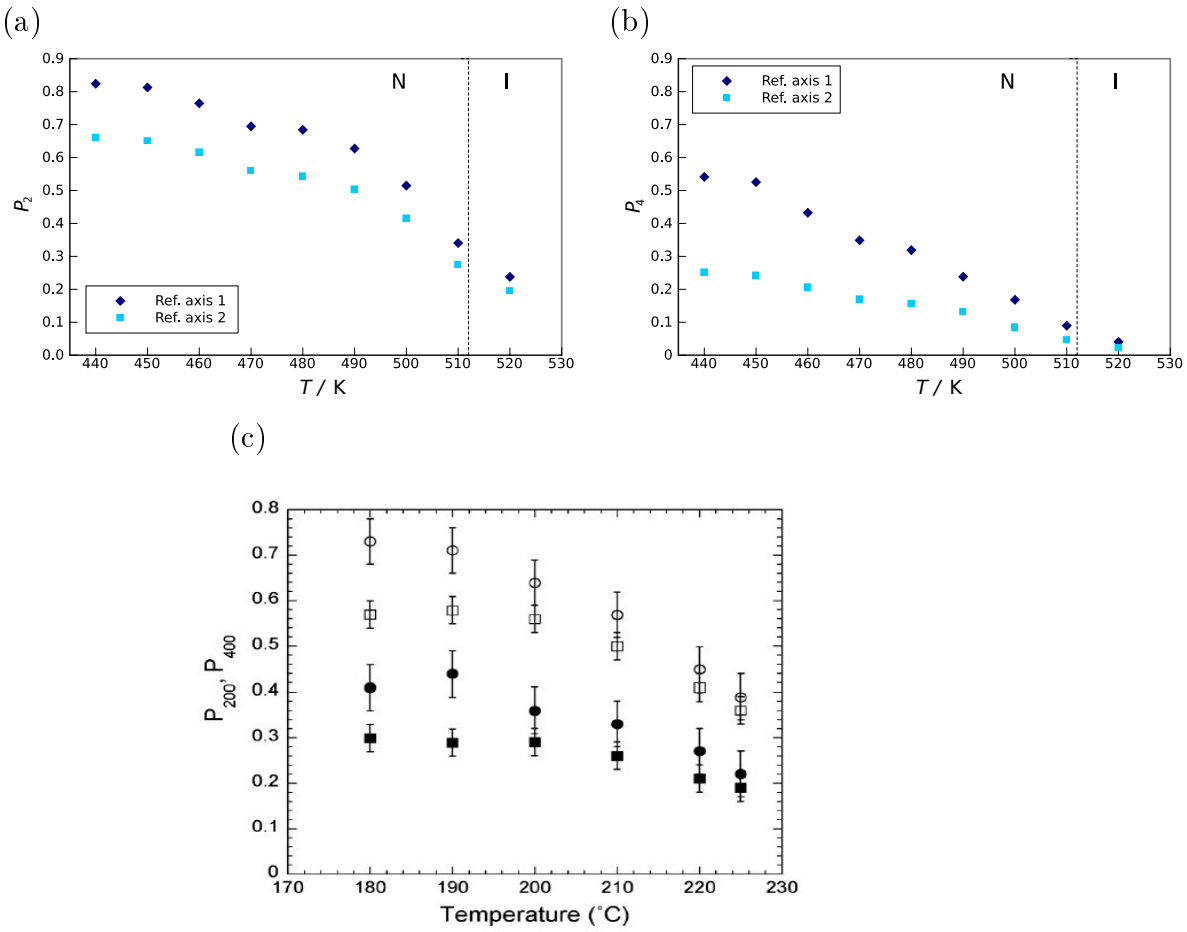

Figure 5.10: The average uniaxial order parameters as a function of temperature for C5-Ph-ODBP-Ph-OC12 and the $N = 248$ system; (a) $\langle P_2 \rangle$ and (b) $\langle P_4 \rangle$ (c) Experimentally deduced uniaxial order parameters $\langle P_{200} \rangle$ (open symbols) and $\langle P_{400} \rangle$(filled symbols). The circles result from a model that includes a 140° molecular bend angle (two scatterers) and the squares are the systematically lower values obtained when the bend angle is not included. Reproduced from reference[72] with permission of the American Physical Society.

al.'s Raman scattering measurements of order parameters for the A131 bent-core mesogen show identical $\langle P_{200} \rangle$ values regardless of whether the probe originates from one arm or two arms.[140] They suggest that consideration of the bend angle in the measurement of order parameters is not important and that rotational freedom in the nematic phase would average out the influence of the bent shape, and even if it was important, then the influence of temperature on the value of the angle would need to be tested.

Figure 5.11a shows the average bend angle for C5-Ph-ODBP-Ph-OC12 calculated from the simulations at temperatures ranging from just above T_{NI} and throughout the nematic range. The bend angle represents an angle between two vectors parallel with the arms of the Ph-ODBP-Ph core only (see Figure 5.9). The results show that in the nematic phase, the mean bend angle increases by as little as 2.6° with decreasing temperature. In addition, the distribution of angles are narrow and broadly similar for selected simulated temperatures, with peak values occuring at ≈ 140°, (see Figure 5.11b). These results suggest that the assumption of a temperature independent (fixed bend angle) in the analysis of Raman scattering data for the C5-Ph-ODBP-Ph-OC12 system in[162] is probably justified.

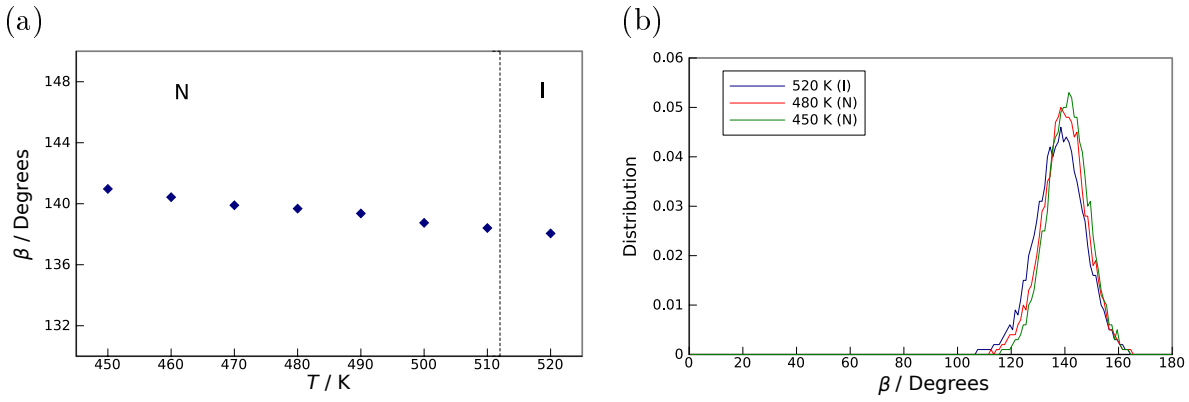

Figure 5.11: (a) The average bend angle, β of the Ph-ODBP-Ph core as a function of temperature for C5-Ph-ODBP-Ph-OC12. (b) Distribution of the bend angle, β in the simulated phases.

C4-Ph-ODBP-Ph-C7

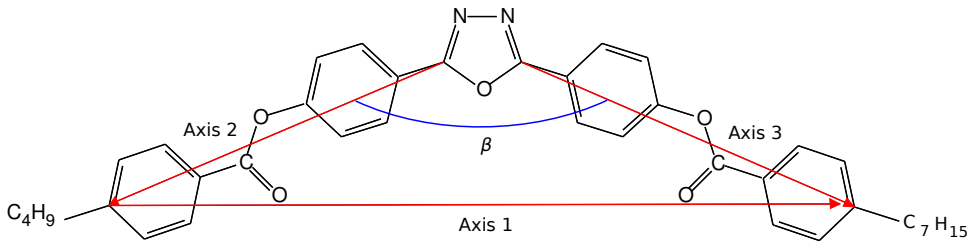

Figure 5.12: The chemical structure of C4-Ph-ODBP-Ph-C7 showing the bend angle, β and molecular reference axes.

Table 5.3 shows the average uniaxial order parameters, $\langle P_2 \rangle$, as a function of temperature for the C4-Ph-ODBP-Ph-C7 system for the three different choices of molecular reference axis (see Figure 5.12). Figure 5.13a shows the values plotted as a function of temperature for ref. axis 1 and ref. axis 2 (one core arm vector) only. Results for the uniaxial order parameters are shown for the $N = 248$ system only, as system size effects in reproducing T_{NI} through the monitoring of P_2 values for ref. axis 1, were found to be very small (see Chapter 4, Section 4.6.1).

Table 5.3: The average uniaxial order parameter, $\langle P_2 \rangle$ for C4-Ph-ODBP-Ph-C7 and for the three different choices of molecular reference axis ($N = 248$).

T / K	$\langle P_2 \rangle$ Axis 1	$\langle P_2 \rangle$ Axis 2	$\langle P_2 \rangle$ Axis 3
520	0.1553	0.1307	0.1325
510	0.1636	0.1381	0.1397
500	0.2357	0.1943	0.1982
490	0.4929	0.3992	0.4111
480	0.6109	0.4937	0.5101
470	0.6703	0.5459	0.5561
460	0.6781	0.5516	0.5669
450	0.7274	0.5928	0.6067
440	0.7274	0.5904	0.6096
430	0.7683	0.6279	0.6403

As with C5-Ph-ODBP-Ph-OC12, systematically lower values are found for molecular ref. axis 2 and 3 (core arm vectors) compared with those for ref. axis 1 (the vector parallel with the Ph-ODBP-Ph core long axis). The magnitude of $\langle P_2 \rangle$ in the nematic range is broadly similar to that found for C5-Ph-ODBP-Ph-OC12, except

at lower temperatures where values are marginally lower. The $\langle P_2 \rangle$ values for ref. axis 3 (attached to the core arm adjacent to the longer terminal chain), are slightly greater (≈ 0.01 to 0.02) than those for ref. axis 2, although the difference is very small and not as great as that observed for C5-Ph-ODBP-Ph-OC12.

The calculated $\langle P_4 \rangle$ values shown in Table 5.4 again display systematically lower values for the core arm axes compared with those for ref. axis 1. However, $\langle P_4 \rangle$ calculated for C4-Ph-ODBP-Ph-C7 displays an initial increase after which values level off and are consistently lower than those for C5-Ph-ODBP-Ph-OC12 (see Figure 5.13b and $\langle P_4 \rangle$ plotted for ref. axis 1 and 2 only). The order parameter, $\langle P_4 \rangle$, depends on higher powers of the cosine of the angle, ϕ (the angle between the molecular reference axis and the director, $\mathbf{n}$) and is thus more sensitive to molecular fluctutations.

Table 5.4: The average uniaxial order parameter, $\langle P_4 \rangle$ for C4-Ph-ODBP-Ph-C7 and for the three different choices of molecular reference axis ($N = 248$).

T / K	$\langle P_4 \rangle$ Axis 1	$\langle P_4 \rangle$ Axis 2	$\langle P_4 \rangle$ Axis 3
520	0.0145	0.0101	0.0075
510	0.0216	0.0140	0.0138
500	0.0428	0.0250	0.0238
490	0.1434	0.0720	0.0812
480	0.2538	0.1233	0.1426
470	0.3069	0.1527	0.1628
460	0.3196	0.1596	0.1734
450	0.3714	0.1852	0.1985
440	0.3753	0.1837	0.2051
430	0.4357	0.2146	0.2326

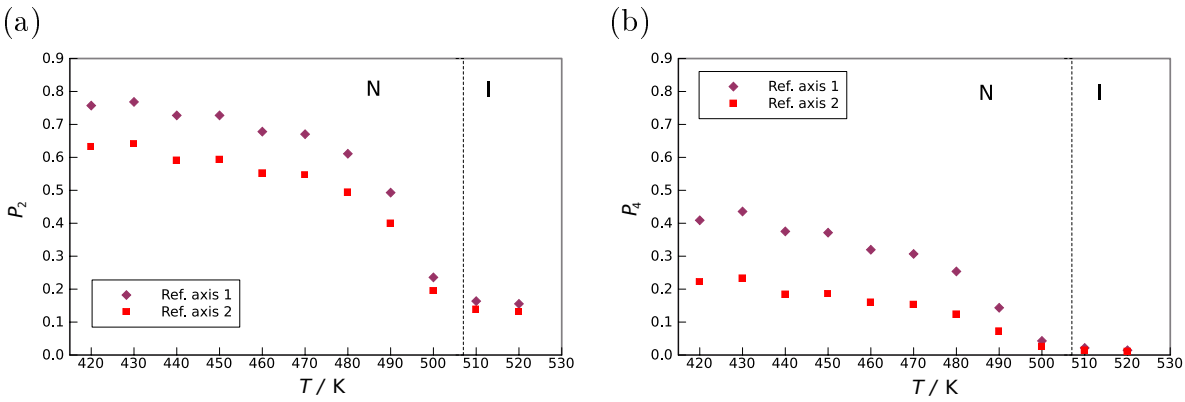

Figure 5.13: The average uniaxial order parameters as a function of temperature for C4-Ph-ODBP-Ph-C7 and $N = 248$ system; (a) $\langle P_2 \rangle$ and (b) $\langle P_4 \rangle$.

A literature search has not revealed any experimentally measured uniaxial order parameters for C4-Ph-ODBP-Ph-C7. However, comparisons with $\langle P_{200} \rangle$ and $\langle P_{400} \rangle$ determined using PRS for a number of other ODBP mesogens (Figure 9 in ref.[73]) indicate that $\langle P_2 \rangle$ values from the simulations for molecular ref. axis 1 of the C4-Ph-ODBP-Ph-C7 mesogen lies within the range of experimentally obtained $\langle P_{200} \rangle$ values for these mesogens. The experimentally determined $\langle P_{400} \rangle$ for this class of ODBP mesogens showed greater variation compared with $\langle P_{200} \rangle$, and within this context, $\langle P_4 \rangle$ for ref. axis 1 for C4-Ph-ODBP-Ph-C7 appears in the low range of the experimental values.

The average bend angle for C4-Ph-ODBP-Ph-C7 (measured as the angle between two vectors parallel with the Ph-ODBP-Ph core, as for C5-Ph-ODBP-Ph-OC12) was largely temperature independent throughout the nematic phase, showing a small increase from 137.6° (500 K) to 140.0°(430 K) a difference of 2.4°(see Figure 5.14a). There is a very subtle difference in the shape of the graph shown in Figure 5.14a, compared with that plotted for the C5-Ph-ODBP-Ph-OC12 system (see Figure 5.11a). The average bend angle for C4-Ph-ODBP-Ph-C7 appears to stabilise to $\approx 140°$ in the mid to lower nematic temperature range, whereas a very slightly steeper gradient is observed for the C5-Ph-ODBP-Ph-OC12 system with decreasing temperature. The distribution of bend angles for C4-Ph-ODBP-Ph-C7 shown in Figure 5.14b for selected temperatures show peak values at $\approx 140°$ in the nematic phase whereas for C5-Ph-ODBP-Ph-OC12 there is a small shift to a peak

value of $\approx 142°$ in the low temperature nematic range (see Figure 5.11b). This may be indicative of the influence of the terminal chains, with the specific terminal chains of the C5-Ph-ODBP-Ph-OC12 mesogen exerting a small effect on the central Ph-ODBP-Ph core bend angle. However, the overall differences between the two systems remain rather imperceptible, indicating that a temperature independent bend angle can be assumed in the measurement of order parameters for both mesogens.

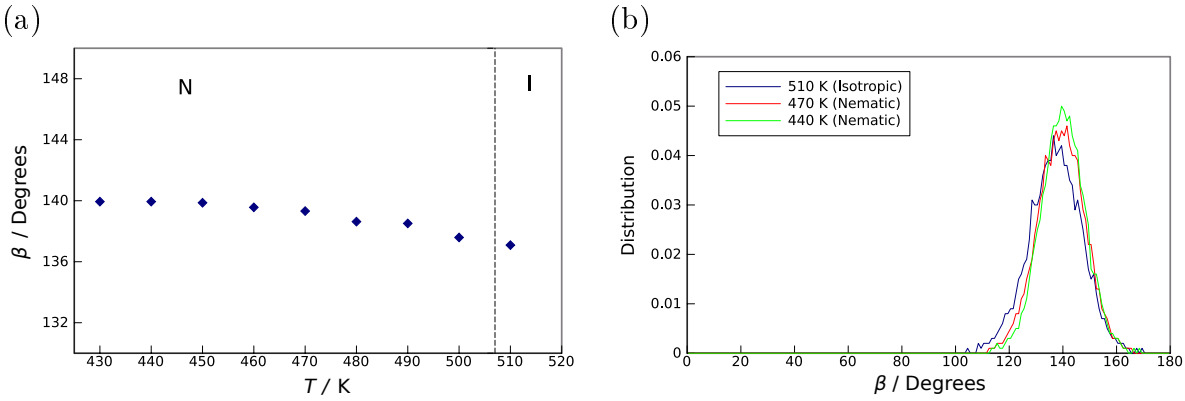

Figure 5.14: (a) The average bend angle, β of the Ph-ODBP-Ph core as a function of temperature for C4-Ph-ODBP-Ph-C7. (b) Distribution of the bend angle, β in the simulated phases.

5.5.3 Biaxial orientational order parameters in the nematic phase

C5-Ph-ODBP-Ph-OC12

The *intrinsic* phase biaxial order parameters, $\langle Q_{22}^2 \rangle$, calculated as mean values over the last 60 ns of production runs for each temperature for the C5-Ph-ODBP-Ph-OC12 system are shown in Figure 5.15a. Positive values for $\langle Q_{22}^2 \rangle$ imply that the molecular x and y axes are on average orientated closer to their corresponding X and Y axes of the laboratory system than vice-versa (i.e Y and X)[135] (see Chapter 3 for a full definition and equations for biaxial order parameters). The results are given for a set of orthogonal molecular axes representing the Ph-ODBP-Ph core only (see method (b) for axis selection in Section 5.5.2) as the results for the three principle inertia axes did not differ significantly, implying that the biaxiality of the core is imposed on the molecule as a whole, as was the case in the atomistic simulations of

ODBP-Ph-C7.[143]

(a)

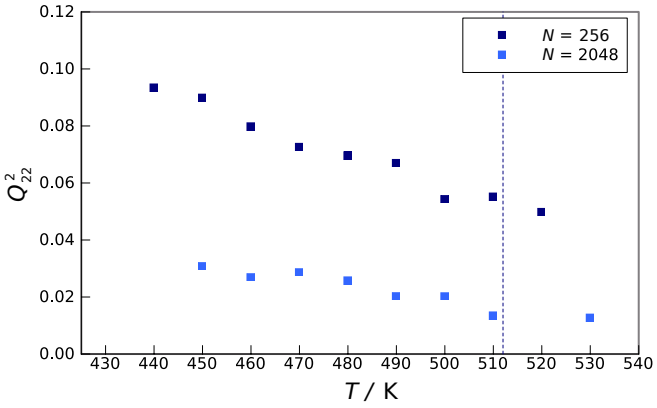

(b)

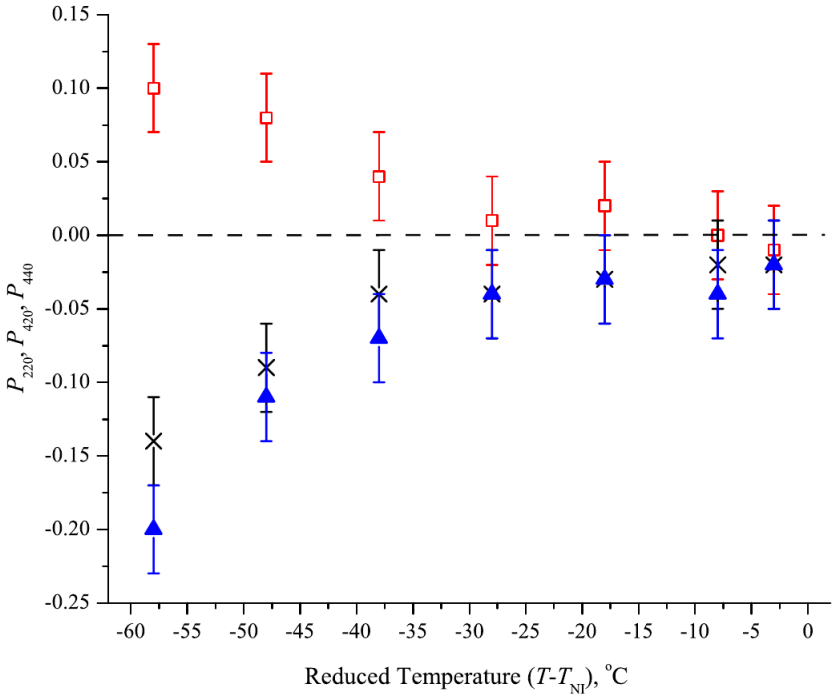

Figure 5.15: (a) The average biaxial order parameters for the C5-Ph-ODBP-Ph-OC12 system and $N = 256$ and $N = 2048$ systems. (b) Experimentally deduced biaxial order parameters. The red open squares, $\langle P_{220} \rangle$ are compared with simulated $\langle Q_{22}^2 \rangle$ values discussed in the text. Reproduced from reference[162] with permission of Europhysics Letters.

Overall, the measured *intrinsic* biaxiality is small, in particular for the $N = 2048$ system. The results for the $N = 256$ system do indicate a small degree of orientational order of the short axis with decreasing temperature. In particular, the magnitude of these values in the low temperature regime are broadly similar to

$\langle P_{220} \rangle$ values deduced from the Raman scattering study described in Section 5.2.1, where at 30 K below the isotropic to nematic temperature the calculated biaxial order parameter increases from approximately 0.05 to 0.1. It was proposed by the authors that this material exhibits a uniaxial to biaxial phase transition at this temperature. The Raman scattering study was based on a model that involved summing the electric field contributions from both arms, using a fixed bend angle parameter of 140°, as well as a number of additional fitting parameters. Some caution is therefore required in making direct comparisons with these results and those from the simulations.

Although not shown in Figure 5.15a, at 430 K there was a significant increase in the magnitude of $\langle Q_{22}^2 \rangle$ to 0.22. [This point is not shown in Figure 5.15a as the temperature is outside the nematic range and its inclusion would distort the scale of the graph and make comparisons with the$\langle Q_{22}^2 \rangle$ values in the nematic phase for other ODBP derivatives difficult]. This suggests a phase transition occurred into an underlying, more structured phase between 440 and 430 K. This also coincides with the obviously more ordered structure noted in the visual analysis at 430 K (seen in Figure 5.8), which may represent the DC phase characterized by experimental studies.

C4-Ph-ODBP-Ph-C7

The $\langle Q_{22}^2 \rangle$ values for the C4-Ph-ODBP-Ph-C7 system in the nematic phase are shown in Figure 5.16. The magnitude and rate at which $\langle Q_{22}^2 \rangle$ increases with decreasing temperature for the small system size ($\approx$ 0.05 to 0.07) is not as great as that observed for the C5-Ph-ODBP-Ph-OC12 system ($\approx$ 0.05 to 0.1). As with C5-Ph-ODBP-Ph-OC12, there is a marked reduction in the magnitude of $\langle Q_{22}^2 \rangle$ for the larger system size.

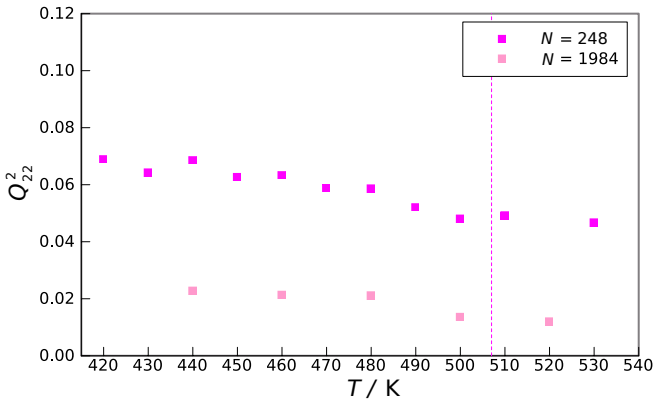

Figure 5.16: The average biaxial order parameters for the C4-Ph-ODBP-C7 system and $N = 248$ and $N = 1984$ systems.

There are no experimentally derived biaxial order parameters for C4-Ph-ODBP-Ph-C7 to make any direct comparisons with. However, nematic phase biaxiality has been investigated by Nagaraj *et al.* for a closely related symmetrical mesogen (ODBP-Ph-C7) using polarized IR spectroscopy.[135] In this study, two vibrational modes and their corresponding dipoles, parallel and perpendicular to the long axis of the mesogen core, were used to calculate the biaxial order parameters. The effect of an external electric field and an aligning force (rubbing of the substrates of the cell) on the magnitude of the biaxial order parameters were also examined. In the absence of an electric field and aligning force, the intrinsic biaxiality was found to be small (≈ 0.06) and comparable with the results found for the C4-Ph-ODBP-Ph-C7 small system in the current work. The authors suggested that in the absence of an aligning force and/or electric field, the low elastic constant involved in the rotation of the short axis and large enough fluctuations destroy any spontaneous long-range alignment of the short axis, so that only short-range local biaxial and polar ordering is possible in the nematic phase.

For both ODBP mesogens, the calculated $\langle Q_{22}^2 \rangle$ values are slightly lower than those obtained from the only other known fully atomistic simulation of an ODBP mesogen (ODBP-Ph-C7)[143] which employed the same criteria for assigning molecular orientation. The authors calculated $\langle Q_{22}^2 \rangle$ values of ≈ 0.09 to 0.11 as a function of decreasing temperature for a system of 256 molecules in the nematic phase. These latter values are also greater than those deduced from polarized IR spectroscopy for

ODBP-Ph-C7 described above.

Finally, both ODBP systems show a reduction in $\langle Q_{22}^2 \rangle$ for the large systems when compared with the small ones, indicating some degree of system size dependence. This is to be expected, as small systems magnify the influence of fluctuations in order. However, the $\langle Q_{22}^2 \rangle$ values for C5-Ph-ODBP-Ph-OC12 still maintain slightly higher values than those for C4-Ph-ODBP-Ph-C7 throughout the nematic range. System size effects alone cannot explain the greater rate of increase in $\langle Q_{22}^2 \rangle$ with decreasing temperature for C5-Ph-ODBP-Ph-OC12 compared with that for C4-Ph-ODBP-Ph-C7 for the small systems. In addition, the results from the current study supports the general hypothesis that the experimentally observed nematic biaxiality in bent-core mesogens is local as opposed to macroscopic. The simulation box sizes for the small systems were $\approx$ (63 Å)^3 and (68 Å)^3 for C4-Ph-ODBP-Ph-C7 and C5-Ph-ODBP-Ph-OC12 respectively and $\approx$(125 Å)^3 and (135 Å)^3 for the larger systems. It is possible that if small biaxial domains or clusters are present in the nematic systems, the average biaxial order would be reduced in the larger systems if these were randomly orientated, as the larger systems are more likely to encompass several clusters.

5.5.4 Structural analysis - comparisons between the two bent-core systems

C5-Ph-ODBP-Ph-OC12

Mesophase structural information can be obtained through the evalution of pair distribution functions. The simplest of these is the radial distribution function, $g(r)$, which gives the probability of finding a particle at a distance r, irrespective of orientations.[142] Figure 5.18 compares radial distributions for various groups of the C5-Ph-ODBP-Ph-OC12 mesogen. (Please note - all subsequent atom and ring numbers relate to Figure 5.17). The temperatures 500, 480 and 450 K represent the simulated nematic phase ($\langle P_2 \rangle > 0.4$), whereas 520 K represents the isotropic phase in the vicinity of the T_{NI} temperature ($\langle P_2 \rangle \approx 0.2$). It should be noted that the experimentally observed DC phase transition occurs at 457.6 K. Visual observation of the simulations at 450 K do not suggest a typical nematic structure, possibly indicating some pre-transitional behaviour.

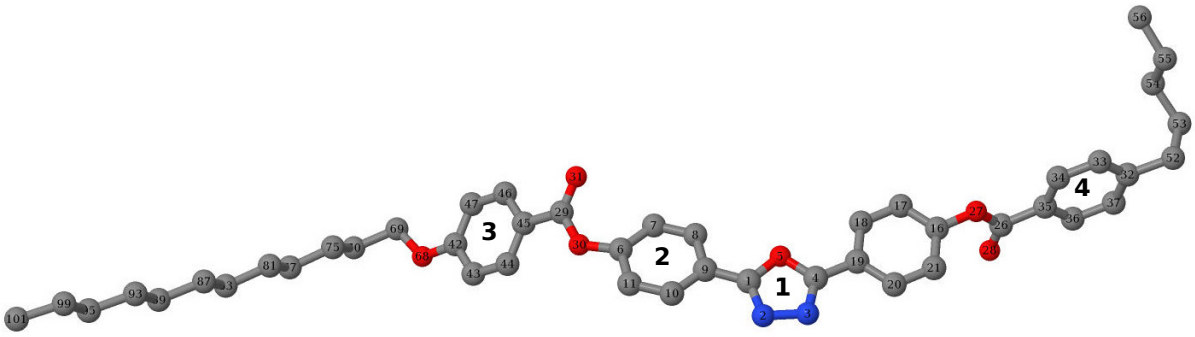

Figure 5.17: C5-Ph-ODBP-Ph-OC12 (shown without hydrogens).

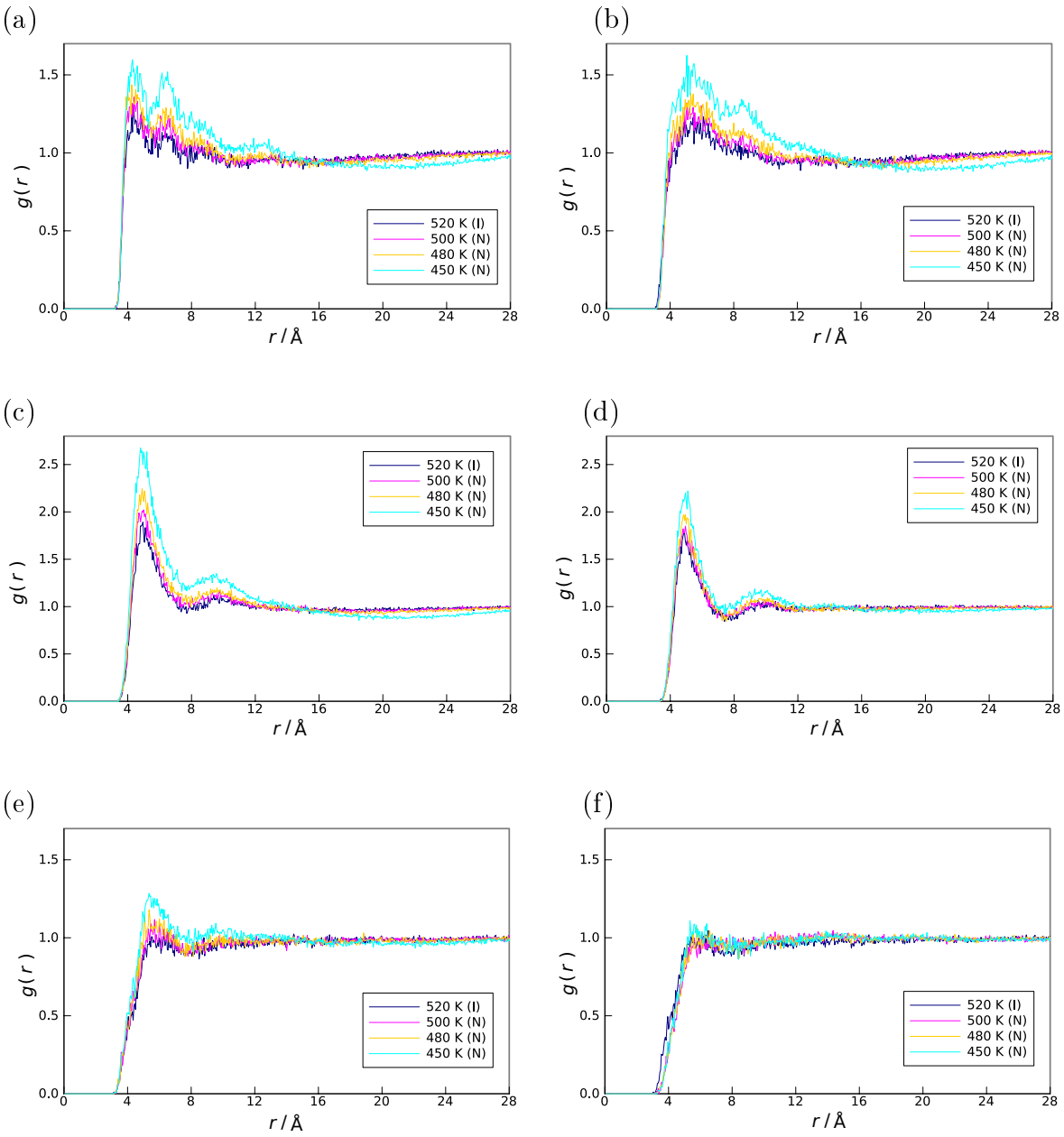

Figure 5.18: Radial distribution functions for various groups of the C5-Ph-ODBP-Ph-OC12 mesogen calculated for several different temperatures. (a) oxadiazole-oxadiazole (ring 1), (b) phenyl-2-phenyl-2, (c) tail-tail (OC12 end-group), (d) tail-tail (C5 end-group), (e) phenyl-3-phenyl-3, (f) phenyl-4-phenyl-4.

The distributions between the oxadiazole pairs (where the reference point is defined as the centre of the oxadiazole ring (ring 1), all show liquid-like behaviour, which can be inferred by a number of structured peaks in the short range, hints of some minor structure in the medium range at lower temperatures in particular, and an absence of long range peaks (>15 Å) at all temperatures (see Figure 5.18a). The

first main peak, which is split into two subsidiary peaks at 4.2 and 6.3 Å, reflects the distance between nearest-neighbour molecules in the first coordination shell. The peaks become more pronounced with decreasing temperature, suggesting greater correlation of the oxadiazole pairs at the lower temperatures. At 450 K, $g(r)$ shows a broad region of lower probability between 16 and 28 Å compared with $g(r)$ at the higher temperatures, suggesting a greater segregation of the cores with respect to the alkoxy/alkyl chains at this particular temperature. Interestingly, at 520 K (isotropic phase), $g(r)$ shows similar behaviour to that displayed in the nematic phase, although the peaks are less pronounced.

As a general trend, the behaviour of $g(r)$ in the isotropic phase is expected to show one initial contact peak followed by a rapid fading away of any further short-range structure.[169] In contrast to this description, the behaviour of $g(r)$ at 520 K shows enhanced short range structure with more than one peak discernible. This suggests a small degree of molecular organization (structural change) in the isotropic phase prior to entering the nematic phase, and is consistent with the observations reported from DSC experiments for this class of mesogens described in Section 5.1.

The distributions between the phenyl-2 pairs adjacent to the oxadiazole ring for all temperatures, including the isotropic temperature at 520 K, show a broad initial peak at ≈ 5.2 Å and a less well defined secondary peak at ≈ 8.5 Å, both of which are at greater distances than those calculated for the oxadiazole pairs (see 5.18b). This may indicate a parallel displaced arrangement of the phenyl-2 pairs of the nearest neighbour molecules compared with the oxadiazole pairs.

The pair distributions between the end groups of the tails, (defined as the mid-point between the terminal C99-C101 atoms of the long alkoxy tail and the mid-point between the terminal C55-C56 atoms of the shorter alkyl tail), are shown in Figure 5.18c and Figure 5.18d. Both show liquid-like behaviour for each temperature, with a pronounced first peak at ≈ 4.9 Å, followed by a secondary smaller peak at around 9.3 Å (longer tail) and 9.6 Å (shorter tail). The peaks are more intense for the end groups of the longer tail, suggesting greater correlation of these pairs compared with the end groups of the shorter tail. Additionally, the distribution for the end groups of the longer tail show a broad region of low probability between 16 and 28 Å at 450 K

which is not apparent at the higher temperatures, nor for any of the temperatures for the shorter tail end groups. This suggests that at 450 K there is greater segregation of the alkoxy tails, with the low probability region representing areas where the oxadiazole pairs are found. As with the previous distributions, the presence of more than one peak in the short range is perceivable in the istropic phase at 520 K, again indicating a structural change prior to formation of the nematic phase.

The radial distribution functions for the two outer phenyl rings of the core structure (phenyl-3 and phenyl-4) are shown in Figure 5.18e and Figure 5.18f. The distributions between the phenyl-3 pairs adjacent to the alkoxy tail for each temperature show a well defined first peak between 5.3 and 5.5 Å, with the latter representing the higher temperature, and a small but observable secondary peak at $\approx$ 9.5 Å. In contrast, the distributions beween the phenyl-4 pairs adjacent to the alkyl tail show a significantly smaller first peak which occurs between 5.6 and 6.1 Å and no discernible secondary peak. It is possible that the alkoxy connection and the specific topology in this region increases the contact of the phenyl-3 rings in the nearest environment of the C5-Ph-ODBP-Ph-OC12 mesogen with respect to the phenyl-4 rings, and this is supported by the greater height of the first peak and slight shift to a smaller contact distance for the phenyl-3 pairs compared with that for the phenyl-4 pairs.

The pair distribution function, $g_2(r)$, calculates the average relative orientation of molecules as a function of their intermolecular distance and is obtained as the second-rank Legendre polynomial of the angle beween the molecular axis of two molecules as a function of their distance.[137] Figure 5.19a shows $g_2(r)$ obtained for the oxadiazole axis (C1 to C4 atoms). At T = 500, 480 and 450 K, and following an initial broad peak corresponding to the short range orientational ordering, $g_2(r)$ converges to a value of $< P_2 >^2$ (the square of the order parameter of the phase), which is expected at large intermolecular distances. In contrast, $g_2(r)$ converges to zero at T = 520 K, which is coincident with the isotropic phase. The behaviour of $g_2(r)$ therefore confirms the approximate temperature at which a phase transition occurs (between 520 and 500 K). The behaviour of $g_2(r)$ for the long alkoxy tail (defined as an axis along the C83-C87 bond), shows far less stucture, with one

sharp peak at ≈ 3.8 Å, quickly converging to zero at all temperatures (Figure 5.19b) suggesting that the alkoxy tails are significantly more orientationally disordered than the oxadiazole cores.

The dipole pair distribution function, $g_1(r)$, can provide insight into the local structure around a C5-Ph-ODBP-Ph-OC12 mesogen through the calculation of dipole-dipole orientational correlations. As C5-Ph-ODBP-Ph-OC12 possesses a large transverse dipole, it is likely that the most favourable geometric arrangement between nearest neighbours would be anti-parallel. Examination of the orientational function $g_1(r)$, calculated with respect to the centre of mass of the dipole (defined as an axis across the oxadiazole ring from the N2 to O5 atoms), indicates that only an anti-parallel arrangement of neighbouring molecules occurs up to a distance of 4.4 Å ($g_1(r) < 0$), as this also coincides with the first split of the main peak of $g(r)$ (see Figure 5.19c and Figure 5.19d). Beyond this distance, $g_1(r)$ becomes positive with a fairly broad peak at ≈ 6.3 Å, which also coincides with the second split of the main peak of $g(r)$. This suggests that at this intermolecular distance the arrangement between neighbouring molecules is specifically a parallel one.

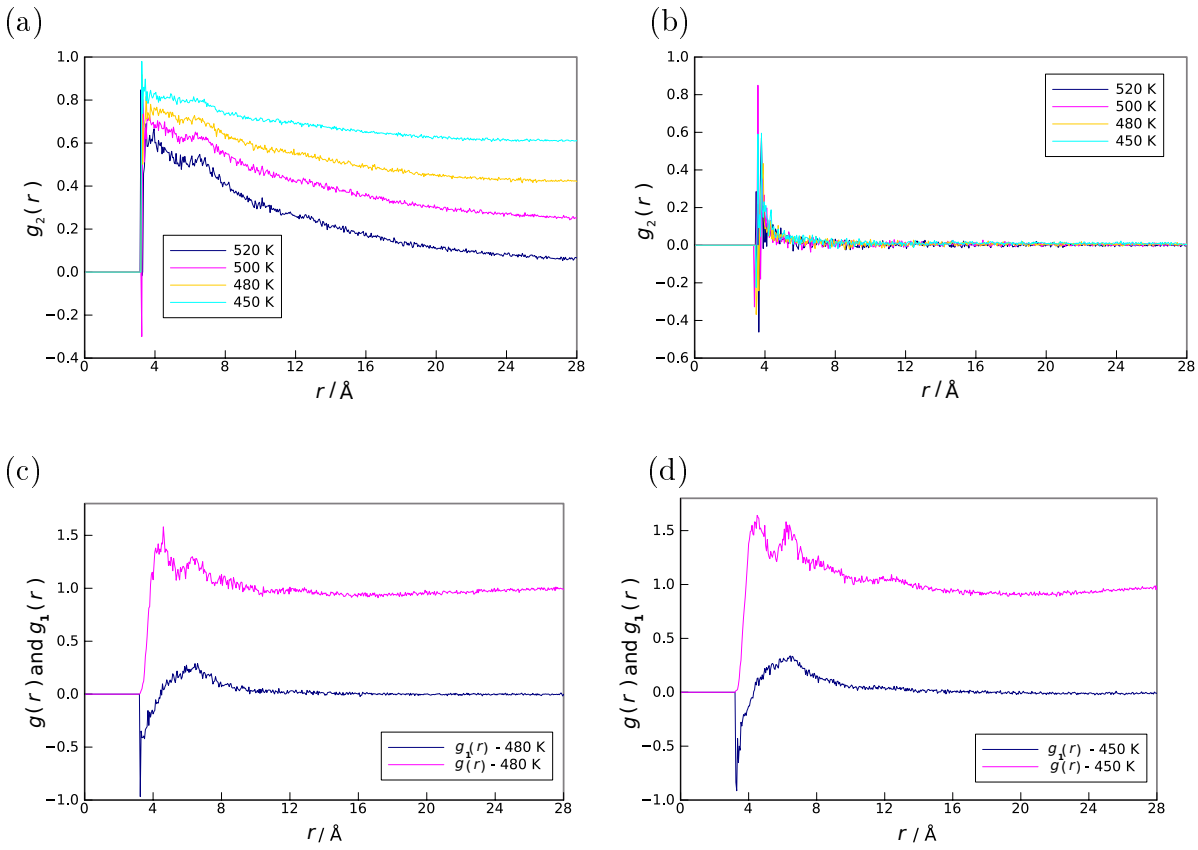

Figure 5.19: Orientational distribution functions for the C5-Ph-ODBP-Ph-OC12 mesogen. (a) oxadiazole C1-C4 axis, (b) tail C83-C87 axis, (c) and (d) dipole-dipole distributions at 480 K and 450 K with $g\ (r)$ shown for reference.

Additional information on mesophase structure can be obtained by resolving $g\ (r)$ into components parallel and perpendicular to the director, $\boldsymbol{n}$ (see Figure 5.20a and Figure 5.20b). Peaks at regular intervals in $g_{\parallel}(r)$ are characteristic of smectic ordering, with low amplitude peaks indicative of local smectic-like clustering of molecules within the nematic phase, due to dipolar interactions and packing effects.[198] The lack of any peaks whatsoever in $g_{\parallel}(r)$ at all temperatures examined suggests the absence of smectic-like clusters in the nematic phase of this particular system. Examination of $g_{\perp}(r)$ indicates that the distribution between the oxadiazole cores is short ranged with minimal structure beyond a weak contact peak at ≈ 4.2 Å due to neighbouring molecules.

As previously discussed in Section 5.2.2, the mesophase structure of the vast majority of bent-core nematics consists of nanometric size clusters characterized by short-range smectic positional order whose cluster size is strongly temperature

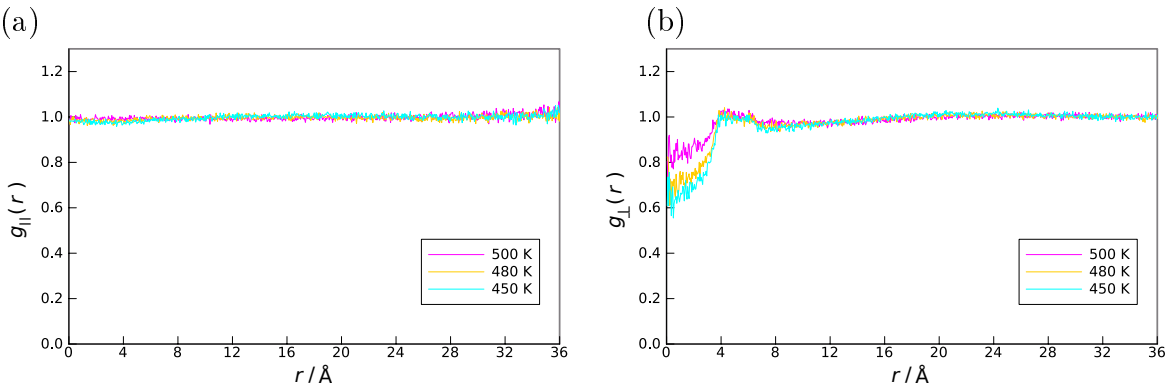

Figure 5.20: Radial distribution functions obtained for the oxadiazole core axis of C5-Ph-ODBP-Ph-OC12 (a) along the director and (b) perpendicular to the director.

dependent (cybotaxis).[183] It has been proposed that cybotaxis is associated with microsegregation (the segregation of incompatible segments or groups) and depends on the strength of the segregation. Bent-core mesogens display particularly strong microsegregation due to the combination of extended aromatic cores and relatively long aliphatic chains.[170] Although there are some indications from the results of the various pair distribution functions above that there is a degree of segregation of the tails with respect to the ODBP cores, it is not possible to identify the nematic phase of C5-Ph-ODBP-Ph-OC12 as cybotactic from these results alone.

To gain a deeper insight into the local molecular arrangement in the nematic phase, two additional pair distribution functions were calculated. These were named $g(d_{\parallel})$ and $g(d_{\perp})$ in order to distinguish them from $g_{\parallel}(r)$ and $g_{\perp}(r)$. Unlike $g_{\parallel}(r)$ and $g_{\perp}(r)$, which calculate the components of the intermolecular vectors relative to the average molecular direction (the system director), these additional distribution functions enabled the intermolecular vectors (represented as the distances between the molecules centres of mass) to be analyzed relative to the instantaneous orientation of each molecule. A parallel direction was defined as a vector linking atom x to atom y of each individual molecule, which was then rescaled to unity. A perpendicular direction could then be defined as normal and therefore radial to this direction. Parallel and perpendicular cut-offs could be varied semi-independently as long as the inequality, $(d_{\parallel})^2 + (d_{\perp})^2 \leq$ (0.5 x box length)^2 was satisfied, allowing longer and narrower cut-offs to be defined. The following results refer to a mesogen

direction linking atom C6 to atom C16, representing the long axis of the ODBP core (see Figure 5.17).

Figure 5.21a and Figure 5.21b shows the results for $g(d_{\parallel})$ and $g(d_{\perp})$ at T = 480, 460 and 450 K, representing the high and low region of the simulated nematic phase. The results are also shown for T = 430 K for comparison purposes, as visual observations indicate that at this temperature the simulation represents the underlying DC phase. At T = 480, 460 and 450 K, $g(d_{\parallel})$ shows an initial contact peak is followed by a secondary much weaker peak at $\approx$ 41 Å after which the correlation functions decay to unity. This indicates there is a favourable interaction in the very short range. The amplitude of the secondary peak suggests that in the vicinity of one molecular length in the direction parallel with the long axis of the ODBP core, there is only a very weak tendency of the molecules to arrange into layers (a maximum of three). In addition, the weaker peak at $\approx$ 41 Å corresponds to a distance which is less than the average molecular length deduced from the simulations - see Section 5.5.5. This suggests there is some degree of intercalation of the alkyl chains and/or tilting of the ODBP cores. In contrast, at T = 430 K, $g(d_{\parallel})$ shows large oscillatory peaks indicating a stronger local preference for arranging into multiple layers.

The results for $g(d_{\perp})$ at T = 480, 460 and 450 K (nematic phase) show a strong initial peak and an absence of discernible peaks in the long range. The profiles for $g(d_{\perp})$ are very similar in each case with transverse correlation lengths $\approx$ 15 to 20 Å . At T = 430 K, there is a significant difference in the profile of $g(d_{\perp})$ with the appearance of well defined peaks and a transverse correlation length of at least 60 Å .

In summary, the behaviour of the pair distribution functions described above, along with the previous results obtained from the standard pair distribution functions, are not consistent with the current accepted description of the structure of most bent-core nematics, which proposes that the nematic phase is composed of clusters, with local smectic order and a strongly temperature dependent size. Although there is some sparse evidence for a weak tendency to form into smectic-like fragments (of no more than three layers), the predominant findings indicate that

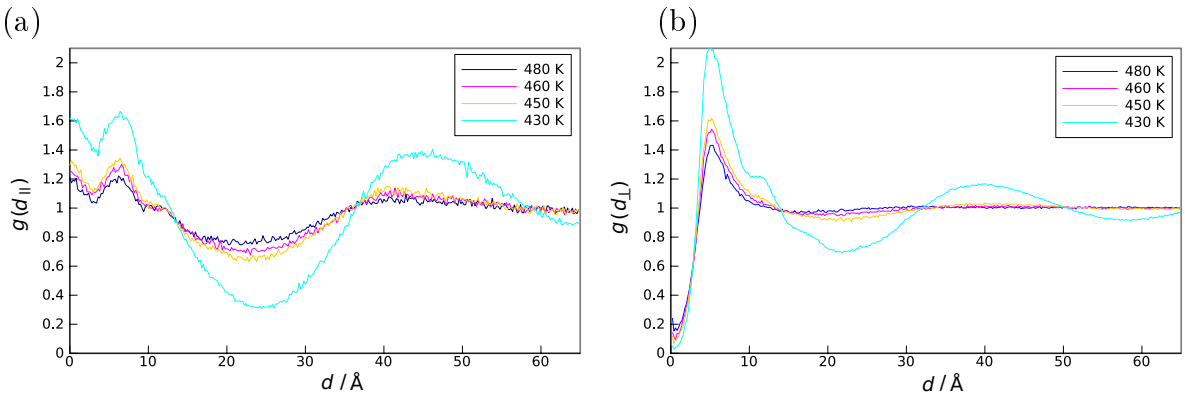

Figure 5.21: Pair distribution functions as a function of temperature for C5-Ph-ODBP-Ph-OC12 (a) $g(d_{\parallel})$ and (b) $g(d_{\perp})$

the nematic phase of C5-Ph-ODBP-Ph-OC12 is composed of small clusters with dimensions of predominantly one molecular length in the longitudinal direction and a few molecules in the transversal direction. The size of the clusters does not appear to be temperature dependent for most of the nematic phase, although there is a weak indication of a slight extension of the transversal correlation length at 450 K. These results suggest that the origin of the 4-spot pattern observed in the small angle XRD pattern for this system is not directly related to the structure factor (the tilted arrangement of molecules in SmC-type clusters). Additionally, the lack of any notable temperature dependence of the correlation lengths in the nematic phase also supports the temperature independent behaviour of the XRD structural parameters. This tends to support the explanation proposed by Keith *et al.*, which states that for medium chain length 4-cyanorescorcinol bent-core mesogens, a complex interplay exists between cluster size, tilt angle of mesogens (structure factor) and the distinct mesogen bent shape (form factor) which collectively result in the specific XRD pattern for this system.

In addition, there are some indications from various radial distribution functions that prior to formation of the nematic phase there is a small degree of molecular organization above and beyond that expected in a normal isotropic phase, which is again consistent with experimental observations.

Finally, the dramatic change in the profile of both $g(d_{\parallel})$ and $g(d_{\perp})$ at 430 K, suggests that a phase transition has occurred into a more structured phase (possibly

a DC phase) somewhere between 450 and 430 K. This supports the visual observations and the previously noted discontinuity in the biaxial order parameter between these temperatures.

C4-Ph-ODBP-Ph-C7

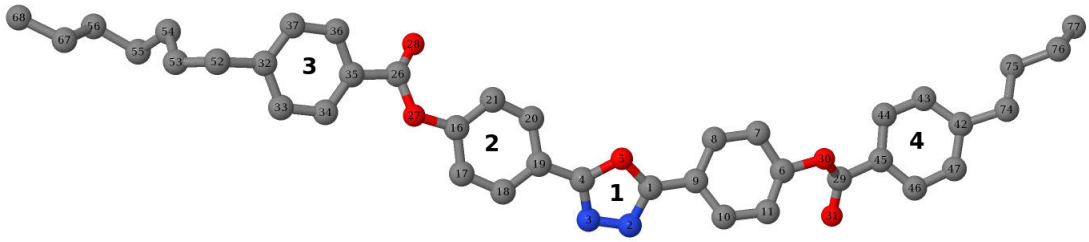

Figure 5.22: C4-Ph-ODBP-Ph-C7 (shown without hydrogens).

In order to make comparisons between the nematic phase structure of the two ODBP bent-core systems, the various pair distribution functions described above were also calculated for the C4-Ph-ODBP-Ph-C7 system at a selection of temperatures, with 510 K representing the isotropic phase ($\langle P_2 \rangle > 0.2$), and 490, 470 and 440 K representing the nematic phase ($\langle P_2 \rangle > 0.4$). The temperatures selected were lower than those chosen for C5-Ph-ODBP-Ph-OC12 so as to account for the slightly lower experimental as well as simulated T_{NI} for the C4-Ph-ODBP-Ph-C7 system. Figure 5.23a shows the radial distribution function, $g(r)$, for the oxadiazole pairs (ring 1). For all simulated temperatures $g(r)$ displays liquid-like behaviour, with no structure in the medium-long range and values tending to unity in the long-range. In the short-range, $g(r)$ shows a slight shoulder at ≈ 4.6 Å followed by a contact peak at ≈ 6.3 Å which incidently coincides with the second split of the main peak of $g(r)$ for the analoguous pairs of C5-Ph-ODBP-Ph-OC12, but is significantly smaller in height. A minimum coinciding with a lower probability region for the oxadiazole pairs, occurs between 7 and 11 Å. No further peaks in the short range are discernible, suggesting that correlation between oxadiazole pairs outside the first coordination shell is lost. In contrast to C5-Ph-ODBP-Ph-OC12, $g(r)$ for the oxadiazole pairs in the isotropic phase (510 K), displays minimal structure with the presence of one

small contact peak only.

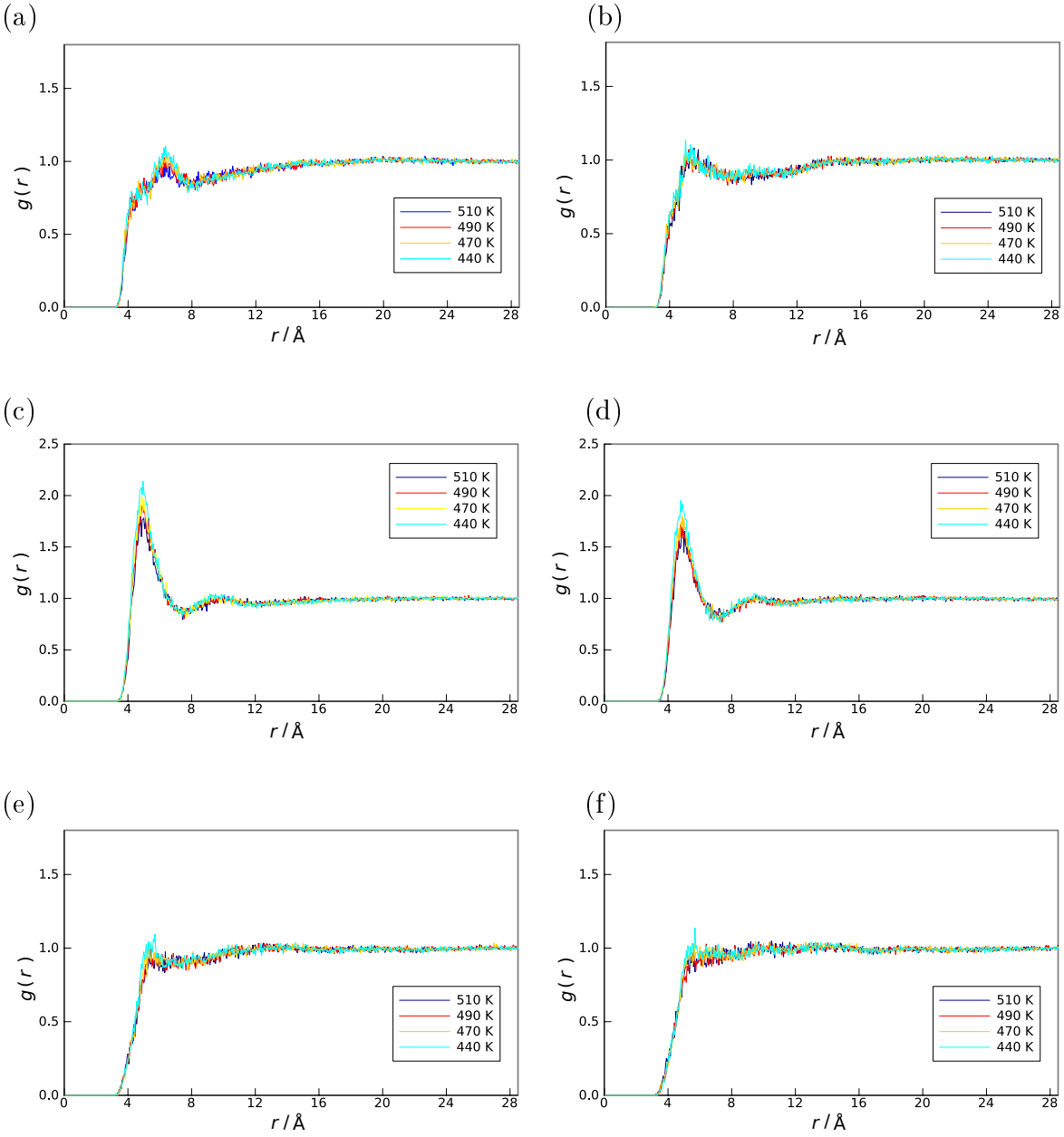

Figure 5.23: Radial distribution functions for various groups of the C4-Ph-ODBP-Ph-C7 mesogen calculated for several different temperatures. (a) oxadiazole-oxadiazole (ring 1), (b) phenyl-2-phenyl-2, (c) tail-tail (C7 end-group), (d) tail-tail (C4 end-group), (e) phenyl-3-phenyl-3, (f) phenyl-4-phenyl-4.

The distribution between the phenyl-2 pairs adjacent to the oxadiazole ring shows a weak contact peak at $\approx$ 5.4 Å (see Figure 5.23b) and minimal structure in the medium-long range for all simulated temperatures, which is in contrast to the phenyl-2 distribution for C5-Ph-ODBP-Ph-OC12 mesogen, which shows a noticeably more

ordered structure in the short to medium range with more pronounced peaks.

Pair distributions between the end groups of the tails also show liquid like behaviour at each temperature, with a pronounced contact peak at ≈ 4.8 Å and a small secondary peak at ≈ 9.3 Å in the nematic phase, although this secondary peak is not perceptable at 510 K, the isotropic temperature immediately above the T_{NI}, (see Figure 5.23c and Figure 5.23d). The behaviour of $g(r)$ for the tail end groups are broadly similar to those for the tail end groups of C5-Ph-ODBP-Ph-OC12 with peaks occuring at similar distances. However the peaks are less pronounced than those observed for C5-Ph-ODBP-Ph-OC12, and there is also an absence of secondary peaks in the isotropic phase for the tail end groups of the C4-Ph-ODBP-Ph-C7 mesogen.

An additional difference in the pair distributions also occurs for the outer phenyl-3 and phenyl-4 rings (Figure 5.23e and Figure 5.23f). Unlike C5-Ph-ODBP-Ph-OC12, which shows distinct differences between these pair distributions, the corresponding phenyl groups of the C4-Ph-ODBP-Ph-C7 mesogen show almost identical features, with both displaying a weak contact peak at ≈ 5.6 Å and beyond this no further structure. This pattern is very similar to the phenyl-4 distribution for the C5-Ph-ODBP-Ph-OC12 mesogen, which is also attached to an alkyl chain, but differs markedly from the phenyl-3 distribution of C5-Ph-ODBP-Ph-OC12 attached to the alkoxy tail. This tends to confirm that the local structure in the vicinity of the alkoxy chain is different to that for the alkyl chains.

The orientational pair distribution function, $g_2(r)$, for the oxadiazole axis of the C4-Ph-ODBP-Ph-C7 mesogen shows a broad peak at short-range which then decays to $< P_2 >^2$ in the long range (see Figure 5.24a). However, the main peak for each temperature is slightly lower than those for C5-Ph-ODBP-Ph-OC12, which reflects the slightly lower P_2 order parameters found for this system compared with those for C5-Ph-ODBP-Ph-OC12 . The results of $g_2(r)$ also confirm an approximate phase transition between 510 K and 490 K. Also, similar to $g_2(r)$ for the alkoxy chain of C5-Ph-ODBP-Ph-OC12, $g_2(r)$ for the alkyl C7 tail shows one sharp peak at ≈ 3.8 Å and then quickly converges to zero at all temperatures, indicating orientationally disordered tails in the long range (see Figure 5.24b).

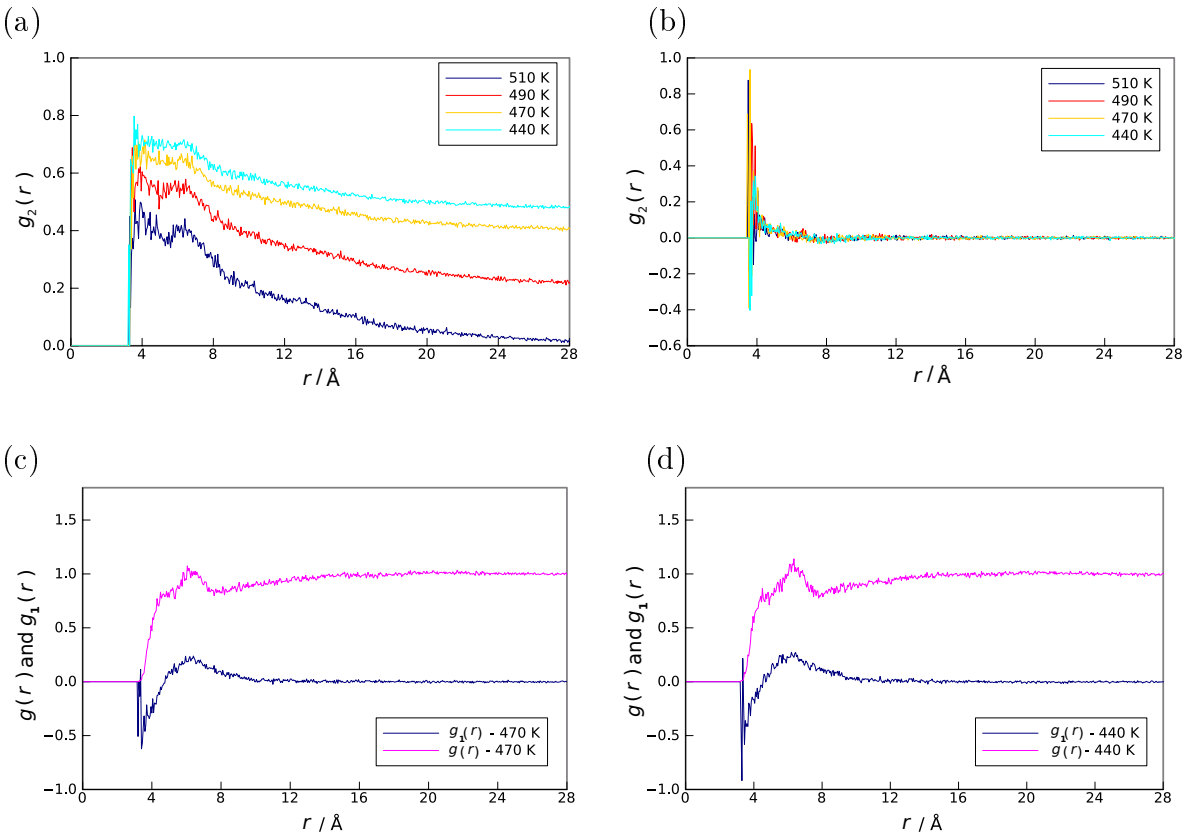

Figure 5.24: Orientational distribution functions for C4-Ph-ODBP-Ph-C7: (a) oxadiazole C1-C4 axis, (b) tail C55-C56 axis, (c) and (d) dipole-dipole distributions at 470 K and 440 K with $g(r)$ shown for reference.

Further structural differences between the two systems can be derived from the behaviour of $g_1(r)$ which is shown for the dipole pairs in Figure 5.24c and Figure 5.24d at two temperatures in the nematic phase ($g(r)$ is also shown for reference). In contrast to C5-Ph-ODBP-Ph-OC12, which shows very localized anti-parallel dipole correlations at short range, the position of the main peak for $g(r)$ at ≈ 6.3 Å is only compatible with parallel dipole correlations ($g_1(r)$ >0 at this distance). However, it is likely that some individual molecules will show anti-parallel as well as parallel dipole correlations in the very short range.

The pair distribution function, $g_{\parallel}(r)$ calculated for the oxadiazole axis at three temperatures in the nematic phase shows no peaks at regular intervals and therefore an absence of translational order in the nematic phase (see Figure 5.25a). With the exception of a fairly broad but small contact peak at around 5.0 Å due to favourable interactions between neighbouring molecules, $g_{\perp}(r)$ also shows very little stucture

in the long range. However, the position of the contact peak has shifted to a slightly larger distance compared with that for the oxadiazole cores of the C5-Ph-ODBP-Ph-OC12 mesogen where the highest point of the peak occurs at ≈ 4.2 Å.

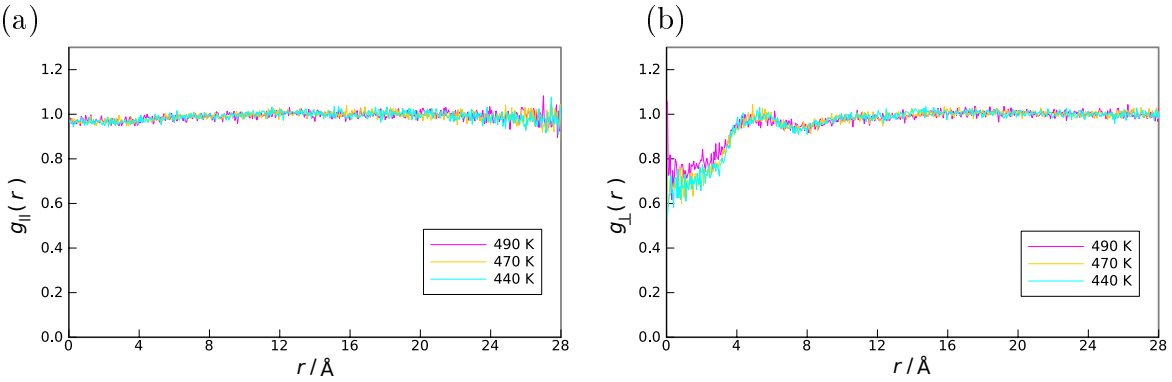

Figure 5.25: Radial distribution functions obtained for the oxadiazole axis for C4-Ph-ODBP-Ph-C7 (a) along the director and (b) perpendicular to the director.

Analysis of the pair distribution functions, $g(d_{\parallel})$ and $g(d_{\perp})$ was also conducted for the nematic phase of C4-Ph-ODBP-Ph-C7 (see Figure 5.26). These distribution functions were previously described in relation to C5-Ph-ODBP-Ph-OC12 in order to gain a greater insight into the local arrangement of molecules in the nematic phase of this system. At each temperature examined, $g(d_{\parallel})$ for C4-Ph-ODBP-Ph-C7 shows very little structure in the short range. A very weak peak is discernible at ≈ 35 Å for all temperatures, which suggests that in their local environment there is almost no tendency for the molecules to arrange into layers in the nematic phase. The results for $g(d_{\perp})$ (see Figure 5.26b) show one initial peak combined with very short correlation lengths (≈ 7 to 8 Å) at all temperatures, suggesting that any clusters present in the nematic phase are very small.

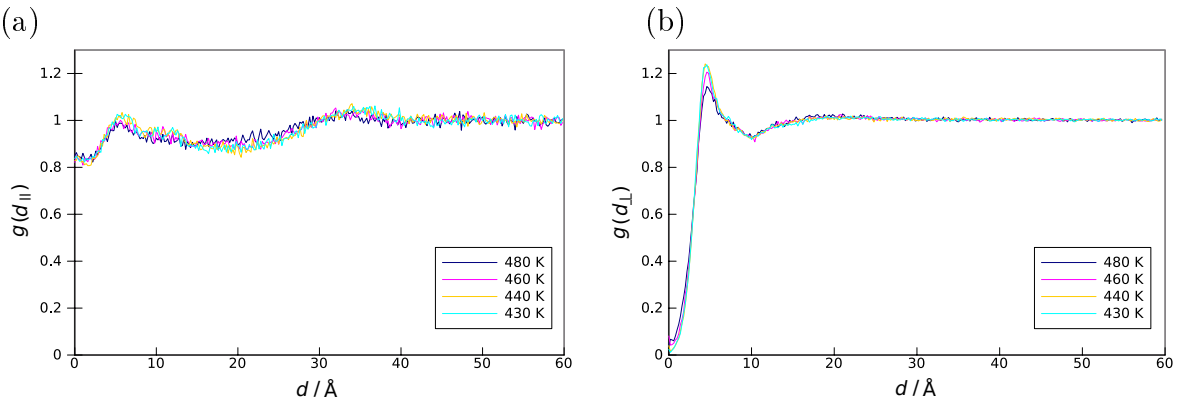

Figure 5.26: Pair distribution functions as a function of temperature for C4-Ph-ODBP-Ph-C7 (a) $g(d_{\parallel})$ and (b) $g(d_{\perp})$.

Collectively, the results for the various pair distributions discussed above, indicate that the nematic and the adjacent isotropic structure close to the T_{NI} for the C4-Ph-ODBP-Ph-C7 system is less ordered compared with that for C5-Ph-ODBP-Ph-OC12, and that the nematic phase is closer to an ordinary nematic, with only short range correlation between nearest-neighbour molecules. The lack of evidence to substantiate the presence of cybotactic clusters could be due to the relatively short alkyl tails, as proposed by Keith *et al.*[102] This may explain the marginally lower uniaxial order parameters found for this system compared with those found for C5-Ph-ODBP-Ph-OC12, as the organization into smectic layer fragments within a cybotactic nematic enables a much higher orientational order parameter to be achieved.[102] Additionally, these results provide no clear evidence for a structural change in the isotropic phase of C4-Ph-ODBP-Ph-C7 prior to entering the nematic phase. This is in contrast to the simulated results obtained for C5-Ph-ODBP-Ph-OC12, as well as the experimental observations noted for C5-Ph-ODBP-Ph-OC12 and a number of other ODBP bent-core mesogens, which do indicate molecular pre-organization in the isotropic phase in the vicinity of the phase transition temperature (T_{NI}).

5.5.5 Molecular shape comparisons

The molecular structure is an important feature in understanding liquid crystal (LC) phase behaviour.[145] Due to the relatively dense molecular packing in LC phases, the shape of the molecules determines the anisotropy of their local coordination environment, which in turn affects the nature and thermodynamic stability of the mesophases formed, as well as influencing the appearance of mesophases at specific temperatures.[79,126] The actual shape of a molecule however, is a difficult concept to define, as many different populations of conformations are possible, which vary with temperature.[145] A huge number of conformations will be possible for both mesogens due to the chain dihedrals and ester linkages to the ODBP unit. Despite this, parameters such as molecular dimensions and aspect ratios (length / breadth) obtained as average values with respect to temperature, can provide some useful insight into the average shape of mesogens. The following results refer to molecular dimensions obtained from the average moment of inertia tensor, $\langle I \rangle$ where $\langle I_1 \rangle$, $\langle I_2 \rangle$ and $\langle I_3 \rangle$ are the averaged principle moments of inertia. These values enable the average length, width and breadth of a mesogen to be calculated (see Chapter 4, Section 4.5.3 for the method of obtaining molecular dimensions).

The average molecular length for C5-Ph-ODBP-Ph-OC12 (see Figure 5.27a) shows a small increase with decreasing temperature in the nematic phase from $\approx$ 46.8 to 48.9 Å. These values are slightly greater than the length reported by Southern *et al.* from SAXS experiments, where an average temperature independent d spacing of 43 Å was obtained, which the authors proposed corresponds to the approximate molecular length for this mesogen. The shorter average molecular length displayed by C4-Ph-ODBP-Ph-C7 (Figure 5.27a) shows almost no temperature dependence in the nematic phase, varying from$\approx$ 40.0 to 40.9 Å. Despite the longer molecular length of C5-Ph-ODBP-Ph-OC12, both mesogens show broadly similar average aspect ratios (L/B) where in this instance B represents (breadth + width) / 2, except in the low temperature nematic regime where C5-Ph-ODBP-Ph-OC12 displays higher L/B compared with C4-Ph-ODBP-Ph-C7. This suggests an enhancement of the ordered phase stability for C5-Ph-ODBP-Ph-OC12, and is also supported by slightly higher uniaxial order parameters, $\langle P_2 \rangle$ and $\langle P_4 \rangle$ in the lower temperature

range of the nematic phase compared with those for C4-Ph-ODBP-Ph-C7.

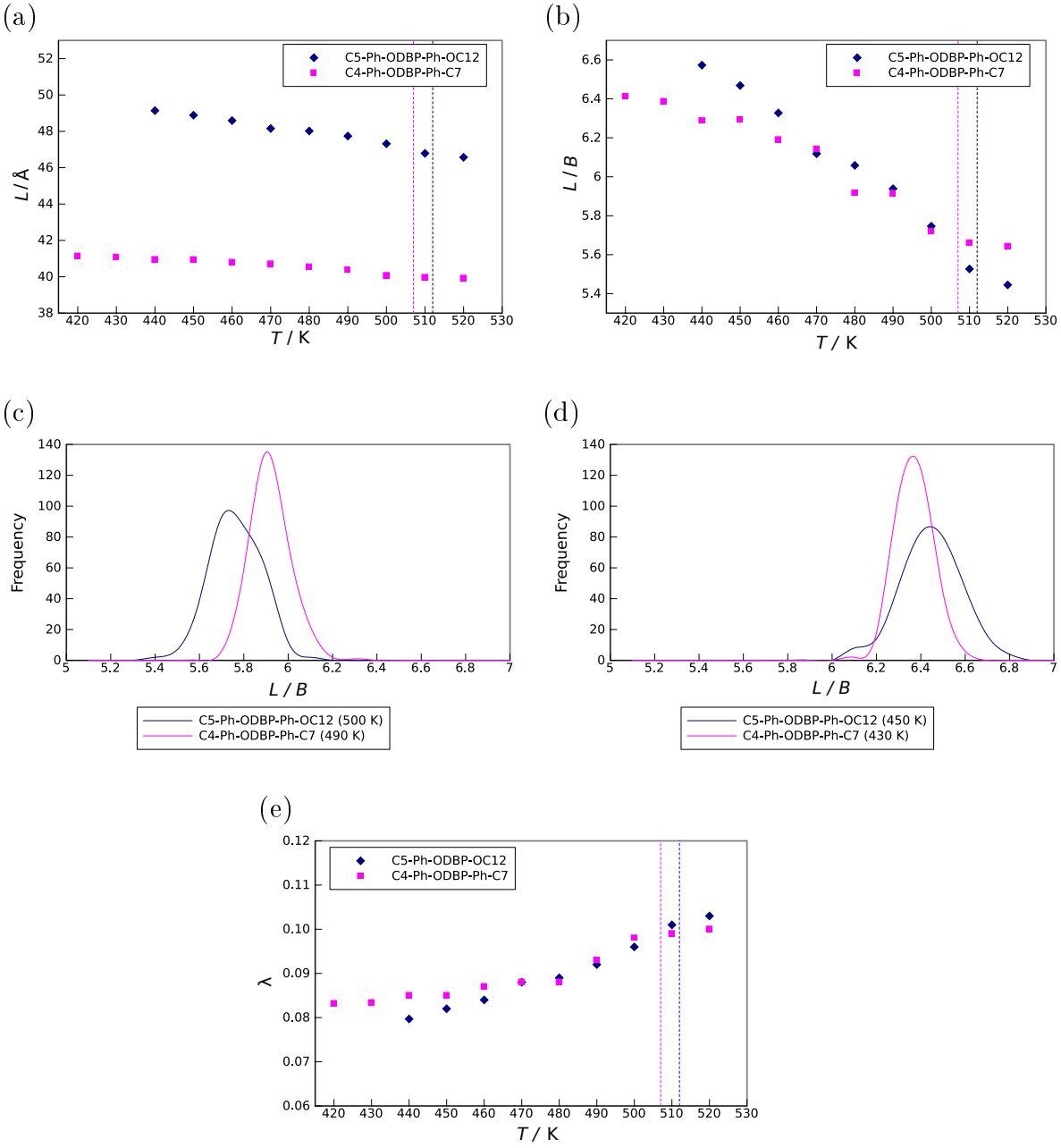

Figure 5.27: Comparisons of: (a) The average molecular length as a function of temperature for the two ODBP systems, (b) The average length to breadth ratio as a function of temperature for the two systems, (c) and (d) The frequency of length to breadth ratio in the high and low temperature nematic range for each mesogen, (e) The average molecular biaxiality as a function of temperature for the two systems. [Dotted vertical lines show the respective T_{NI}].

Further insight into the mesogen shape can be gained by looking at the distribution of aspect ratios at specific temperatures. Figure 5.27c shows the distributions

of aspect ratio at the first simulated temperature below T_{NI} for each mesogen and it can be seen that C5-Ph-ODBP-Ph-OC12 displays a broader distribution of aspect ratios and lower value at the peak frequency (≈ 5.9) compared with C4-Ph-ODBP-Ph-C7 (maximum frequency value ≈ 5.7). This suggests that C5-Ph-ODBP-Ph-OC12 assumes a wider range of conformations in the vicinity of the phase transition compared with C4-Ph-ODBP-Ph-C7. This is also apparent at low temperatures in the nematic phase (see Figure 5.27d) where again the distribution is broader for C5-Ph-ODBP-Ph-OC12, although here the maximum L/B ratio occurs for C5-Ph-ODBP-Ph-OC12. These observations suggest that C5-Ph-ODBP-Ph-OC12 assumes a greater range of conformations throughout the nematic range compared with C4-Ph-ODBP-Ph-C7.

The biaxiality of the molecular dimensions, λ, calculated as $\sqrt{3/2}(W-B)/2L-B-W$,[169] provides an indication of the amount of deviation from an effective uniaxial molecular symmetry.[169] Both mesogens show a decrease in shape biaxiality with decreasing temperature in their respective nematic phases (Figure 5.27e), with values broadly similar except at the low temperatures, where C5-Ph-ODBP-Ph-OC12 shows a more marked decrease in λ compared with C4-Ph-ODBP-Ph-C7. This is counter to intuitive expectations, as C5-Ph-ODBP-Ph-OC12 shows greater phase biaxiality in the low nematic temperature range compared with C4-Ph-ODBP-Ph-C7. This reinforces the fact that the nematic order of a specific system is a complex interplay between both energetic and entropic factors.[23] In addition, this also supports the findings that molecular shape biaxiality alone is not a crucial factor in determining the degree of biaxial order in the nematic phase.[19,183]

5.5.6 The influence of the alkoxy core-chain linkage on structure and orientational order

In the preceding sections the two closely related mesogens have shown differences, sometimes subtle, in orientational order, short range structure and molecular shape. However, the most striking difference between the two systems is apparent from visual observations of the low temperature nematic regions, where the emergence of ribbon or wave-like structures occurs in the C5-Ph-ODBP-Ph-OC12 system but not

in C4-Ph-ODBP-Ph-C7. It would therefore appear that the specific characteristics of these two nematic phases are highly sensitive to the fine details (chemical and structural) of each mesogen.

Besides the differing length of terminal chains, the most notable difference between the two mesogens is the substitution of an alkoxy terminal chain in C5-Ph-ODBP-Ph-OC12 as opposed to alkyl terminal chains on both sides of the aromatic core which are present in C4-Ph-ODBP-Ph-C7. In addition to introducing an outer lateral dipole, the oxygen of the alkoxy group extends the length of the rigid core and enhances the polarizability anisotropy, due to π-conjugation with the aromatic core.[41] Also, the topology of the connection of the alkoxy chain differs from that of the alkyl-ring connection as the torsional potential of the C_{ar}-O bond leads to a geometry corresponding to the O-CH_2 bond lying in the same plane as that of the aromatic ring, whereas the C_{ar}-CH_2 torsional potential exhibits two equivalent minima ($\pm 90°$) corresponding to the first CH_2-CH_2 bond of the alkyl chain lying on a plane perpendicular to the plane of the aromatic ring.[100] The relative core-chain orientation for C5-Ph-ODBP-Ph-OC12 is therefore different for each side of the aromatic core, whereas for C4-Ph-ODBP-Ph-C7 it is the same. As stated by Cinacchi *et al.*,[34] the region in which the core and chain encounter one another can play an important role in structure-property relationships. These differences in core-chain geometries are therefore likely to lead to distinct conformations which may affect the packing density of the mesogens, resulting in specific mesophase structures.[102]

To explore the possibility that the alkoxy chain-core connection in C5-Ph-ODBP-Ph-OC12 may be important in defining the molecular organization of the low temperature nematic region and partly explain the differences in the specific nematic phase characteristics of the two ODBP mesogens, two independent minor changes were made to the force field parameters. The first change (Test 1) involved replacing the RB coefficients for the C_{ar}-O bond with those for the C_{ar}-CH_2 bonds, with the intention of establishing the same torsional potential, and hence core-chain geometry, at each side of the aromatic core, similar to those displayed by C4-Ph-ODBP-Ph-C7. The effect of this change was tested by performing a single molecule gas phase simulation and obtaining the torsional potential by an Boltzmann inversion of the

dihedral angle distributions (see Figure 5.28c).

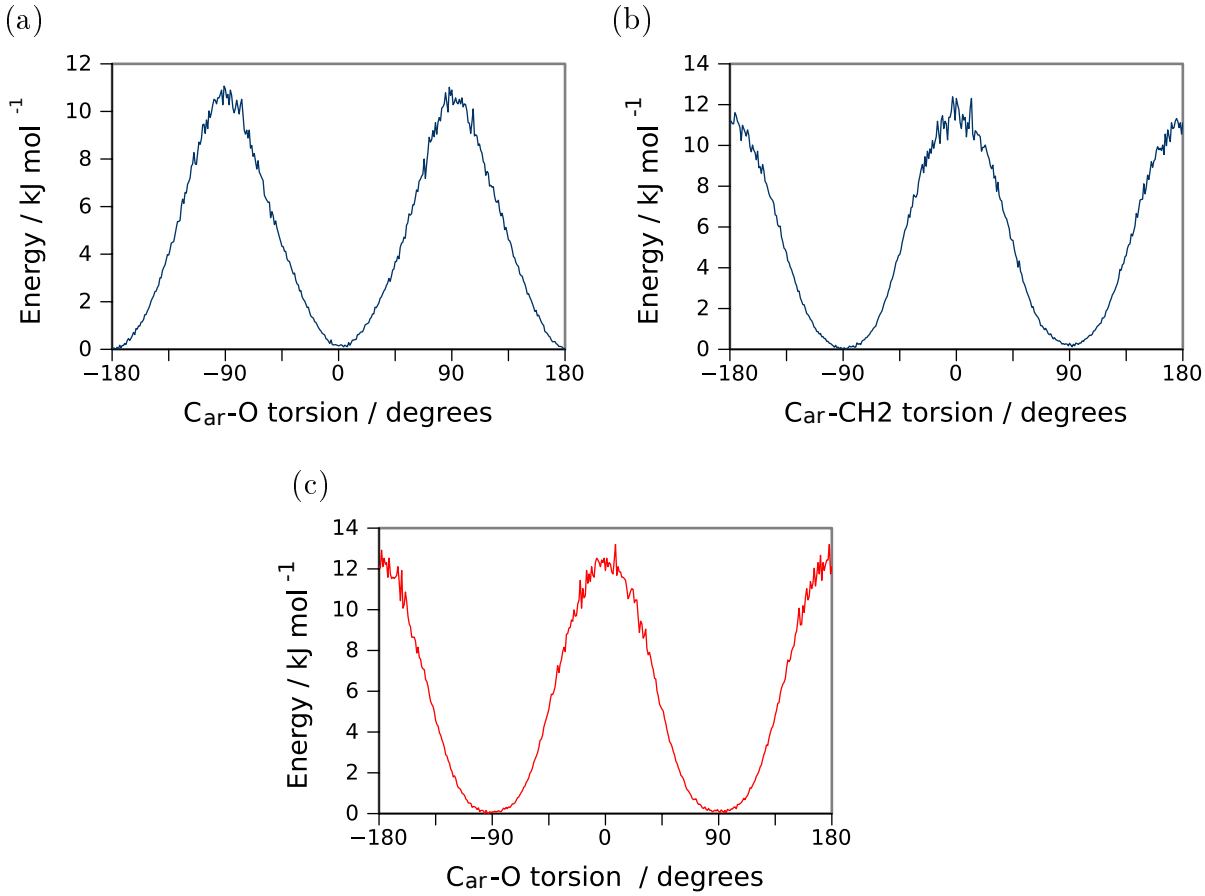

Figure 5.28: Effective torsional potentials obtained by Bolztmann inversion of dihedral distributions obtained from gas phase simulations of C5-Ph-ODBP-Ph-OC12. (a) C_{ar}-O torsion (GAFF-LCFF), (b) C_{ar}-CH_2 torsion (GAFF-LCFF), (c) C_{ar}-O torsion (Test 1).

The second change (Test 2), involved an approximate method of removing the effect of the outer lateral dipole caused by the presence of the alkoxy group. To represent this dipole, the GAFF-LCFF partial atomic charges assigned to the alkoxy atoms are as follows; C_{ar} ($+0.1781e$), O ($-0.3029e$) and C_{alkyl} ($+0.1964e$). The GAFF-LCFF partial charges assigned to the atoms of the core-alkyl linkages of C5-Ph-ODBP-Ph-OC12 as well as C4-Ph-ODBP-Ph-C7 are in contrast small (in the range of $+0.0129e$ to $-0.0744e$) with minimal differences. (The original GAFF charges were unaltered in GAFF-LCFF). To avoid introducing an artificial overall charge to the system, balanced incremental changes to the partial charges of the alkoxy atoms were made to reduce the charge separation and effectively eliminate

the outer dipole, with the Test 2 charges set at C_{ar} ($+0.0381e$), O (-0.0029) and C_{alkyl} ($+0.0364e$).

It is also recognized that other features specific to the core-alkoxy junction are the presence of an atom oxygen and its associated LJ parameters, and a greater C_{ar}-O-CH_2 bond angle compared with C_{ar}-C-CH_2 . For C5-Ph-ODBP-Ph-OC12 the C_{ar}-O-CH_2 average bond angle from a single molecule gas phase calculation was found to be 123.4° and the C_{ar}-C-CH_2 angle 113.0°. Although these additional features may contribute to the mesophase molecular organisation, it was decided to explore the effect of the two parameter changes in Tests 1 and 2 as it was considered that these factors may exert a more significant influence.

New simulations were performed for each test starting with the original $N = 256$ system at 470 K and re-equilibrating for 60 ns with the altered parameters, followed by a further production run of 120 ns. This was followed by further cooling in 10 K intervals down to 450 K with the same simulation time for each step. For the visual analysis of the larger system, the original $N = 2048$ system was re-equilibrated at 450 K for 20 ns with the altered parameters in Test 1 and Test 2, followed by a further production run of 20 ns.

Table 5.5 shows the effect of Test 1 and Test 2 on the average uniaxial order parameters, $\langle P_2 \rangle$, in the lower temperature region of the nematic phase compared with the those for the unaltered GAFF-LCFF. Altering the geometry of the core-alkoxy connection (Test 1) leads to a reduction in the magnitude of $\langle P_2 \rangle$, suggesting that this change may reduce the alignment of the terminal OC12 chain with the molecular long axis, thus reducing the order parameter slightly. Also, these $\langle P_2 \rangle$ values are closer to those calculated for C4-Ph-ODBP-Ph-C7 in the lower temperature region of the nematic phase. Removing the outer dipole (Test 2) appears to have had less of an effect on $\langle P_2 \rangle$, with very limited changes evident.

T / K	$\langle P_2 \rangle$ (GAFF-LCFF)	$\langle P_2 \rangle$ (Test 1)	$\langle P_2 \rangle$ (Test 2)
470	0.70	0.64	0.72
460	0.77	0.70	0.76
450	0.81	0.76	0.78

Table 5.5: The average uniaxial orientational order parameters for C5-Ph-ODBP-Ph-OC12 ($N = 256$ system and molecular reference axis 1).

Table 5.6 shows the effect of Test 1 and Test 2 the biaxial order parameter, $\langle Q_{22}^2 \rangle$. It would be difficult to claim any significant change in $\langle Q_{22}^2 \rangle$ values for each independent test as values are small in the first place. However, quoting values to three decimal places shows a small, subtle reduction in $\langle Q_{22}^2 \rangle$ for each test, indicating that perhaps both the specific geometry and outer dipole of the core-alkoxy junction may contribute to the enhanced local biaxial order observed in the low temperature region of the nematic phase of C5-Ph-ODBP-Ph-OC12 compared with that for C4-Ph-ODBP-Ph-C7.

T / K	$\langle Q_{22}^2 \rangle$ (GAFF-LCFF)	$\langle Q_{22}^2 \rangle$ (Test 1)	$\langle Q_{22}^2 \rangle$ (Test 2)
470	0.070	0.067	0.067
460	0.079	0.073	0.070
450	0.090	0.080	0.082

Table 5.6: The average biaxial orientational order parameters for C5-Ph-ODBP-Ph-OC12 (N = 256 system). Results are given for a set of orthogonal molecular axes representing the core only.

Viewing snapshots of the system at 450 K for Test 1 (Figure 5.29a) shows a dramatic difference in molecular organization (compared with those shown in Figure 5.7b at the same temperature and with the unaltered GAFF-LCFF). The presence of ribbon or wave-like structures are no longer apparent and the system appears significantly more homogeneous. Snapshots of the system at 450 K for Test 2 (Figure 5.29b) also show some differences in molecular organization, although these are not quite as dramatic as for Test 1 as there still appears to be some structural organization of the ODBP cores. These results tentatively suggest that the combination of both alkyl and alkoxy terminal chains specific to the C5-Ph-ODBP-Ph-OC12 system may be important in defining the nanostructure and particular characteristics of the nematic low temperature region. This combination of both alkyl and alkoxy terminal chains was also proposed to be responsible for the unique properties displayed by C5-Ph-ODBP-Ph-OC12 in the DC phase.[134]

(a)

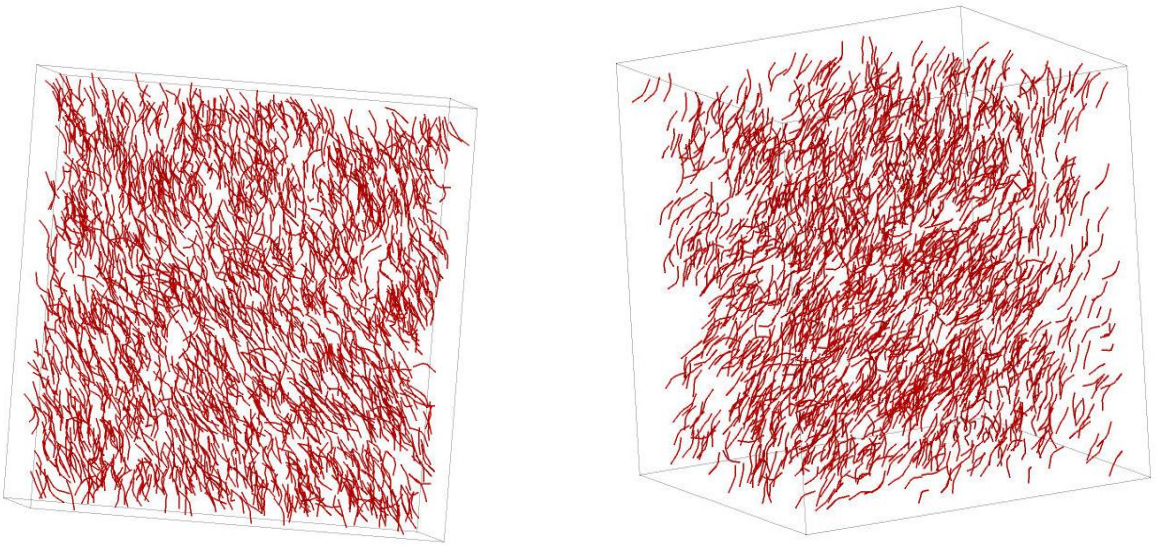

(b)

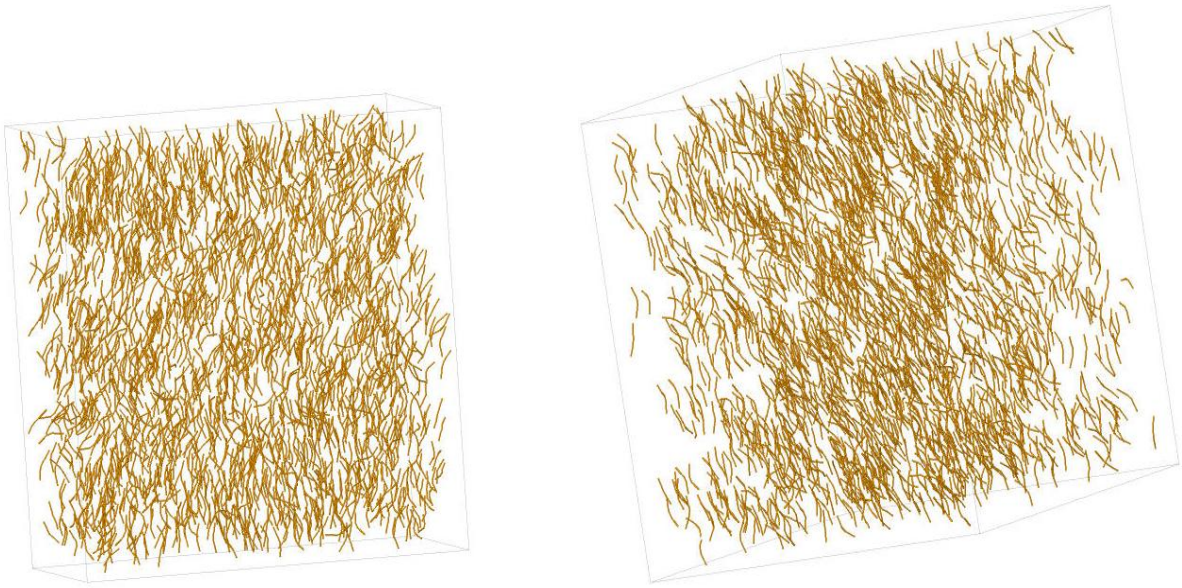

Figure 5.29: Snapshots of the C5-Ph-ODBP-Ph-OC12 system showing simplified ODBP cores only at 450 K for $N = 2048$ molecules: (a) Test 1 and (b) Test 2.

5.6 Conclusions

In this study, fully atomistic simulations of the nematic phases of two bent-core mesogens, C5-Ph-ODBP-Ph-OC12 and C4-Ph-ODBP-Ph-C7, have been performed, employing the GAFF-LCFF force field. The T_{NI} temperatures have been predicted within 10 K of experimental values, indicating the validity of the force field.

Visual analysis of the simulations show unusual ribbon like nanostructures in the low temperature region of the nematic phase of C5-Ph-ODBP-Ph-OC12. In contrast, the nematic phase of C4-Ph-ODBP-Ph-C7 appeared broadly homogenous, lacking any obvious nanostructures.

The calculation of uniaxial and biaxial order parameters for the C5-Ph-ODBP-Ph-OC12 system are in good agreement with experimental values. The results from this study indicate that omission of the mesogen bend angle in the calculations reduces the magnitude of the uniaxial order parameters, which again is in good agreement with experimental measurements. Biaxial ordering was found to be higher for the small system size compared with the large system, supporting the hypothesis that only local biaxial order exists in the nematic phases of bent-core mesogens claimed to display nematic biaxiality. The C4-Ph-ODBP-Ph-C7 system showed marginally lower uniaxial and biaxial order parameters in the nematic phase compared with C5-Ph-ODBP-Ph-OC12, but similar to C5-Ph-ODBP-Ph-OC12 displayed a decrease in the magnitude of the biaxial order parameters for the large system compared with the small system.

The bend angle of C5-Ph-ODBP-Ph-OC12 remained broadly fixed throughout the nematic phase, supporting the assumption of a temperature independent bend angle in the experimental measurements of order parameters for this system. Similarly, C4-Ph-ODBP-Ph-C7 also displayed a fixed and largely temperature independent bend angle throughout the nematic phase.

The nematic phase structure of C5-Ph-ODBP-Ph-OC12 deduced through the analysis of various RDFs and pair correlation functions, does not fully support the model of cybotactic organization of molecules into strongly temperature dependent SmC type clusters. Although there is some indication of segregation of the alkoxy chains, particularly at the lower temperatures, the results suggest that the nematic

phase predominantly consists of a temperature independent cluster size of a few molecules in the transverse direction. The evidence for local ordering of molecules into layers is very weak. The results for C4-Ph-ODBP-Ph-C7 indicate that the local packing of molecules in the nematic phase is less organized and very short ranged, and therefore more comparable with an ordinary nematic with only short range correlation between nearest neighbour molecules.

Molecular shape comparisons between the two mesogens, obtained through the analysis of average aspect ratios and shape biaxiality, show very little difference in their respective nematic phases. However, the distributions of aspect ratios as a function of temperature showed some subtle differences and suggest a wider range of conformations for C5-Ph-ODBP-Ph-OC12 compared with those for C4-Ph-ODBP-Ph-C7.

The presence of one alkoxy terminal chain in C5-Ph-ODBP-Ph-OC12 with its associated structural and chemical features, was tentatively proposed as a possible explanation for the differences in structure and orientational order between the two ODBP mesogens. To test this, two minor independent parameter changes were made to the force field. Changing the torsional parameters of the alkoxy-aromatic core junction to mirror those of the alkyl-aromatic core junction, led to significant disruption of the ribbon like nanostructures, as well as a small reduction in the uniaxial and biaxial order parameters. Eliminating the outer dipole for the alkoxy core junction had a similar, if less pronounced effect on both structure as well as orientational order. These results suggest that the combination of an alkoxy and alkyl terminal chains may be important in defining the specific characteristics of the C5-Ph-ODBP-Ph-OC12 system.

Finally, and while not the primary initial focus of this study, the simulations of the C5-Ph-ODBP-Ph-OC12 system indicate a second phase transition into the DC phase at a temperature close to the experimental value ($\sim$10 K). However, further analysis is needed to confirm this and to fully characterize this specific DC phase.

Chapter 6

Investigation into the Influence of the Addition of Methyl Groups to Oxadiazole Based Mesogens on the Nematic Phase Molecular Organization

6.1 Introduction

During the latter stages of the research undertaken for this thesis, an interesting study reported the first definitive X-ray diffraction (XRD) evidence of local biaxial order in the nematic phase for two members of the *bis*-(phenyl)oxadiazole family of bent-core mesogens, possessing three laterally substituted methyl groups (trimethylated-ODBP mesogens).[182,183] This was not observed for the non-methylated and monomethylated derivatives (see Figure 6.1 for structures of compounds investigated).

In contrast to compounds 1 to 3, the trimethylated-ODBP mesogens, compounds 4 and 5, show a much reduced nematic onset temperature as well as nematic phases that can be supercooled down to room temperature. All of the five compounds however, exhibited the 4-spot small-angle (SA) XRD pattern which for most bent-core

nematics, (BCNs), is generally accepted to be indicative of the presence of cybotactic groups, characterized by short-range smectic positional order and assumed intrinsic biaxial order (although it is noted that this interpretation of the 4-spot pattern may not be fully applicable to the BCNs, C4-Ph-ODBP-Ph-C7 and C5-Ph-ODBP-Ph-OC12 discussed in Chapter 5).

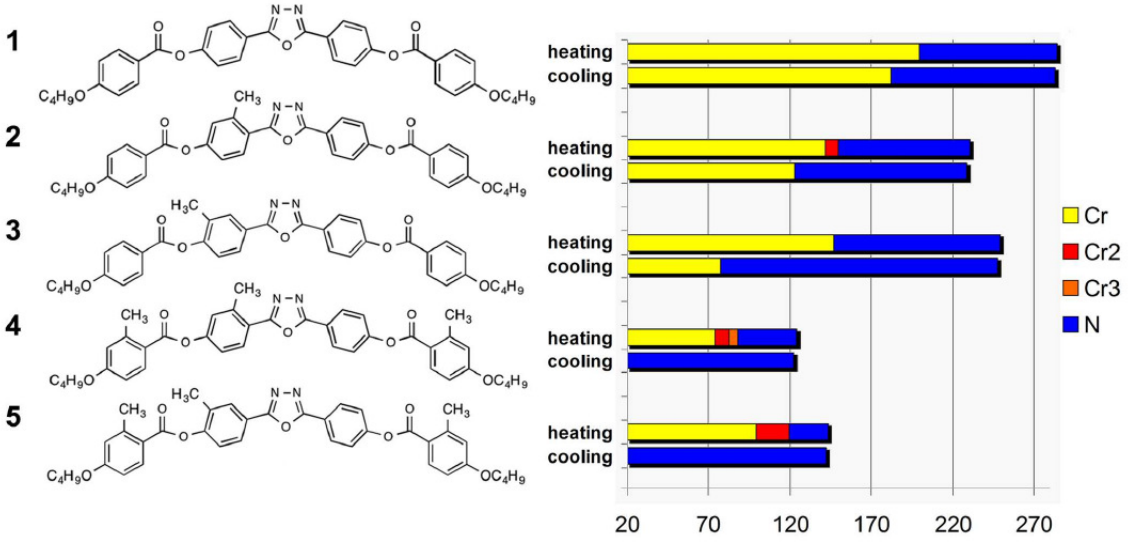

Figure 6.1: The molecular structures and corresponding phase transitions (on initial heating and cooling) of five ODBP bent core mesogens. Temperature are given in °C. Reprinted with permission from Vita *et al.*, Chemistry of Materials, 26, Copyright 2014 American Chemical Society.[183]

The interesting findings obtained from the investigations of the trimethylated-ODBP mesogens did not arise from the SA-XRD data, but instead from the wide-angle (WA) XRD data. The WA diffraction patterns reflect the mesogens ordering in the lateral direction (i.e. orthogonal to **n**, the average orientation of the molecular long axes). In contrast to typical bent-core mesogens, including compounds 1 to 3, which show a single, broad diffuse peak in the WA region irrespective of temperature, the trimethylated-ODBP mesogens 4 and 5 displayed markedly different XRD patterns, with the splitting of the WA XRD into two distinct peaks related to two intermolecular distances in the transverse plane orthogonal to the primary director, **n** (see Figure 6.2). The values of the d-spacings obtained from these peak positions for both compounds showed two distinct lateral distances, $d_1 \approx 5.0$ Å and $d_2 \approx$

3.8 Å, with d_2 being typical of the face-to-face distance between stacked π-systems and d_1 close to the width of a planar phenyl ring, with the latter comparable to the typical intermolecular distance normally observed in conventional uniaxial nematics, including BCNs.[102,115,182] The difference between d_1 and d_2 decreased slightly with increasing temperature but was still $\geq$ 1.0 Å on approaching the T_{NI} temperature. The d-spacings for compounds 1 to 3 on the other hand, were characterized by a single average d-spacing of $\approx$ 4.4 Å to 4.8 Å. This indicates that the differences in the mean lateral distances for compounds 1 to 3 are not great enough to be detected and resolved into two distinct diffraction peaks, even though the cybotactic clusters are assumed to be biaxial. However, for compounds 4 and 5 the differences in the lateral distances are large enough to be detected.

Additional information deduced from the XRD data gave two different correlations lengths for the trimethylated compounds, 4 and 5, corresponding to directions along the transverse, **m** and **l** directors (see Figure 6.2). These were $\approx$ 10 to 12 Å (or $\approx 2d_1$) along **m** and $\approx$ 17 to 19 Å (or $\approx 4-5d_2$) along **l**. The authors claimed that the latter value implies that the close packing constraints for compounds 4 and 5 favours the face-to-face stacking of aromatic cores more strongly than their in-plane arrangement. This is in contrast to that found for compounds 1 to 3 for which a single transverse correlation length of $\approx$ 13 Å was obtained, a value expected for ordinary nematics whose liquid-like positional order only corresponds to nearest-neighbour correlations.[183]

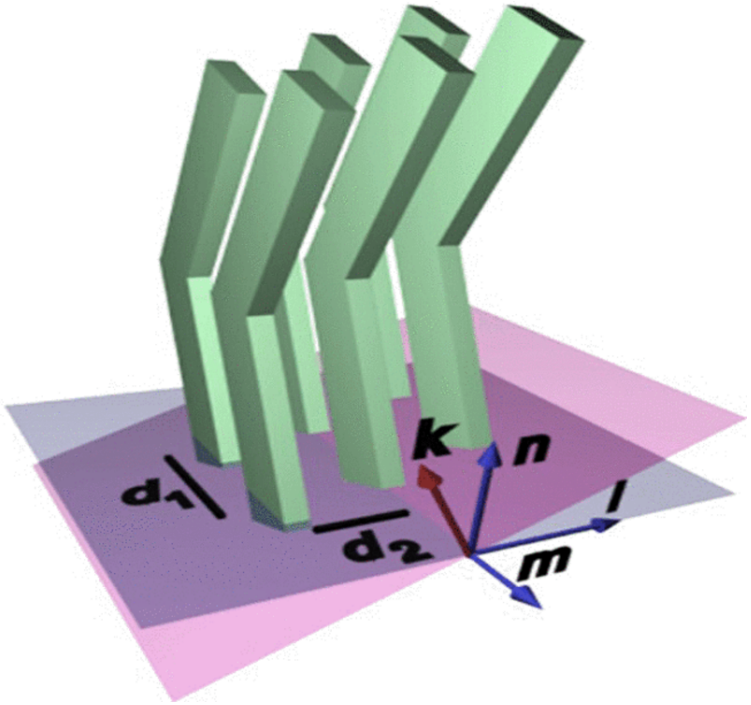

Figure 6.2: Schematic drawing of the molecular ordering within a cybotactic cluster: **k** indicates the normal to the smectic plane (purple); **n**, **m** and **l** are the three orthogonal molecular directors; and d_1 and d_2 are the intermolecular distances in the plane normal to **n**. Reproduced from reference[103] with permission of the American Physical Society.

The authors concluded that the unique WA splitting for the trimethylated compounds, 4 and 5, reflects a higher degree of local biaxial order compared to other related compounds. The authors also state that as the molecular shape biaxiality of the trimethylated compounds does not differ significantly from compounds 1 to 3 (and most of the BCNs reported so far in the literature), the enhanced biaxial order is possibly due to stronger anisotropic interactions between nearest-neighbour mesogens. This, they suggest, could be the result of the methyl substituents on the outer phenyl rings of the aromatic core leading to specific conformations which promote enhanced molecular packing in the transverse direction.

The initial XRD study of the trimethylated compounds 4 and 5, did not determine whether the biaxial order in the nematic phase extends beyond the size of the cybotactic clusters (i.e. on a macroscopic scale). A very recent study of these compounds employing a combination of XRD and optical studies suggests that the biaxial order is expressed differently at the short and long-range scales.[103] At the

local scale of a few molecules, the data demonstrated biaxial order, but on a macroscopic length scale the data showed uniaxial orientational ordering in the nematic phase including the supercooled region of the nematic. However, the authors of this study stress that the enhanced local biaxial order diplayed by these trimethylated mesogens is unique compared with other BCNs and suggest that variants of these molecules may have the potential to extend the local biaxial correlations to the macroscopic scale.

The objectives for this chapter were to use fully atomistic simulations, utilizing the GAFF-LCFF force field, to compare the nematic phase biaxial orientational order and short-range transverse positional order of one of the trimethylated mesogen (compound 5 in Figure 6.1) reported to show enhanced local biaxial order, with those for the parent non-methylated mesogen C4O-Ph-ODBP (compound 1 in Figure 6.1) that does not exhibit enhanced biaxial correlations. Comparisons between molecular shape, dimensions and bend angle were also examined. Where possible, it was intended to compare any simulated features with the experimental observables for these mesogens. The objectives for this particular investigation were necessarily limited due to time pressures, but proposals for further investigations that could not be addressed in this thesis are noted in Chapter 7 . Firstly, however it was necessary to test GAFF-LCFF on the predictions of the experimental T_{NI} temperatures for both the trimethylated-ODBP and C4O-Ph-ODBP mesogens, in order to test its effectiveness at modelling molecules with similar chemical structures to the ODBP mesogens investigated in Chapter 5. These results are presented in Section 6.3.

6.2 Computational details

The MD simulations of both the trimethylated-ODBP and C4O-Ph-ODBP mesogens consisted of a cubic box containing 256 molecules. Each system was started from a disordered configuration and then progressively cooled at 10 K intervals with equilibration runs of 60 ns and production runs of 120 ns. The results of the simulations relate to ensemble averages over the final 60 ns of production trajectories, unless otherwise stated. (Note: full details of molecule preparation and simulation

methods are given in Chapter 3, Section 3.3). Larger system sizes were not explored within this chapter due to time and CPU capacity constraints.

The uniaxial order parameter, $\langle P_2 \rangle$, was calculated as the largest eigenvalue obtained from diagonalization of the ordering matrix, Q, with the chosen molecular reference axis (z axis) representing a vector parallel with the aromatic core (see axis 1 in Figure 6.3). The nematic phase biaxiality was explored by measuring the differences in the ordering of the molecular x and y axes with respect to the director X and Y axes, given by $\langle Q_{22}^2 \rangle$ and with molecular axes, x and y defined as orthogonal to the z axis of the mesogen aromatic core (see Chapter 3 and Section 3.5.1 for full details on measuring orientational order). Structural organization was inferred from the calculations of various pair distribution functions, including $g(r)$, $g_1(r\ )$ and $g_\perp(r)$ (see Chapter 3 and Section 3.5.1 and 3.5.2 for full details and equations for measuring orientational order and structural organization).

6.3 Results and discussion

6.3.1 Testing GAFF-LCFF

Trimethylated-ODBP

Figure 6.3 shows the chemical structure and experimental phase transition temperatures for the trimethylated-ODBP mesogen. This mesogen can also be supercooled to room temperature in a metastable, highly viscous nematic state.[183]

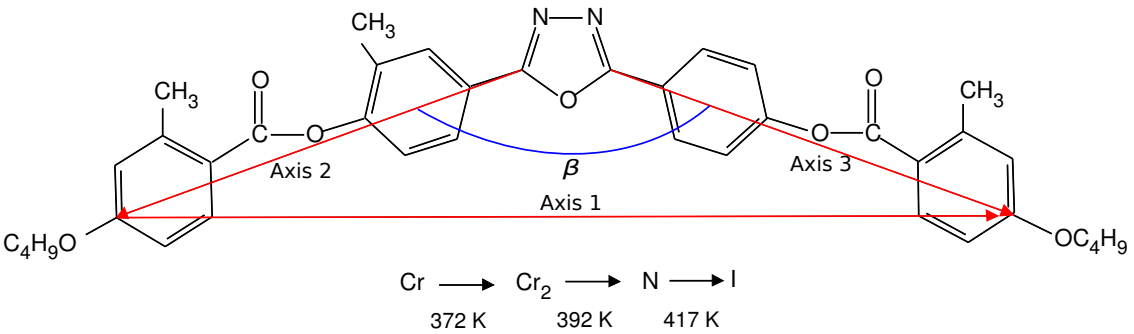

Figure 6.3: The chemical structure and experimental phase transition temperatures for the trimethylated-ODBP mesogen. The molecular reference axes and bend angle, β are also shown.

An estimate of T_{NI} for the trimethylated-ODBP with the original GAFF force field resulted in a T_{NI} of $\approx$ 60 K greater than experiment, and although not as great a divergence as the estimates for the C4-Ph-ODBP-Ph-C7 and C5-Ph-ODBP-Ph-OC12 mesogens ($\approx$ 100 K too high) this was still considered to represent a major discrepancy. With the exception of the C-C-C-C torsional parameters, the GAFF-LCFF parameters were transferred to the trimethylated-ODBP and C4O-Ph-ODBP mesogens. (See Chapter 4, Tables 4.7 and 4.12 for amended torsional and vdW parameters respectively). As both compounds possess very short alkoxy (OC4) chains, it was decided to retain the original GAFF LJ parameters for the C4 fragment of the terminal chains, as estimates for density and $\Delta_{\mathrm{vap}}H$ for butane with the original GAFF force field were in good agreement with experimental values.[184] The C-C-C-C torsional parameters however, were adopted from GAFFLipid (see Chapter 4, Table 4.16 for new RB coefficients).

Figure 6.4 shows P_2 values calculated as a function of decreasing temperature and averaged over the final 60 ns of production runs (blue symbols). The tem-

peratures extend down to room temperature ($\approx$ 300 K) to include the expected supercooled nematic region for this system. A gradual increase in these values is observed, from effectively isotropic with $\langle P_2 \rangle < 0.3$ at 430 K and above, to $\langle P_2 \rangle \geq 0.4$ at 420 K and below. This indicates a transition to a more ordered phase has occurred in the vicinity of 420 K, although the magnitude of $\langle P_2 \rangle$ values does not show the usual characteristic jump (weak first-order transition), associated with a nematic to isotropic (NI) phase transition. However, averaging P_2 over the full 120 ns of production run close to the phase transition (red symbols) shows a more pronounced jump in $\langle P_2 \rangle$ between 420 and 410 K, after which$\langle P_2 \rangle$ stabilizes to almost identical values regardless of whether the averages are calculated over 60 or 120 ns of production trajectories. It appears that there are considerable fluctuations in P_2 close to the phase transition, which result in larger differences in $\langle P_2 \rangle$ depending on the length of time these averages are calculated over. This effect was also observed for the ODBP mesogens previously investigated (see Chapter 4, Section 4.6.1) as well as in other atomistic simulations of liquid crystal systems showing NI phase transitions.[138,169]

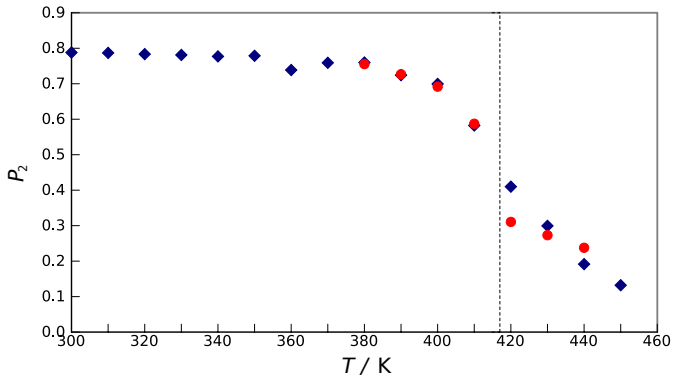

Figure 6.4: The averaged uniaxial order parameters for the trimethylated-ODBP system and for $N = 256$ molecules. The blue symbols = $\langle P_2 \rangle$ over 60 ns and red symbols =$\langle P_2 \rangle$ over 120 ns. The dotted line represents the experimental T_{NI} .

These results indicate that for the trimethylated-ODBP system, GAFF-LCFF is sufficiently accurate at predicting an ordering transition very close to the experimental T_{NI} of 417 K . This is particularly encouraging as the partial re-parametrization process described in Chapter 4, derived new parameters for the phenyl acetate/phenyl benzoate and *bis*-phenyl-oxadiazole (ODBP) fragments which do not possess later-

ally substituted methyl groups. This suggests that GAFF-LCFF is readily transferable to a variety of ODBP bent-core derivatives with chemically similar structures, with or without additional methyl substituents.

C4O-Ph-ODBP

Figure 6.5 shows the chemical structure and experimental phase transition temperatures for the C4O-Ph-ODBP mesogen. It can be seen that the nematic onset temperature of 558 K is significantly higher than that for the trimethylated-ODBP mesogen (417 K) and this demonstrates the impact of the inclusion of methyl substituents on the mesogen core, on reducing the T_{NI} .

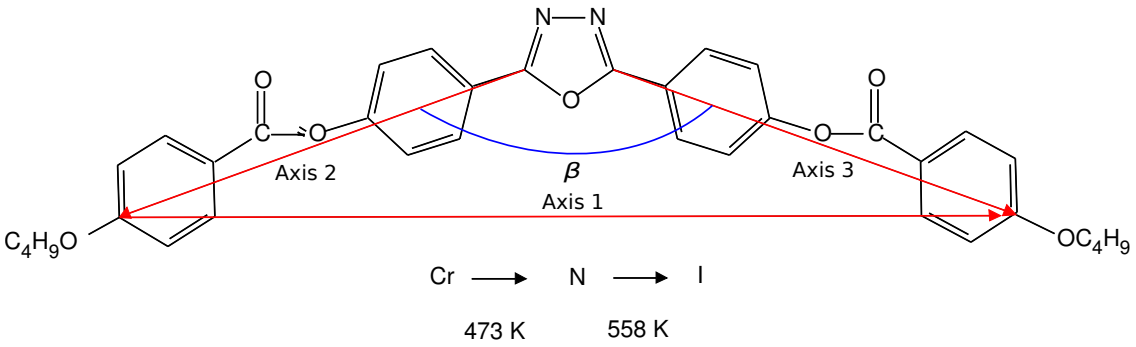

Figure 6.5: The chemical structure and experimental phase transition temperatures for the C4O-Ph-ODBP mesogen. The molecular reference axes and bend angle, β are also shown.

The uniaxial order parameter, $\langle P_2 \rangle$ calculated as a function of decreasing temperature for the C4O-Ph-ODBP system is shown in Figure 6.6. The blue and red symbols represent averages over 60 ns and 120 ns of production trajectories respectively. The system appears isotropic above 560 K ($\langle P_2 \rangle < 0.3$) and ordered at 550 K and below ($\langle P_2 \rangle \geq 0.4$). There appears to be a greater fluctuation in $\langle P_2 \rangle$ at 550 K, as larger differences in this value are obtained depending on the length of trajectory the averages are calculated over. This suggest that the system is close to a phase transition at 550 K which is in very good agreement with the experimental value of 553 K and indicates that the GAFF-LCFF is also readily transferable to this system as well as to the trimethylated-ODBP system.

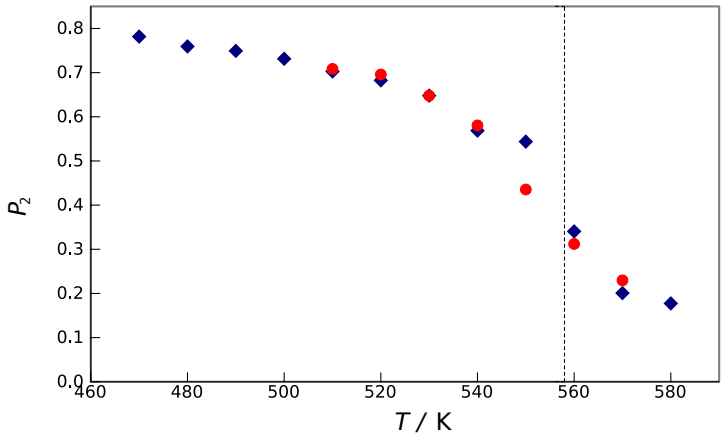

Figure 6.6: The averaged uniaxial order parameters for C4O-Ph-ODBP and for N = 256 molecules. The blue symbols = $\langle P_2 \rangle$ over 60 ns and red symbols =$\langle P_2 \rangle$ over 120 ns. The dotted line represents the experimental T_{NI}.

6.3.2 Biaxial orientational order

Trimethylated-ODBP

Figure 6.7 shows the biaxial order parameter, $\langle Q_{22}^2 \rangle$, calculated as a function of decreasing temperature and averaged over the final 60 ns of the production trajectories. Overall, the magnitude of $\langle Q_{22}^2 \rangle$ is small and variable throughout the nematic phase, including the super cooled region and close to the T_{NI} in the isotropic phase. This could be a result of local biaxial fluctuations in a small system. There is evidence however, of a small overall increase in $\langle Q_{22}^2 \rangle$ at the T_{NI} temperature of 417 K down to 350 K, after which there is an abrupt decrease to insignificant values with decreasing temperature. These results support the experimental evidence from XRD and optical measurements for the trimethylated-ODBP system,[103] which suggest that the biaxial order is very short-ranged, encompassing no more than a few molecules, and that on a macroscopic scale the orientational order is uniaxial. Although a system size of N= 256 molecules is considered small, it is probable that any significant local biaxial order on the scale of a few molecules is averaged out and therefore reduced when values are calculated over 256 molecules.

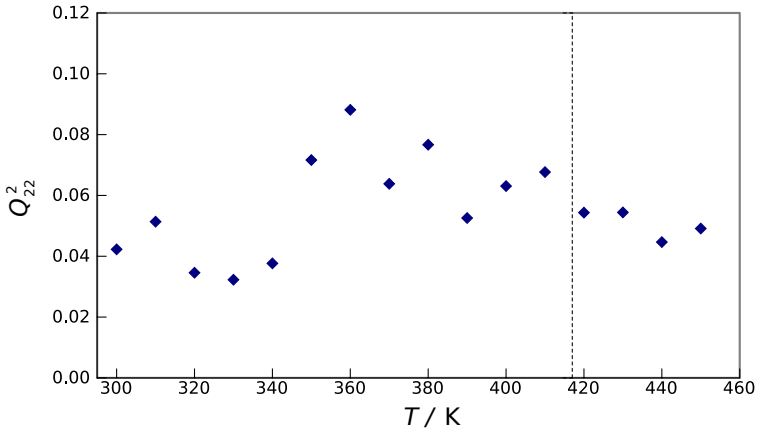

Figure 6.7: The averaged biaxial order parameters for the trimethylated-ODBP system and $N = 256$ molecules. The dotted line represents the experimental T_{NI} .

C4O-Ph-ODBP

Figure 6.8 shows the biaxial order parameter, $\langle Q_{22}^2 \rangle$, calculated as a function of decreasing temperature and averaged over the final 60 ns of the production trajectories.

These results again show limited biaxiality, with a small but incremental increase in the magnitude of $\langle Q_{22}^2 \rangle$ in the nematic phase. In contrast to the trimethylated-ODBP system, $\langle Q_{22}^2 \rangle$ for the C4O-Ph-ODBP system appears more stable and without the fluctuations noted in Figure 6.7. Overall, the $\langle Q_{22}^2 \rangle$ values are small, and again these results suggests that any local biaxial ordering of molecules, if present in this system, coexists with macroscopic uniaxial orientational order, as proposed by Kim *et al.*[103]

Interestingly, and in contrast to the non-methylated ODBP bent-core systems investigated in this thesis, only the trimethylated-ODBP system shows a distinctly variable pattern of biaxiality (albeit still at low levels) throughout the cooling process, which is not evident for the non-methylated compounds which all show a small but gradual increase in the biaxial order parameter with decreasing temperature.

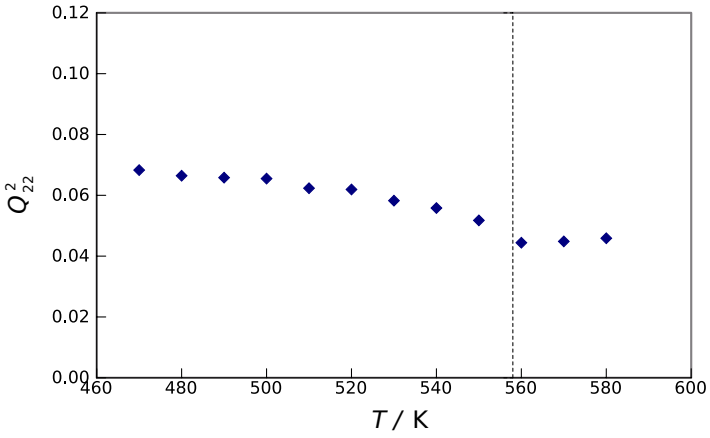

Figure 6.8: The averaged biaxial order parameters for the C4O-Ph-ODBP system and $N = 256$ molecules. The dotted line represents the experimental T_{NI} .

6.3.3 Molecular organization

Trimethylated-ODBP

According to Vita *et al.*, the XRD measurements obtained for the trimethylated-ODBP mesogens clearly indicate that the face-to-face stacking of aromatic cores is more favourable than the in-plane arrangement and that this is distinctly different from that observed for other typical BCNs. In order to establish whether the results from the simulations also reflect this local arrangement of the trimethylated-ODBP mesogens in the nematic phase, the radial distribution functions, $g(r)$, $g_{\perp}(r)$ and the orientational distribution function, $g_1(r)$ was calculated for the central oxadiazole ring 1 and the two adjacent phenyl rings 2 and 3 of the ODBP core of the trimethylated-ODBP mesogen (see Figure 6.9 for labelled rings and atom numbers).

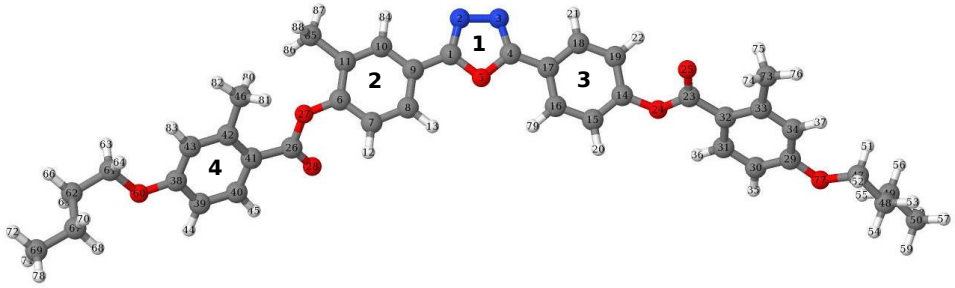

Figure 6.9: Trimethylated-ODBP

Figure 6.10a shows $g(r)$ for the oxadiazole pairs (ring 1), calculated with respect to the oxadiazole centres of mass and for two different temperatures, representing the high and low region of the nematic phase. An initial contact peak occurs at $\approx$ 4.1 Å at 390 K, decreasing down to $\approx$ 3.9 Å at 330 K. These intermolecular distances are close to the typical distance between face-to-face stacking of $\pi-$systems ($\approx$ 3.8 Å) and to the intermolecular d_2 distance of $\approx$ 3.9 Å obtained from the WA XRD measurements in reference[183] for the trimethylated-ODBP mesogens (see Figure 6.2). An additional small peak occurs at $\approx$ 6.0 Å, followed by two further peaks at $\approx$ 8.8 Å and 13 to 15 Å for both temperatures, indicating the presence of at least four local coordination shells. The extent of the short-range positional order, and hence correlation lengths, are $\approx$ 16.0 Å at 390 K, increasing to $\approx$ 20.0 Å at 330 K. These values are greater than the lateral correlation distance of $\approx$ 13.0 Å displayed by conventional nematics, including BCNs, and are closer in value to the correlation lengths of $\approx$ 17 to 19 Å associated with the transverse director**, l,** and hence the d_2 direction obtained from the WA XRD data. It is not possible to extract from $g(r)$ alone the two distinct transverse intermolecular distances, d_1 and d_2 described in reference.[183] However, the distance at which the first peak occurs is only compatible with the face-to-face stacking of neighbouring oxadiazole rings and therefore is very likely to represent the d_2 intermolecular distance shown in Figure 6.2.

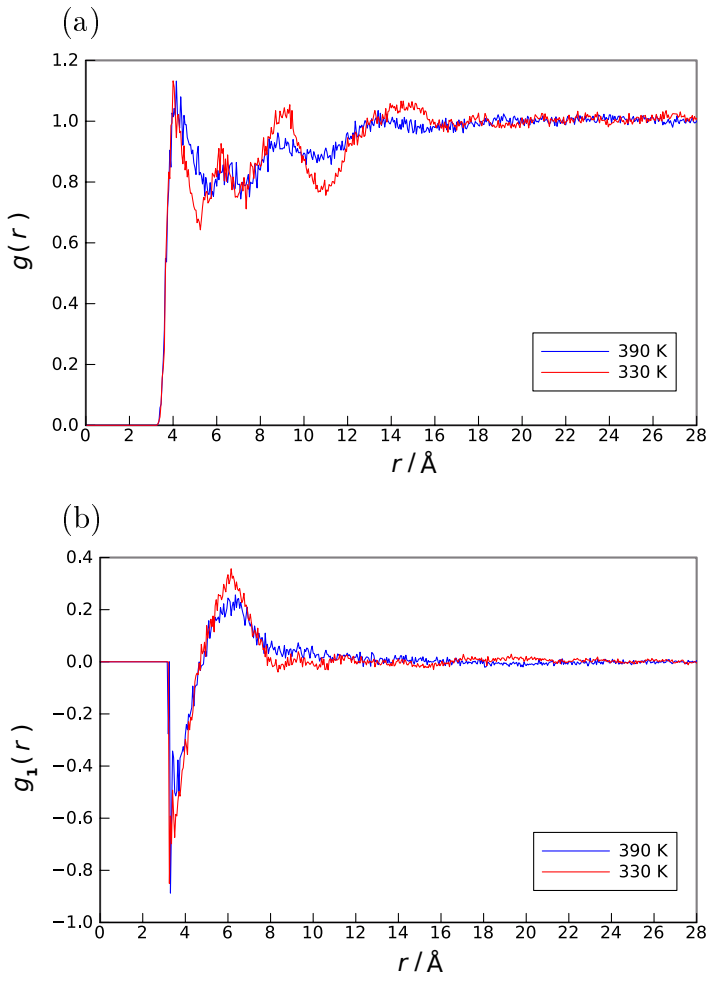

Figure 6.10: (a) The radial distribution function for the oxadiazole pairs (ring 1) of the trimethylated-ODBP mesogen. (b) The orientational distribution for the dipole-dipole pairs.

To gain insight into the geometrical arrangement between nearest neighbour molecules the orientational distribution function, $g_1(r)$ for the steric dipole (N to O) across the oxadiazole ring was calculated and is shown in Figure 6.10b. At short range and up to $\approx$ 4.6 Å, $g_1(r\ )$ is clearly negative and this region also coincides with the first peak of $g(r)$ for the oxadiazole pairs shown in Figure 6.10a. These results suggest that the neigbouring oxadiazole pairs prefer an anti-parallel arrangement of the steric dipoles, although it is noted that some $g_1(r)$ values are higher than -1, indicating some deviations from the perfect anti-parallel arrangement.

The radial distribution function, $g_\perp(r)$ can be used to monitor the intermolecular separation in the transversal direction, perpendicular to the system director, **n**. Figure 6.11 shows $g_\perp(r)$ for the oxadiazole pairs at 390 and 330 K. For both

temperatures, an initial peak occurs at ≈ 3.9 Å followed by additional peaks at regular intervals of ≈ 4.0 Å, with these becoming more pronounced and increasing in number at 330 K. These results also suggest face-to-face stacking, as opposed to an in plane arrangement, of the oxadiazole pairs, and that this arrangement becomes stronger and more long ranged with decreasing temperature.

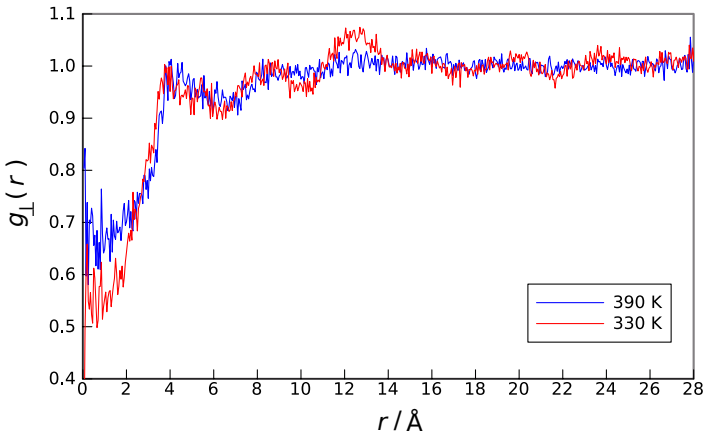

Figure 6.11: The radial distribution function along the direction perpendicular to the director, **n**, for the oxadiazole pairs of the trimethylated-ODBP mesogen.

Additional information on the arrangement of the nearest-neighbour molecules is provided by the distribution function for each of the phenyl-2 and phenyl-3 pairs adjacent to the oxadiazole ring 1, where the reference points are defined as the centres of the C6-C9 and C14-C17 vectors (see Figure 6.9 for ring numbers and atom labels). As seen in Figure 6.12a and Figure 6.12b, $g(r)$ shows an initial weak contact peak at ≈ 3.9 Å for both the phenyl-2 and phenyl-3 pairs and at both temperatures (390 and 330 K). These initial peaks occur at an intermolecular distance that is too small to represent an in-plane alignment of the phenyl-2 and phenyl-3 pairs, but instead are more compatable with the face-to-face stacking of the phenyl pairs.

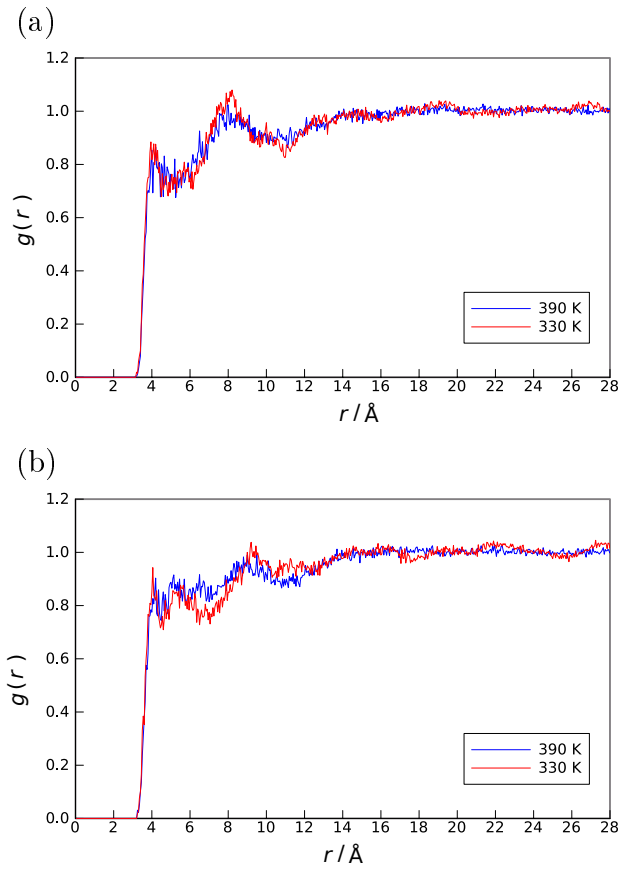

Figure 6.12: The radial distribution function for (a) phenyl-2 pairs and (b) phenyl-3 pairs of the trimethylated-ODBP mesogen.

However, the proposed anti-parallel arrangement of nearest-neighbour molecules deduced from the alignment of the steric dipoles (see Figure 6.10b) would result in the phenyl-2 and phenyl-3 pairs being displaced with respect to the face-to-face configuration due to the bent structure of the mesogens. It is therefore possible that these initial weak peaks at $\approx$ 3.9 Å are due to the presence of a third molecule in the first coordination shell, which adopts an in-plane arrangement with the second molecule, but a displaced anti-parallel arrangement with respect to the reference molecule. This is consistent with the $g_1(r)$ results for the oxadiazole central ring 1. A schematic of a possible preferred arrangement of nearest-neighbour molecules is shown in Figure 6.13. In this case the phenyl-2 and phenyl-3 pairs in molecules 1 and 3 could adopt a face-to-face configuration with the associated small separation distance of $\approx$ 3.9 Å.

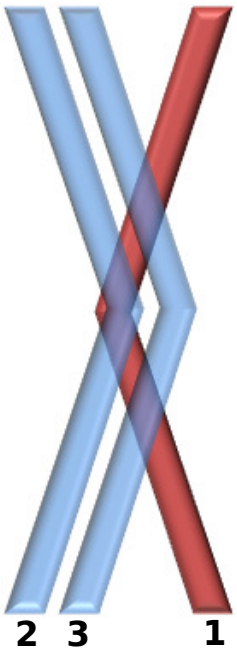

Figure 6.13: Schematic of proposed arrangement of nearest-neighbour molecules for the trimethylated-ODBP mesogen. Molecule 1 represents the reference molecule.

Following this weak initial contact peak at $\approx$ 3.9 Å for both the phenyl-2 and phenyl-3 pairs at both temperatures, the structure of $g(r)$ then differs somewhat between the two pairs (see Figure 6.12). A stronger secondary peak is observed for the phenyl-2 pairs at $\approx$ 7.8 Å, whereas further small intermediary peaks followed by more pronounced peaks at $\approx$ 8.8 Å and $\approx$ 9.0 Å for 390 and 330 K respectively are found for the phenyl-3 pairs. These stronger peaks are possibly due to the correlation between the phenyl pairs of molecules 1 and 2, in which case the separation distances between these pairs would be greater due to the anti-parallel arrangement of these two molecules. It is likely that the structure of $g(r)$ for each phenyl pair is different due to the presence or absence of a methyl group on the phenyl rings.

To gain additional information about the nearest-neighbour configuration, $g(r)$ and $g_1(r)$ were calculated for the inner methyl pairs (attached to the phenyl-2 rings and approximated by a position and direction represented by the atoms C11 to C85) and the outer methyl pairs (attached to the phenyl-4 rings and approximated by a position and direction represented by the atoms C42 to C46). See Figure 6.9 for ring

numbers and atom labels. As presented in Figure 6.14a, $g(r)$ for the inner methyl pairs shows an initial contact peak at $\approx$ 4.8 Å for both temperatures, although this peak is more pronounced at 330 K. Additional peaks in $g(r)$ are also observed at 330 K, suggesting greater correlation of these pairs at this temperature. The distance dependent orientation of these inner methyl pairs deduced from $g_1(r)$ and presented in Figure 6.14b shows a small negative peak at $\approx$ 4.8 Å at both 390 and 330 K. The distance at which these negative peaks occur coincide with those for the initial contact peaks shown in $g(r)$ and again suggests a tendency towards an anti-parallel arrangement of the adjacent methyl pairs of molecules 1 and 2 in Figure 6.13.

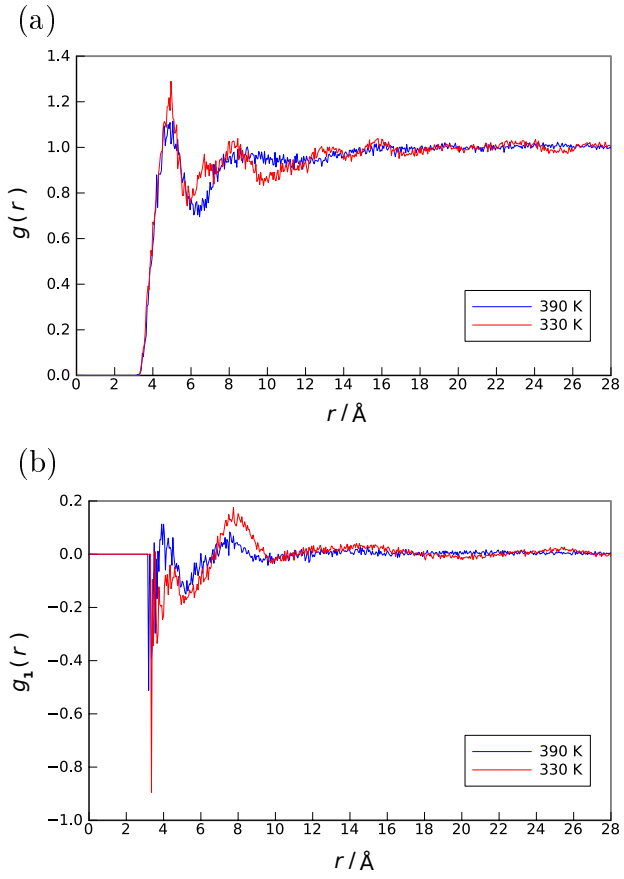

Figure 6.14: (a) The radial distribution function for the inner methyl pairs (attached to phenyl ring 2). (b) The orientational distribution function for the inner methyl pairs.

The form of $g(r)$ for the outer methyl pairs (attached to the phenyl-4 rings) presented in Figure 6.15a at both 390 and 330 K, shows an initial contact peak at $\approx$ 4.9 Å followed by very little structure in the long range. The intensity of these

peaks is less than that observed for the inner methyl pairs at the corresponding temperatures. A small negative peak at the same distance of ≈ 4.9 Å is also apparent in $g_1(r)$ for the outer methyl pairs (see Figure 6.15b), again suggesting a tendency towards an anti-parallel arrangement of these pairs. However, it is highly unlikely that the first peaks of the pair distribution functions for the outer methyl pairs relate to molecules 1 and 2 in Figure 6.13, due to the anti-parallel arrangement of the bent-core structure, as this would lead to greater distance between the adjacent outer methyl groups. It is therefore considered more likely that these results represent correlations between the outer methyl groups of molecules 1 and 3 from Figure 6.13. This interpretation would however, be based on the assumption that the prevalent molecular confirmations of the aromatic core favours the outer methyl group on the outside of the bent-core structure.

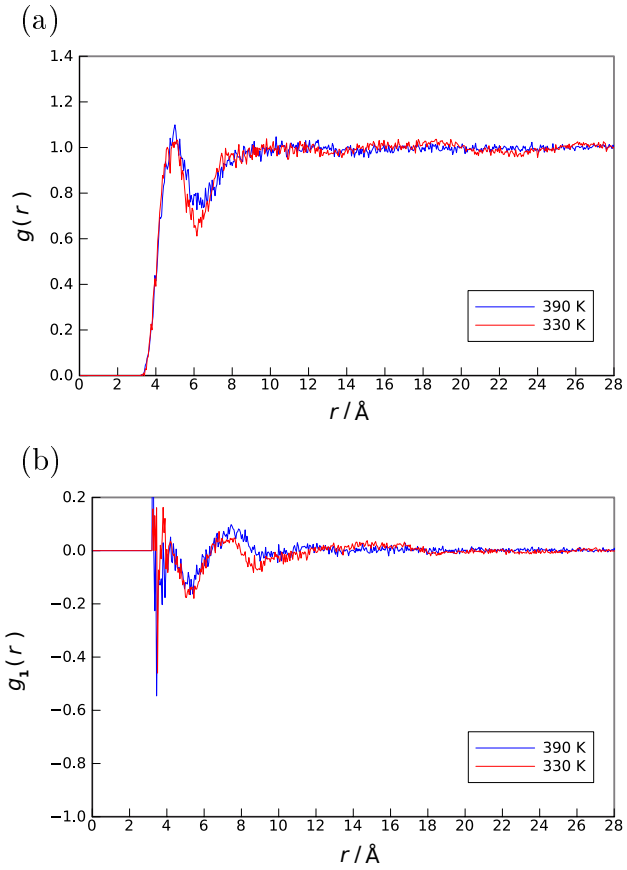

Figure 6.15: (a) The radial distribution function for the outer methyl pairs (attached to phenyl ring 4). (b) The orientational distribution function for the outer methyl pairs.

These results suggest that there is a degree of correlation for each of the inner and outer methyl pairs, in particular for the inner methyl pairs. However, the presence of methyl groups on the inner phenyl ring (ring 2) does not appear to be critical to the establishment of enhanced local biaxial order, as the monomethylated ODBP mesogens reported by Vita *et al.*[183] possessing only a single methyl group on the inner phenyl ring (molecules 2 and 3 in Figure 6.1) are not reported to show enhanced biaxial correlations. This suggests that the presence of the outer methyl groups, either with or without an additional inner methyl group, is particularly significant in determining the enhanced biaxial order displayed by the trimethylated-ODBP mesogen.

Collectively, these initial results obtained from the calculation of various pair distribution functions for different groups of the trimethylated-ODBP mesogen, suggest a possible preferred nearest-neighbour configuration that differs from the molecular ordering proposed in references[103,182] (see Figure 6.2 for their schematic drawing of the molecular ordering). Their suggested arrangement shows molecules closely packed in a parallel face-to-face configuration, which accounts for the differential d -spacings obtained from the WA XRD data. While the results from the simulations support the face-to-face and hence close packing of nearest-neighbour molecules, in contrast to the molecular ordering depicted in Figure 6.2, the simulations suggest that the central row adopts an anti-parallel configuration with respect to neighbouring molecules. This arrangement would still maintain the key features of face-to-face packing of the aromatic ODBP cores as well as the two distinct d -spacings deduced from the WA XRD data.

C4O-Ph-ODBP

In contrast to the trimethylated-ODBP system, the XRD measurements performed by Vita *et al.* on the non-methylated C4O-Ph-ODBP system resulted in WA patterns typical of ordinary nematics. In order to compare the average transverse intermolecular distances and possible geometric arrangement between the nearest-neighbour molecules in the nematic phase of the two ODBP systems, $g(r)$, $g_{\perp}(r)$ and the orientational distribution function, $g_1(r)$ were also calculated for C4O-Ph-

ODBP for various rings of the aromatic core (see Figure 6.16 for labelled rings and atom numbers).

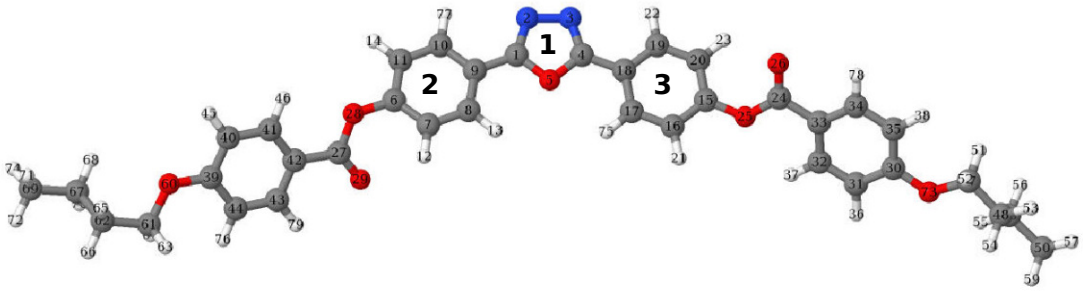

Figure 6.16: C4O-Ph-ODBP

Figure 6.17a shows $g(r)$ for the oxadiazole pairs (ring 1), calculated with respect to the oxadiazole centers of mass for two different temperatures, representing the high and low temperature region of the nematic phase. It can be seen that $g(r)$ shows a broad initial contact peak split into two minor subsidiary peaks, of which the first peak occurs at a distance of $\approx$ 4.8 to 4.6 Å and the second at $\approx$ 6.3 to 6.2 Å. The former distance is close to the average intermolecular distances of $\approx$ 4.6 to 4.3 Å obtained from the XRD data for this mesogen and the mono-methylated ODBP compounds described in reference.[183] In addition, this first peak occurs at a distance further away than that found for the analogous pairs of the trimethylated-ODBP mesogen, indicating that in the first coordination shell the face-to-face stacking of oxadiazole pairs is less favourable for the C4O-Ph-ODBP mesogen. The correlation lengths for the oxadiazole pairs appear largely temperature independent ($\approx$ 14 Å) and are significantly different from that observed for the trimethylated-ODBP system for which the extent of the short-range positional order increased to greater lengths with decreasing temperature (up to $\approx$ 20 Å). The correlation length of $\approx$ 14 Å for the C4O-Ph-ODBP system however, is as previously stated, typical of the transversal correlation lengths exhibited by ordinary nematics.

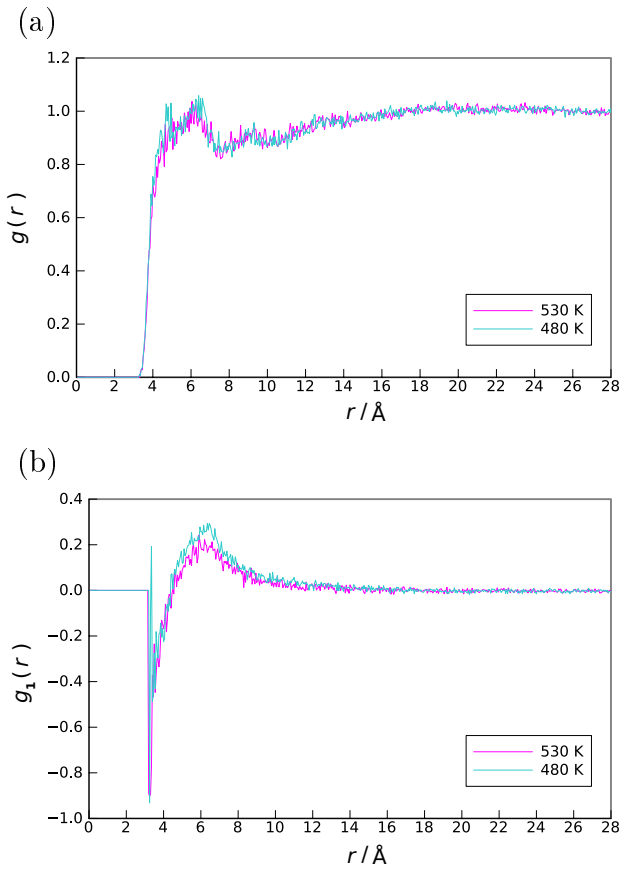

Figure 6.17: (a) The radial distribution function for the oxadiazole pairs (ring 1) of the C4O-Ph-ODBP mesogen. (b) The orientational distribution for the dipole-dipole pairs.

In contrast to that found for the trimethylated-ODBP mesogen, the orientational distribution function, $g_1(r)$ for the steric dipole across the oxadiazole ring 1, indicates a parallel arrangement of nearest-neighbour molecules, as the positive peak of $g_1(r)$ encompasses a distance of $\approx$ 4.5 to 8.0 Å, which also coincides with the initial peak of $g(r)$ for the oxadiazole pairs (see Figure 6.17b). The initial negative peak of $g_1(r)$ up to $\approx$ 4.5 Å, coincides with distances where there are very few nearest-neighbour interactions. This suggests that the anti-parallel arrangement of nearest-neighbour molecules observed for the trimethylated-ODBP mesogen is not a favourable arrangement for the C4O-Ph-ODBP mesogen pairs.

Additional differences between the two ODBP systems are apparent from examining the distribution function, $g_\perp(r)$, along the direction perpendicular to the system director. For example, $g_\perp(r)$ for the oxadiazole pairs of C4O-Ph-ODBP at both 530 and 480 K, shows an absence of structure beyond a small contact peak at

≈ 4.6 Å due to neighbouring molecules (see Figure 6.18). This is in contrast to that found for the oxadiazole pairs of trimethylated-ODBP mesogen, where $g_{\perp}(r)$, exhibited an initial peak at ≈ 3.9 Å followed by regular and more pronounced additional peaks, in particular at lower temperatures, indicating greater long range structure.

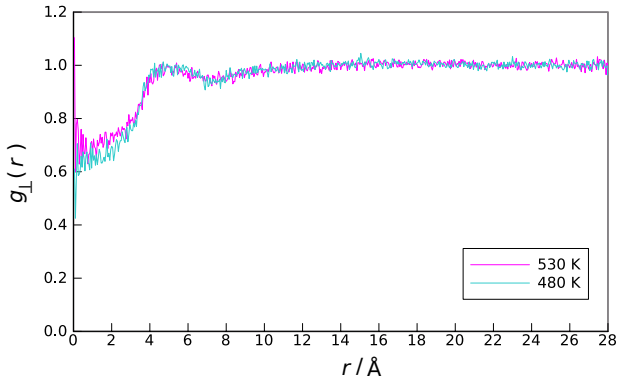

Figure 6.18: The radial distribution function along the direction perpendicular to the director, **n**, for the oxadiazole pairs of the C4O-Ph-ODBP mesogen.

The distribution functions, $g(r)$ were also calculated for each of the phenyl-2 and phenyl-3 rings with the reference points defined as the centre of these rings (see Figure 6.16). In contrast to that found for the analogous pairs of the trimethylated-ODBP mesogen, the short-range structure of $g(r)$ for both the phenyl-2 and phenyl-3 pairs of C4O-Ph-ODBP show almost identical features, with the presence of one initial peak of similar magnitude at ≈ 5.3 Å for both temperatures in the nematic phase (see Figure 6.19a and Figure 6.19b). These results, along with those for the oxadiazole pairs, suggest that the ODBP cores of the C4O-Ph-ODBP mesogens do not pack as tightly together as those of the trimethylated-ODBP mesogens and that the intermolecular distances reflect those of typical nematics, including typical BCNs.

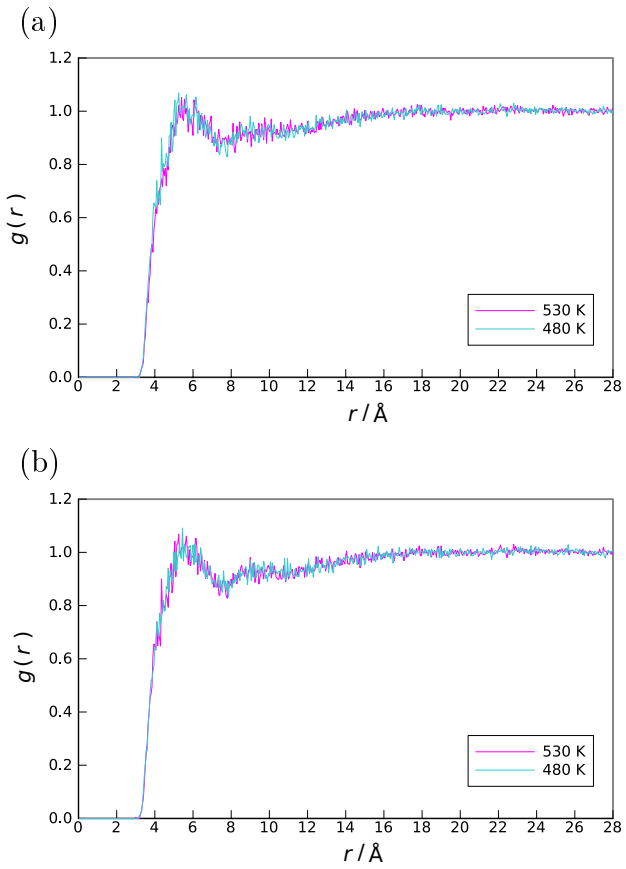

Figure 6.19: The radial distribution function for (a) phenyl-2 pairs and (b) phenyl-3 pairs of the C4O-Ph-ODBP mesogen.

6.3.4 Molecular shape comparisons

In order to make shape comparisons between the two mesogens, the molecular dimensions were obtained from the average moment of inertia tensor, $\langle I \rangle$ where $\langle I_1 \rangle$ $\langle I_2 \rangle$ and $\langle I_3 \rangle$ are the averaged principle moments of inertia. (See Chapter 4, Section 4.5.3 for the method of obtaining molecular dimensions from the simulations). Figure 6.20a and Figure 6.20b show the average molecular length as a function of temperature for both mesogens. The presence of laterally substituted methyl groups would not intuitively be expected to significantly affect the average molecular lengths and this is supported by the results in Figure 6.20a and Figure 6.20b. Both mesogens show a small temperature dependence, with average length increasing from ≈ 39 Å in the isotropic phase to ≈ 40 Å in the lower temperature region of their respective nematic phases.

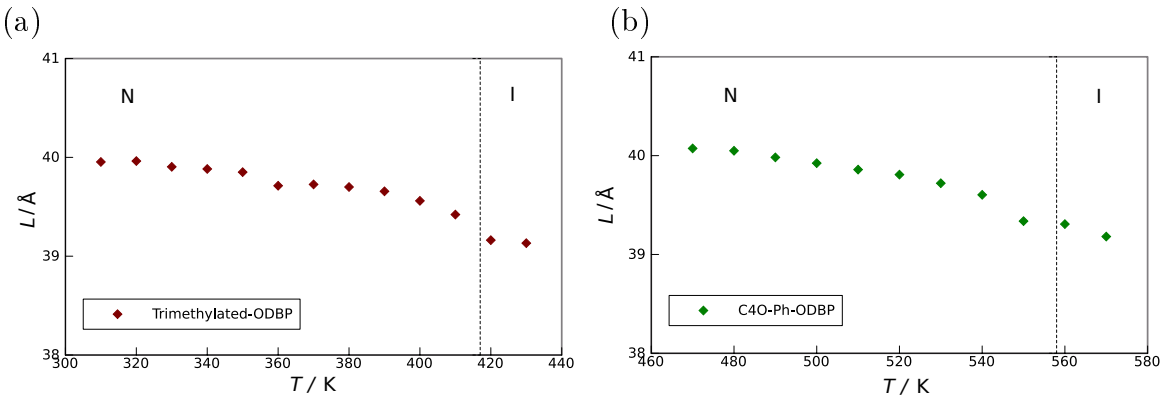

Figure 6.20: The average molecular length as a function of temperature for (a) trimethylated-ODBP and (b) C4O-Ph-ODBP. [Dotted vertical lines show the respective T_{NI}].

The average aspect ratios, (L/B) where L represents the length and B represents the (breadth + width) / 2 for each mesogen, provides an indication of their average shape anisotropy. It can be seen in Figure 6.21a and Figure 6.21b that this value generally increases with decreasing temperature, although the temperature dependent rate at which this increases is less for the trimethylated-ODBP mesogen compared with that for C4O-Ph-ODBP.

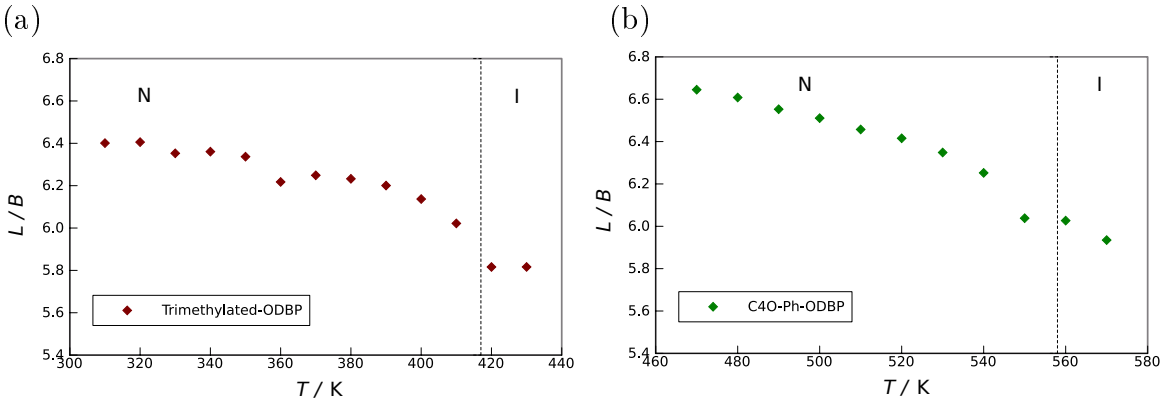

Figure 6.21: The average length to breadth ratio as a function of temperature for (a) trimethylated-ODBP and (b) C4O-Ph-ODBP. [Dotted vertical lines show the respective T_{NI}].

In the lower nematic temperature region, the L/B ratio approaches a value of ≈ 6.4 for trimethylated-ODBP, whereas for C4O-Ph-ODBP the L/B ratio approaches a slightly greater value of ≈ 6.6. This suggests that the laterally substituted methyl groups do have some impact on the average molecular dimensions, and in particular

increase the average breadth of the trimethylated-ODBP mesogen compared with that for the non-methylated C4O-Ph-ODBP mesogen.

Vita *et al.*, the authors of the study reporting the first XRD evidence of biaxial order in the cybotactic nematic phase of two trimethylated ODBP mesogens (described in Section 6.1) stated that the molecular shape biaxiality of these compounds did not differ significantly from that of the non- and mono-methylated derivatives, or from other typical BCNs reported so far in the literature, although it is not clear from their study how the molecular shape biaxiality was deduced. Figure 6.22a and Figure 6.22b shows the average molecular shape biaxiality parameter, λ obtained from the simulations for the trimethylated-ODBP and C4O-Ph-ODBP mesogens, plotted as a function of temperature. As described in Chapter 5, Section 5.5.5, this quantity was calculated as $\sqrt{3/2}(W-B)/2L-B-W$, where L, B and W represent molecular length, breadth and width respectively.

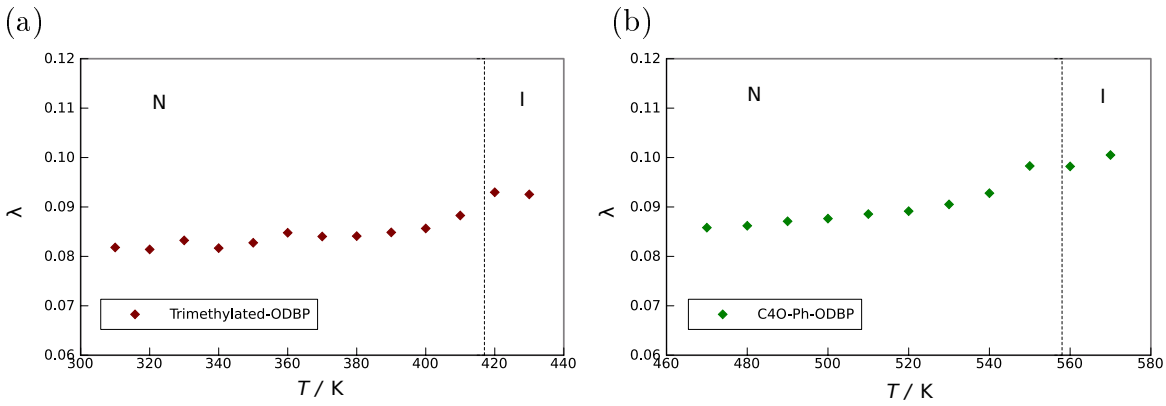

Figure 6.22: The average molecular biaxiality as a function of temperature for the (a) trimethylated-ODBP and (b) C4O-Ph-ODBP. [Dotted vertical lines show the respective T_{NI}].

In their respective nematic phases, both mesogens show an overall decrease in λ with decreasing temperature. C4O-Ph-ODBP displays a slightly greater average shape biaxiality ($\approx$ 0.1 to just below 0.09) compared with that for the trimethylated ODBP mesogen ($\approx$ 0.09 to 0.08). Although the difference is not significant, this is a little suprising considering the trimethylated ODBP mesogen possesses the smaller average aspect ratio of the two mesogens. These values are also broadly similar to those calculated for both the C5-Ph-ODBP-Ph-OC12 and C4-Ph-ODBP-Ph-C7 mesogens investigated in Chapter 5 (see Figure 5.27e). This suggests that the

magnitude of the shape biaxiality is not an important factor for the establishment of enhanced local biaxial order observed for the trimethylated ODBP compounds, which also supports the claim made by Vita *et al.*[181]

The molecular shape biaxiality, λ is deduced from specific relationships between the molecular dimensions, i.e., the length, breadth and width of the entire molecule. It is possible however, that the magnitude or difference in the shape biaxiality of the individual arms of the trimethylated-ODBP mesogen may exert an influence on the local biaxial orientational order for this system. For example, Grzybowski *et al.*[80] constructed a molecular model for bent-core mesogens using Onsager-type theory and Gay-Berne(GB) interacting ellipsoids. The arms of the V-shaped molecules in this model were constructed to be either uniaxial or biaxial ellipsoids, with or without a central transverse dipole. The inclusion of biaxial GB arms in the model destabilized the uniaxial nematic phase with respect to the biaxial nematic phase, even without the presence of a central transverse dipole. The shape biaxiality of the individual arms of the trimethylated-ODBP mesogen has not been explored within this thesis, but is highlighted in Chapter 7 as a consideration for further research.

Finally, for each of the parameters, L, L/B and λ, and for the trimethylated-ODBP mesogen, there appears to be a strong correlation between the nematic and isotropic regions, with a distinct change in these values occurring very close to the experimental T_{NI}, consistent with the first order nature of this transition (see Figure 6.20a, Figure 6.21a and Figure 6.22a). This sudden change in these values is also apparent for the C4O-Ph-ODBP mesogen, although the temperature at which this occurs is ≈ 10 K lower than the experimental T_{NI} (see Figure 6.20b, Figure 6.21b and Figure 6.22b). However, the temperature dependent, average uniaxial orientational order parameter for the C4O-Ph-ODBP mesogen, does suggests a phase transition very close to the experimental T_{NI}. As alluded to by Pizzirrusso *et al.*,[145] the average molecular shape parameter can be an important parameter in understanding liquid crystal phase stability and changes in transition temperatures due to small chemical modifications, but is not a robust predictive tool alone, due to the fact that the actual shape of molecules is determined by several possible conformations differently populated as the temperature changes.

The addition of lateral methyl groups alter the chemical structure of the Ph-ODBP-Ph aromatic core of the trimethylated mesogen and it is possible that this may have some influence on the average bend angle, β shown in Figure 6.3. The bend angle, β obtained form the simulations was measured as an average angle beween ref. axis 1 and ref. axis 2 representing vectors originating from the C atoms of the oxadiazole ring and terminating at the outer C atoms of the phenyl rings linking the terminal chains (see Figure 6.3). Figure 6.23a, shows the average bend angle, β, as function of temperature for the trimethylated-ODBP mesogen. It can be seen that $\langle\beta\rangle$ is largely temperature independent, increasing from $\approx 138.9°$ just above the T_{NI} to $\approx 140.9°$ in the lower nematic region. The distributions of bend angles shown in Figure 6.23b for a selection of temperatures are fairly narrow and broadly similar with peak values close to 140.0°

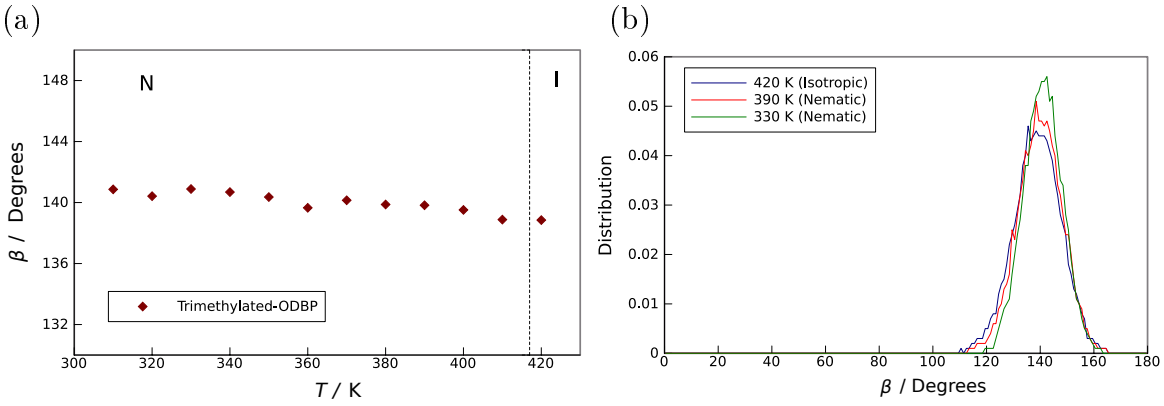

Figure 6.23: (a) The average bend angle, β of the Ph-ODBP-Ph core as a function of temperature for the trimethylated-ODBP mesogen. (b) Distribution of the bend angle, β in the simulated phases.

Comparisons of the above results with those calculated for the C4O-Ph-ODBP mesogen, where the bend angle, β, of the Ph-ODBP-Ph core was measured in the same way as that for trimethylated-ODBP, show minor differences between the two systems (see Figure 6.24). The average bend angle as a function of temperature again displays a very small increase from $\approx 137.3°$ just above T_{NI} to $\approx 140.9°$ in the lower temperature nematic region. The distribution of angles also show peak values close to 140.0° at selected temperatures. However, there is a subtle difference in the spread of angles, with C4O-Ph-ODBP showing a slightly wider range of bend angles compared with that for the trimethylated-ODBP mesogen (see Figure 6.24b).

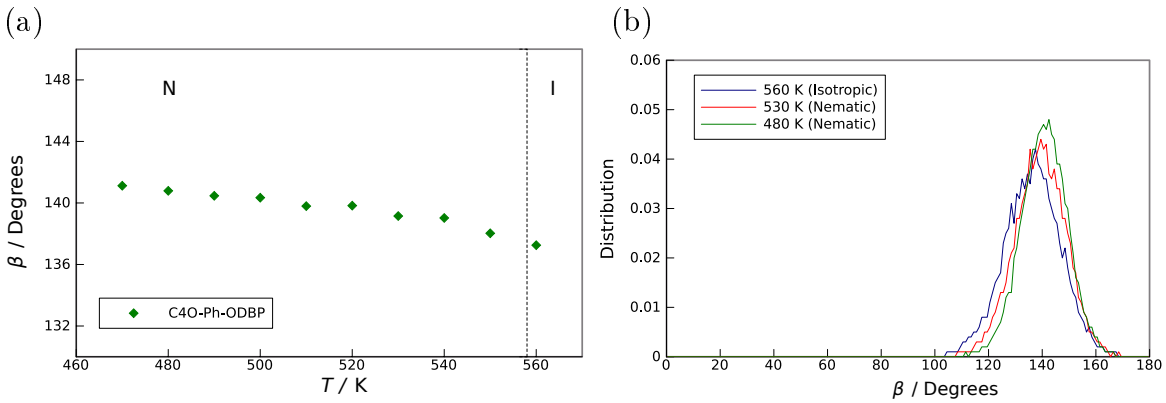

Figure 6.24: (a) The average bend angle, β of the Ph-ODBP-Ph core as a function of temperature for the C4O-Ph-ODBP mesogen. (b) Distribution of the bend angle, β in the simulated phases.

The above comparisons of molecular dimensions, overall shape and bend angle between the trimethylated-ODBP and the non-methylated, C4O-Ph-ODBP mesogens, indicate that the structural modification of the aromatic core through the addition of three lateral methyl groups does not significantly alter these quantities. However, the addition of lateral methyl groups clearly reduces the nematic onset temperature significantly compared with that for C4O-Ph-ODBP, as well as imparting markedly different short range molecular ordering. Vita *et al.* suggested that the presence of additional methyl groups, specifically in the outer part of the aromatic core structure, may lead to peculiar conformations which help to promote the enhanced local biaxial ordering of molecules.

Prior to the Vita *et al.* study, an XRD investigation (including WA measurements) was performed on ODBP bent-core derivatives possessing lateral methyl groups.[164] This included an analogue of the trimethylated-ODBP mesogen simulated in this work, with the exception that the methyl groups located on the outer phenyl rings were shifted to carbon positions adjacent to the terminal chains (the *meta* position with respect to the phenyl carbon linking the oxadiazole ring). The authors of this study provide no reference to the presence of two distinct d -spacings for this particular trimethylated-ODBP mesogen. It is possible that the precise position of the outer methyl groups on the aromatic core may be important in establishing the enhanced orientational molecular correlation in the transverse direction. In addition, the distribution of the dihedral angles associated with these specifically

located lateral methyl groups would need to be examined in order to ascertain the effect this may have on the molecular conformations, which in turn may lead to a specific type of molecular packing in the transverse direction. It was not possible to address these issues within the current work, although future work will include an examination of these factors.

6.3.5 Visual analysis

Finally, snapshots of the C4O-Ph-ODBP and trimethylated-ODBP systems in their respective nematic phases suggest similar structures, with varying degrees of long range order of the molecular long axes, with a broadly homogenous distribution of molecules (see Figure 6.25) . The distinct differences in local molecular organization between these two systems determined and described in the prevous sections, are not apparent from these snapshots alone. Interestingly, based on visual analysis of all four of the ODBP mesogens studied in this thesis, only the C5-Ph-ODBP-Ph-OC12 system (see Chapter 5) displays the unusual nanostructures in the lower temperature nematic region (although ideally this would need to be confirmed with visual analysis of large system sizes for the C4O-Ph-ODBP and trimethylated-ODBP systems). This is distinctly different from the other three systems studied, and is likely to be related to the presence of the highly unusual underlying DC phase observed for this mesogen.

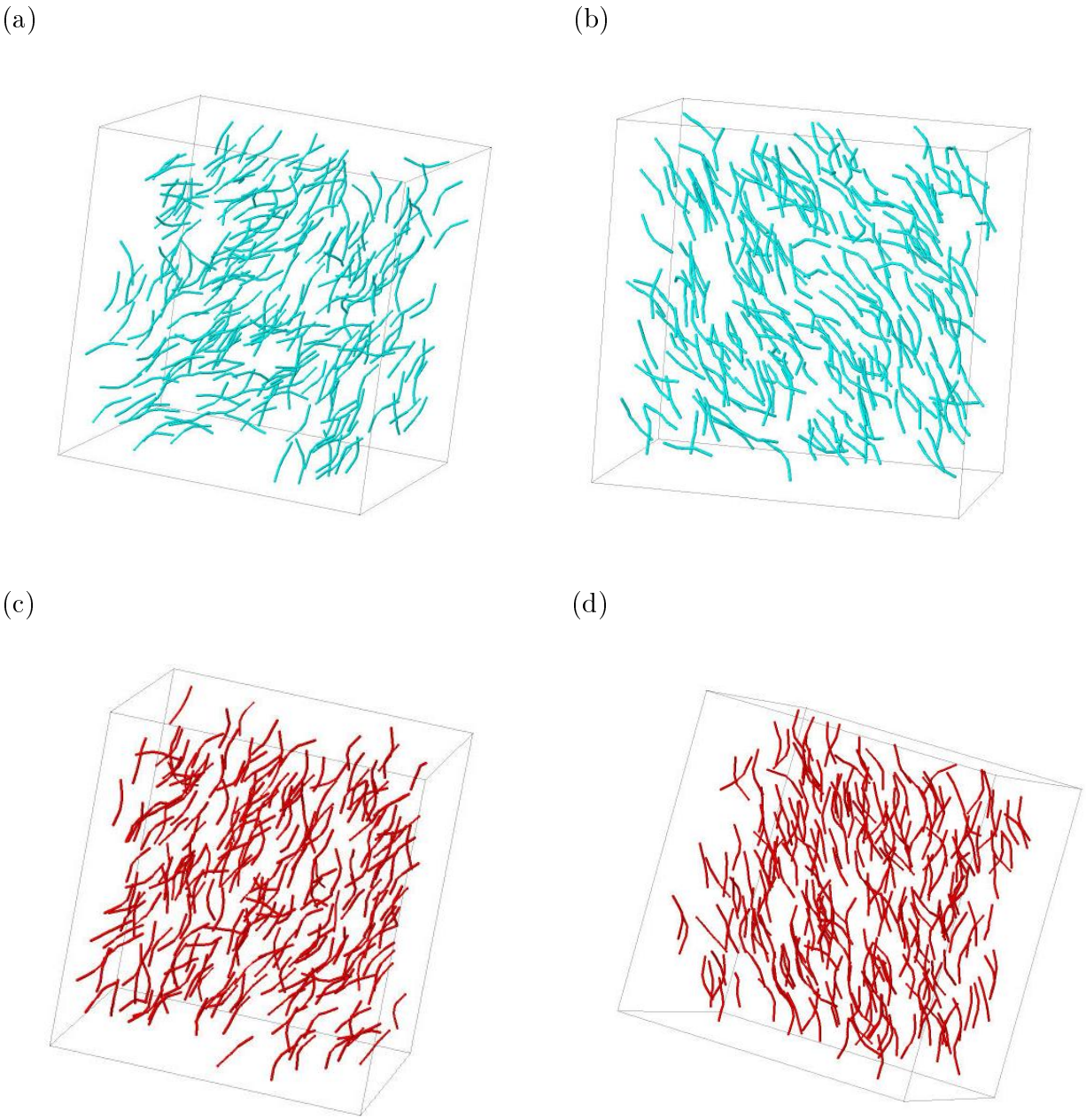

Figure 6.25: Snapshots of the C4O-Ph-ODBP and trimethylated-ODBP nematic phase systems showing coarse-grained representations of the ODBP core structures only and for $N = 256$ molecules. (a) C4O-Ph-ODBP (530 K) (b) C4O-Ph-ODBP (480 K) (c) Trimethylated-ODBP (390 K) (d) Trimethylated-ODBP (330 K).

6.4 Conclusions

The GAFF-LCFF force field was tested on reproducing the nematic-isotropic transition temperature for a trimethylated and a non-methylated-ODBP mesogen with sample sizes of 256 molecules. The results showed good agreement with experiment, with T_{NI} estimates within 10 K of experimental values. The biaxial orientational order parameters for each system, measured as average values over 256 molecules, resulted in disappointingly low values in the nematic phase, although the trimethylated-ODBP mesogen showed greater variation in this quantity compared with C4O-Ph-ODBP. This supports the experimental evidence, that indicates that these mesogens do not exhibit macroscopic biaxiality in the nematic phase.

In accordance with the results from XRD measurements, the simulations of the nematic phase suggest that at the local scale of a few molecules there is enhanced close packing of aromatic cores, along with greater correlation lengths in the transverse direction for the trimethylated-ODBP mesogen, leading to greater local biaxial correlations. This was not observed for C4O-Ph-ODBP, with the simulation results suggesting more typical local molecular organization in the nematic phase. In addition, and in contrast to that found for C4O-Ph-ODBP, a preferred anti-parallel molecular pair arrangement with respect to the dipole direction along the oxadiazole ring, is proposed for the trimethylated-ODBP mesogen. The effective molecular shape, dimensions and average bend angles of the two mesogens were found not to differ significantly, suggesting that the presence of laterally substituted methyl groups on the aromatic core has a more subtle effect on determining the unique molecular organization exhibited by the trimethylated-ODBP mesogen compared with that for the C4O-Ph-ODBP and other typical BCNs. The results from the pair distribution functions for the laterally substituted methyl group located on the inner phenyl ring of the bent-core structure showed enhanced correlations, compared with those for the outer methyl group. However, it appears that the presence of outer methyl groups in the bent-core structure is more significant in determining the enhanced local biaxial order displayed by the trimethylated-ODBP mesogen.

Chapter 7

Conclusions and Further Work

The realisation of a thermotropic biaxial liquid crystal (LC) phase of low molecular mass mesogens is of great technological interest, due to the possibility of application in fast-switching LC displays. A number of experimental methods have indicated the existence of phase biaxiality for low molecular mass bent-core oxadiazole (ODBP) derivatives. Controversy still remains as to whether the biaxiality is spontaneous or induced by surfaces or applied fields, whether it exists at the macroscopic or local length scale, or whether the biaxiality exists only for single molecules or clusters. The emerging consensus appears to support the cluster interpretation, which proposes that the biaxial nematic phase is composed of cybotactic groups characterized by short-range smectic positional order and varying amounts of local biaxiality.

The research presented in this thesis employed fully atomistic simulations and force field methods to study four bent-core oxadiazole derivatives, and encompassed two distinct parts. The first part focused on the optimization of the Generalized Amber Force Field (GAFF) in order to improve the description of liquid crystal molecules. Testing of the GAFF force field through the reproduction of the experimental T_{NI} for a selection of mesogens, found that the simulated T_{NI} was overestimated by up to 110 K, indicating that any results from the simulations may not be representative of the real mesogens. To keep force field alterations to a minimum, the GAFF force field was partially re-parametrized, through the careful tuning of a selected number of LJ parameters of component fragments of standard calamitic mesogens, with the aim of reproducing the experimental properties of density and

$\Delta_{\text{vap}}H$, and in particular, to obtain a density deviation of less than 1% from experimental values. The re-parametrization of a number of torsional potentials of fragment molecules was also undertaken, using high-level quantum chemical calculations, with the aim of improving the description of the overall 'shape' and flexibility of the mesogens.

The new optimized force field, GAFF-LCFF, was tested on a typical rod-like calamitic mesogen, 1,3-benzenedicarboxylic acid,1,3-*bis*(4-butylphenyl)ester, accurately reproducing the experimental T_{NI} to within ≈ 5 K. Further minor amendments to the alkane parameters of GAFF-LCFF were subsequently found to be necessary to account for the longer alkyl chains on some of the oxadiazole derivatives investigated. This involved adopting alkane parameters from the GAFFlipid force field. The simulated estimates of T_{NI} were found to be within 10 K of experimental values for the oxadiazole derivatives, C4-Ph-ODBP-Ph-C7, C5-Ph-ODBP-Ph-OC12, C4-Ph-ODBP and a trimethylated ODBP mesogen. Simulation system size effects were tested on the estimates of T_{NI} for the C4-Ph-ODBP-Ph-C7 and C5-Ph-ODBP-Ph-OC12 systems and were found to be negligible in comparison to errors in locating T_{NI}. Additionally, the nematic to dark conglomerate (DC) phase transition was predicted for the C5-Ph-ODBP-Ph-OC12 mesogen to within ≈ 15 K compared to experiment. These results suggested that GAFF-LCFF is readily transferable to a range of liquid crystal mesogens based on the fragments and associated functional groups used in the parametrization process, including to a variety of oxadiazole bent-core derivatives with chemically similar structures, with or without additional methyl substituents.

Further validation of GAFF-LCFF would ideally require the reproduction of additional experimental macroscopic properties besides phase transition temperatures, for example, phase diffusion coefficients and bulk densities, although the experimental data for these are not currently available for the mesogens studied in this thesis. The transferability of GAFF-LCFF to a wider range of other mesogens could be enhanced by the testing and re-parametrization where appropriate of additional liquid crystal fragments containing functional groups not present in those considered in this work. This could include heterocyclic rings with atoms other than oxygen

and nitrogen, for example sulphur, or liquid crystal fragments containing laterally substituted halogen atoms.

In the second part of the thesis, a detailed analysis of the molecular organization of the simulated nematic phases of the four oxadiazole derivatives was conducted. In terms of orientational order, questions have been raised within the literature regarding the role of the bend angle in the experimental measurement of order parameters. This was tested on the C4-Ph-ODBP-Ph-C7 and C5-Ph-ODBP-Ph-OC12 systems, for which the simulations showed that the uniaxial order parameter, $\langle P_2 \rangle$, was systematically lower when the bend angle was not accounted for in the calculations. The $\langle P_2 \rangle$ values in the nematic phase deduced from the simulations, with and without the bend angle, were found to be consistent with experimental values obtained from a Raman scattering study. All four oxadiazole derivatives showed an average bend angle in the nematic phase that was effectively independent of temperature, supporting the assumption of a fixed bend angle in the experimental calculation of order parameters.

All four mesogens displayed small positive biaxial orientational order parameters in their respective nematic phases for the small sample sizes. The C5-Ph-ODBP-Ph-OC12 mesogen showed the largest biaxial orientational order parameter, in particular in the low nematic temperature region, with the magnitude broadly consistent with the experimental measurements obtained from a Raman scattering study of this mesogen. However, the magnitude of biaxial order became negligible for the larger system size, indicating that the biaxiality is not long-ranged at the macroscopic level.

Results obtained from various pair distribution functions, showed that in terms of transverse positional order, and in contrast to the non-methylated ODBP mesogens, there was enhanced close packing of the trimethylated-ODBP mesogen leading to a higher degree of local biaxial order. This was consistent with the experimental wide-angle XRD data relating to the transverse positional order obtained for this mesogen, although the simulations suggest a different geometric arrangement of nearest-neighbour molecules than that proposed from the experimental XRD data.

The average molecular shape biaxiality and the aspect ratio of the four oxadia-

zole derivatives, obtained from the simulated nematic phases, did not differ significantly, suggesting that differences in the magnitude of the biaxial order parameters, as well as the enhanced local biaxiality (transversal correlations) displayed by the trimethylated-ODBP mesogen only, are not due to these features. It has been proposed in the literature that the presence of methyl groups on the outer phenyl rings of the molecular core structure may promote the enhanced local biaxiality observed for the trimethylated-ODBP mesogen. The results from the simulations however, showed stronger correlations between the inner methyl groups and therefore the specific influence exerted by the outer methyl groups remains unclear.

To address this gap in knowledge, and identify specific features that may be important in establishing the enhanced local biaxiality, further research could include identifying whether the addition of methyl groups, and more specifically the addition of methyl groups on the outer phenyl rings, alters the distribution of molecular conformations of the ODBP core compared to a non-methylated core. Additionally, further atomistic simulations of analogous bent-core nematics, with methyl groups moved to alternative positions on the outer phenyl rings, would also help to establish whether the specific location of the methyl groups on the outer phenyl rings is important in determining the enhanced local biaxiality. It would also be interesting to explore whether a non-symmetric core structure is necessary for the emergence of enhanced biaxial correlations. This would entail performing new atomistic simulations of symmetric dimethylated ODBP bent-core nematics and comparing the nematic phase molecular organization with that for the non-symmetric trimethylated-ODBP mesogens. The measurements of the differences in the shape biaxiality of non-symmetric mesogen arms may also be worth investigating further.

In the context of the cybotactic cluster model of the biaxial nematic phase, the results from the simulations for the shorter chain compounds, C4-Ph-ODBP-Ph-C7 and C4O-Ph-ODBP were not entirely consistent with this model. The nematic phases were composed of temperature independent, small clusters, and were closer in structure to ordinary nematics, whose liquid-like positional order only reflects nearest-neighbour correlations. This was also consistent with the available experimental XRD data for the C4O-Ph-ODBP mesogen. The simulations of the longer

chained C5-Ph-ODBP-Ph-OC12 mesogen also did not fully support the cybotactic cluster model, which was again consistent with the analysis of experimental XRD data. The simulations showed temperature independent, but marginally longer, correlation lengths for this mesogen compared with those for the shorter chain ODBP derivatives above, in particular for the transverse direction.

In contrast to the non-methylated ODBP derivatives, the simulations of the trimethylated-ODBP mesogen in the nematic phase displayed in addition to closer packing of nearest-neighbour molecules, longer transverse correlations lengths, which showed some temperature dependence. The simulated results suggested a cybotactic nematic, composed of small clusters, with inherent local biaxial order, and were consistent with the experimental wide-angle XRD data for this particular mesogen.

In terms of further work, additional quantitative structural information about the nematic phases of these four OPBP mesogens could be obtained from the calculation of diffraction patterns from larger simulations, as larger systems are normally needed to simulate X-ray data. This could provide an additional tool to validate the interpretation and analysis of the data obtained from the real X-ray diffraction patterns for these mesogens.

Finally, visual inspection of the nematic phases of the four ODBP mesogens showed distinct differences in the molecular organization of the C5-Ph-ODBP-Ph-OC12 system. While the nematic phases of C4-Ph-ODBP-Ph-C7, C4O-Ph-ODBP and the trimethylated-ODBP, appeared broadly homogenous at all temperatures examined, in contrast the emergence of ribbon-like nanostructures appeared in the lower temperature nematic region of the C5-Ph-ODBP-Ph-OC12 system. It was tentatively suggested that the chemical and structural features specific to the alkoxy core-chain junction present in the C5-Ph-ODBP-Ph-OC12 mesogen may be responsible for these ribbon-like nanostructures, as well as the somewhat enhanced biaxial orientational order parameter in the lower nematic temperature region. At a temperature expected to represent the underlying DC phase, which has previously been experimentally characterized for the C5-Ph-ODBP-Ph-OC12 system, visual inspection also revealed the existence of layers displaying saddle splay curvature, which was consistent with the experimentally determined structure of this underlying DC

phase.

In summary, the new optimized GAFF-LCFF force field has demonstrated its value in teasing out the distinct, but often subtle, differences in molecular organization of the mesophases of a closely related group of bent-core liquid crystal molecules. This work represents the first real attempt to understand these relationships at an atomistic level *via* molecular dynamics simulations. A number of experimental observables have also been replicated, including accurate predictions of the nematic-isotropic phase transition temperatures, further validating GAFF-LCFF. Biaxiality was found to be predominantly local, and there was no evidence for the formation of large cybotactic clusters in the nematic phases. A number of structure-property relationships have been identified, and additionally, the work demonstrates the first simulation evidence for a DC phase, with further potential developments suggested for future research.

Bibliography

[1] Advanced Chemistry Development (ACD/Labs) Software V11.02, 1994-2014.

[2] B. R. Acharya, A. Primak, and S. Kumar. Biaxial nematic phase in bent-core thermotropic mesogens. *Phys. Rev. Letts.*, 92:145506, 2004.

[3] N. L. Allinger, Y. H. Yuh, and J. H. Lii. Molecular mechanics - the MM3 force-field for hydrocarbons .1. *J. Am. Chem. Soc.*, 111:8551–8566, 1989.

[4] R. M. Balabin. Enthalpy difference between conformations of normal alkanes: Raman spectroscopy study of n-pentane and n-butane. *J. Phys. Chem. A*, 113:1012–1019, 2009.

[5] D. Barna, B. Nagy, J. Csontos, A. G. Csaszar, and G. Tasi. Benchmarking experimental and computational thermochemical data: A case study of the butane conformers. *J. Chem. Theory Comp.*, 8:479–486, 2012.

[6] M. A. Bates. Influence of flexibility on the biaxial nematic phase of bent core liquid crystals: A Monte Carlo simulation study. *Phys. Rev. E*, 74:061702, 2006.

[7] M. A. Bates. Bent core molecules and the biaxial nematic phase: A transverse dipole widens the optimal angle. *Chem. Phys. Letts*, 437:189–192, 2007.

[8] M. A. Bates and G. R. Luckhurst. Computer simulation studies of anisotropic systems. XXX. The phase behavior and structure of a Gay-Berne mesogen. *J. Chem. Phys.*, 110:7087–7108, 1999.

[9] M. A. Bates and G. R. Luckhurst. Biaxial nematic phases and V-shaped molecules: A Monte Carlo simulation study. *Phys. Rev. E*, 72:051702, 2005.

[10] M. A. Bates and G. R. Luckhurst. Biaxial nematics: computer simulation studies of a generic rod-disc dimer model. *Phys. Chem. Chem. Phys.*, 7:2821–2829, 2005.

[11] R. Berardi, L. Muccioli, S. Orlandi, M. Ricci, and C. Zannoni. Computer simulations of biaxial nematics. *J. Phys.-Condens. Mat*, 20, 2008.

[12] R. Berardi and C. Zannoni. Do thermotropic biaxial nematics exist? A Monte Carlo study of biaxial Gay-Berne particles. *J. Chem. Phys.*, 113:5971–5979, 2000.

[13] R. Berardi and C. Zannoni. Biaxial discotic Gay-Berne mesogens and biaxial nematics. *Mol. Cryst. Liq. Cryst.*, 396:177–186, 2003.

[14] R. Berardo, C. Fava, and C. Zannoni. A generalized Gay-Berne intermolecular ootential for biaxial particles. *Chem. Phys. Lets.*, 236:462–468, 1995.

[15] F. Biscarini, C. Chiccoli, P. Pasini, F. Semeria, and C. Zannoni. Phase-diagram and orientational order in a biaxial lattice model - A Monte-Carlo study. *Phys. Rev. Letts.*, 75:1803–1806, 1995.

[16] A. D. Boese, J. M. L. Martin, and N. C. Handy. The role of the basis set: Assessing density functional theory. *J. Chem. Phys.*, 119:3005–3014, 2003.

[17] P. Bolhuis and D. Frenkel. Tracing the phase boundaries of hard spherocylinders. *J. Chem. Phys.*, 106:666–687, 1997.

[18] N. J. Boyd and M. R. Wilson. Optimization of the GAFF force field to describe liquid crystal molecules: the path to a dramatic improvement in transition temperature predictions. *Phys. Chem. Chem. Phys.*, 17:24851–24865, 2015.

[19] D. W. Bruce. Towards the biaxial nematic phase through molecular design. *Chem. Rec.*, 4:10–22, 2004.

[20] I. Cacelli, A. Cimoli, L. De Gaetani, G. Prampolini, and A. Tani. Chemical detail force fields for mesogenic molecules. *J. Chem. Theory Comp.*, 5:1865–1876, 2009.

[21] I. Cacelli, A. Cimoli, P. R. Livotto, and G. Prampolini. An automated approach for the parameterization of accurate intermolecular force-fields: Pyridine as a case study. *J. Comp. Chem.*, 33:1055–1067, 2012.

[22] I. Cacelli, C. F. Lami, and G. Prampolini. Force-field modeling through quantum mechanical calculations: Molecular dynamics simulations of a nematogenic molecule in its condensed phases. *J. Comp. Chem.*, 30:366–378, 2009.

[23] I. Cacelli and G. Prampolini. Parametrization and validation of intramolecular force fields derived from DFT calculations. *J. Chem. Theory Comp.*, 3:1803–1817, 2007.

[24] I. Cacelli, G. Prampolini, and A. Tani. Atomistic simulation of a nematogen using a force field derived from quantum chemical calculations. *J. of Phys. Chem. B*, 109:3531–3538, 2005.

[25] C. Caleman, P. J. van Maaren, M. Hong, J. S. Hub, L. T. Costa, and D. van der Spoel. Force field benchmark of organic liquids: Density, enthalpy of vaporization, heat capacities, surface tension, isothermal compressibility, volumetric expansion coefficient, and dielectric constant. *J. Chem. Theory Comp.*, 8:61–74, 2012.

[26] P. J. Camp and M. P. Allen. Phase diagram of the hard biaxial ellipsoid fluid. *J. Chem. Phys.*, 106:6681–6688, 1997.

[27] P. J. Camp, M. P. Allen, and A. J. Masters. Theory and computer simulation of bent-core molecules. *J. Chem. Phys.*, 111:9871–9881, 1999.

[28] C. M. Care and D. J. Cleaver. Computer simulation of liquid crystals. *Rep. Prog. Phys.*, 68:2665–2700, 2005.

[29] A. Carella, A. Castaldo, R. Centore, A. Fort, A. Sirigu, and A. Tuzi. Synthesis and second order nonlinear optical properties of new chromophores containing 1,3,4-oxadiazole and thiophene rings. *J. Chem. Soc. Perk. T 2*, pages 1791–1795, 2002.

[30] S. Chakraborty, J. T. Gleeson, A. Jakli, and S. Sprunt. A comparison of short-range molecular order in bent-core and rod-like nematic liquid crystals. *Soft Matter*, 9:1817–1824, 2013.

[31] F. Chami, M. R. Wilson, and V. S. Oganesyan. Molecular dynamics and EPR spectroscopic studies of 8CB liquid crystal. *Soft Matter*, 8:6823–6833, 2012.

[32] D. Chandler, J. D. Weeks, and H. C. Andersen. Van der Waals picture of liquids, solids, and phase-transformations. *Science*, 220(4599):787–794, 1983.

[33] P. Cieplak, F. Dupradeau, Y. Duan, and J. Wang. Polarization effects in molecular mechanical force fields. *J. Phys., Conds. Matter*, 21:333102, 2009.

[34] G. Cinacchi and G. Prampolini. DFT study of the torsional potential in ethylbenzene and ethoxybenzene: The smallest prototypes of alkyl- and alkoxy-aryl mesogens. *J. Phys. Chem. A*, 107:5228–5232, 2003.

[35] G. Cinacchi and G. Prampolini. Density functional theory study of the conformational space of phenyl benzoate, a common fragment in many mesogenic molecules. *J. Phys. Chem. A*, 109:6290–6293, 2005.

[36] V. Circu, T. J. K. Gibbs, L. Omnes, P. N. Horton, M. B. Hursthouse, and D. W. Bruce. Orthometallated palladium(II) imine complexes as candidate materials for the biaxial nematic phase. Crystal and molecular structure of three palladium imine complexes. *J. Mat. Chem.*, 16:4316–4325, 2006.

[37] P. J. Collings and M. Hird. *Introduction to Liquid Crystals*, page 5. Taylor & Francis, 1997.

[38] P. J. Collings and M. Hird. *Introduction to Liquid Crystals*, page 47. Taylor & Francis, 1997.

[39] P. J. Collings and M. Hird. *Introduction to Liquid Crystals*, pages 48–82. Taylor & Francis, 1997.

[40] P. J. Collings and M. Hird. *Introduction to Liquid Crystals*, page 50. Taylor & Franci, 1997.

[41] P. J. Collings and M. Hird. *Introduction to Liquid Crystals*, chapter 12. Taylor & Francis, 1997.

[42] P. J. Collings and M. Hird. *Introduction to Liquid Crystals*, pages 265–266. Taylor & Francis, 1997.

[43] P. J. Collings and M. Hird. *Introduction to Liquid Crystals*, chapter 3, page 61. Taylor & Francis, 1997.

[44] D. Compton, S. Montero, and W. Murphy. Low-frequency Raman-spectrum and asymmetric potential function for internal-rotation of gaseous normal-butanne. *J. Phys. Chem.*, 84:3587–3591, 1980.

[45] L. L. Cooper, E. T. Samulski, and E. Scharrer. Towards room temperature biaxial nematics. *Mol. Cryst. Liq. Cryst.*, 511:1673–1687, 2009.

[46] Cramer. *Essentialls of Computational Chemistry, Theories and Models*, chapter 7. Wiley, 2004.

[47] C. J. Cramer. *Essentials of Computational Chemistry, Theories and Models*, pages 88–89. Wiley, 2004.

[48] C. J Cramer. *Essentials of Computational Chemistry, Theories and Models*, page 92. Wiley, 2004.

[49] C. J. Cramer. *Essentials of Computational Chemistry, Theories and Models*, pages 47, 90. Wiley, 2004.

[50] C. J Cramer. *Essentials of Computational Chemistry, Theories and Models*, chapter 6. Wiley, 2004.

[51] G.W. Gray H.-W. Spiess D. Demus, J. W. Goodby and V. Vill. *Handbook of Liquid Crystals Vol 1:Fundamentals*, page 177. Wiley-VCH, 1998.

[52] G.W. Gray H.-W. Spiess D. Demus, J. W. Goodby and V. Vill. *Handbook of Liquid Crystals Vol 1:Fundamentals*, page 44. Wiley-VCH, 1998.

[53] G.W. Gray H.-W. Spiess D. Demus, J. W. Goodby and V. Vill. *Handbook of Liquid Crystals Vol.1:Fundamentals*, chapter 2. Wiley-VCH, 1998.

[54] D. Demus, J. W. Goodby, G.W. Gray, H.-W. Spiess, and V. Vill. *Handbook of Liquid Crystals Vol.1:Fundamentals*, pages 135–136. Wiley-VCH, 1998.

[55] A. Devries. X-ray-diffraction studies of the structure of the skewed cybotactic nematic phase - a review of the literature. *J. Mol. Liq*, 31:193–202, 1986.

[56] A. Dewar and P. J. Camp. Dipolar interactions, molecular flexibility, and flexoelectricity in bent-core liquid crystals. *J. Chem. Phys.*, 123, 2005.

[57] C. J. Dickson, L. Rosso, R. M. Betz, R. C. Walker, and I. R. Gould. GAFFlipid: a General Amber Force Field for the accurate molecular dynamics simulation of phospholipid. *Soft Matter*, 8:9617–9627, 2012.

[58] T. J. Dingemans, L. A. Madsen, N. A. Zafiropoulos, W. B. Lin, and E. T. Samulski. Uniaxial and biaxial nematic liquid crystals. *Philos. Trans. R. Soc. Lond., A*, 364:2681–2696, 2006.

[59] R. Y. Dong. Recent developments in biaxial liquid crystals: An NMR perspective. *Int. J. Mod. Phys. B*, 24:4641–4682, 2010.

[60] R. Y. Dong and A. Marini. Conformational study of a bent-core liquid crystal: C-13 NMR and DFT computation approach. *J. Phys. Chem. B*, 113:14062–14072, 2009.

[61] J. W. Emsley, G. DeLuca, G. Celebre, and M. Longeri. The conformation of the aromatic rings relative to the alkyl chain in 4-n-pentyl-4'-cyanobiphenyl. *Liq. Cryst.*, 20:569–575, 1996.

[62] L. Firlej, B. Kuchta, M. W. Roth, and C. Wexler. Molecular simulations of intermediate and long alkanes adsorbed on graphite: Tuning of non-bond interactions. *J. Mol. Mod.*, 17:811–816, 2011.

[63] J.B. Foresman and A. Frisch. *Exploring Chemistry with Electronic Structure Methods*. Gaussian Inc., 1996.

[64] O. Francescangeli and E. T. Samulski. Insights into the cybotactic nematic phase of bent-core molecules. *Soft Matter*, 6:2413–2420, 2010.

[65] O. Francescangeli, V. Stanic, S. I. Torgova, A. Strigazzi, N. Scaramuzza, C. Ferrero, I. P. Dolbnya, T. M. Weiss, R. Berardi, L. Muccioli, S. Orlandi, and C. Zannoni. Ferroelectric response and induced biaxiality in the nematic phase of a bent-core mesogen. *Adv. Funct. Mater.*, 19:2592–2600, 2009.

[66] O. Francescangeli, F. Vita, F. Fauth, and E. T. Samulski. Extraordinary magnetic field effect in bent-core liquid crystals. *Phys. Rev. Letts.*, 107:207801, 2011.

[67] O. Francescangeli, F. Vita, C. Ferrero, T. Dingemans, and E. T. Samulski. Cybotaxis dominates the nematic phase of bent-core mesogens: a small-angle diffuse X-ray diffraction study. *Soft Matter*, 7:895–901, 2011.

[68] O. Francescangeli, F. Vita, and E. T. Samulski. The cybotactic nematic phase of bent-core mesogens: state of the art and future developments. *Soft Matter*, 10:7685–7691, 2014.

[69] M. J. Freiser. Ordered states of a nematic liquid. *Phys. Rev. Letts.*, 24:1041, 1970.

[70] D. Frenkel. Structure of hard-core models for liquid-crystals. *J. Phys. Chem.*, 92:3280–3284, 1988.

[71] W. M. Gelbart. Molecular theory of nematic liquid-crystals. *J. Phys. Chem.*, 86:4298–4307, 1982.

[72] H. F. Gleeson and P. D. Brimicombe. Comment on "Raman scattering study of phase biaxiality in a thermotropic bent-core nematic liquid crystal". *Phys. Rev. Letts.*, 107:109801, 2011.

[73] H. F. Gleeson, C. D. Southern, P. D. Brimicombe, J. W. Goodby, and V. Gortz. Optical measurements of orientational order in uniaxial and biaxial nematic liquid crystals. *Liq. Cryst.*, 37:PII 923874813, 2010.

[74] H.F. Gleeson, S. Kaur, V. Goertz, A. Belaissoui, S. Cowling, and J.W. Goodby. The nematic phases of bent-core liquid crystals. *ChemPhysChem*, 15:1251–1260, 2014.

[75] M. V. Gorkunov, M. A. Osipov, A. Kocot, and J. K. Vij. Molecular model of biaxial ordering in nematic liquid crystals composed of flat molecules with four mesogenic groups. *Phys. Rev. E*, 81, 2010.

[76] V. Gortz and J. W. Goodby. Enantioselective segregation in achiral nematic liquid crystals. *Chem. Commun.*, pages 3262–3264, 2005.

[77] V. Gortz, C. Southern, N. W. Roberts, H. F. Gleeson, and J. W. Goodby. Unusual properties of a bent-core liquid-crystalline fluid. *Soft Matter*, 5:463–471, 2009.

[78] Gortz.V. Chiral resolution in bent-core nematic liquid crystals. *Liquid Crystals Today*, 19:37–48, 2010.

[79] C. Greco, A. Marini, E. Frezza, and A. Ferrarini. From the molecular structure to spectroscopic and material properties: Computational investigation of a bent-core nematic liquid crystal. *ChemPhysChem*, 15:1336–1344, 2014.

[80] P. Grzybowski and L. Longa. Biaxial nematic phase in model bent-core systems. *Phys. Rev. Letts.*, 107:027802, 2011.

[81] M. J. Hafezi and F. Sharif. Study of the torsional potential energies of 2-methylpropane, *n*-butane, and 2-methylbutane with high-level *ab initio* calculations. *J. Mol. Struct. Theochem*, 814:43–49, 2007.

[82] W. M. Haynes, editor. *RC Handbook of Chemistry and Physics, 92nd Edition.* CRC Press, 2011.

[83] R. Heenan and L. Bartell. Electron-diffraction studies of supersonic jets .4. conformational cooling of normal-butance. *J. Chem. Phys.*, 78:1270–1274, 1983.

[84] W. Herrebout, B. Vanderveken, A. Wang, and J. Durig. Enthalpy difference between conformers of n-butane and the potential function governing conformational interchange. *J. Phys. Chem.*, 99:578–585, 1995.

[85] C. Hogberg, A. Nikitin, and A. Lyubartsev. Modification of the CHARMM force field for DMPC lipid bilayer. *J. Comp. Chem.*, 29:2359–2369, 2008.

[86] A. Holt, J. Bostrom, G. Karlstrom, and R. Lindh. A NEMO potential that includes the dipole-quadrupole and quadrupole-quadrupole polarizability. *J. Comp. Chem.*, 31:1583–1591, 2010.

[87] L. E. Hough, H. T. Jung, D. Kruerke, M. S. Heberling, M. Nakata, C. D. Jones, D. Chen, D. R. Link, J. Zasadzinski, G. Heppke, J. P. Rabe, W. Stocker, E. Korblova, D. M. Walba, M. A. Glaser, and N. A. Clark. Helical nanofilament phases. *Science*, 325:456–460, 2009.

[88] http://ambermd.org/antechamber/gaff.html.

[89] https://jcheminf.springeropen.com/articles/10.1186/1758 2946-4-17.

[90] T. Imase, S. Kawauchi, and J. Watanabe. Conformational analysis of 1,3-benzenediol dibenzoate as a model of banana-shaped molecules forming chiral smectic phases. *J. Mol. Struct.*, 560:275–281, 2001.

[91] F. Jensen. *Introduction to Computational Chemistry*, pages 30–31. Wiley, 2007.

[92] F. Jensen. *Introduction to Computational Chemistry*, page 453. Wiley, 2007.

[93] F. Jensen. *Introduction to Computational Chemistry.* Wiley, 2007.

[94] F. Jensen. *Introduction to Computational Chemistry*, chapter 6. Wiley, 2007.

[95] F. Jensen. *Introduction to Computational Chemistry*, chapter 5. Wiley, 2007.

[96] S. J. Johnston, R. J. Low, and M. P. Neal. Computer simulation of polar bent-core molecules. *Phys. Rev. E*, 66:061702, 2002.

[97] W. L. Jorgensen, D. S. Maxwell, and J. TiradoRives. Development and testing of the OPLS all-atom force field on conformational energetics and properties of organic liquids. *J. Am. Chem. Soc.*, 118:11225–11236, 1996.

[98] P. K. Karahaliou, P. H. J. Kouwer, T. Meyer, G. H. Mehl, and D. J. Photinos. Long- and short-range order in the mesophases of laterally substituted calamitic mesogens and their radial octapodes. *J. Phys. Chem. B*, 112:6550–6556, 2008.

[99] P. K. Karahaliou, A. G. Vanakaras, and D. J. Photinos. Symmetries and alignment of biaxial nematic liquid crystals. *J. Chem. Phys.*, 131:124516, 2009.

[100] S. Kaur, J. Addis, C. Greco, A. Ferrarini, V. Goertz, J. W. Goodby, and H. F. Gleeson. Understanding the distinctive elastic constants in an oxadiazole bent-core nematic liquid crystal. *Phys. Rev. E*, 86:041703, 2012.

[101] S. Kaur, H. Liu, J. Addis, C. Greco, A. Ferrarini, V. Goertz, J. W. Goodby, and H. F. Gleeson. The influence of structure on the elastic, optical and dielectric properties of nematic phases formed from bent-core molecules. *J. Mater. Chem. C*, 1:6667–6676, 2013.

[102] C. Keith, A. Lehmann, U. Baumeister, M. Prehm, and C. Tschierske. Nematic phases of bent-core mesogens. *Soft Matter*, 6:1704–1721, 2010.

[103] Y. Kim, G. Cukrov, F. Vita, E. Scharrer, E. Samulski, O. Francescangeli, and O. Lavrentovich. Search for microscopic and macroscopic biaxiality in the cybotactic nematic phase of new oxadiazole bent-core mesogens. *Phys. Rev. E*, 93:062701, 2016.

[104] J. Klauda, B. Brooks, A. MacKerell, R. Venable, and R. Pastor. An *ab initio* study on the torsional surface of alkanes and its effect on molecular simulations of alkanes and a DPPC bilayer. *J. Phys. Chem. B*, 109:5300–5311, 2005.

[105] J. Klauda, R. Pastor, and B. Brooks. Adjacent gauche stabilization in linear alkanes: Implications for polymer models and conformational analysis. *J. Phys. Chem. B*, 109:15684–15686, 2005.

[106] Koch and Holthausen. *A Chemist's Guide to Density Functional Theory.* Wiley-VCH, 2007.

[107] Koch and Holthausen. *A Chemist's Guide to Density Functional Theory*, chapter 4. Wiley-VCH, 2007.

[108] R. Korlacki, M. Steiner, A. J. Meixner, J. K. Vij, M. Hird, and J. W. Goodby. Conformational distribution of a ferroelectric liquid crystal revealed using fingerprint vibrational spectroscopy and the density functional theory. *J. Chem. Phys.*, 126:224904, 2007.

[109] C. Kramer, P. Gedeck, and M. Meuwly. Atomic multipoles: Electrostatic potential fit, local reference axis systems, and conformational dependence. *J. Comp. Chem.*, 33:1673–1688, 2012.

[110] C. Kramer, P. Gedeck, and M. Meuwly. Multipole-based force fields from *ab initio* interaction energies and the need for jointly refitting all intermolecular parameters. *J. Chem. Theory Comp.*, 9:1499–1511, 2013.

[111] S. A. R. Krishnan, W. Weissflog, G. Pelzl, S. Diele, H. Kresse, Z. Vakhovskaya, and R. Friedemann. DFT and MD studies on the influence of the orientation of ester linkage groups in banana-shaped mesogens. *Phys. Chem. Chem. Phys.*, 8:1170–1177, 2006.

[112] E. Kuprusevicius, R. Edge, H. Gopee, A. N. Cammidge, E. J. L. McInnes, M. R. Wilson, and V. S. Oganesyan. Prediction of EPR spectra of liquid crystals with doped spin probes from fully atomistic molecular dynamics simulations: Exploring molecular order and dynamics at the phase transition. *Chem.-Eur. J.*, 16:11558–11562, 2010.

[113] H. Kurosu, M. Kawasaki, M. Hirose, M. Yamada, S. M. Kang, M. Sone, H. Takezoe, and J. Watanabe. Solid-state C-13 NMR study of chiral twisted

conformation attributable to chirality in smectic phases of achiral banana-shaped molecules. *J. Phys. Chem. A*, 108:4674–4678, 2004.

[114] M. Lehmann, S. W. Kang, C. Kohn, S. Haseloh, U. Kolb, D. Schollmeyer, Q. B. Wang, and S. Kumar. Shape-persistent V-shaped mesogens-formation of nematic phases with biaxial order. *J. Mat. Chem.*, 16:4326–4334, 2006.

[115] M. Lehmann, C. Kohn, J. L. Figueirinhas, G. Feio, C. Cruz, and R. Y. Dong. Biaxial nematic mesophases from shape-persistent mesogens with a fluorenone bending unit. *Chem.-Eur. J.*, 16:8275–8279, 2010.

[116] M. Lehmann, J. Seltmann, A. A. Auer, E. Prochnow, and U. Benedikt. Synthesis and mesomorphic properties of new V-shaped shape-persistent nematogens containing a thiazole or a thiadiazole bending unit. *J. Mat. Chem.*, 19:1978–1988, 2009.

[117] M. Lehmann, J. Seltmann, A. A. Auer, E. Prochnow, and U. Benedikt. Synthesis and mesomorphic properties of new V-shaped shape-persistent nematogens containing a thiazole or a thiadiazole bending unit. *J. Mat. Chem.*, 19:1978–1988, 2009.

[118] R. J. Low. Measuring order and biaxiality. *Eur. J. Phys.*, 23:111–117, 2002.

[119] G. R. Luckhurst. Biaxial nematic liquid crystals: fact or fiction? *Thin Solid Films*, 393:40–52, 2001.

[120] G. R. Luckhurst. Liquid crystals - a missing phase found at last? *Nature*, 430:413–414, 2004.

[121] G. R. Luckhurst. Biaxial nematics composed of flexible molecules: a molecular field theory. *Liq. Cryst.*, 36:1295–1308, 2009.

[122] G. R. Luckhurst, S. Naemura, T. J. Sluckin, T. B. T. To, and S. Turzi. Molecular field theory for biaxial nematic liquid crystals composed of molecules with C(2h) point group symmetry. *Phys. Rev. E*, 84:011704, 2011.

[123] A. Lyubartsev and A. Rabinovich. Recent development in computer simulations of lipid bilayers. *Soft Matter*, 7:25–39, 2011.

[124] L. A. Madsen, T. J. Dingemans, M. Nakata, and E. T. Samulski. Thermotropic biaxial nematic liquid crystals. *Phys. Rev. Letts.*, 92:145505, 2004.

[125] C. H. Mao, Q. M. Wang, R. Q. Huang, L. Chen, J. Shang, and H. B. Song. 2-(3,5-dimethylphenyl)-5-(4-ethylphenyl)-1,3,4-oxadiazole. *Acta Crystallogr E*, 60:O1823–O1825, 2004.

[126] A. Marini and V. Domenici. Conformational changes at mesophase transitions in a ferroelectric liquid crystal by comparative DFT computational and C-13 NMR study. *J. Phys. Chem. B*, 114:10391–10400, 2010.

[127] J. M. L. Martin. What can we learn about dispersion from the conformer surface of *n*-pentane? *J. Phys. Chem. A*, 117:3118–3132, 2013.

[128] R. J. Meier. Are DFT level calculations the answer to real-world molecular systems? *Comp. Mater. Sci.*, 27:219–223, 2003.

[129] R. J. Meier and E. Koglin. On the problem of theoretical evaluation of the rotational barrier in aromatics with adjacent conjugated group: benzaldehyde and *n*-methylbenzamide. *Chem. Phys. Letts.*, 353:239–243, 2002.

[130] J. Miao, S. Hua, and S. Li. Assessment of density functionals on intramolecular dispersion interaction in large normal alkanes. *Chem. Phys. Lett.*, 541:7–11, 2012.

[131] E. Moore. *Molecular Modelling and Bonding*. The Open University, 2002.

[132] Mottram. Introduction to Q-tensor theory. Technical report, Department of Mathematics, University of Strathclyde, 2004.

[133] W. Murphy, J. Fernandezsanchez, and K. Raghavachari. Harmonic force-field and raman-scattering intensity parameters of normal-butane. *J. Phys. Chem.*, 95:1124–1139, 1991.

[134] M. Nagaraj, J. C. Jones, V. P. Panov, H. Liu, G. Portale, W. Bras, and H. F. Gleeson. Understanding the unusual reorganization of the nanostructure of a dark conglomerate phase. *Phys. Rev. E*, 91:042504, 2015.

[135] M. Nagaraj, K. M., J. K. Vij, and A. Kocot. Macroscopic biaxiality and electric-field-induced rotation of the minor director in the nematic phase of a bent-core liquid crystal. *EPL-Europhys. Lett.*, 91:66002, 2010.

[136] S. Orlandi, R. Berardi, J. Steltzer, and C. Zannoni. A Monte Carlo study of the mesophases formed by polar bent-shaped molecules. *J. Chem. Phys.*, 124:124907, 2006.

[137] M. F. Palermo, A. Pizzirusso, L. Muccioli, and C. Zannoni. An atomistic description of the nematic and smectic phases of 4-n-octyl-4 ' cyanobiphenyl (8CB). *J. Chem. Phys.*, 138:204901, 2013.

[138] M. F. Palermo, A. Pizzirusso, L. Muccioli, and C. Zannoni. An atomistic description of the nematic and smectic phases of 4-n-octyl-4 ' cyanobiphenyl (8CB). *J. Chem. Phys.*, 138:204901, 2013.

[139] P. Palffy-Muhoray. Orientationally ordered soft matter: The diverse world of liquid crystals. *Physics Today*, 60:8–23, 2007.

[140] M. S. Park, B. J. Yoon, J. O. Park, S. Kumar, and M. Srinivasarao. Comment on "Raman scattering study of phase biaxiality in a thermotropic bent-core nematic liquid crystal" reply. *Phys. Rev. Letts.*, 107:109802, 2011.

[141] M. S. Park, B. J. Yoon, J. O. Park, V. Prasad, S. Kumar, and M. Srinivasarao. Raman scattering study of phase biaxiality in a thermotropic bent-core nematic liquid crystal. *Phys. Rev. Letts.*, 105:027801, 2010.

[142] R. Pecheanu and N. M. Cann. Molecular dynamics simulations of the liquid-crystal phases of 2-(4-butyloxyphenyl)-5-octyloxypyrimidine and 5-(4-butyloxyphenyl)-2-octyloxypyrimidine. *Phys. Rev. E*, 81:041704, 2010.

[143] J. Pelaez and M. R. Wilson. Atomistic simulations of a thermotropic biaxial liquid crystal. *Phys. Rev. Letts.*, 97:267801, 2006.

[144] S. D. Peroukidis, P. K. Karahaliou, A. G. Vanakaras, and D. J. Photinos. Biaxial nematics: symmetries, order domains and field-induced phase transitions. *Liq. Cryst.*, 36:727–737, 2009.

[145] A. Pizzirusso, M. Savini, L. Muccioli, and C. Zannoni. An atomistic simulation of the liquid-crystalline phases of sexithiophene. *J. Mat. Chem.*, 21:125–133, 2011.

[146] V. Prasad, S. W. Kang, K. A. Suresh, L. Joshi, Q. B. Wang, and S. Kumar. Thermotropic uniaxial and biaxial nematic and smectic phases in bent-core mesogens. *J. Am. Chem. Soc.*, 127:17224–17227, 2005.

[147] K. Raghavachari and J. B. Anderson. Electron correlation effects in molecules. *J. Phys. Chem.*, 100:12960–12973, 1996.

[148] T. D. Rasmussen, P. Ren, J. W. Ponder, and F. Jensen. Force field modeling of conformational energies: Importance of multipole moments and intramolecular polarization. *Int. J. Quantum Chem.*, 107:1390–1395, 2007.

[149] P. Y. Ren and J. W. Ponder. Consistent treatment of inter- and intramolecular polarization in molecular mechanics calculations. *J. Comp. Chem.*, 23:1497–1506, 2002.

[150] Hofer Rode and Kugler. *The Basics of Theoretical and Computational Chemistry.* Wiley-VCH, 2007.

[151] E. T. Samulski. meta-Cybotaxis and nematic biaxiality. *Liq. Cryst.*, 37:669–678, 2010.

[152] J. C. Sancho-Garcia, J. L. Bredas, and J. Cornil. Assessment of the reliability of the Perdew-Burke-Ernzerhof functionals in the determination of torsional potentials in pi-conjugated molecules. *Chem. Phys. Letts.*, 377:63–68, 2003.

[153] J. C. Sancho-Garcia and J. Cornil. Assessment of recently developed exchange-correlation functionals for the description of torsion potentials in pi-conjugated molecules. *J. Chem. Phys.*, 121:3096–3101, 2004.

[154] J. C. Sancho-Garcia and J. Cornil. Anchoring the torsional potential of biphenyl at the *ab initio* level: The role of basis set versus correlation effects. *J. Chem. Theory Comp.*, 1:581–589, 2005.

[155] J. C. Sancho-Garcia and A. J. Perez-Jimenez. Nitrobenzene rotational energy barrier: A survey of several *ab initio* methods. *J. Chem. Phys.*, 119:5121–5127, 2003.

[156] S. Sarman. Biaxial nematic liquid crystal phases of a soft ellipsoid-string fluid. *Phys. Chem. Chem. Phys.*, 2:3831–3839, 2000.

[157] J. Scherer and R. Snyder. Raman-spectra of liquid n-alkanes .2. longditudinal acoustic modes and the gauche-trans energy difference. *J. Chem. Phys.*, 72:5798–5808, 1980.

[158] L. D. Schuler, X. Daura, and W. F. Van Gunsteren. An improved GROMOS96 force field for aliphatic hydrocarbons in the condensed phase. *J. Comp. Chem.*, 22:1205–1218, 2001.

[159] L. D. Schuler and W. F. van Gunsteren. On the choice of dihedral angle potential energy functions for n-alkanes. *Mol. Simulat.*, 25:301–319, 2000.

[160] G. Shanker, M. Prehm, M. Nagaraj, Jagdish K. Vij, M. Weyland, A. Eremin, and C. Tschierske. 1,2,4-oxadiazole-based bent-core liquid crystals with cybotactic nematic phases. *ChemPhysChem*, 15:1323–1335, 2014.

[161] G. Smith and R. Jaffe. Quantum chemistry study of conformational energies and rotational energy barriers in n-alkanes. *J. Phys. Chem.*, 100:18718–18724, 1996.

[162] C. D. Southern, P. D. Brimicombe, S. D. Siemianowski, S. Jaradat, N. Roberts, V. Gortz, J. W. Goodby, and H. F. Gleeson. Thermotropic biaxial nematic order parameters and phase transitions deduced by Raman scattering. *EPL-Europhys. Lett.*, 82:56001, 2008.

[163] C. D. Southern and H. F. Gleeson. Using the full Raman depolarisation in the determination of the order parameters in liquid crystal systems. *Eur. Phys. J. E*, 24:119–127, 2007.

[164] F. Speetjens, J. Lindborg, T. Tauscher, N. LaFemina, J. Nguyen, E. T. Samulski, F. Vita, O. Francescangeli, and E. Scharrer. Low nematic onset temperatures and room temperature cybotactic behavior in 1,3,4-oxadiazole-based bent-core mesogens possessing lateral methyl groups. *J. Mater. Chem.*, 22:22558–22564, 2012.

[165] R. Stannarius, A. Eremin, M. . G. Tamba, G. Pelzl, and W. Weissflog. Field-induced texture transitions in a bent-core nematic liquid crystal. *Phys. Rev. E*, 76:061704, 2007.

[166] B. Stevensson, A. V. Komolkin, D. Sandstrom, and A. Maliniak. Structure and molecular ordering extracted from residual dipolar couplings: A molecular dynamics simulation study. *J. Chem. Phys.*, 114:2332–2339, 2001.

[167] J. P. Straley. Ordered phases of a liquid of biaxial particles. *Phys. Rev. A*, 10:1881–1887, 1974.

[168] S.W.I Sui, K. Pluhackova, and R. Bockmann. Optimization of the OPLS-AA force field for long hydrocarbons. *J. Chem. Theory Comput.*, 8:1459–1470, 2012.

[169] G. Tiberio, L. Muccioli, R. Berardi, and C. Zannoni. Towards in silico liquid crystals. realistic transition temperatures and physical properties for *n*-cyanobiphenyls via molecular dynamics simulations. *ChemPhysChem*, 10:125–136, 2009.

[170] C. Tschierske. Microsegregation: From basic concepts to complexity in liquid crystal self-assembly. *Isr. J. Chem.*, 52:935–959, 2012.

[171] C. Tschierske and D. J. Photinos. Biaxial nematic phases. *J. Mat. Chem.*, 20:4263–4294, 2010.

[172] T. Tsuji, H. Takeuchi, T. Egawa, and S. Konaka. Effects of molecular structure on the stability of a thermotropic liquid crystal. gas electron diffraction study of the molecular structure of phenyl benzoate. *J. Am. Chem. Soc.*, 123:6381–6387, 2001.

[173] S. Tsuzuki, H. Houjou, Y. Nagawa, and K. Hiratani. High-level *ab initio* calculations of torsional potential of phenol, anisole, and o-hydroxyanisole: Effects of intramolecular hydrogen bond. *J. Phys. Chem. A*, 104:1332–1336, 2000.

[174] E van den Pol, A Lupascu, P Davidson, and G Vroege. The isotropic-nematic interface of colloidal goethite in an external magnetic field. *J. Chem. Phys.*, 133, 2010.

[175] E. van den Pol, A. V. Petukhov, D. M. E. Thies-Weesie, D. V. Byelov, and G. J. Vroege. Experimental realization of biaxial liquid crystal phases in colloidal dispersions of boardlike particles. *Phys. Rev. Letts.*, 103, 2009.

[176] van den Pol E., D. M. E. Thies-Weesie, A. V. Petukhov, D. V. Byelov, and G. J. Vroege. Uniaxial and biaxial liquid crystal phases in colloidal dispersions of board-like particles. *Liq. Cryst.*, 37, 2010.

[177] D van der Spoel, E. Lindahl, B. Hess, R. van Buuren, E. Apol, P.J. Meulenhoof, D.P. Tieleman, A.L.T.M. Sijbers, K.A. Feenstra, R. van Drunen, and H.J.C Berendsen. *Gromacs User Manual*, verion 4.0 edition, 2005.

[178] K. Van Le, M. Mathews, M. Chambers, J. Harden, Q. Li, H. Takezoe, and A. Jákli. Electro-optic technique to study biaxiality of liquid crystals with positive dielectric anisotropy: The case of a bent-core material. *Phys. Rev. E*, 79:030701, 2009.

[179] A. G. Vanakaras and D.J. Photinos. Thermotropic biaxial nematic liquid crystals: Spontaneous or field stabilized? *J. Chem. Phys.*, 128, 2008.

[180] N. Vaupotic, J. Szydlowska, M. Salamonczyk, A. Kovarova, J. Svoboda, M. Osipov, D. Pociecha, and E. Gorecka. Structure studies of the nematic phase formed by bent-core molecules. *Phys. Rev. E*, 80:030701, 2009.

[181] F. Vita, I. F. Placentino, E. T. Samulski, and O. Francescangeli. Extraordinary field sensitivity of bent-core cybotactic nematics. *Mol. Cryst. Liq. Cryst.*, 573:46–53, 2013.

[182] F. Vita, T. Tauscher, F. Speetjens, C. Ferrero, E. T. Samulski, E. Scharrer, and O. Francescangeli. Insights into biaxial ordering of bent-core nematics: X-ray diffraction evidence. *Mol. Cryst. Liq. Cryst.*, 611:171–179, 2015.

[183] F. Vita, T. Tauscher, F. Speetjens, E. T. Samulski, E. Scharrer, and O. Francescangeli. Evidence of biaxial order in the cybotactic nematic phase of bent-core mesogens. *Chem. Mater.*, 26:4671–4674, 2014.

[184] J. Wang and T. Hou. Application of molecular dynamics simulations in molecular property prediction. 1. density and heat of vaporization. *J. Chem. Theory Comp.*, 7:2151–2165, 2011.

[185] J. M. Wang, R. M. Wolf, J. W. Caldwell, P. A. Kollman, and D. A. Case. Development and testing of a general amber force field. *J. Comp. Chem.*, 26:114–114, 2005.

[186] M. R. Wilson. Molecular dynamics simulations of flexible liquid crystal molecules using a Gay-Berne/Lennard-Jones model. *J. Chem. Phys.*, 107:8654–8663, 1997.

[187] M. R. Wilson. Molecular simulation of liquid crystals: Progress towards a better understanding of bulk structure and the prediction of material properties. *Chem. Soc. Rev.*, 36:1881–1888, 2007.

[188] M. R. Wilson and M. P. Allen. Structure of trans-4-(trans-4-normal-pentylcyclohexyl)cyclohexylcarbonitrile (cch5) in the isotropic and nematic phases - a computer-simulation study. *Liq. Cryst.*, 12:157–176, 1992.

[189] M.R. Wilson. Unpublished.

[190] M.R. Wilson. Progress in computer simulations of liquid crystals. *Int. Rev. Phys. Chem.*, 24:421–455, 2005.

[191] R. Wrzalik, K. Merkel, and A. Kocot. *Ab initio* study of phenyl benzoate: structure, conformational analysis, dipole moment, IR and Raman vibrational spectra. *J. Mol. Mod.*, 9:248–258, 2003.

[192] X. P. Xuan and C. P. Zhai. Quantum chemical studies of FT-IR and Raman spectra of methyl 2,5-dichlorobenzoate. *Spectrochim. Acta. A*, 79:1663–1668, 2011.

[193] X. Ye, S. Cui, V. F. de Almeida, and B. Khomami. Effect of varying the 1-4 intramolecular scaling factor in atomistic simulations of long-chain N-alkanes with the OPLS-AA model. *J. Mol. Mod.*, 19:1251–1258, 2013.

[194] H. G. Yoon, S. W. Kang, R. Y. Dong, A. Marini, K. A. Suresh, M. Srinivasarao, and S. Kumar. Nematic biaxiality in a bent-core material. *Phys. Rev. E*, 81:051706, 2010.

[195] C. Zannoni. *Advances in the Computer Simulations of Liquid Crystals*, page 116. Kluwer Academic Publishers, 2000.

[196] C. Zannoni. *Advances in the Computer Simulations of Liquid Crystals*, pages 116–117. Kluwer Academic Publishers, 2000.

[197] C. Zannoni. Molecular design and computer simulations of novel mesophases. *J. Mat. Chem.*, 11:2637–2646, 2001.

[198] J. Zhang, J. Su, and H. Guo. An atomistic simulation for 4-cyano-4 '-pentylbiphenyl and its homologue with a reoptimized force field. *J. Phys. Chem. B*, 115:2214–2227, 2011.

[199] Z. Zhang and H. Guo. The phase behavior, structure, and dynamics of rodlike mesogens with various flexibility using dissipative particle dynamics simulation. *J. Chem. Phys.*, 133:144911, 2010.

Appendix A

Conferences, Courses and Seminars Attended

A.1 Conferences

British Liquid Crystal Society Winter Workshop

University of Hull, U.K., 10th-12th January, 2011

British Liquid Crystal Society Conference

University of Durham, U.K., 14th-16th April, 2014

Work presented in poster format.

British Liquid Crystal Society Conference

University of Edinburgh, U.K., 21st-23rd March, 2016

Work presented as a talk (presented by Professor Mark R. Wilson)

A.2 Courses

Introduction to FORTRAN Programming (self taught)

Open University MST209 Mathematical Methods and Models, Blocks 1 - 3 (self taught)

A.3 Publications

Boyd, N.J. and Wilson, M.R., Optimization of the GAFF force field to describe liquid crystal molecules: the path to a dramatic improvement in transition temperature prediction, *Phys. Chem. Chem. Phys*, **17**, 24851 (2015)